THE ELECTRONIC STRUCTURE OF THE (1X1) AND (5X1) SURFACES OF Pt(100) STUDIED BY ANGLE-RESOLVED PHOTOEMISSION SPECTROSCOPY

Miss Wichuda Suraban

การศึกษาโครงสร้างทางอิเล็กทรอนิกส์ของผิวแพลทินัม (100) ชนิด (1x1)

และ (5x1) โดยวิธีโฟโตอิมิสชันสเปกโทรสโกปีแบบแยกแยะเชิงมุม

นางสาววิชุดา สุรบรรณ์

THE ELECTRONIC STRUCTURE OF THE (1X1) AND (5X1) SURFACES OF Pt(100) STUDIED BY ANGLE-RESOLVED PHOTOEMISSION SPECTROSCOPY

Suranaree University of Technology has approved this thesis submitted in partial fulfillment of the requirements for a Doctoral Degree

Thesis Examining Committee

………………………………

(Dr. Worasit Uchai)

Chairperson

………………………………

(Prof. Dr. Takehiko Ishii)

Member (Thesis Advisor)

………………………………

(Prof. Dr. Akito Kakizaki)

Member

………………………………

(Assoc. Prof. Dr. Prasart Suebka)

Member

………………………………

(Dr. Prayoon Songsiririthigul)

Member

…………………………………..   …………………………………….

(Assoc. Prof. Dr. Tawit Chitsomboon)   (Assoc. Prof. Dr. Prasart Suebka)

Vice Rector for Academic Affairs   Dean of the Institute of Science

วิชุดา สุรบรรณ์: การศึกษาโครงสร้างทางอิเล็กทรอนิกส์ของผิวแพลทินัม (100) ชนิด (1x1) และ (5x1) โดยวิธีโฟโตอิมิสชันสเปกโทรสโกปีแบบแยกแยะเชิงมุม (THE ELECTRONIC STRUCTURE OF THE (1X1) AND (5X1) SURFACES OF Pt(100) STUDIED BY ANGLE-RESOLVED PHOTOEMISSION SPECTROSCOPY) อ. ที่ปรึกษา: Prof. Dr. Takehiko Ishii, 240 หน้า. ISBN 974-533-248-8

งานวิทยานิพนธ์นี้ได้ใช้แสงจากเครื่องกำเนิดแสงซินโครตรอนศึกษาโครงสร้างแถบพลังงานพื้นผิวของผิวแพลทินัมชนิด (100) ทั้งบนผิวหน้าที่มีการสร้างใหม่แบบ (5x1) และผิวหน้าที่มีการเรียงตัวปกติแบบ (1x1) โดยใช้เทคนิคโฟโตอิมิสชันสเปกโทรสโกปีแบบแยกแยะเชิงมุม โดยการใช้โมเดลแถบพลังงานการดูดกลืนแสงแบบตรงของอิเล็กตรอน และวัดโฟโตอิเล็กตรอนในแนวตั้งฉากกับผิวของแพลทินัมโดยใช้แสงซินโครตรอนในช่วงพลังงาน 15 ถึง 30 อิเล็กตรอนโวลต์ ทำให้สามารถหาโครงสร้างแถบพลังงานในแนว $\Gamma - \Delta - X$ ของ Brillouin zone สามมิติได้ และจากการวัดอิเล็กตรอนโดยการเปลี่ยนมุมของหัววัด และใช้แสงซินโครตรอนที่พลังงาน 21 และ 25 อิเล็กตรอนโวลต์ ทำให้ได้โครงสร้างแถบพลังงานพื้นผิวของแพลทินัมในแนว $\overline{\Gamma} - \overline{\Delta} - \overline{X}$ และ $\overline{\Gamma} - \overline{\Sigma} - \overline{M}$ ของ Brillouin zone สองมิติ ผลการวิเคราะห์โฟโตอิเล็กตรอนที่หลุดออกมาจากแนวสมมาตรบน Brillouin zone สองและสามมิติของผิวหน้าทั้งสองของแพลทินัม เปรียบเทียบกับโครงสร้างแถบพลังงานซึ่งได้จากการคำนวณพบว่ามีความขัดแย้งกัน โดยงานวิทยานิพนธ์นี้อธิบายความขัดแย้งที่เกิดขึ้น

สาขาวิชาฟิสิกส์   ลายมือชื่อนักศึกษา ....

ปีการศึกษา 2545   ลายมือชื่ออาจารย์ที่ปรึกษา ....

WICHUDA SURABAN: THE ELECTRONIC STRUCTURE OF THE (1X1) AND (5X1) SURFACES OF Pt(100) STUDIED BY ANGLE-RESOLVED PHOTOEMISSION SPECTROSCOPY, THESIS ADVISOR: PROF. Dr. TAKEHIKO ISHII, Ph.D. 240 PP. ISBN 974-533-248-8

PHOTOEMISSION SPECTROSCOPY, SURFACE RECONSTRUCTION, ELECTRONIC STRUCTURE

The electronic structure of the clean reconstructed Pt(100)-(5x1) and unreconstructed Pt(100)-(1x1) surfaces has been investigated by means of angle-resolved photoemission spectroscopy, using synchrotron radiation. Within a direct-transition model, valence-band states on the $\Gamma - \Delta - X$ line are probed in the normal emission mode measurements over a photon energy range from 15 to 30 eV. Through extensive studies carried out in the off-normal emission measurements at selected excitation energies, 21 and 25 eV, and under specific polarization geometries, the surface energy bands can be identified and mapped along two high symmetry lines, $\overline{\Gamma} - \overline{\Delta} - \overline{X}$ and $\overline{\Gamma} - \overline{\Sigma} - \overline{M}$, in the surface Brillouin zone of both surfaces. The experimental results have been compared with the band structure calculation as well as those obtained by experiments by other authors. It is found that some experimental results show a good agreement between the experiments and calculation. However, qualitative discrepancy between the experiments and the calculation has been found in some data. They are discussed in this thesis.

School of Physics   Signature of Student …………….…………

Academic Year 2002   Signature of Advisor …………………..………

Acknowledgments

All of my friends in KEK, especially Miss Hiromi Suzuki and Mrs.Yoshimi Takahashi, for their help in daily life in a foreign city.

The Association of International Education in Japan (AIEJ) and KEK for the scholarship which covered expenses for study and daily subsistence allowance in Tsukuba.

My friends in Suranaree University of Technology for their friendships.

My husband, Satit Boonyaratkalin, for all his care, patience and sacrifice in every detail of my life and for his love.

My mother and family members for their support and love, which cannot be expressed by any words on the earth.

Wichuda Suraban

Contents

Page

Chapter

Contents (Continued)

Contents (Continued)

Contents (Continued)

List of Tables

List of Figures

List of Figures (Continued)

List of Figures (Continued)

List of Figures (Continued)

List of Figures (Continued)

List of Figures (Continued)

List of Figures (Continued)

List of Figures (Continued)

List of Figures (Continued)

Figure   **Page**

List of Figures (Continued)

Figure   **Page**

List of Figures (Continued)

List of Figures (Continued)

Chapter I

Introduction

1.1 Overview of the Study

In this thesis, the electronic structures of the clean reconstructed Pt(100)-(5x1) and unreconstructed Pt(100)–(1x1) surfaces are studied. They have been measured by means of Angle-Resolved Photoemision Spectroscopy (ARPES). Since we need a clean well-defined surface to measure the intrinsic electronic states, a lot of time was used to prepare sample surfaces to be used for the experiments. In this thesis work, the preparation of the clean well-defined surface had occupied the majority of the experimental period. Thus this part presents the important part of the studies.

About twenty years ago, many solid-state physicists and chemists were interested in the investigations of the atomic and electronic structure of solid surfaces. Because of the peculiar environment of the surface, i.e., no transnational symmetry toward the direction normal to the surface layer, the elementary electronic processes occurring there are distinctive. For instance, surface atoms form a two dimensional structure of their own, which is distinguished from the three dimensional structure of the bulk. The two-dimensional system on the surface has provided a variety of interesting physical phenomena, which cannot be encountered in the bulk. Furthermore, the understanding of surface phenomena has great importance in modern high technology. For example, the growth of electronic device materials and electronic processes leading to their useful functions like rectification are quite surface sensitive.

Also, the catalyses utilized in chemical engineering are nothing but surface chemical reactions. The applications of photoemission appear to be one of the promising experimental methods as those of Scanning Tunneling Microscopy (STM). In order to realize the requested resolution and accuracy, one needs a brilliant excitation source. This has resulted in the demand of the third generation synchrotron light sources. This has been realized by now.

Pt is a metal, which is widely used in catalytic processes and as a substrate for magnetic materials in magnetic recording media. In order to use Pt for such industrial applications efficiently, the knowledge of the electronic properties is indispensable. Because the electronic states of valence and core electrons in atoms, molecules and solids determine the essential fraction of their fundamental properties such as physical and chemical ones occurring in, mechanical, thermal, optical, electric and magnetic phenomena. Therefore, experimental probes to obtain information of the electronic structure are crucially important for understanding the microscopic properties of matter.

In case of solids, atomic arrangement and the associated interatomic interactions are also essential in determining the properties of solids. The electronic structure is closely related with the atomic arrangement as well as the electronic structure of the constituent atoms. The surface electronic structure is definitely governed by the atomic arrangement on the surface. On the other hand, the atomic arrangement is crucially governed by the electronic interaction between the constituent atoms. In spite of the importance of the atomic structure, it is not investigated directly in the present thesis. The atomic structure is observed only to find a well-defined surface.

In the present thesis work, the Pt metal surface has been selected as the object of the research. Historically, the Pt metal attracted people's attention as a material for personal ornaments.   Pt is precious because it is rare on the earth. It has a mechanical property to have easy machining and transformation.   It has a chemical property to be very resistant to corrosion.

In the modern industrialized era, people found the excellent catalytic nature of Pt. This material is found to be a good absorber of hazardous toxic species contained in exhausted gases from an automobile.   Thus, a great deal of researches was carried out on this material as a catalyst.   Since the catalytic reactions occur on the surface, it is natural that surface researches have been carried out on this material.

Then it was observed that this material performs the surface reconstruction. Famous cases of the surface reconstruction are found in a Si crystal, which is a semiconductor. In metals, only a few materials are found to make the surface reconstruction. They occur in the late $5d$ transition metal row in the periodic table. Then a question arises: What is the motive force of the surface reconstruction? Does it relate with the nature of the $5d$ states in the pertaining material? Such questions have caused the motivation of selecting Pt as the object of the research.

This thesis will be organized in the following way: In Chapter I, the general introduction to this thesis work along with the purpose of the study is presented. In this part, the necessary background knowledge is described.   Not only the properties of platinum as a bulk are described but also the surface properties are explained. In addition, the electronic structure of both the bulk and the surface is mentioned. Then the theoretical aspects of Photoemission Spectroscopy (PES) and ARPES are described in a practical point of view with emphasis on the relevance to the analyses

to be made in this work. The important excitation source, synchrotron light, is also explained in Chapter I. The subsequent three chapters describe the experimental procedure, experimental results and discussion with summary. In Chapter II, detailed descriptions are presented for the experimental apparatus, the preparation of clean sample surfaces and the practical experimental procedures. Among them, the preparation of the clean sample surfaces is quite important. A lot of time was spent to accomplish this part of work. The whole experimental results are dealt with in Chapter III. A considerable number of photoelectron Energy Distribution Curves (EDC's) used in energy band mapping along with the experimentally drawn energy bands (mapped bands) are exhibited. In Chapter IV, the detailed results are discussed. The comparison of the energy bands obtained experimentally in the present work with available theoretically calculated data is made in this Chapter. Then, finally, a summary of this work and prospects for further studies follow to conclude the thesis.

1.2 Chemical and Solid State Properties of Platinum

Platinum is a *5d* transition metal in which atoms are characterized by partially filled *d*-shells. The electron configuration of atomic Pt expected from the periodic table is [Xe] $4f^{14}5d^86s^2$ where [Xe] represents the electron configuration of Xe. The Xe atom has a closed shell structure as $1s^22s^22p^63s^23p^63d^{10}4s^24p^64d^{10}$. In condensed matter like a metal, however, the electronic state is described by the energy band picture. In case of Pt, the average electron configuration of an atom is [Xe] $4f^{14}5d^96s$. This means that the 5*d* state is hybridized with the 6*s* state and the numbers of 6*s* and 5*d* electrons are fluctuating. The average picture is that one valence electron is in the 6s state and 9 valence electrons are in the 5*d* state. The valence state is totally formed

by 10 electrons and they are well localized around the ionic core. This makes Pt not oxidized in air at any temperature. This is explainable in term of the immobility of oxygen adsorbed on the surface. Oxygen atoms in the surface layer cannot penetrate into the bulk. Thus oxygen layer formed on the surface prevents the further reaction of oxygen atoms with substrate Pt.

On the other hand, Pt is corroded by halogen molecules, cyanides, sulfur and caustic alkali metals. It is soluble in neither hydrochloric nor nitric acid but dissolves in their mixture as aqua regia, forming chloroplatinic acid (H_2PtCl_6) that is an important compound. Catalytic metals are in practical use by being dispersed in porous materials. In pores, very small grains of the catalytic metal with a size of a particle composed of a few atoms are formed. They are produced by a series of chemical reactions in aqueous solutions of reactive elements and the acid mixture as aqua regia followed heat treatments. Repeated synthesization, decomposition and eventual precipitation generate small grains of Pt in pores. In case of the Pt catalyst, a compound like H_2PtCl_6 is formed in the course of the reactions.

The solid state properties of Pt are summarized in Table 1.1. As is found in the table, the crystal structure is face center cubic (fcc) with lattice constant 3.92 $\overset{o}{A}$. Pt is very ductile and malleable.

Pt is extensively used in ornaments, wire, and vessels for laboratory use and many valuable instruments. In such mechanical applications, the ductility (softness) and the malleability are fully utilized. The great durability without corrosion is also an important factor. Because of its low thermal conductivity and chemical stability, Pt is also used for electric contacts, resistance wire, thermocouples, standard weights and laboratory dishes. It should be remarked that its electrical resistivity of 10.4 x 10^{-6}

ohm.cm (see Table 1.1) is 6.7 and 4.7 times as high as those of Cu and Au, respectively. Probably, this is caused by the $5d$ electron contributing to the electron densities at the Fermi level. The same found in the case of the relations between Pd and Ag as well as Ni and Cu.

Since Pt is too soft to be used as a pure metal, it is used in many cases as the form of alloys with harder metals with similar properties, such as osmium (Os, in the $5d$ row with $5d^7 6s$), iridium (Ir, in the $5d$ row with $5d^8 6s$) and rhodium (Rh, in the $4d$ row with $4d^8 5s$).

Important uses of Pt metal are those as catalysts and the substrates for magnetic materials. Pt is perhaps the most widely used meal catalyst in the chemical and petroleum-refining industries (Rodriguez and Kuhn, 1995). Its chemical stability in both oxidizing and reducing conditions makes this metal an ideal catalyst in many applications such as the isomerization of hydrocarbons, olefin hydrogenation, the oxidation of ammonia and carbon monoxide, the synthesis of hydrogen cyanide, etc.

As regards magnetic properties, platinum is the transition metal used for the base for metallic ultrathin films, sandwiches, and multilayers. One can expect new properties to arise from the particular atomic arrangements at the interfaces between magnetic species and Pt as the substrate. This is brought about by the transfer of conduction electrons or d electrons in the valence level. For example, systems of thin transition-metals on Pt with large magnitude of magnetic anisotropy have been sought and several systems with appreciable anisotropic magnetic properties have been found. Their magnetic characteristics have been investigated. A good example is the Co-Pt interface. This system in the ordered tetragonal L 1_0 phase has a magnetic axis with a high permeability along the [001] direction (Leroux et al., 1988; Boeglin et al.,

1992). Such heterogeneous magnetic properties are generated through the surface layers of foreign atoms. They invoke the studies of the surface electronic structure of a Pt crystal as the substrate.

Table 1.1 The solid state properties of platinum (Kittel, 1991). The RT and ATP denote the room temperature and atmospheric pressure, respectively.

Properties	Reported Values
Crystal structure (RT)	Face centered cubic
Atomic number	78
Electron configurations	$[Xe]5d^96s^1$
Lattice parameter (RT)	3.92 $\overset{\circ}{A}$
Density (RT, ATP)	21.47 g/cm^3
Atomic concentration (RT, ATP)	6.62 x10^{22}/cm^3
Nearest neighbor distance (RT, ATP)	2.77 $\overset{\circ}{A}$
Cohesive energies (0K, 1 ATM)	564 kJ/mol, 5.84 eV/atom
Melting points	2045 K
Isothermal bulk modulus	2.783 x 10^{11} N/m^2
Ionization energy (one electron)	8.96 eV
Electrical conductivity (259 K)	0.96 x 10^5 (ohm-cm)$^{-1}$
Electrical resistivity (259 K)	10.4 x 10^{-6} ohm-cm

1.3 Electronic Structure

1.3.1 Energy Band Structure

In metallic materials, the electronic structure is described by the energy band picture in the first approximation. In other words, electrons in metals form energy bands as their energy states. Since the investigation of the electronic state of the Pt metal is the object of the research of this work, a brief description of the energy band is presented in this section.

Suppose there are N atoms in a solid. They are arranged symmetrically in this solid material. The symmetrical layout of atoms in a crystal is verified by the X-ray diffraction pattern that the crystal shows. An atom in a solid is ionized to a considerable extent and charged. Suppose the ion thus formed has a charge amount Ze where e is the charge of an electron. We call this ion as an ionic core. Then, obviously, Z is the valence number of the ionic core. Thus there are ZN electrons in the solid material we are dealing with. Here we do not count the electrons in the core. This is reasonable since core electrons do not contribute the solid state properties.

An electron sees the attractive potential from core ions as

$$V_1 = -\sum_j \frac{Ze^2}{\left|\mathbf{r}_i - \mathbf{R}_j\right|}. \tag{1.1}$$

Here, $\mathbf{r}_i$ and $\mathbf{R}_j$ represent the locations of i-th electron and j-th core, respectively. The repulsive potential acts between a pair of electrons as

$$V_2 = \sum_{i \neq j} \frac{e^2}{\left|\mathbf{r}_i - \mathbf{r}_j\right|}. \tag{1.2}$$

In addition to these, there is repulsive potential working between ion cores as

$$V_3 = \sum_{i \neq j} \frac{Z^2 e^2}{\left| \mathbf{R}_i - \mathbf{R}_j \right|} . \qquad (1.3)$$

If we ignore the magnetic interaction arising from the interactions between magnetic momenta, the hamiltonian describing the electronic state is written as

$$H = -\frac{\hbar^2}{2m} \sum_i \nabla_i^2 - \sum_{i,j} \frac{Ze^2}{\left| \mathbf{r}_i - \mathbf{R}_j \right|} + \sum_{i \neq j} \frac{e^2}{\left| \mathbf{r}_i - \mathbf{r}_j \right|} + \sum_{i \neq j} \frac{Z^2 e^2}{\left| \mathbf{R}_i - \mathbf{R}_j \right|} . \qquad (1.4)$$

In some cases, the spin-orbit interaction is not negligible. This introduces extra complexity. The number of the resulting energy bands increases. The hamiltonian equation is handled by the relativistic treatment. In Pt whose atomic number is large, the relativistic effect is not negligible. In spite of the neglect of the relativistic effect, however, the essence of the energy band treatment is unchanged.

If we can solve the hamiltonian equation

$$H \Phi \ (\mathbf{r}_1 \mathbf{r}_2 ...... \mathbf{r}_{ZN}) = E \Phi \ (\mathbf{r}_1 \mathbf{r}_2 ...... \mathbf{r}_{ZN}) , \qquad (1.5)$$

we obtain the eigen energy and eigenfunction describing the state of the solid. Among four terms in equation (1.4), the last terms, V_3 as in equation (1.3), does not contain the coordinate of an electron. Then it is a constant term in the electronic hamiltonian, which will be omitted from the hamiltonian. The result is given as

$$H = -\frac{\hbar^2}{2m} \sum_i \nabla_i^2 - \sum_{i,j} \frac{Ze^2}{\left| \mathbf{r}_i - \mathbf{R}_j \right|^2} + \sum_{i \neq j} \frac{e^2}{\left| \mathbf{r}_i - \mathbf{r}_j \right|} . \qquad (1.6)$$

It is impossible to solve the hamiltonian equation (1.5) using equation (1.6), since it contains the electron-electron interaction term in equation (1.2).

One method to simplify the hamiltonian equation and derive the one electron equation formally is the Hartree-Fock approximation in which the one electron equation is formed in a self-consistent way. (Kittel, 1963). In the Hartree-Fock approximation, the many electron state $F(\mathbf{r}_1\mathbf{r}_2......\mathbf{r}_{ZN})$ is approximated as the Slater determinant of one electron function $F_n(\mathbf{r}_i)$. By inserting the Slater determinant to the many electron hamiltonian equation in the manner that the energy expectation value is calculated as

$$E = \left\langle F \left| H \right| F \right\rangle. \qquad (1.7)$$

Thus, using equation (1.7), the relation that a one-electron function must satisfy is written down. In this equation many electron interaction parts are involved. If we formally integrate those parts in the self-consistent way, we can obtain the one electron solution in the scheme of the self-consistent approximation.

It is out of the scope of this thesis to describe the Hartree-Fock approximation in a quantitative way. However, it should be pointed out that carrying out this calculation in our system does not make sense. This is because we have ZN electrons, and therefore, we have to solve ZN variables simultaneous equations. Note $NZ \sim 10^{24}$. The Hartree-Fock approximation is useful in a small electron number system like an isolated atom, a molecule or an equivalent system.

Instead, we will make a drastically simplifying assumption. Let us start with one electron. The interactions between electrons are so complicated that the electron sees only the average field. In this average field, the potential acting on one electron

is a function of the coordinate of this electron. All other contributions are averaged out. In the approximation like this, the core ion is regarded as being singly charged. (Z-1) charges are screened by electrons around the core to give resultant single charge. Thus, the total number of electron to consider is N. Then, the hamiltonian is given as

$$H = -\frac{h^2}{2m}\sum_i \left(\tilde{N}_i^2 + V(\mathbf{r}_i) \right). \tag{1.8}$$

With this hamiltonian, the Schrödinger equation is separable. We define the one-electron hamiltonian as

$$H_i \, ° \, -\frac{h^2}{2m}\tilde{N}_i^2 + V(\mathbf{r}_i). \tag{1.9}$$

Similarly, we define the one-electron eigenfunction and the one-electron energy eigenvalue as $f(\mathbf{r}_i)$ and $\varepsilon^{(i)}$, respectively.

It is easy to prove that the solution of the Schrödinger eigenequation (1.5) is given as

$$F = f(\mathbf{r}_I)f(\mathbf{r}_2)\dots\dots f(\mathbf{r}_N)$$

$$\tag{1.10}$$

$$E = e^{(1)} + e^{(2)} + \dots\dots + e^{(N)}.$$

Here, the one-electron Schrödinger eigenequation is given as

$$H_i f(\mathbf{r}_i) = e^{(i)} f(\mathbf{r}_i). \tag{1.11}$$

In what follows, just for convenience, we omit subscript and superscript in treating the one-electron Schrödinger eigenequation as

$$H = -\frac{h^2}{2m}\tilde{N}^2 + V(\mathbf{r}) \tag{1.12}$$

$$Hf(\mathbf{r}) = ef(\mathbf{r}). \tag{1.13}$$

The one-electron potential, $V(\mathbf{r})$, is symmetric in space. The symmetry is the same as that of the crystal, i. e., the solid material we are dealing with. The crystal has both rotational and translational symmetry. Thus the hamiltonian has the similar symmetry. We ignore the mathematical rigorousness and try to understand the situation from observation and intuition. Mathematically, what we describe below are proved by using the group theory.

The crystal symmetry is one described as follows:

(i) A crystal has centers of symmetry. Some kinds of rotation and reflection around one center do not change the crystal. Thus, $V(\mathbf{r})$ is not changed by such symmetry operations.

(ii) There are many equivalent symmetry centers. The translation of a symmetry center by an amount equal to a translational symmetry vector brings the crystal to the same situation as one before the translation is made. Nothing is changed by the translation. The symmetry of a crystal is illustrated schematically in Fig. 1.1 as taking the two dimensional square lattice as an example. The lattice has the four-fold symmetry around a center of symmetry. The lattice consists of symmetry points, which have the translational symmetry in the manner that they are brought to other equivalent symmetry points through an amount equal to an inter-lattice-point spacing. It is convenient to define a primitive translation vector, which is equal to a lattice vector as shown in Fig. 1.1. In the figure, the typical translation directions bringing

the lattice to overlap completely by the translation are shown by solid lines. In fact, there are much more directions that make symmetrical translation than those shown in the figure. It should be pointed out that other ways to define the primitive translation vector exist. The symmetry translation in the three dimensional space is made by the translation vector defined as

$$\mathbf{L} = n_1\mathbf{a}_1 + n_2\mathbf{a}_2 + n_3\mathbf{a}_3 . \qquad (1.14)$$

Here, $\mathbf{a}_i$ (i=1,2,3) are three independent primitive translation vectors and n_i (i=1,2,3) are integers. In the orthogonal lattice, i corresponds to the cartesian coordinate, (x,y,z).

The crystal structure of an ordinary metal is simple. They are the body centered cubic (bcc) lattice, the face centered cubic (fcc) lattice and the hexagonal closed packed (hcp) lattice. There is the simplest lattice structure called the simple cubic (sc) lattice, which is realized only in a special case like a sublattice. The unit lattices are shown in Fig. 1.2.

The simple cubic lattice is formed by piling up cubes. An atom occupies the site at every corner of the cube. The body centered cubic lattice is formed if one more atom occupies at the body center of the cube. The face centered cubic lattice is formed if atoms occupy the centers of six cube faces in addition to the cube corners. The hexagonal closed packed lattice has a more complicated structure. Six atoms occupy hexagon corners. The hexagons pile up compactly to form the hexagonal closed packed structures. If we pile up balls of the same size compactly, we obtain two different closed packed structures according to the horizontal location of atoms in
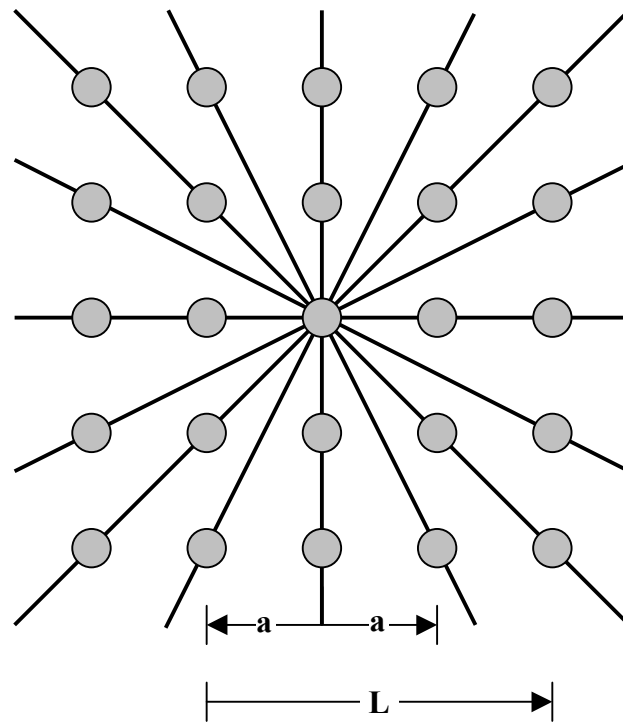
Fig. 1.1 The two dimensional square lattice. **a** is the lattice vector. **L** is a symmetric translation vector. Symmetry centers (location of an atom) are shown with circles. Each symmetry center has the translational symmetry toward the directions to other lattice points. The symmetry translation lines are indicated in the figure.
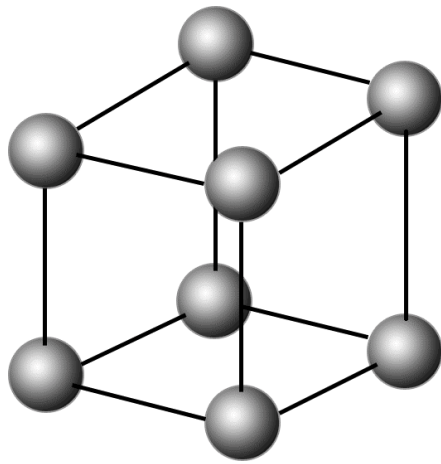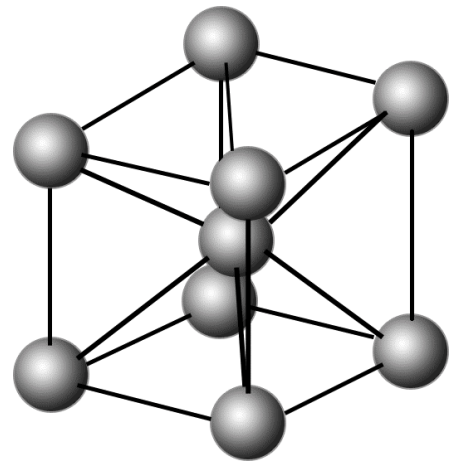
Simple cubic   **Body centered cubic**
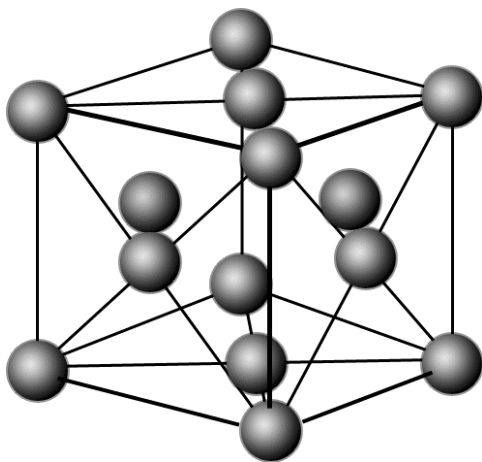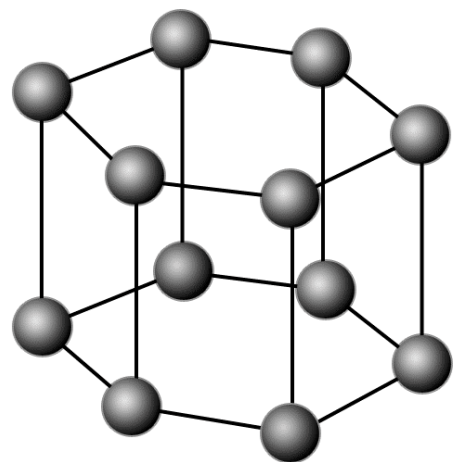
Face centered cubic   **Hexagonal close packed**

Fig. 1.2 Four kinds of typical crystal structure.

the third plane. One is the hexagonal closed packed structure and the other is the face centered cubic lattice. The details are not explained here.

The crystal structure is conveniently described by a unit cell. Whole crystal lattice is formed by the symmetrical translation of the unit cell. A unit cell contains the smallest number of atoms. In Fig. 1.3, a unit cell of the face centered cubic lattice is shown. The unit cell contains only one atom.

The unit cell of the type shown in Fig. 1.3 is not convenient for the practical theoretical treatment. The most convenient and widely used unit cell is the Wigner-Seitz cell (Ziman, 1963).   Hereafter, we abbreviate the Wigner-Seitz cell to the WS cell. The WS cell is formed as follows:

(i)   Select one atomic site in the lattice

(ii) Make planes normal to the line connecting the selected lattice site to the nearest equivalent lattice sites at the corners of the lattice.

Instead of mentioning the geometrical details of the procedure described above, two examples of the WS cells are shown in Fig. 1.4. The drawing in the upper part of the figure is the WS cell of the face centered cubic lattice and that in the lower part of the figure is that of the body centered cubic lattice.

In this way, the potential occurring in the one electron hamiltonian in equation (1.12) has the translational symmetry expressed as

$$V(\mathbf{r} + \mathbf{L}) = V(\mathbf{r}). \qquad (1.15)$$

According to Bloch's theorem (Zeiman, 1963; Kittel, 1963), the solution of the hamiltonian eigenequation under the condition given in equation (1.15) has the form expressed as

$$f_{\mathbf{k}}(\mathbf{r}) = exp(i\,\mathbf{k}\,\mathbf{r})\,u_{\mathbf{k}}(\mathbf{r}) \qquad (1.16)$$

$$u_{\mathbf{k}}(\mathbf{r}+\mathbf{L}) = u_{\mathbf{k}}(\mathbf{r}). \qquad (1.17)$$

Here, $\mathbf{k}$ is determined by the boundary condition. Empirically, the Born-von-Karlmann boundary condition, known as the periodic boundary condition, has been widely used and explained the experimental data quite well. It states

$$V(\mathbf{r}+\mathbf{L}) = V(\mathbf{r})$$

or

$$V(\mathbf{r}+\mathbf{R}) = V(\mathbf{r}). \qquad (1.18)$$

Here, $\mathbf{R}$ defines the size of the crystal in the rectangular (cubic) crystal case as

$$
\begin{aligned}
R_x &= N_x a_x \\
R_y &= N_y a_y \\
R_z &= N_z a_z
\end{aligned}
\qquad (1.19)
$$

R_x, R_y and R_z are the lengths defining the size of the parallelepiped. $N_i(i = x,y,z)$ are large integers of the order of 10^8. With the Born-von-Karlmann boundary condition, $\mathbf{k}$ is given as

$$\mathbf{k} = \xi\,\mathbf{K}_x + \eta\,\mathbf{K}_y + \zeta\,\mathbf{K}_z, \qquad (1.20)$$

with the reciprocal lattice vectors defined as

18
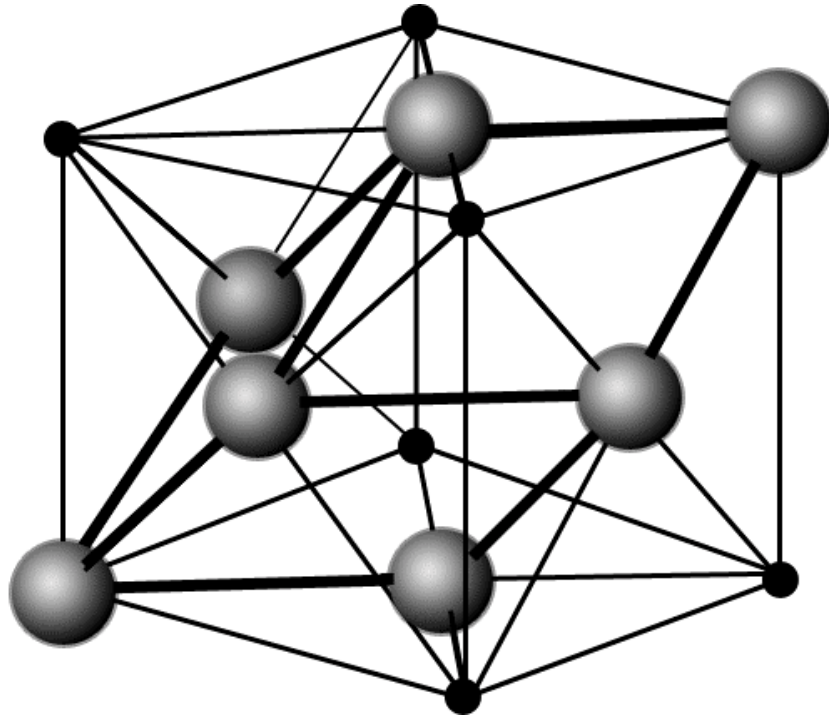
Fig. 1.3 A unit cell of the face centered cubic structure.
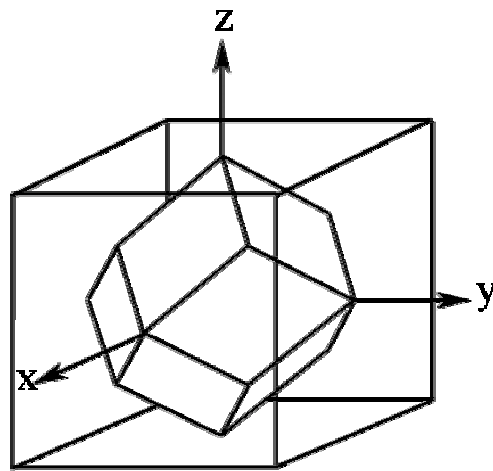
Face centered cubic
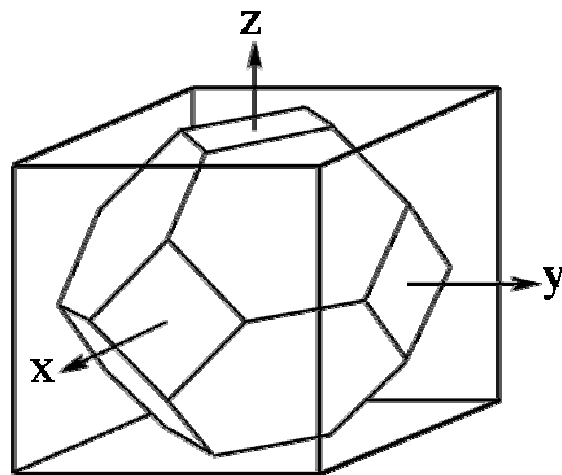
Body centered cubic

Fig. 1.4 Wigner-Seitz cells of cubic lattices.

$$\mathbf{K}_x = \frac{2\pi(\mathbf{a}_y \times \mathbf{a}_z)}{\mathbf{a}_x \cdot (\mathbf{a}_y \times \mathbf{a}_z)}$$

$$\mathbf{K}_y = \frac{2\pi(\mathbf{a}_z \times \mathbf{a}_x)}{\mathbf{a}_y \cdot (\mathbf{a}_z \times \mathbf{a}_x)} \tag{1.21}$$

$$\mathbf{K}_z = \frac{2\pi(\mathbf{a}_x \times \mathbf{a}_y)}{\mathbf{a}_z \cdot (\mathbf{a}_x \times \mathbf{a}_y)}$$

$$\xi = \frac{n_x}{N_x}$$

$$\eta = \frac{n_y}{N_y} \tag{1.22}$$

$$\zeta = \frac{n_z}{N_z}.$$

From the definition given in equation (1.21), the absolute values of the components of

$\mathbf{K}$ are expressed as

$$K_x = \frac{2\pi}{a_x}$$

$$K_y = \frac{2\pi}{a_y} \tag{1.23}$$

$$K_Z = \frac{2\pi}{a_z}.$$

$n_i (i = x, y, z)$ appearing in (1.22) are integers. Since N_i is large an integer number,

ξ, η, and ζ change only by small amounts when n_i change by 1. Obviously, we

see

$$\Delta\xi = \frac{1}{N_x}$$

$$\Delta\eta = \frac{1}{N_y} \tag{1.24}$$

$$\Delta\zeta = \frac{1}{N_z}.$$

In this way, the absolute value of $\mathbf{k}$ is practically regarded as a continuous number. In other words, $\mathbf{k}$ is regarded as a continuous vector.

The space formed by the translation of $\mathbf{K}$ is a sort of lattice. This lattice is called the reciprocal lattice. It is proved that the reciprocal lattice of the sc lattice is also the sc lattice; the reciprocal lattice of the bcc lattice is the fcc lattice; the reciprocal lattice of the fcc lattice is the bcc lattice. In case of the hcp lattice, the situation is complicated and we do not describe it here. When we specify the lattice structure, we usually specify that of the real space.

The function described as equation (1.16) is called the Bloch function. The energy eigenvalues of equation (1.13) and the corresponding eigenfunctions are obtained by solving equation (1.13) in the unit cell, since the eigenfunction, $u_{\mathbf{k}}(\mathbf{r})$, is translationally symmetric as shown in equation (1.17).

Here, it should be remarked that the energy eigenvalues, ε, of equation (1.13) is a periodic function of $\mathbf{k}$ as

$$\varepsilon\,(\mathbf{k}+\mathbf{K}_{\ell}) = \varepsilon\,(\mathbf{k}).\qquad\qquad(1.25)$$

$\mathbf{K}_{\ell}$ is defined as

$$\mathbf{K}_{\ell} \equiv (\lambda\,\mathbf{K}_{\mathrm{x}},\ \mu\,\mathbf{K}_{\mathrm{y}},\ \nu\,\mathbf{K}_{\mathrm{z}})\qquad\qquad(1.26)$$

where $\lambda,\ \mu$ and ν are integers. We express three integers $(\lambda,\ \mu,\ \nu)$ as ℓ symbolically. The relation represented as (1.25) is not obvious. The relation (1.25) is based on the fact that the reciprocal lattice space is periodic with a period of the

translation vector, $\mathbf{K}_\ell$. Thus, the corresponding eigenstate must be translationally symmetric in the $\mathbf{k}$ space with the translation vector, $\mathbf{K}_\ell$. This is written as

$$\phi_{\mathbf{k}+\mathbf{K}_\ell}(\mathbf{r}) = \phi_{\mathbf{k}}(\mathbf{r}). \tag{1.27}$$

This immediately tells us that equation (1.25) holds. If the relation

$$u_{\mathbf{k}+\mathbf{K}_\ell}(\mathbf{r}) = e^{-i\mathbf{K}_\ell \cdot \mathbf{r}} u_{\mathbf{k}}(\mathbf{r}) \tag{1.28}$$

is fulfilled, the relation (1.27) holds.

Since the energy eigenvalues are periodic, we have to consider the energy states only in the unit cell. The unit cell is defined as

$$-\frac{\mathbf{K}_1}{2} \leq \mathbf{k} \leq \frac{\mathbf{K}_1}{2}. \tag{1.29}$$

From equation (1.23), the condition (1.29) is more definitely expressed as

$$\begin{aligned}
-\frac{\pi}{a_x} \leq k_x \leq \frac{\pi}{a_x} \\
-\frac{\pi}{a_y} \leq k_y \leq \frac{\pi}{a_y} \\
-\frac{\pi}{a_z} \leq k_z \leq \frac{\pi}{a_z}.
\end{aligned} \tag{1.30}$$

The space confined in the region specified by relation (1.30) is called the Brillouin zone or the first Brillouin zone. Since the Brillouin zone is the unit cell, the WS cell, of the reciprocal lattice space, the border is depicted easily. Three examples are shown in Fig. 1.5. They are for sc, fcc, and bcc lattices. It should be remarked that

the reciprocal lattice of the fcc lattice has the bcc structure and that of the bcc lattice has the fcc structure.

The energy eigenvalues are obtained by solving the hamiltonian eigen-equation (1.13) in the unit cell, i.e., the WS cell. First we assign $\mathbf{k}$. Then we insert the Bloch function with this $\mathbf{k}$ into equation (1.13) and solve it.

The WS cell has the center of symmetry. Therefore the WS cell has the rotational and mirror reflection symmetry. In solving the eigenequations, the use of the results provided by the group theory is quite helpful. It is out of scope of this thesis to touch the group theory, since it is found in many textbooks (Heine, 1960; Kittel, 1963; Slater, 1965). Suppose that there are some special points, axes or mirror planes in the WS cell of the reciprocal lattice space and the rotation or mirror operation with respect to them do not change the reciprocal lattice space. The assemblies of such operations form the groups. The operations commute with the hamiltonian and the dimension of the irreducible representation presents the degeneracy states of the eigenstate.

The solutions of the eigenequation (1.13) in the WS cell are degenerate in general. However, for $\mathbf{k}$ not at the symmetric points, all the degeneracy is lifted. In this case, the number of the basis functions necessary to solve eigenequation by the perturbation approach is appreciable and solving the eigenequation is almost impossible. The state degeneracy reduces the number of the basis functions. Thus, in the energy band treatment, the only the energy eigenvalues with $\mathbf{k}$ is such symmetric points or lines are calculated. In recent years, the computer capacity and the speed of processing have greatly enhanced. This has increased the dimension, the size, of the secular equation to be solved to a great extent and the accuracy of the calculated
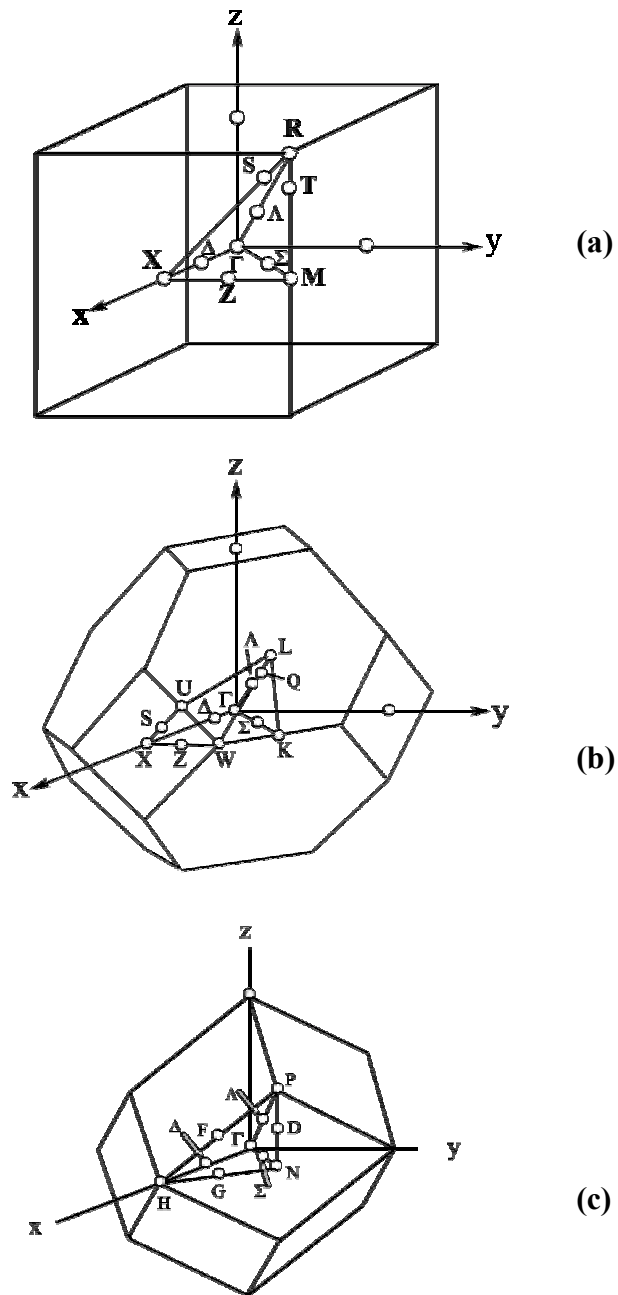
Fig. 1.5 Three examples of the Brillouin zone. (a) sc lattice. (b) fcc lattice. (c) bcc lattice. See text for various notations in each figure.

results. However, the situation that the calculation is made for highly symmetric points or lines has not been changed.

Examples of such symmetric points and lines are indicated with various notations in Fig. 1.5. The notation was first used by Bouchaert, Smoluchowski and Wigner (1936) and the notation has been employed by many authors. Now it is the world standard. The notation that they used to specify the energy bands have also been widely used. It appears that the characters used in the notation have no specific meaning. They are just the signs to distinguish different points or lines.

The energy eigenvalues are the function of $\mathbf{k}$ that varies continuously. Accordingly $\varepsilon_n(\mathbf{k})$ varies continuously. Here n distinguishes the different eigenstate as $u_{n\mathbf{k}}(\mathbf{r})$. For $\mathbf{k}$ in the Brillouin zone, $\varepsilon_n(\mathbf{k})$ is confined in the range as

$$\varepsilon_n^{(\min)} \le \varepsilon_n(\mathbf{k}) \le \varepsilon_n^{(\max)}$$

$$\text{for } -\frac{\mathbf{K}_1}{2} \le \mathbf{k} \le \frac{\mathbf{K}_1}{2}$$

(1.31)

Since $\varepsilon_n(\mathbf{k})$ is an even function of $\mathbf{k}$ (Kittle, 1963), $\varepsilon_n^{(\min)}$ and $\varepsilon_n^{(\max)}$ occur in the range $0 \le \mathbf{k} \le \frac{\mathbf{K}_1}{2}$ and $-\frac{\mathbf{K}_1}{2} \le \mathbf{k} \le 0$. Since $\varepsilon_n(\mathbf{k})$ is continuous and confined in a finite range, it appears to have a finite width. This is contrasted to the case of an isolated atom for which the eigenvalues are the energy levels. Thus the assembly of the energy eigenvalues specified by $\varepsilon_n(\mathbf{k})$ is called the energy band. In case where we draw $\varepsilon_n(\mathbf{k})$ as a function of $\mathbf{k}$, the curve is referred to as the energy band dispersion curve or just dispersion curve. The dispersion curves are illustrated schematically in Fig. 6. In practice, the notation such as

$\Gamma_1, \Gamma_2, \Gamma_{12}, \Gamma_{25}, ...,\Delta_1, \Delta_2,...,X_1,X_2,...,\Lambda_1,\Lambda_2,...,\Sigma_1,\Sigma_2,...$ etc. are used instead of $\varepsilon_1, \varepsilon_2, \varepsilon_3,...$. The energy bands, which can be occupied by electrons, are called the allowed bands and the energy regions between adjacent allowed are called the forbidden bands. The size of the forbidden band, the shortest distance between two adjacent bands is called the band gap. The periodic nature of the energy bands is shown in Fig. 1.7.

Electrons occupy an energy band successively from the low energy to the high energy. $2N$ electrons can occupy one band. One $\mathbf{k}$ site is occupied by two electrons with opposite spins. If a band is filled with electrons completely and the bands above it are completely empty, the corresponding material is an insulator. If a band filled up to a certain level and the level above its is empty, the material is a metal. The level, up to which in a band is filled with electrons, is called the Fermi level. In an insulator, the Fermi level is located halfway in the band gap. If the band gap of a material is very narrow, the material is a semiconductor. The location of the Fermi level of a semiconductor in the band gap is decided by the locations of the levels of impurities such as donors and acceptors. The locations of the Fermi levels in three types of the solids are shown in Fig. 1.8. In the figure, small dots represent the situation that the energy band is occupied. Panel (a) is for a metal, (b) for an insulator and (c) for a semiconductor.

Practical calculation to obtain $\varepsilon(\mathbf{k})$ is carried out by various approximations. Some approximations are very useful in understanding the essence of the energy band, although they are not used in the practical calculations. They are the nearly free electron approximation and the tight binding approximation. They are found in every

textbook on solid state physics and we will not explain them here. Other approximations are

- Orthogonalized plane wave (OPW) approximation

- Pseudopotential approximation

- Augumented plane wave (APW) approximation

- Green function method (Korringa-Kohn-Rostocker:KKR method)

- Xα approximation

- Generating function method.

Recently, the capacity and the speed of computers are quite large and high, the generating function method is widely used by many authors. If we want to introduce the spin-orbit interaction, we have to use the relativistic formalism. The Xα method is to introduce the effect of the correlation interactions. Although the method is basically the one-electron approximation, the correction to the complete neglect of the correlation is made to a considerable extent.

In concluding this part of the section, two examples of calculated energy bands are presented in Figs. 1.9 and 1.10. In Fig. 1.9, the energy band dispersion curves for Na metal are shown (Inoue, Asano and Yamashita, 1971). In Fig. 1.10, the energy band dispersion curves of Ni calculated by Moruzzi et al. are presented (Moruzzi, Janak and Williams, 1978). Figure 1.11 shows the comparison of the angle-resolved photoemission data and the calculated energy band structure for Cu (111) (Thiry, Chandesris, Lecante, Guillot, Pinchaux and Petroff, 1979).

An important quantity describing the energy states of a solid material is the density of states (DOS). DOS indicates the number of states in the unit energy range.
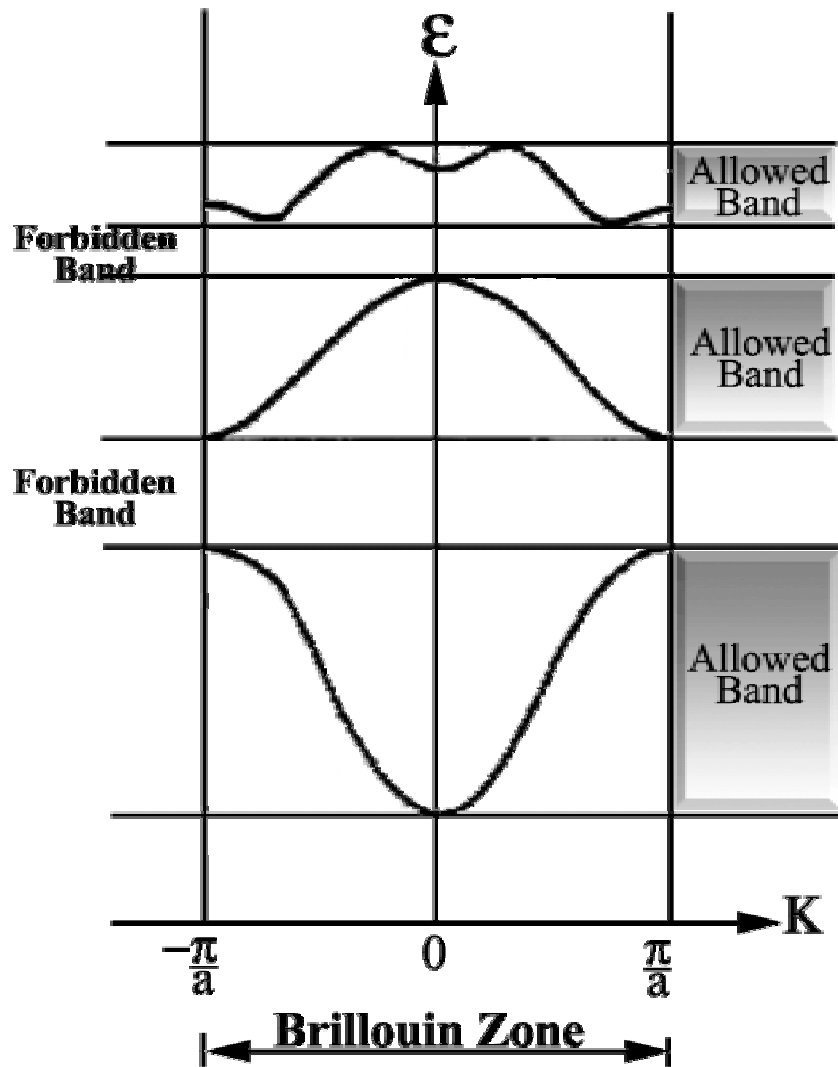
Fig. 1.6 Schematic illustration of energy bands.
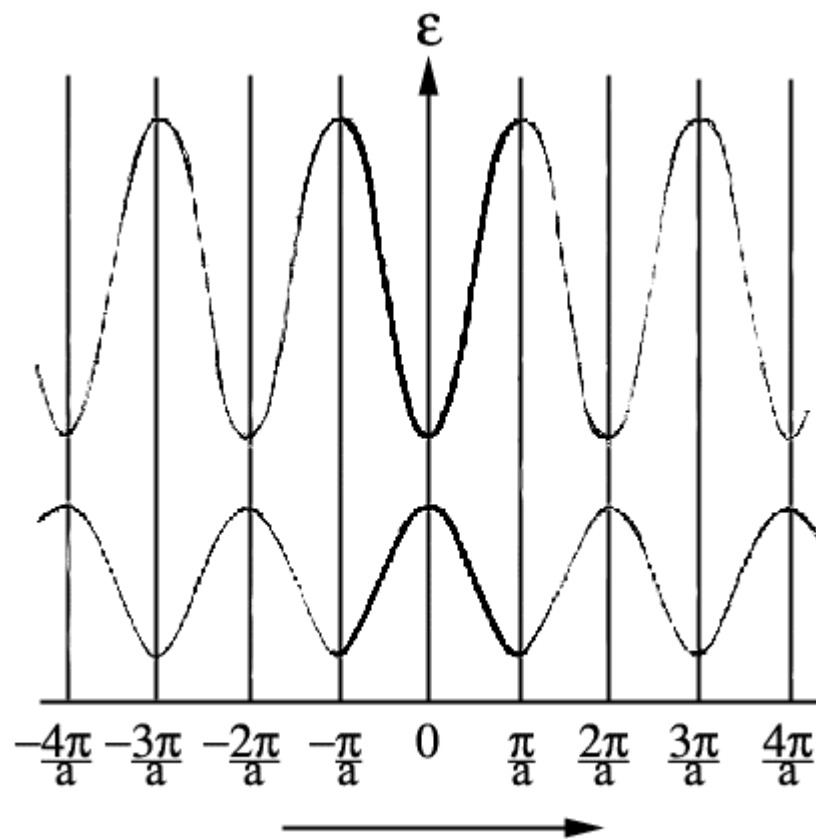
Fig. 1.7 Schematic illustration of the periodic nature of energy bands.
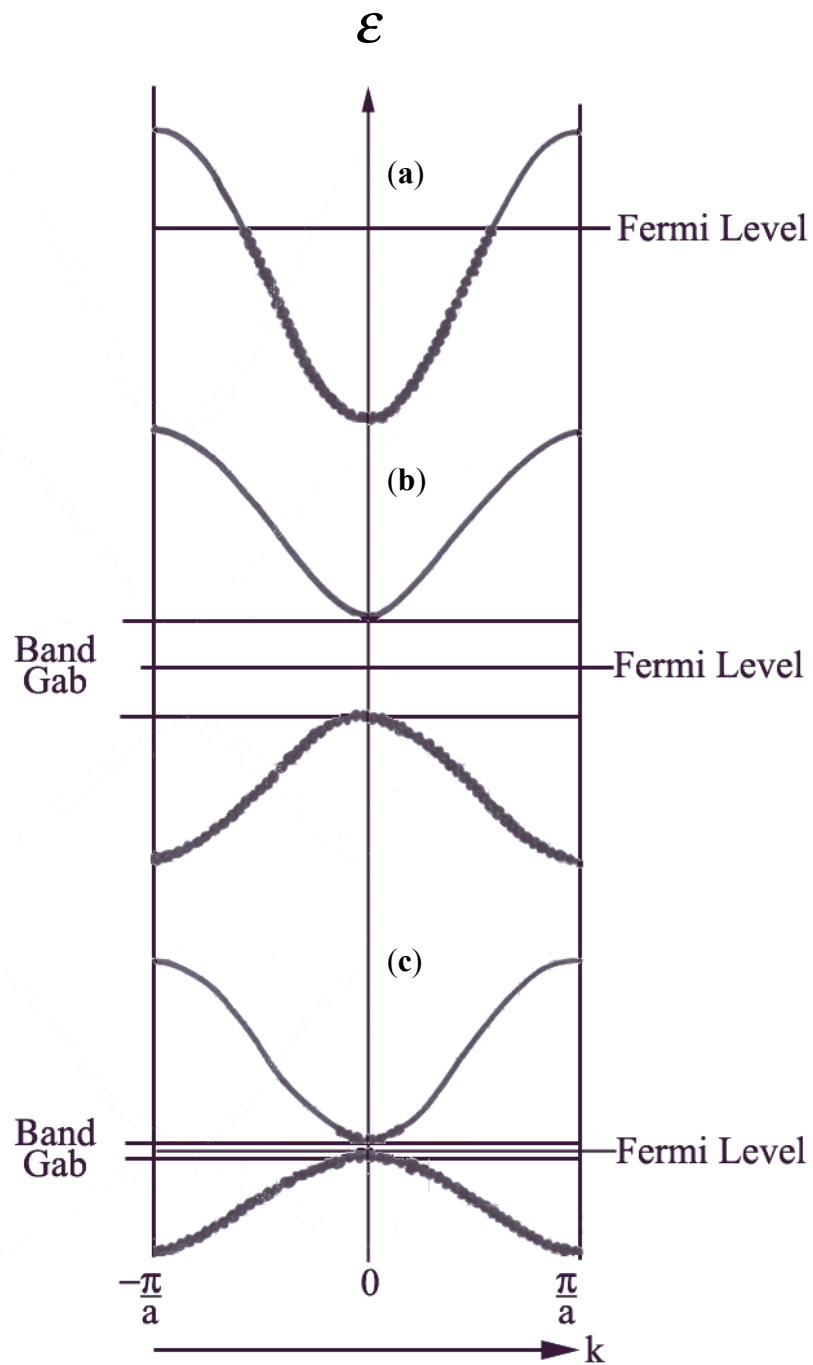
Fig. 1.8 Three types of solids. (a) Metal. (b) Insulator. (c) Semiconductor. Small dots represent the occupation of bands by electrons.

This is obtained by summing up all possible state number in the energy range from ε to $\varepsilon + d\varepsilon$ and the dividing the sum by $d\varepsilon$ as

$$D(\varepsilon) \ d\varepsilon = \frac{2}{(2\pi)^3} \int\int\int_{\varepsilon}^{\varepsilon + d\varepsilon} d\,\mathbf{k} \qquad (1.32)$$

$$= \frac{2}{(2\pi)^3} \int\int_{\varepsilon} \frac{d\,S}{|\nabla_k \varepsilon(\mathbf{k})|}, \qquad (1.33)$$

where $d(\varepsilon)$ is DOS. The surface integration is carried out on the surface of a given constant energy. When the energy band calculation is made, DOS is calculated numerically using equation (1.32). An example of calculated DOS curve as compared with measured photoelectron energy distribution curve for $CeCu_2Si_2$ is shown in Fig. 1.12. (Soda, Mori, Onuki, Komatsubara and Ishii, 1988).

1.3.2 Energy Band Structure of Pt

Calculated Energy Band Structure of Pt

The energy band structure of the Pt metal has been calculated by many authors (Mackintosh, 1966; Andersen and Mackintosh, 1968; Andersen, 1970; Smith, 1974; Ray, Chowdhuri and Chatterjee, 1983; Leschik, Courths, Wern, Hüfner, Eckardt and Noffke, 1984; Eckardt, Frische, Noffke, 1984; Tamura, Piepke and Feder, 1989; Needs and Mansfield, 1989; Stampfl, Martin, Gardner and Bradshow, 1995). The calculations cover not only the bulk band structure but also the surface band structure. As an example the E($\mathbf{k}$) curves calculated by Andersen and Mackintosh (1968) with the Relativistic Augmented Plane Wave method (RAPW) are shown in Fig. 1.13. The calculations were performed using muffin tin potentials constructed from self-consistent Dirac-Slater atomic charge density. The calculations were made along
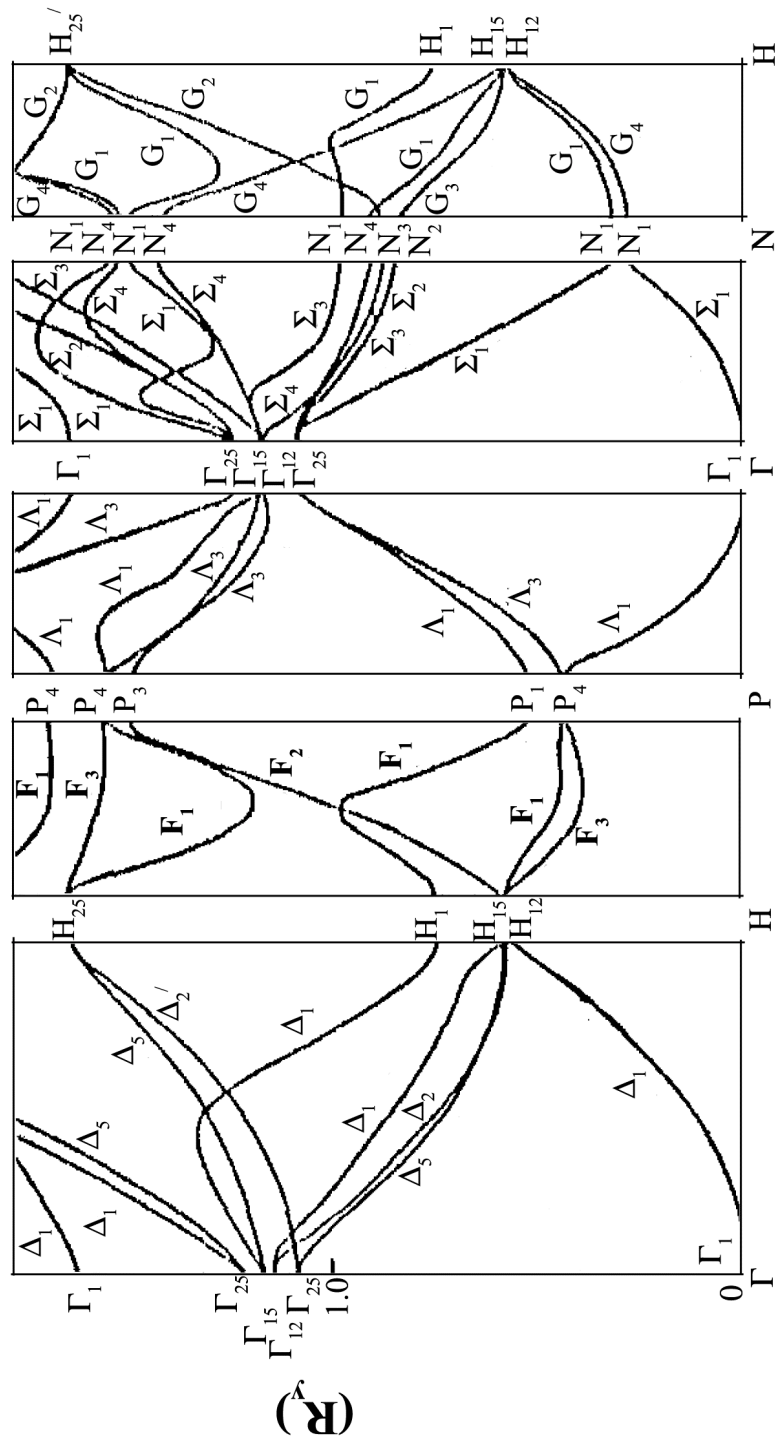
Fig. 1.9 The energy band structure of Na.

Fig. 1.10 The energy band structure of Ni.
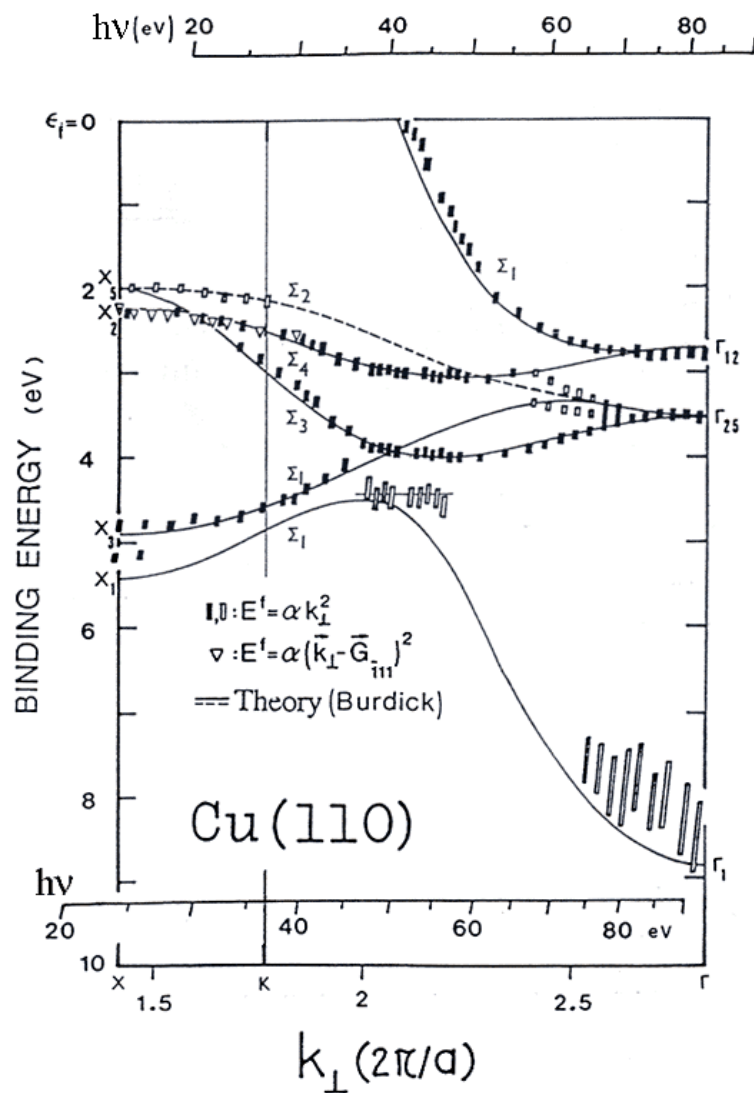
Fig. 1.11 Energy band dispersion determined by normal emission angle-resolved photoemission (ARPES). Rectangles: Experimental points. Solid lines: E-k curves calculated by the APW method. Broken line: E-k curve, the emission from which is forbidden for the normal emission. Data points are obtained by tilting the sample. Filled symbols: Well-defined peaks in energy distribution curves (EDC). Open symbols: Weak features and shoulders. Open triangles: Umklapp lines in EDC.
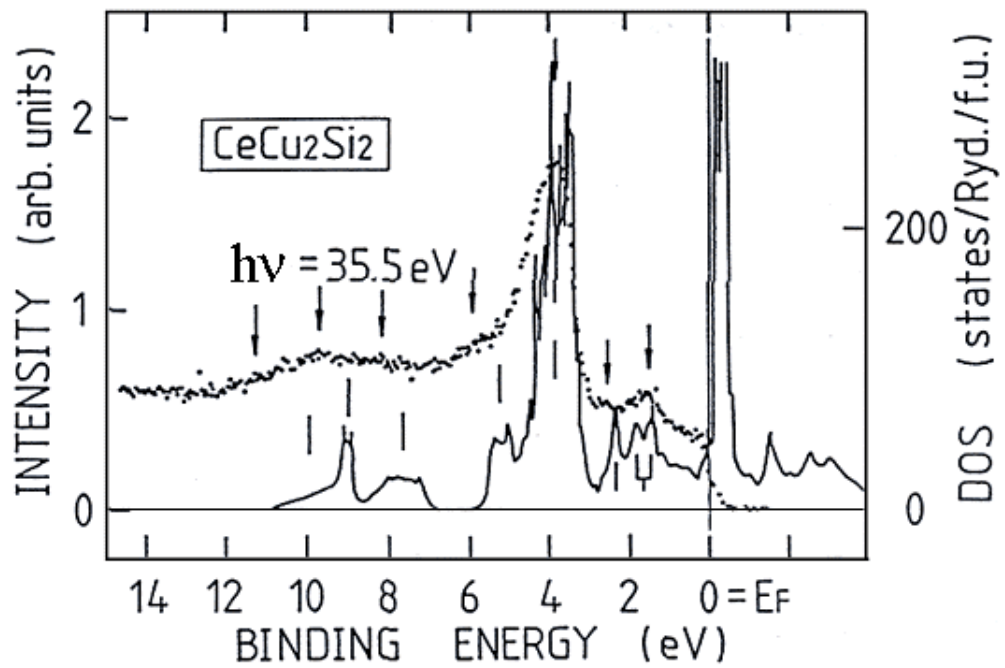
Fig. 1.12 Comparison of the calculated density of states (DOS) curve with the measured energy distribution curve (EDC) for CeCu$_2$Si$_2$. Features in the DOS curve are shown by vertical bars and those in the EDC by arrows. The energy of excitation light is 35.5 eV.

the lines of high symmetry. Relativistic effects are quite important for the heavier elements like Pt. In the heavy atom, the spin-orbit interaction is strong and the relativistic effect is not negligible. Since the spin-orbit interaction is taken into account, the energy bands are described by the double space group. As a measure of the widths of the d bands, including relativistic effect, the energy separation between the uppermost X_7^+ and the lowermost X_6^+ levels or the separation between the uppermost L_4^+ L_5^+ and the lowermost L_5^+ levels, may be used. Both measures show that the width of the d band of the $5d$ transition metal is 1.34 times as large as that of the $4d$ transition metal. On the other hand, the width of the d band of the 10-valence-electron metal is larger than that of the 9-valence-electron metal. Of the increment of the width by a factor of 0.22, about a half is considered to be caused by the decrease in the lattice constant arising from the addition of a d electron. Another case of the variation in the width of the virtual d level is ascribable to the change in the potential at one lattice site.

Andersen and Mackintosh also calculated the energy bands along the symmetry line Δ in the nonrelativistic case using the same Dirac-Slater potential as in the relativistic calculation. It is found that relativistic effects lowers the $6s$-like $\Gamma_1(\Gamma_6^+)$ level by 0.25 Ry (3.4 eV) in Pt. The comparison of the value with that obtained by the first-order perturbation calculation on the nonrelativistic atom indicates that this lowering results from a large negative mass-velocity term and a compensating positive Darwin term. Apparently the sp band is broadened and lowered with respect to the d band by the mass velocity and Darwin terms, but at the Fermi level, near the top of the d band, the effects are relatively small for Pt. The d-

band narrowing due to mass-velocity and Darwin corrections compensates the band broadening due to the spin-orbit splitting at the top of the band (X_5 and L_3). Therefore, the overall effect of the relativistic terms on the total width of the *d* band is apparently small. However, the spin-orbit splitting are important for the shape of the Fermi surface and the Fermi momenta. The cross sections of Fermi surface in the (100) and (110) planes obtained by Andersen and Mackintosh are shown in Fig. 1.14. The change in the Fermi surface due to the surface reconstruction is very interesting regarding the band nesting.

The interesting band structure of Pt is the relativistic self-consistent band structure calculated by Noffke and Eckardt (Fritsche, Noffke, and Eckardt, 1987). It was referred in many published papers (Wern, Courths, Leschik and Hüfner, 1985; Venus, Garbe, Suga, Schneider and Kirschner, 1986; Garbe and Kirschner, 1989; Irmer, David, Schmiedeskamp and Heinzmann, 1992). Figure 1.15 shows the bands.

Band Structure of Pt from PES Experiments.

The band structure of Pt has been investigated by means of photoemission by several authors (Mills, Davis, Kevan, Thornton and Shirley, 1980; Leschik Courths, Wern, Hüfner, Eckardt and Noffke, 1984; Wern, Leschik, Hau and Courths, 1984; Wern, Courths, Leschik and Hüfner, 1985). The data obtained, however, are much less complete than those of the noble metals. This has experimental reasons that the EDC's for the filled bands of this metal are less sharp. This is caused by shorter hole lifetimes. DOS at the Fermi energy is high as shown in Fig. 1.16. The DOS curve shown in Fig 1.16 was calculated by Ray, Chowdhuri and Chatterjee (1983). During the photoexcitation process leading to the emission of an electron occupying the
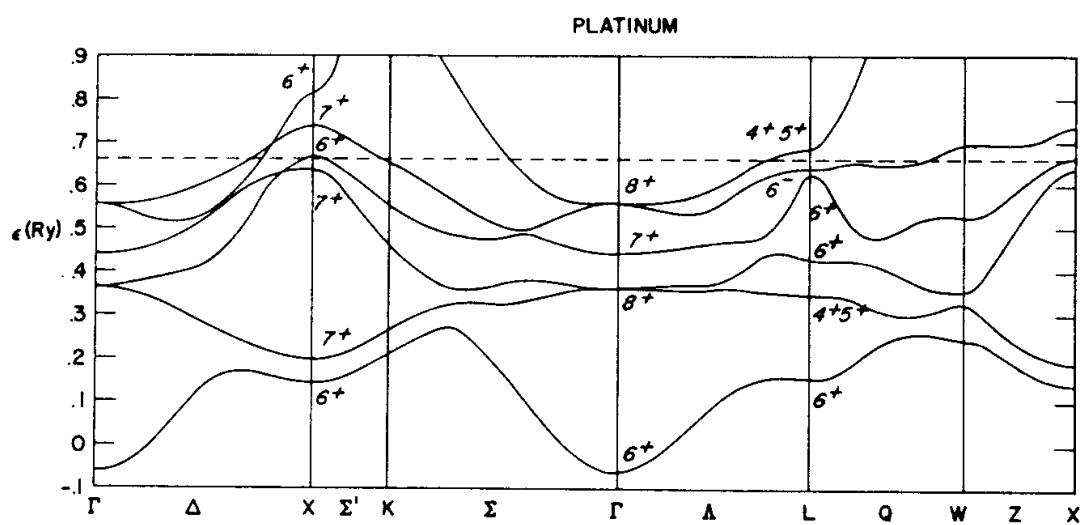
Fig. 1.13 Relativistic energy bands of Pt as calculated by Mackintosh. Double-group labeling has been used.
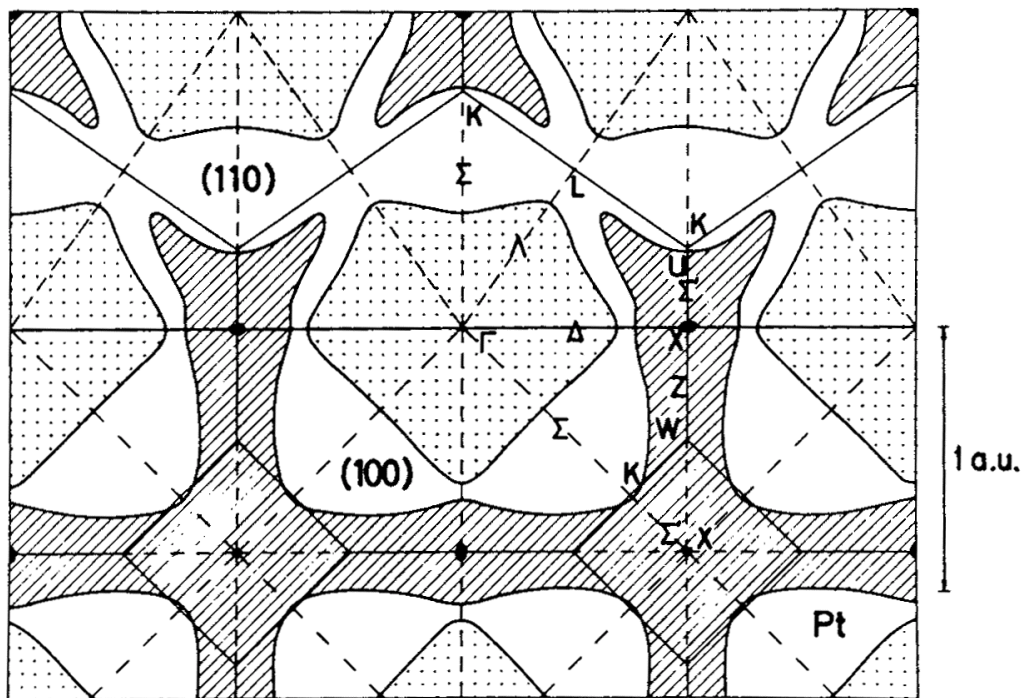
Fig. 1.14 Section of the Fermi surface of Pt in the (100) and (110) planes in the periodic zone scheme. This metal has a closed electron surface of the primary *s-p* character, and one closed and one open hole surface of primarily *d*-character.
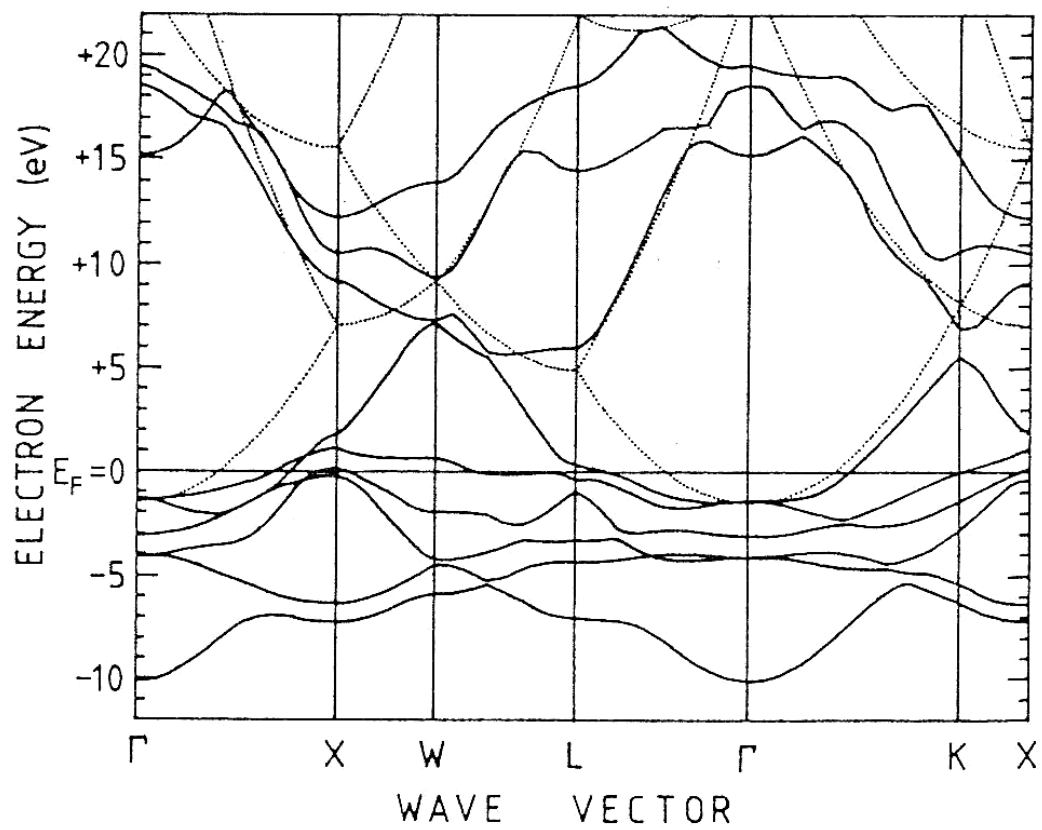
Fig. 1.15 The relativistic band structure of platinum along high symmetry lines.

valence band, a photoproduced hole is destroyed the interband Auger effect as shown in Fig. 1.17. The probability of the intraband Auger transition is proportional to the densities of states of electrons making the transition. The high densities of states around the Fermi level enhance the transition probability for the Auger electron emission from the levels located near the Fermi level. Accordingly, the lifetime of the valence band hole created by excitation light becomes short. In the case where the emission of a primary photoelectron and the subsequent Auger emission occur almost as one process without definite relaxation of the hole state, the high probability of the Auger emission makes the hole lifetime short and obscuring the final state of the photoemission owing to the uncertainty principle (the intraband resonance). Thus, the corresponding photoemission line is broadened.

On the other hand, Pt is an interesting metal in physi-and chemisorption studies. Therefore the precise knowledge of this metal is of high interest for an understanding of the chemical reactions that occur on it. Among the investigations of band structures of Pt, those of the Pt(111) surface have been studied mostly. The reason is that this surface is the least difficult to prepare and characterize because it is close packed and does not tend to reconstruct. In addition this surface does not give rise to emission from the secondary cone as suggested by Mahan (1975), the analysis is simplified.

The band structure of the Pt(100) surface has been studied by Thornton, Davis, Mills and Shirley (1980). They used synchrotron radiation to record angle-resolved normal photoemission spectra of the clean reconstructed Pt(100)-(5x1) structure in the photon energy range 6 eV $\leq$ hν $\leq$ 32 eV. The results of their work are presented in Fig. 1.18. The other published band structure of the Pt(100) surface is that obtained

by Stampfl, Martin, Gardner and Bradshaw (1995). They carried out angle resolved photoemission measurements to map the surface band structure along two high symmetry lines $\overline{\Gamma}$-$\overline{\Sigma}$-$\overline{M}$ and $\overline{\Gamma}$-$\overline{\Delta}$-$\overline{X}$ of the reconstructed (5x1) and unreconstructed (1x1) phases. Here, their result on the (1x1) phase is presented in Fig. 1.19. Stampfl et al. found significant difference between the surface electronic structures at the Fermi edge of the (1x1) and (5x1) phases of Pt(100). The surface Fermi-surface disappears on reconstruction. There a very flat nondispersing band is left at about 0.2 eV below the Fermi level and it covers the nearly entire reduced surface Brillouin zone. Furthermore, the occurrence of nesting was found. The nesting vector*s* spanning around the $\overline{X}$ point on the (1x1) phase are found to be exactly the same size as that of on side of the (5x1) phase supercell. Although this observation did not show that this system exhibits a Peierls-like distortion, the surface Fermi-surface is very well nested. It suggests that Pt may exhibit spin-density waves if the appropriate conditions are satisfied.

The other interesting observation on Pt(100) is the band structure above Fermi energy which was obtained by Drube, Dose and Goldmann (1988). They carried out angle-dependent inverse photoemission experiments at photon energy $h\nu = 9.5$ eV on the (1x1) and (5x20) surfaces. These isochromat results show clear evidence for bulk band transitions, which are intensity-modulated by the reconstruction. Their energy positions remain stationary. Transitions into image potential states located outside the surface were observed on both faces at 0.6 ± 0.2 eV below the vacuum level. A surface band that located near the $\overline{X}$ point in the surface Brillouin zone was identified on the (1x1) surface.
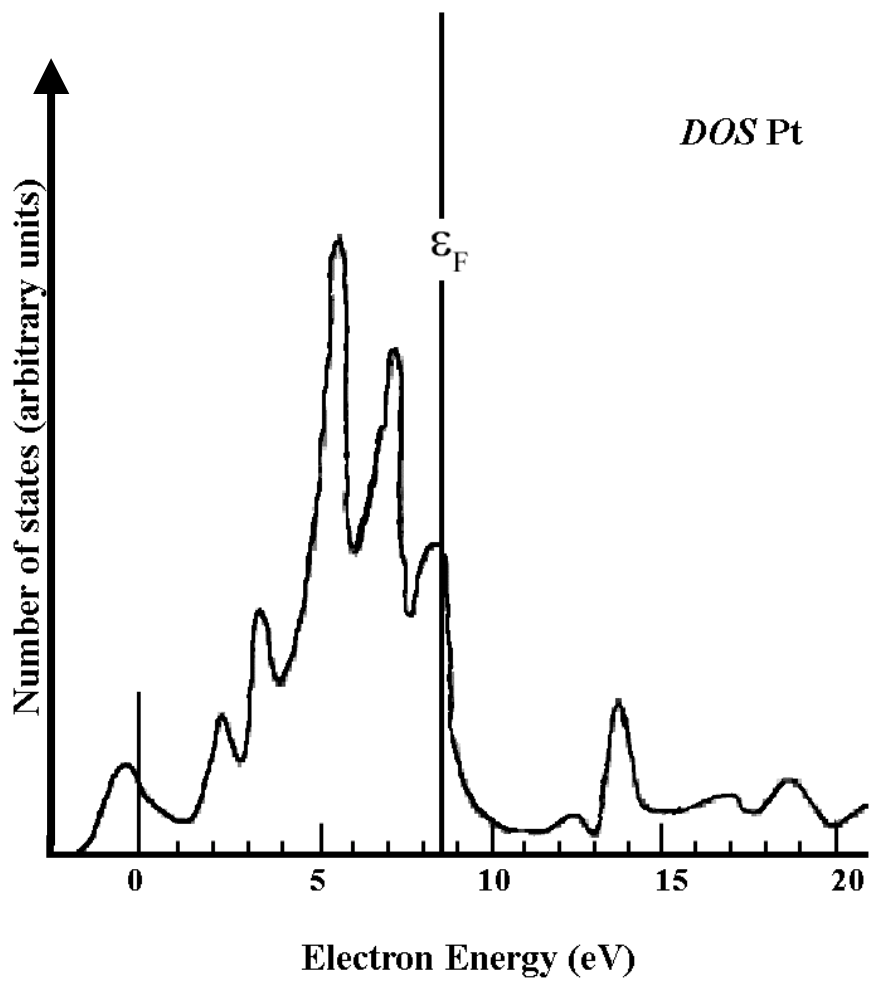
Fig. 1.16 Density of states (DOS) of Pt (Ray, Chowdhuri and Chatterjee, 1983).
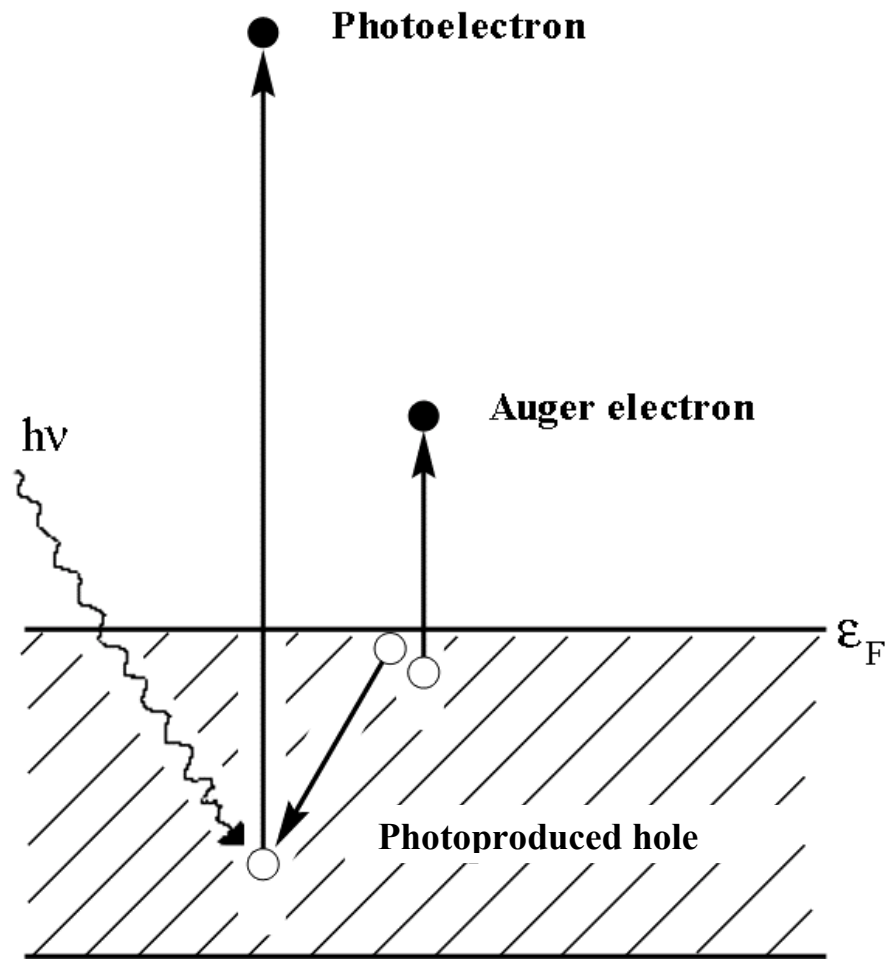
Fig. 1.17 Intraband Auger transition and a photoproduced hole.
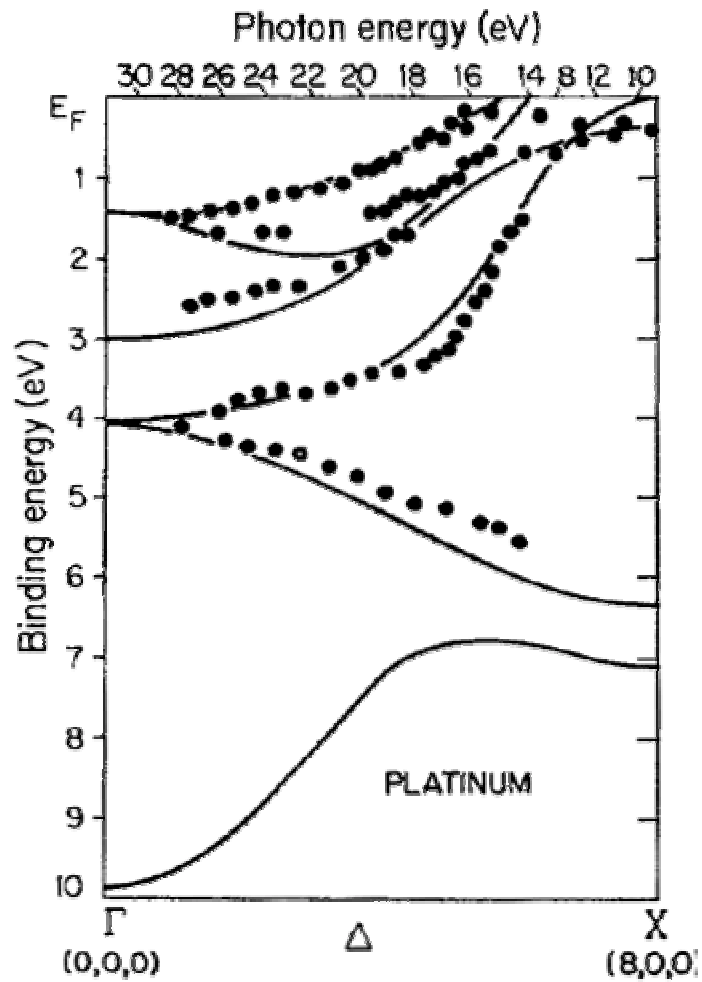
Fig. 1.18 The normal emission band structure of Pt(100)-(5x1) along Δ direction of

Thornton's work (Thornton et al., 1980). The solid lines represent the

band structure calculated by Andersen (1970).
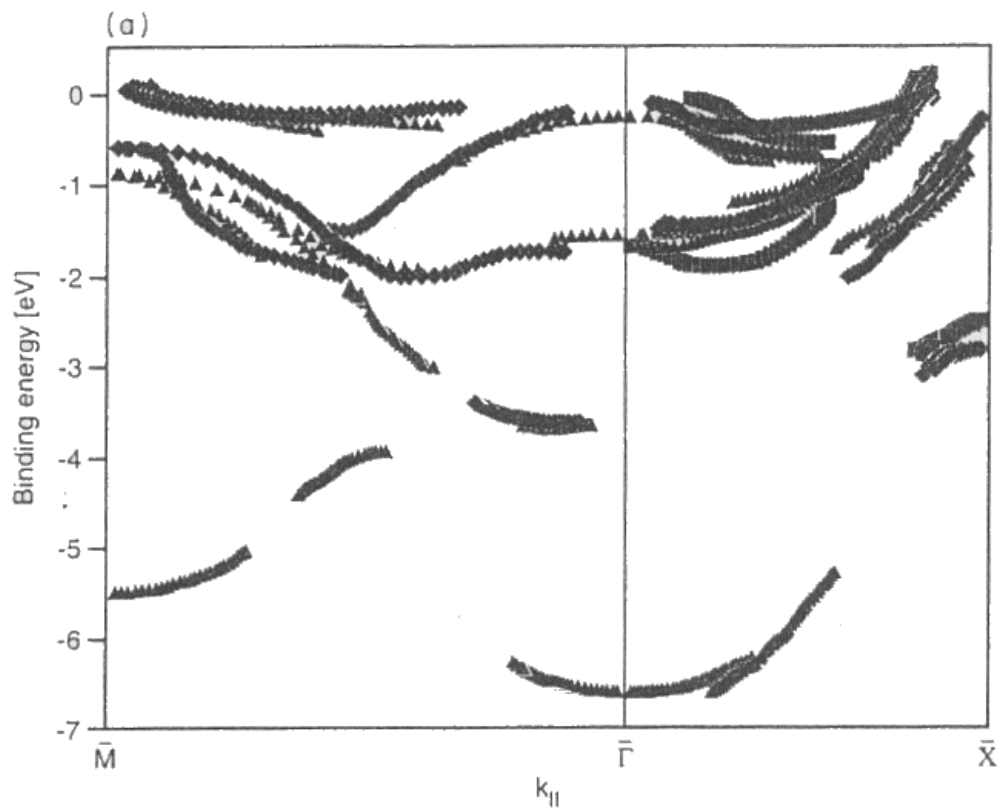
Fig. 1.19 The experimental surface band structure of Pt(100)-(1x1) of Stampfl's work. Squares, diamonds and triangles represent surface band structures preformed by $hv = 20$ eV, 30 eV, 40 eV, respectively.

1.4 Surface Electronic States

1.4.1 Surface and Bulk States

So far, we have used the concept of the surface state without defining what it is. Therefore, it is appropriate for us to describe the surface energy state below. For instance, the state characteristic of the Pt(100)-(1x1) surface is mentioned.

The energy state, which is not introduced by the adsorbtion of foreign atoms but is inherent to the clean surface, is called the intrinsic surface state. Since atoms on the surface are arranged with two dimensional symmetry, the intrinsic surface state forms two dimensional energy bands and the bands have dispersion. The wave vectors have components parallel to the surface only. If foreign atoms are adsorbed on the surface, the electronic state of the surface is altered. If a kind of foreign atom forms a monolayer, then this foreign atom layer gives rise to a two dimensional energy band system. In this case, the theoretical treatment of the surface is practically the same as that of the intrinsic surface state. If the concentration of the adsorbed atoms or molecules is low and they are dispersed on the surface, their energy states are similar to those of the isolated atoms or molecules.

In more rigorous consideration, we should remind of a simple but important fact. In the three dimensional energy band approximation made before, we assume the Born-von-Karlmann boundary condition, equation (1.18), in each of the three dimensional direction, x, y and z. In the layers near the surface, the Born-von-Karlmann boundary condition does not hold in the direction normal to the surface. This is obvious, since the crystal terminates at the surface.

Suppose the crystal surface is located at the plane, $z = 0$, and the bulk crystal exists in the region, $z < 0$. It is not unreasonable to assume that infinite arrays of

atoms exists in the plane, $z = 0$ in the x and y directions. In these arrays, atoms are symmetrically aligned forming the two dimensional crystal. The potential of electrons in the surface layer has the two dimensional symmetry. Thus, the one-electron state forms the two dimensional energy bands, since the Born-von-Karlmann boundary condition holds in the two dimensional direction parallels to the surface.

The two dimensional energy bands can be calculated in manners similar to those for the three dimensional energy bands. Before describing the practical two dimensional energy bands, we consider the surface state using a simple qualitative model below.

A schematic illustration of the electron states and wave functions near the vacuum-crystal interface are given in Figs. 1.20 and 1.21. Figure 1.20 shows the electron wave function in the z direction (the $\mathbf{k}_z$ direction) (Feuerbacher and Willis, 1976). There, e_v represents the vacuum level. Note that $e = 0$ at e_v. Outside the crystal, electrons with energy positive magnitudes of energy can exist. Their states are those of free electrons. Inside the crystal, the electronic states are the energy band states. As we have already seen in Figs. 1.9, 1.10, 1.11, 1.13 and 1.15, the energy levels are discrete for given $\mathbf{k}$. Thus a free electron state outside the crystal cannot always connect the band state inside the crystal. In some cases, the free electron states and the bands states connects smoothly, as shown in curve e. From other view point, any energy band wave functions above e_v are connected to the free electron wave function.

On the other hand, even if a free electron is injected on the crystal surface, the state cannot be connected to the band state unless the energy is the same. The injected electron state is evanescent toward the bulk solid. The electronic state is

confined in the surface layer, as shown in curve d. Although this state is a sort of the intrinsic state, it is called the evanescent state, since the state takes various energies continuously and distinguished from the intrinsic surface state for $e < e_v$ that takes the energy limited by the two dimensional energy band dispersion. If an electronic transition occurs to the bulk band state or the evanescent state at $e > e_v$, the excited electron can come out of the crystal.

Below e_v, three kinds of states are possible to occur. One is the ordinary bulk band state, as shown in curve c. Since the energy is negative, there is no state connecting to this state outside the crystal. The second one is the intrinsic surface state. The state is localized in the surface layer, as shown in curve a. It is also possible that the bulk energy band state and the surface band state are hybridized. In this case, the wave function has the feature of both surface and bulk band states, as shown in curve b. The state like this is referred to as the surface resonance state.

Then the question arises: how the three different states below e_v ($e < 0$) occur. A qualitative explanation is given in Fig. 1.21 (Feuerbacher and Willis, 1976). Figure 1.21 shows the energy band dispersion and related wave functions schematically. The upper figures illustrate energy bands and lower figures eigenfunction. There z stands for the distance from the surface normal to the surface. $\mathbf{k}_\perp$ and $\mathbf{k}_{||}$ represent the components of the wave vector, $\mathbf{k}$, normal and parallel to the surface, respectively. On the left hand side, the energy band of the bulk state is indicated. In the left half of the figure, the dispersion along the direction of $\mathbf{k}$ normal to the surface is shown. If we plot energy levels versus $\mathbf{k}_{||}$, we obtain similar dispersion. If we plot energy levels for general wave vectors versus their components

parallel to the surface, $\mathbf{k}_\parallel$, we have dispersion curves with some width. This width comes from the band dispersion toward the direction perpendicular to the surface. In the Fig. 1.21, this width is depicted as hatched parts. Note that $\mathbf{k}_\perp$ is not a good quantum number at the surface due to the lack of periodicity normal to it, while $\mathbf{k}_\parallel$ is. So, for each value of $\mathbf{k}_\parallel$ a range of states is possible for the different allowed values for $\mathbf{k}_\perp$. For instance, if the energy levels are plotted for bulk state inside the solid, at $\mathbf{k}_\parallel = 0$ they show dispersion as a function of $\mathbf{k}_\perp$ and thus, the bands have widths. The widths of these bands give the quasi-continuum of allowed states at the surface as shown by hatched areas. The state density of these 'bulk' states seen at the surface is not the same as that in the volume. The wave function amplitude, as the lower diagram on the left can be different near the surface, leading to a different local density of states. The bulk energy band plotted versus $\mathbf{k}_\parallel$ is referred to as the bulk band projected to the surface.

If the surface energy level occurs in the band gap of the projected bulk band, the corresponding state is quite localized near the surface and the wave function decays very rapidly toward the interior of the solid as well as toward the vacuum area. The corresponding state is a bound state below the vacuum level. This is obvious, since no state is allowed in the gap in the bulk. The energy level corresponding to this state is experimentally observable. The state is illustrated in the middle part of Fig. 1.21. This is the intrinsic surface state.

If the surface level occurs in a part within the projected bulk band, the surface state and the bulk state mix together to form a state gradually evanescent toward the interior of the solid. This state is referred to as the surface resonance state. This state

is illustrated on the right hand side in Fig. 1.21. A sharp resonance will occur if the decay is forbidden by the symmetry. Otherwise it will be broadened owing to decreased amplitude of the wave function into the volume of the crystal.

Just as an example, the surface energy bands of Si(2x1)-K is shown in Fig. 1.22. The sample is the Si(2x1) surface covered with the K metal to the extent that the perfect monolayer of K is formed. In the figure, full lines represent the energy band dispersion calculated using the double layer model (Morikawa, Kobayashi, Terakura and Blügel, 1991). Thick shaded curves in the figure show the experimentally observed energy band dispersion (Abukawa et al., 1992). The angle-resolved photoemission measurements were carried out with synchrotron radiation as the excitation source. In Fig. 1.22, the abscissa represent $\mathbf{k}_{||}$ along the lines connecting good symmetry points in the surface Brillouin zone, which is shown in Fig. 1.23.

1.4.2 Surface of Pt(100): Surface Reconstruction

As we have described, electrons in the surface layer see the potential, which is different from that in the bulk. In the similar way, atoms in the surface layer receive the force that is different from the interatomic force in the interior of a solid. This is obvious, since no force on the surface atoms from the vacuum side. Thus atoms in the surface layer are arranged in a manner different from those in the layers in the bulk. The interlayer distance is also different from that in the bulk. Atoms in a solid are located at sites where the potential is at minima. Therefore, in some cases, the atomic arrangement in the surface layer is changed by heat treatment. This occurs because different arrangement of potential minima exists. The change of the atomic

52
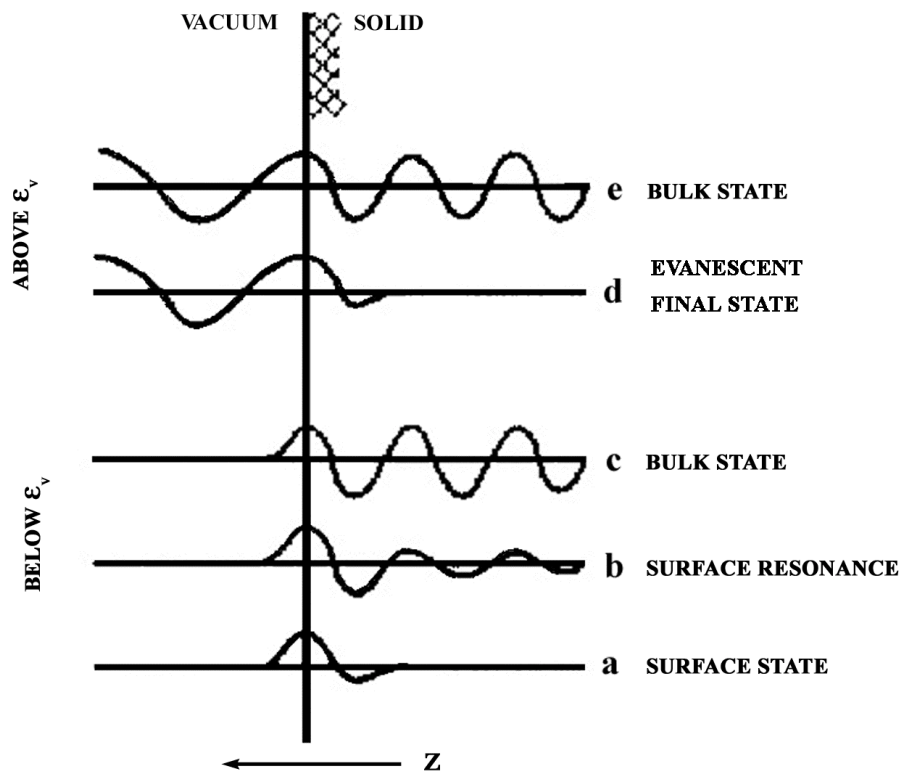
Fig. 1.20 Electronic wave functions in the surface region.
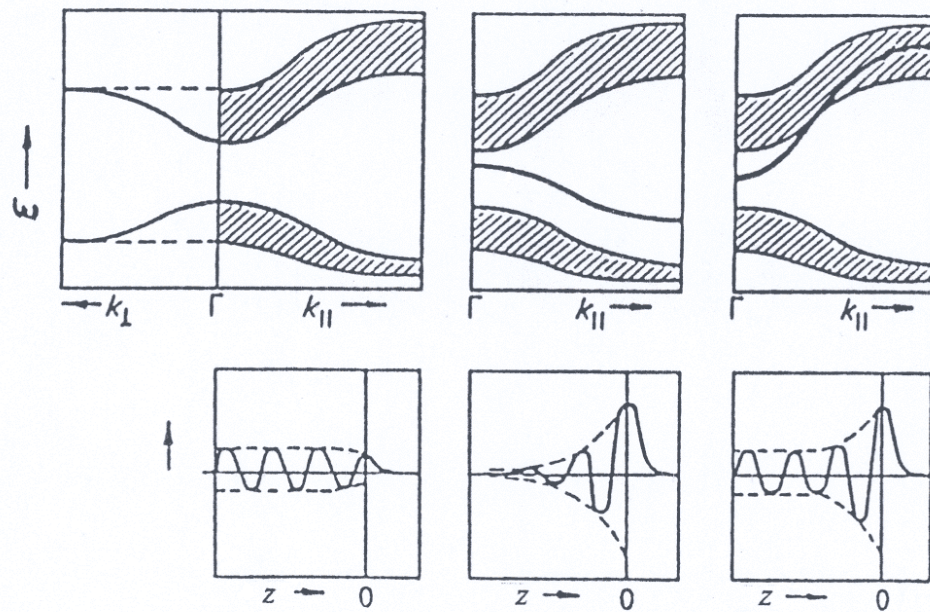
Fig. 1.21 Schematic illustration of the surface energy bands (upper panels) and the surface eigenfunctions (lower panels). The projected bulk bands (hatched part) are shown for comparison. Left: Bulk state. Middle: Surface state. Right: Surface resonance. The surface occurs at $z = 0$ (Feuerbacher and Willis, 1976).
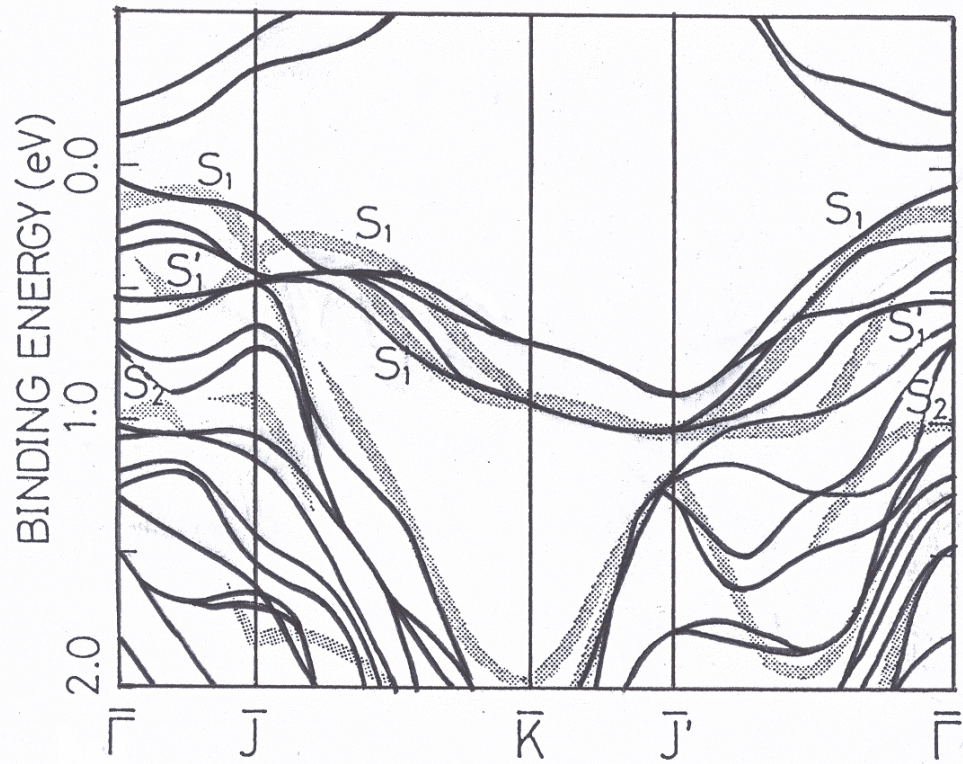
Fig. 1.22 Comparison of experimental e-**k** curves (shaded spectra) and theoretical calculation based on an optimized double layer model (Abukawa et al., 1992).
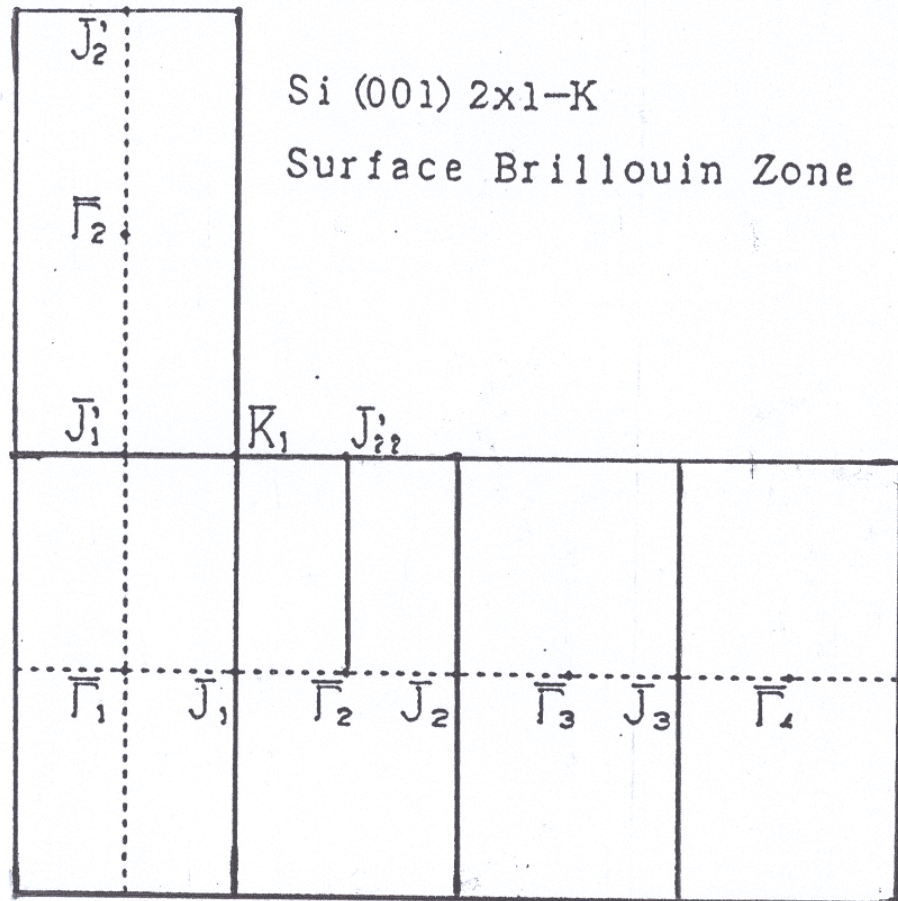
Fig. 1.23   Surface Brillouin zone of the single domain Si(001) 2x1-K surface. Broken lines indicate the mirror planes (Abukawa et al., 1992).

arrangement in the surface is referred to as the surface reconstruction. In what follows, the surface reconstruction will be described in more detail.

It has long been known that clean surfaces of single crystals metal reconstruct, i.e., the atoms in the surface layer adopt an arrangement which is not the same as a simple truncation of the bulk structure. Such reconstruction leads to change in the surface lattice that accompanies a change in the surface band structure, leading to reduction of the density of states at the Fermi level. Particularly, this is the case in a surface state that can drive the surface reconstruction.

The (100) surfaces of some fcc transition and noble metals are known to be reconstructed to a close-packed quasihexagonal (hex) overlayer arrangement that periodically matches the (100) square substrate (Hagstrom, Lyon, and Samorjai, 1965). Because of the different symmetry between the overlayer and the substrate, commensurate hexagonal geometries have rather long periodicity. Typical observed surface cells are (5x1) and (20x5). Here, the (n x m) structure represents that atoms in the array in the direction of one primitive translation vector have the translational symmetry with the periodicity of n atoms. Namely, the same sub-structure repeats in a period of n atoms. Similarly, atoms in the array in the direction of another independent primitive translation vector have the symmetry that the same structure repeats in a period of m atoms.

The phenomenon presents a number of interesting aspects. First, the reconstruction is seen only in elements of the later part of the $5d$ transition series, i.e., Ir, Pt and Au, while their $4d$ transition element counterpart, Rd, Pd and Ag, do not reconstruct. Second, the observed aspects of reconstruction of Ir, Pt and Au, though not identical, are qualitatively very similar to each other; in spite of the difference in

the electronic structures of these materials.   This strongly suggests that surface electronic structure details are not of primary importance in the surface reconstruction. Third, it is known that the (100) surfaces of the late $5d$ metals can be rather easily forced to switch between the unreconstructed and the reconstructed phases by deposition or removal of small amount of adsorbates. This indicates that the energy difference between the two phases is small. Fiorentini, Methfessel and Scheffler (1993) have studied such the reconstructions of the (100) surfaces of the fcc transition metal by a density functional method to understand the underlying physical mechanism establishing a simple picture of the energetics of the phenomena. They have calculated the energy band change accompanying the quasihexagonal reconstruction of the (100) surfaces of representative fcc transition metals and found that the reconstruction is favored for the late $5d$ metals and not for $4d$ metals in accordance with the results of experiments. Correlation has been established between the reconstruction and the magnitudes of the surface stress calculated *ab initio* for the unreconstructed surfaces. The reconstruction results from a delicate balance between surface-substrate mismatch and stress-related energy gain. Only in the case of $5d$ metals, the latter gain is large enough to drive the reconstruction actually against the substrate resistance to misregistry. The origin of the surface stress is the depletion of d electrons at the surface caused by the enhanced *spd* hybridization. The remarkable stress enhancement in $5d$ metals is due to the major relativistic effects on the $6s$ and $6p$ shells.

In case of the clean Pt(100) surface, surface atoms are in an asymmetrical environment different from that of the bulk atomic plane. They take up equilibrium position different from those in the ideal arrangement by forming the new structure at

the surface.

In case of the clean Pt surface, the reconstruction of the clean Pt(100) metal surface was first reported by Hangstrom, Lyon and Somorjai (1965) thirty eight years ago. This metal surface exhibits the (5x1) LEED pattern because of the appearance of diffracted beams in the (1/5)-th order position.   In those days, there was disagreement as to whether or not the (5x1) surface structure was due to surface impurities (Palmberg and Rhodin, 1967; Somorjai, 1967). Therefore, many pieces of work dealing with the surface of Pt(100) were carried out (Grant and Haas, 1969; Heilmann, Heinz and Müller, 1979; Van Hove et al., 1981). Now, it is well recognized that the clean Pt(100) surface exhibits the reconstruction and that the surface atoms reconstruct to form a quasi-hexagonal structure overlayer on top of the square fcc substrate as shown in Fig. 1.24. The reconstruction can be lifted through the interaction with chemisorbed species. This forms the basis of a chemical preparation technique used to produce the virtually clean metastable (1x1) surface as shown in Fig. 1.25.

Figure 1.26 shows the proposed structure of the Pt(100) surface as determined by LEED. From the second atomic layer downwards the successive planes of the crystal have the square structure of the bulk (100) plane. However, the topmost layer is hexagonal and the positions of the atoms in this layer only rarely coincide with simple sites in the underlying plane. The simple model to explain all the observed diffraction features is illustrated in Fig. 1.27. The spot separation Δ shown in Fig. 1.27a gives a sensitive measure of the difference in lattice parameters of the square and hexagonal meshes. It is found that the hexagonal layer is contracted with respect to a bulk plane by about 4 percent. It is also found that there exists also a second anomalous structure, which appears on heating the sample above 1100 K.   The

structure can be interpreted in terms of a rotation of the (5x20) hexagonal overlayer of Fig. 1.26 by an angle of about 0.7^o. Simple calculations based on the overlap of atoms in the hexagonal layer with those in the underlying square arrangement can explain the particular orientation of this second structure.

The clean reconstructed Pt(100) surface was also studied by scanning tunneling microscope (STM) (Ritz, Schmid, Varga, Borg and Ronning, 1997; Chang et al., 1999). In this technique of the imaging process, real-space pictures of the surface in an atomic scale can be obtained. Therefore STM can often identify the surface unit cell. The STM image of the hexagonal reconstructed Pt(100) surface is presented in Fig. 1.28. The figure shows the real atomic arrangement on the surface.

1.5 Surface Magnetism

Platinum metal is neither ferromagnetic nor antiferromagnetic. As we have already described in section 1.3.2, the Fermi surface of Pt is well nested. This suggests the possibility of the occurrence of the antiferromagnetism in this metal, although the metal is not antiferromagnetic. In spite of the situation that the investigation of the magnetic properties of Pt from the electronic structure point of view is necessary, the research work reported so far on the magnetic properties have been directed in a different direction.

In the last decade, it was found that the Co-Pt system exhibits quite interesting magnetic nature. Not only Co-Pt alloys, but multilayers and thin films have been investigated intensively (Lin, Kuo, Her, Wu, Tsay and Shern, 1999; Weller, 1996 and references therein). The interesting properties found in this system are as follows:

1) The thin Co layer on Pt and the multilayer of Co-Pt show the magnetic anisotropy perpendicular to the surface.

Hexagonal overlayer on top of the square face-centered cubic (fcc) substrate.
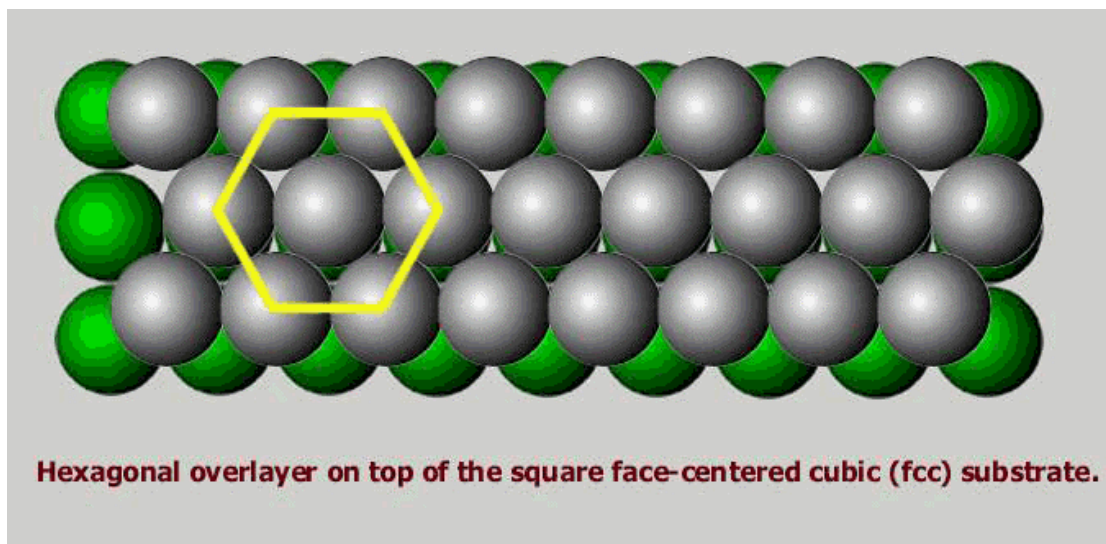
Fig. 1.24 The real surface of clean reconstructed Pt(100) surface.

The ideal (1x1) surface of Pt(100)
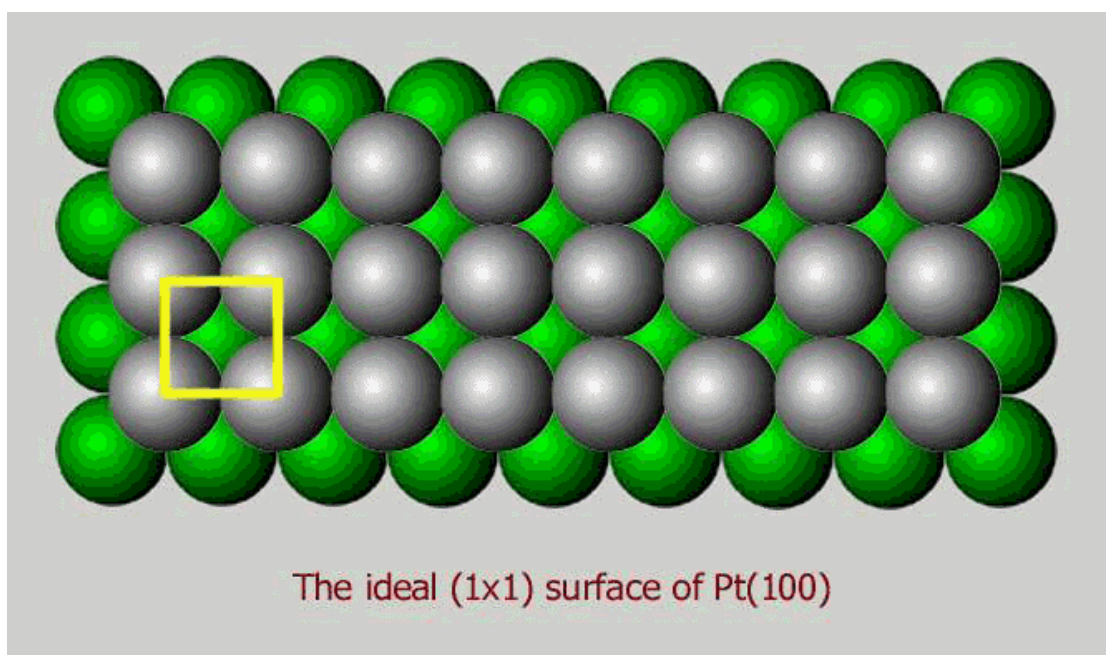
Fig. 1.25 The real surface of ideal clean unreconstructed Pt(100) surface.
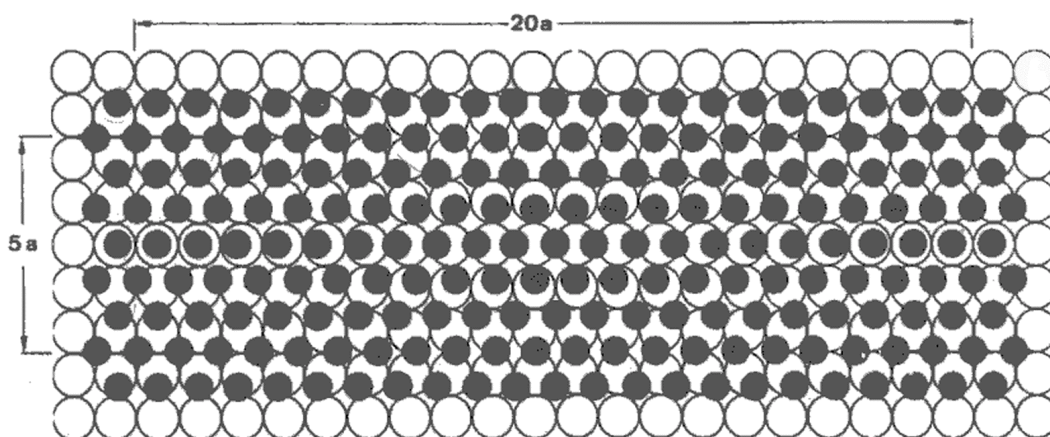
Fig. 1.26 Schematic model of the reconstructed Pt(100) surface. The square mesh of white circles represents the structure of the second atomic layer. The superimposed hexagonal structure represents the top layer (schematically the atoms are drawn smaller for clarity). Near coincidence of the two nets occurs every 20 square lattice spacings in one direction and every five spacings in the direction perpendicular to it. The domain of this structure can occur in the two equiprobable orthogonal orientation (Benard et al., 1983).
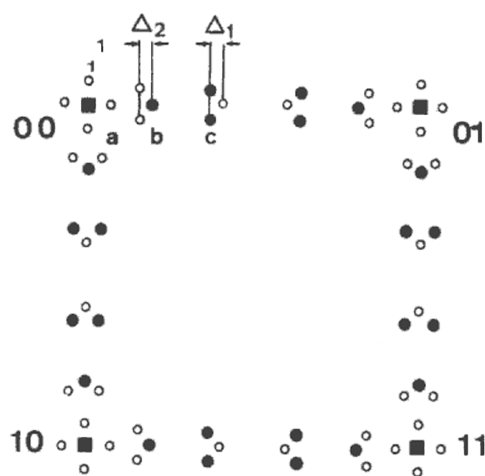
(a).
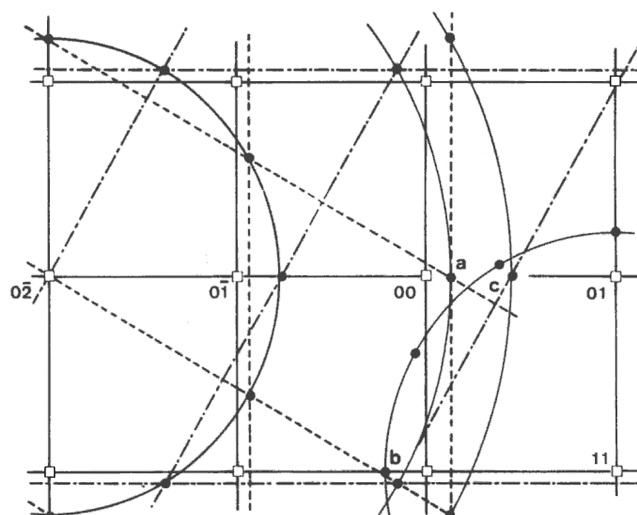
(b).

Fig. 1.27   Schematic representation of the LEED pattern from reconstructed Pt(100). Portion of the pattern showing the spots assignable to a square mesh (solid square) and "extra" spots (solid circles; white circles). A reciprocal lattice plot showing how "extra" spots may be formed by diffraction of beams from an hexagonal layer on the square lattice (white square). Double diffraction is simulated by superimposing hexagonal meshes (solid circles) centered successively on each square lattice spot. This explains the origin of the different features, a, b, c as shown in the upper panel, (a), (Rhead, 1973).
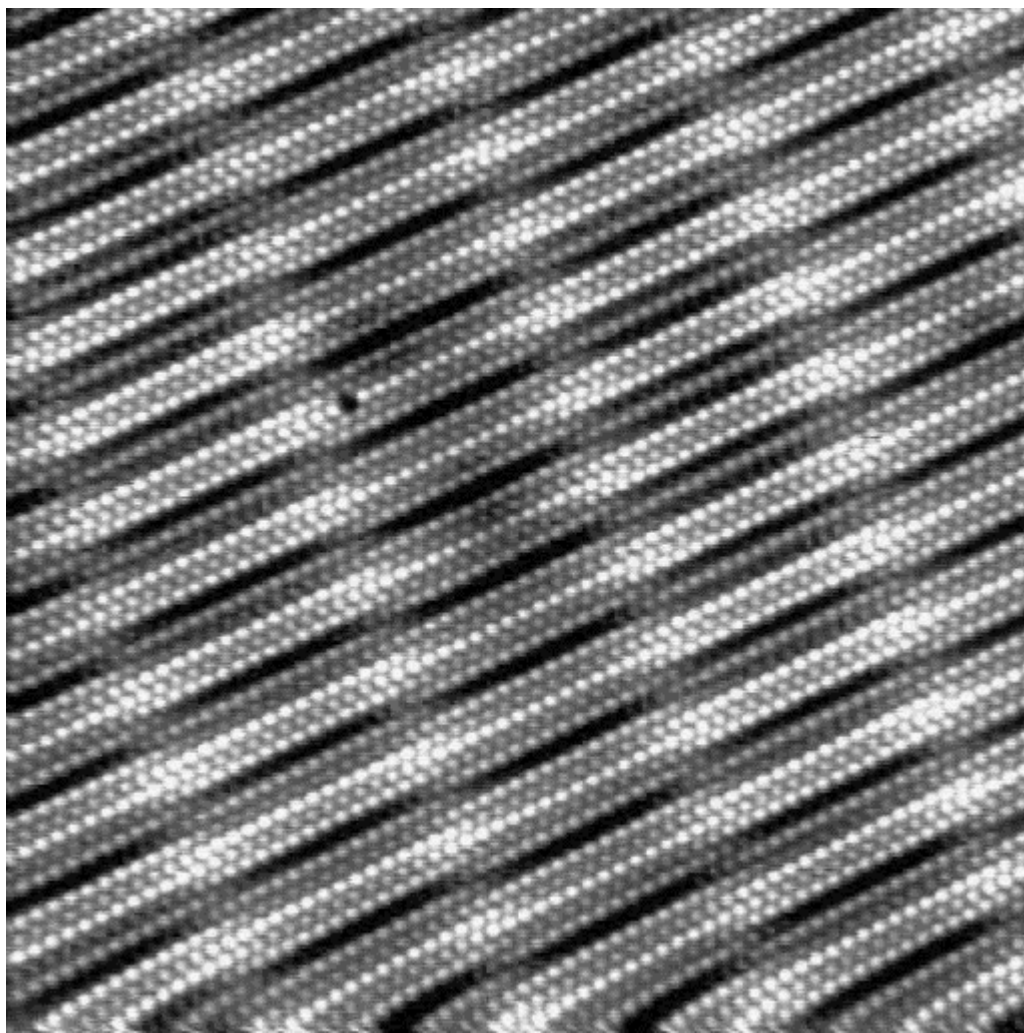
Fig. 1.28 The real image of the clean reconstructed Pt(100) surface from a STM experiment (Ritz, Schmid, Varga, Borg and Ronning, 1997).

2) They show giant magneto-resistance.

3) Theoretical investigations show that the materials have the oscillatory nature in the exchange coupling of the RKKY (Rudermann-Kittel-Kasuya-Yoshida) type (the $5d$ super exchange interaction).

4) The materials are good candidates of high density magneto-optical strong media.

Because of these properties, plenty of researches have been concentrated on the Co-Pt system. The researches have been performed by variety of methods. For instance, the sample preparation and related characterization are good subjects. There, the molecular beam epitaxy, the Auger spectroscopy, the extended X-ray absorption fine structure (EXAFS) analysis, the XPS analysis, and the magneto-Kerr effect have been used. Because of the advanced theoretical work, the causes of the various magnetic properties have been gradually clarified using accumulated experimental data.

In spite of plenty of investigations on the Co layer, the research on the substrate material, particularly the magnetic nature of Pt surface, has not been reported. The investigation of the surface magnetism can be made effectively by the spin- and angle-resolved photoemission. The use of the circularly polarized light as the excitation source will also be quite effective. Since the work in this direction has not reported yet, we do not deal with this aspect any more except mentioning that the surface reconstruction is deeply related with the formation of an interesting thin layer of a foreign metals.

1.6 Photoemission Spectroscopy

In this thesis, the electronic structure of Pt(100) is investigated by means of photoemission. In this section, the fundamentals of photoemission are briefly overviewed. Experimental details will be described in the next chapter. Photoemission intensity gives us the information of the density of states (DOS) as

$$n\,(\varepsilon_{B}, v)\;\propto\;\sigma(v)\,D(\varepsilon_{B})\,. \qquad (1.34)$$

Here, $\sigma(v)$ is the excitation cross section at photon energy, hv. $D(\varepsilon_{B})$ is DOS and ε_{B} is the binding energy which will be defined later. The relation given in equation (1.34) is not rigorous but quite useful.

Another useful information is the energy band dispersion curve expressed as

$$\varepsilon_{\alpha}\,(\mathbf{k}_{\alpha})\quad \text{versus}\quad \mathbf{k}_{\alpha}\,. \qquad (1.35)$$

Here, $\varepsilon_{\alpha}\,(\mathbf{k}_{\alpha})$ is the energy band along a good symmetry line in the Brillouin zone. The process of obtaining the energy band dispersion curves by photoemission is often referred to as the band mapping. Angle-resolved photoemission measurements made in the energy band mapping. The energy band mapping can be made in the spin-resolved mode. However, this is out of scope in the present thesis and its principle is not described here. Since photoelectrons have a small but tunable escape depth, it is possible to see the surface and adsorbate state as well as bulk states. The detailed explanations of photoemission spectroscopy (PES) are described in various books (Höfner, 1996; Cordona and Ley, 1978; Kevan, 1992).

1.6.1 Basic Principle

Photomission is the phenomenon that electrons are emitted out of matter that is exposed to light. The electrons are called *photoelectrons*. Outside the solid, electrons are easy to handle and observe. Kinetic energy, momentum and spin are measured and analyzed. For implementing these, emission angle, θ_e, and azimuthal angle, ϕ_e, of electron emission are measured as shown in Fig. 1.29. From the properties of the photoelectrons in vacuum (kinetic energies and momentum), one can retrieve the properties of electrons inside the system investigated as will be described below.

(1) Energy Distribution Curve (EDC)

Regarding the photoemission spectrum described in equation (1.34), we practically measure the spectrum called the energy distribution curve (EDC). EDC is the number of primary photoelectrons, $n(\varepsilon_u, v) \, d\varepsilon$, emitted per unit time by excitation with light with an energy in the range $hv - h\Delta v/2 \leq hv \leq hv + h\Delta v/2$. The primary photoelectron is regarded to have a kinetic energy in the range $\varepsilon_u - \Delta\varepsilon/2 \leq \varepsilon_u \leq \varepsilon_u + \Delta\varepsilon/2$. Thus, EDC is expressed as

$$n(\varepsilon_u, v) \, d\varepsilon = \frac{N(\varepsilon_u, v) \, d\varepsilon \, dv}{I_o(v) \, dv} \qquad (1.36)$$

$$n(\varepsilon_u, v) = \frac{N(\varepsilon_u \, v)}{I_o(v)}. \qquad (1.37)$$
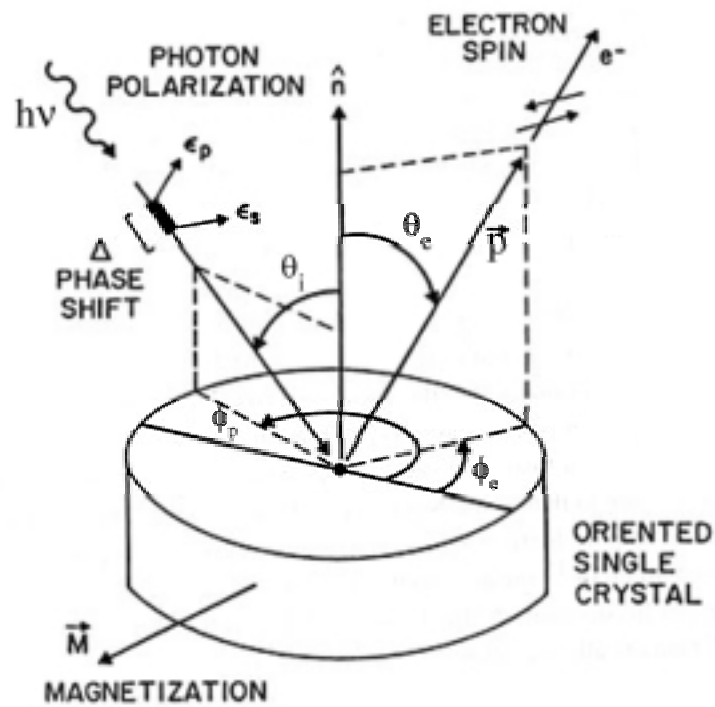
Fig. 1.29 Schematic diagram of spin and angle-resolved photoemission. This

diagram is to show all the angular parameters. θ_i is the polar angle of

photon incidence (incident angle). θ_e is the polar angle of photoelectron

emission. ϕ_p and ϕ_e are azimuthal angles of light incidence and

photoelectron emission, respectively. **p** is the momentum of the

photoelectron. e_s (*s*-polarization) and e_p (*p*-polarization) are electric

vector components of excitation light parallel and normal to the plane of

incidence, respectively.

Here, $N(\varepsilon_u, v) \, d\varepsilon \, dv$ is the number of excited primary photoelectrons and $I_o(v) \, dv$ is

the light intensity.

If we define the binding energy as

$$\varepsilon_B = hv - \varepsilon_u .$$

(1.38)

EDC is also expressed in terms of the binding energy as

$$n(\varepsilon_B, v) \, d\varepsilon = \frac{N(\varepsilon_B, v) \, d\varepsilon \, dv}{I_o(v) \, dv}$$

(1.39)

$$n(\varepsilon_B) = \frac{N(\varepsilon_B, v)}{I_o(v)} .$$

(1.40)

The number of photoelectrons per unit time is equivalent to photocurrents, J. Also,

we measure the photocurrent in a solid angle, $d\Omega$, defined by the detector system.

Thus, what we measure practically is

$$N(\varepsilon_u, v, \theta, \phi) \, d\varepsilon \, dv \frac{d\Omega}{4\pi} .$$

(1.41)

In the actual spectrometer, we have broadening of the measured spectra owing to the

overall energy resolution. Suppose the smearing of the real spectrum by resolution is

given by the window function, $W(\varepsilon)$, the spectra we observe is deformed as

$$\overline{N}(\varepsilon_u, v, \theta, \phi) = \frac{\int\limits_{-\infty}^{\infty} N(u, v, \theta, \phi) W(u - \varepsilon) \, du}{\int\limits_{-\infty}^{\infty} W(u) \, du}.$$ (1.42)

If we know $W(\varepsilon)$ correctly, we can deconvolute $\overline{N}(\varepsilon)$ to obtain $N(\varepsilon)$.

(2) Binding Energy

We have to establish the idea with which useful pieces of information can be drawn out through the analysis of the photoemission phenomena. Many early theoretical investigations targeted this analysis.

First, consider the system consisting of N electrons. Suppose its energy is $E_g(N)$. There a photon with an energy, hv, enters. We regard the system of N electrons and a photon to be the initial state. In the final state of the photoexcitation, the photon disappears and an electron with a kinetic energy, ε_u, and the (N-1) electron system with an energy of $E_f(N-1)$ are left. The electron with ε_u is the photoelectron. From the energy conservation, we have

$$E_g(N) + hv = E_f(N-1) + \varepsilon_u.$$ (1.43)

Then, we have

$$hv - \varepsilon_u = E_f(N-1) - E_g(N).$$ (1.44)

From equation (1.38), we have

$$\varepsilon_B = E_f(N-1) - E_g(N).$$ (1.45)

Since $0 > E_f(N-1) > E_g(N)$, we see $\varepsilon_B > 0$. We have to relate ε_u with a quantity measurable in the space outside the sample (vacuum). Another issue we have to make is to find the meaning of the right hand side of equation (1.43).

(3) Relaxation

We know that a sample and a photon exist in the initial state of photoemission and the photon disappears and a photoelectron comes out of the sample in the final state, as mentioned already. Thus, we have to find what happens in the intermediate state in the sample, which appears to be a black box. Many pieces of theoretical work have been carried out to give the answer to this. None of the work seems to have been successful. Instead, the assumption of the three step process proposed empirically has been successful. (Berglund and Spicer, 1964; Spicer and Krolikovski, 1969).

Suppose we can separate the energy of an electron to come out of the sample after the excitation from the energy of remaining (N-1) electrons. It is not absurd to assume the energy, ε_g, of the excited electron to leave the sample is given as

$$E_g(N) = \varepsilon_g + E_g(N-1). \tag{1.46}$$

From equation (1.45) and (1.46), we have

$$\varepsilon_B = E_f(N-1) - E_g(N-1) - \varepsilon_g. \tag{1.47}$$

Generally, $E_f(N-1)$ is not equal to $E_g(N-1)$. It is the energy of the photoproduced hole. Let $E_f(N-1)$, the hole energy, be written as

$$E_f(N-1) = E_g(N-1) + E_R .\qquad(1.48)$$

E_R is the energy of the many electron interaction of the hole generated by the photoexcitation with the surrounding medium. This energy often called the relaxation energy. The binding energy, ε_B , given in equation (1.47) is written as

$$\varepsilon_B = E_R - \varepsilon_g .\qquad(1.49)$$

In some cases, E_R is negligible. In these cases, one electron approximation is valid as in the case of the energy band approximation.   There we have

$$\varepsilon_B = -\varepsilon_g .\qquad(1.50)$$

In a case like this, the binding energy defined in equation (1.38) gives us the negative of the initial one electron energy of the photoelectron. Remember $\varepsilon_B > 0, \quad \varepsilon_g < 0$.

1.6.2 Three Step Process

In the analyses of EDC's, we usually postulate the three step model, although this model has not yet been verified theoretically from the first principle.   As mentioned before, the theoretical treatments of the photoemission processes from this stand point have not been successful.   However by experience, we know that the three step model explains observed data quite well.   In the three step model, the potoemission in a solid material is regarded to occur as a result of following three consecutive partial processes:

1) Optical excitation of electrons inside the solid

2) Transport of the excited electrons to the surface

3) Transmission of photoelectrons through the surface into vacuum.

In order to see the consequences of the three step process, we have to carry out some simple calculations. We consider the following simplified model, although the simplification does not make the general validity of the model lost: We consider that the first step of photoemission occurs as shown in Fig. 1.30. There, excitation light with energy hv and intensity $I_o(v)$ per unit beam cross section falls normally on a sample of a prism shape with a square surface. The cross section of the sample is S. We assume that light penetrates toward the z direction from $z = 0$. The sample surface is at $z = 0$.

First, suppose photoelectrons are generated at a small portion, $dzdS$, around a point in a slab with a thickness of dz located at z. The photoelectrons migrate toward any directions in space. We consider the photoelectrons propagating toward the direction, (q, f). Here we must emphasize that the three step process postulates the photoelectron production to be a localized process. In the complete many electrons viewpoint, we cannot specify where the photoelectron is produced.

In the first step, we assume that the number of photoelectrons generated in the small slab $dzdS$ is equal to that of photons absorbed in this slab. Then the number of photoelectrons, dN, generated in the small slab is equal to

$$dN = I_o(v)\, dS \cdot \eta(v)\, exp(-\eta(v)\, z)\, dz . \qquad (1.51)$$

Here, $\eta(v)$ is the absorption coefficient. The fraction of photoelectrons migrating in the direction (q, f) is given as

$$d\overset{\backslash}{N}(\theta,\phi) = \frac{dN\,\sin\theta\;d\theta\;d\phi}{4\pi}$$

$$= \frac{I_o dS\;\eta\;exp(-\eta\,z)\;dz\;\sin\theta\;d\theta\;d\phi}{4\pi}.$$

(1.52)

Photoelectrons are scattered while they are travelling to the surface. If the scattering is elastic, the process gives rise to the photoelectron diffraction. If the scattering is inelastic, photoelectrons lose a part of energies they possess and they are not primary electrons with the original kinetic energy, ε_u. In the second process of the three steps, we treat the survival of the primary electron using the mean free path for the scattering. In other words, complicated details of the scattering are renormalized into one parameter, the mean free path, l. The fraction of electrons to survive without being scattered in a migration distance of d is expressed as $exp(-d/l)$. Therefore, the number of primary photoelectrons arriving at the surface in the direction, (θ,ϕ), from a small slab $dz\,dS$ at z is given as

$$dN(\theta,\phi) = d\overset{\backslash}{N}(\theta,\phi)\,exp(\frac{-z}{l\,cos\,\theta})$$

$$= \frac{I_o\;dS\;\eta\;exp\left\{-\left(\eta + \frac{1}{l\,cos\,\theta}\right)z\right\}dz\;\sin\theta\;d\theta\;d\phi}{4\pi}.$$

(1.53)

It should be remarked that the light penetration depth is much smaller than the size of the sample cross section, i.e., $z\,!\;\sqrt{S}$. Therefore, in the integration of equation (1.53), we ignore the dependence of θ and ϕ on z and integration on θ and ϕ can be carried out from $\theta = 0$ to $\pi/2$ and from $\phi = 0$ to 2π, respectively.

First we perform the integration on z, from $z = 0$ to ∞. The result is given as

$$dN_\Omega = \frac{I_o \, dS \left\{ \dfrac{\eta \, l \, cos\,\theta}{(\eta \, l \, cos\,\theta + 1)} \right\} \cdot sin\,\theta \, d\theta \, d\phi}{4\pi}.$$ (1.54)

If we integrate equation (1.54) over S, we obtain the number of primary photoelectrons reaching the surface as

$$\left. \begin{aligned} N_\Omega &= \frac{I_o \, d\Omega \, \eta \, l \, cos\,\theta}{4\pi\,(\eta \, l \, cos\,\theta + 1)} \\[2ex] d\Omega &\equiv sin\,\theta \, d\theta \, d\phi. \end{aligned} \right\}$$ (1.55)

Apart from the treatment of 4π, N_Ω present the case of the angle-resolved photoemission. Since the absorption coefficient of a solid material in the vacuum ultraviolet (VUV) and soft X-ray (SX) region is less than 10^5 cm^{-1} and the mean free path in a solid material is around 10^{-7} cm, $\eta \, l \, cos\,\theta < 10^{-2}$! 1. Then we have

$$N_\Omega = \frac{I_o \, d\Omega \, \eta \, l \, cos\,\theta}{4\pi}.$$ (1.56)

Thus the number of primary photoelectrons reaching the surface is proportional to the absorption coefficient η. If we integrate equation (1.54) over θ and ϕ, we have

$$dN = \frac{I_o \, dS \left\{ 1 - \dfrac{1}{\eta \, l} \, \ln\left(1 + \eta \, l\right) \right\}}{2}.$$ (1.57)

Since $\eta \, l$ is very small as compared with 1, equation (1.57) becomes

$$dN = \frac{I_o \, dS \, \eta \, l}{4}.$$
(1.58)

Integration over S, we have

$$N = \frac{I_o \, S \eta l}{4}.$$
(1.59)

In the third step, we have to consider the escape of primary photoelectrons from the surface. In the three step model, we assume the probability of primary photoelectrons to leave the surface $t(\varepsilon_u)$. With this escape probability, the number of primary photoelectron leaving the surface is given as

$$N = \frac{1}{4} I_o \, S \, \eta \, l \, t(\varepsilon_u)$$
(1.60)

and, in the angle-resolved case

$$N_\Omega = \frac{1}{4\pi} I_o \, d\Omega \, \eta \, l \, cos \, \theta \, t(\varepsilon_u).$$
(1.61)

Spicer and coworkers (Berglund and Spicer, 1964; Spicer and Krolikovski, 1969) suggested that the escape function is given as

$$\left. \begin{aligned} t(\varepsilon_u) &= \frac{1}{2} \left\{ 1 - \left(\frac{\chi}{\varepsilon_u} \right)^{3/2} \right\} \quad \text{for} \quad \varepsilon_u > \chi \\ &= 0 \qquad\qquad\qquad\qquad \text{for} \quad \varepsilon_u < \chi. \end{aligned} \right\}$$
(1.62)

Here, χ is the work function of the sample. The shape of the escape function is presented in Fig. 1.31.

It should be remarked that we are concerned with an isotropic medium and essentially the directional average. Otherwise, $t(\varepsilon_u)$ is dependent on θ and ϕ. Figure 1.31 shows $t(\varepsilon_u)$ versus ε_u/χ. For kinetic energies below about 7χ, $t(\varepsilon_u)$ changes steeply as ε_u changes. Therefore, EDC can be modified considerably by $t(\varepsilon_u)$, if EDC is recorded over an appreciable range of ε_u. The modification occurs in a way that the photoelectron intensity decreases monotonically as the kinetic energy is decreased. Suppose $\chi = 2.0$ eV. Then, $t(\varepsilon_u)$ modifies the photoelectron intensity by 25% for scanning from 4 eV to 3 eV, 14% from 15 eV to 10 eV, and 7% from 30 eV to 20 eV. In PES experiments using synchrotron radiation, energies of excitation light are usually selected above 15 eV. If the excitation energy range is selected properly, $t(\varepsilon_u)$ does not modify EDC seriously.

In many cases, the absolute values of photoemission intensities are not important in the data analyses. Therefore, we make a simplifying assumption on $t(\varepsilon_u)$ based on the discussion described above. The assumption is as follows:

$$\left. \begin{array}{llll} t(\varepsilon_u) = 1 & \text{for} & \varepsilon_u > \chi \\ = 0 & \text{for} & \varepsilon_u < 0. \end{array} \right\} \qquad (1.63)$$

Then, for $\varepsilon_u > \chi$, equations (1.60) and (1.61) are given as
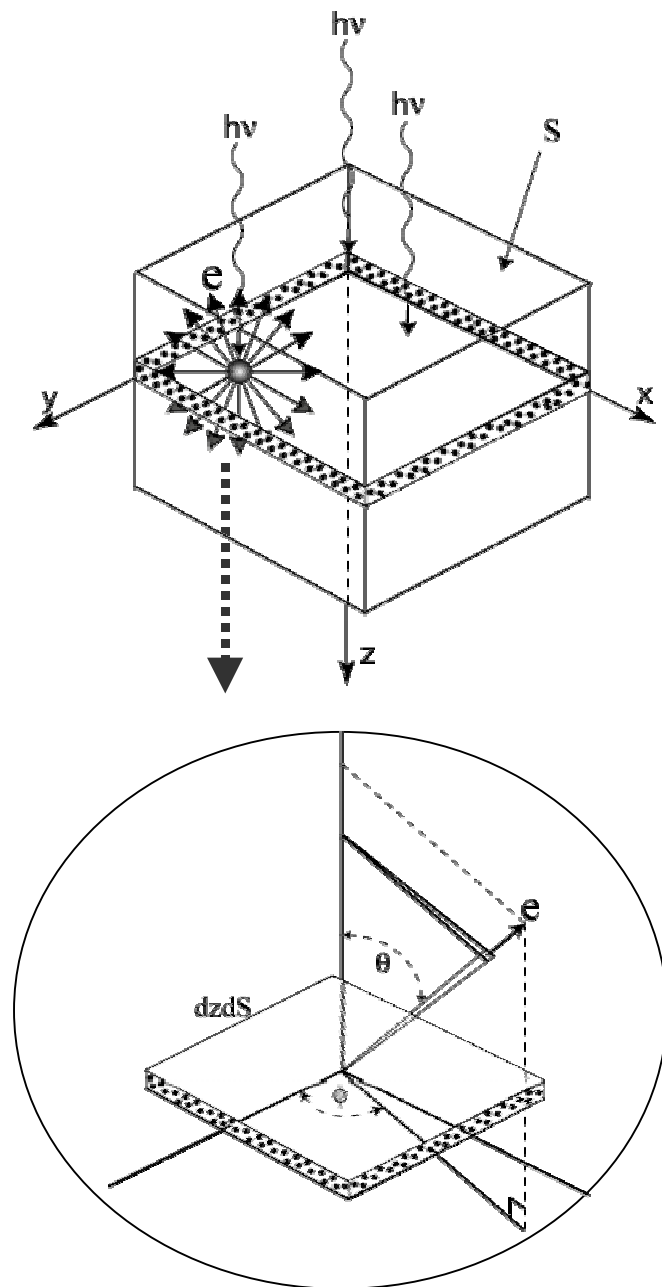
Fig. 1.30 Schematic illustration of the generation of photoelectrons. Excitation light with energy *hv* falls normally on the sample with the surface area, *S*. Photoelectrons generated in a small portion, *dz dS* , at *z* from the surface and progressing toward the direction *(θ,φ)* are considered. The sample surface is at *z* = 0. Excitation light propagates toward *z* > 0.
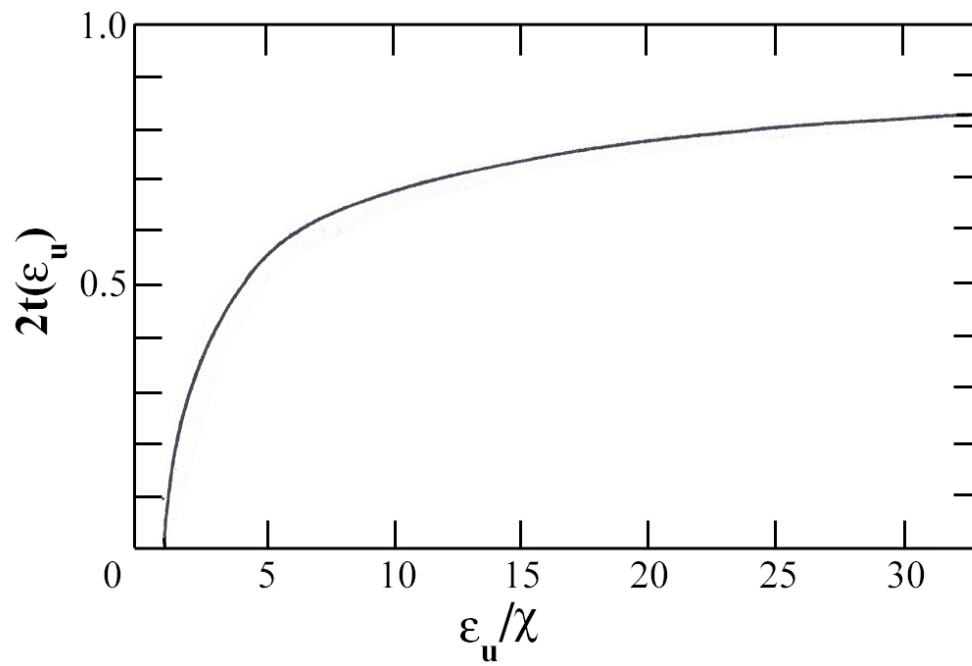
Fig. 1.31 Escape function versus ε_u/χ. ε_u: Kinetic energy; χ: Work function.

$$N = \frac{1}{4} I \eta l$$
$$N_\Omega = \frac{d\Omega}{4\pi} I \eta l_\theta. \qquad \qquad \qquad (1.64)$$

Here, we put $I_o S \equiv I$ and $l \, cos\, \theta \equiv l_\theta$.

In case of a number of isolated absorption centers, η is written as

$$\eta = N_o \, \sigma. \qquad (1.65)$$

Here, N_o is the density of the absorption centers. σ is the absorption cross section. In solids, the optical absorption occurs often cooperatively by many atoms. However, we formally assume that equation (1.65) holds even in solids. In this case, N_o represents the density of absorption centers, atoms or molecules in the solid. By comparing equations (1.40), (1.64), (1.65), EDC is given as

$$n(\varepsilon_B, v) = A \, \sigma(\varepsilon_B, v) \, l(hv - \varepsilon_B). \qquad (1.66)$$

1.6.3 Cross Section

According to equation (1.66), we know EDC expresses the spectrum of the transition cross section $\sigma(\varepsilon_B, v)$. Therefore, we have to analyze $\sigma(\varepsilon_B, v)$ in a more detail. Apart from unimportant factor, which can be renormalized into the factor, A, the transition cross section is written as

$$\sigma(\varepsilon_B, v) = \left| \left\langle \psi_f \left| T \right| \psi_g \right\rangle \right|^2 \delta\left(E_f - E_g - hv\right) \delta\left(E_f(n-1) - E_g - \varepsilon_B\right) \quad (1.67)$$

where ψ_f and ψ_g are the many electron eigenfunctions describing the final and initial states, respectively. T is the transition matrix expressed as

$$T = V_T + V_T \frac{1}{h\nu + E_g - H_o - V_T + iO^+} V_T.$$ (1.68)

V_T is the perturbation potential to cause the transition. V_T includes both optical and Auger transitions. In the present work, we are not dealing with the Auger transition, which is important in the resonant photoemission. In the case like this, the V_T is simplified to be

$$V_T = p_e,$$ (1.69)

where, p_e is the operator for the optical dipole transition.

Before we discuss the transition probability, equation (1.67), we better look into the assumption we made in the three step process leading to the energy relation equations (1.46) and (1.47). The fundamental relation equation (1.43) or (1.44) is correct, since it mention the energy conservation. The relation equation given as (1.46) is not quite so obvious. Since the hamiltonian given in equation (1.6) is correct, its solution obtained by the Hartree-Fock approximation is best approximate solution unless the electron under consideration is not very much localized. The many electron state is expressed as a Slater determinant. The one electron energy, ε_g, as expressed as in equation (1.46) is given by the Koopmans theorem (Kittel, 1967; Seitz, 1940). The Koopmans theorem states that the Hartree-Fock energy of the electron in the n state is just the negative of the energy required to remove the electron

in the state *n* from the solid, provided that the Hartree-Fock functions are extended functions of the Bloch type and that the electronic system is very large.

Because the electron charge is spread throughout the entire crystal, the Hartree-Fock functions will be essentially identical for the problem with or without an electron in the state *n*. This is the basic assumption. Thus, Koopmans theorem indicates that the relation equation (1.46) is valid. A rigorous treatment is found in a textbook on the excitons by Knox (1963).

The fundamental assumption made in the Koopmans theorem is implicitly used in the three step model. In the integration over *dS* leading to equation (1.55), we assume that all points in the thin slab are equivalent. This is equivalent to the fundamental assumption in Koopmans theorem. When we consider the excitation cross section, we consider that the many electron eigenfunctions, ψ_f and ψ_g are written by Slater determinants. We assume that each electronic state is described by an ideal Hartree-Fock solution. Practically we use the approximation such as the energy band or the completely localized functions as in the case of the 4*f* electron.

If we use the Slater determinants as the many electron functions, we may write the Slater determinants in the form of expression as

$$\left|\psi_f\right\rangle = \sum_j \left|f_j\right\rangle \left|\psi_{f_j}(N-1)\right\rangle \qquad (1.70)$$

$$\left|\psi_g\right\rangle = \sum_i \left|g_i\right\rangle \left|\psi_{g_i}(N-1)\right\rangle . \qquad (1.71)$$

Note that the matrix equation $\left|\psi_{f_j}(N-1)\right\rangle$ and $\left|\psi_{g_i}(N-1)\right\rangle$ include signs for expansion.   We select the one electron final state experimentally.   If we write the selected function as $\left|f\right\rangle$, the final state may be written as

$$\left|\psi_f\right\rangle = \left|f\right\rangle\left|\psi_f(N-1)\right\rangle. \tag{1.72}$$

Using equations (1.71) and (1.72), excitation cross section in equation (1.67) is written as

$$\sigma(\mathcal{E}_B, v) = A \sum_i \left|\left\langle \psi_f(N-1)\middle|\psi_{g_i}(N-1)\right\rangle\right|^2 \left|\left\langle f\middle|p_e\middle|g_i\right\rangle\right|^2$$
$$\delta(E_g - E_f - h\nu)\times\delta(\mathcal{E}_B - h\nu + \mathcal{E}_u). \tag{1.73}$$

Here, $\left|g_i\right\rangle$ and $\left|f\right\rangle$ represent the Hartree-Fock one-electron functions.   Paticularly, $\left|g_i\right\rangle$ represents the one-electron orbital of the electron to be excited. If the Koopmans theorem holds and the following relation is valid:

$$\left|\left\langle\psi_f(N-1)\middle|\psi_{g_i}(N-1)\right\rangle\right|^2 = 1 \tag{1.74}$$

then, the transition cross section is given by the one electron functions as

$$\sigma(\mathcal{E}_B, v) = A \sum_i \left|\left\langle f\middle|p_e\middle|g_i\right\rangle\right|^2 \delta(\mathcal{E}_f - \mathcal{E}_g - h\nu)\,\delta(\mathcal{E}_f + \mathcal{E}_B - h\nu). \tag{1.75}$$

The meaning of the condition given by equation (1.74) is clear: When an electron is removed from the system and brought into an excited orbit, the remaining (N-1)-electron system is unchanged.

In case of the energy band approximation is good, equation (1.75) is written as

$$\sigma(\varepsilon_B, \nu) = A \sum_{\alpha, \mathbf{k}, \mathbf{K}} \left| \langle h\nu - \varepsilon_B, \mathbf{k}' | p_e | \alpha, \mathbf{k} \rangle \right|^2 \delta(\mathbf{k}' - \mathbf{k} - \mathbf{K}) \delta(-\varepsilon_{\alpha, \mathbf{k}} - \varepsilon_B)$$

$$= A \sum_{\alpha, \mathbf{k}, \mathbf{K}} \left| \langle h\nu - \varepsilon_B, \mathbf{k} + \mathbf{K} | p_e | \alpha, \mathbf{k} \rangle \right|^2 \delta(-\varepsilon_{\alpha, \mathbf{k}} - \varepsilon_B). \qquad (1.76)$$

The δ function on $\mathbf{k}$ is brought about by the momentum conservation inherent in the transition matrix element. α distinguishes the energy bands. The partial DOS, $\rho^{(l)}$ and DOS ρ, based on the energy band approximation are given, respectively, as

$$\rho^{(l)}(\varepsilon_B) = \sum_{\alpha, k} \delta(-\varepsilon_{\alpha, k}^{(l)} - \varepsilon_B)$$

$$\rho(\varepsilon_B) = \sum_{l} \rho^{(l)}(\varepsilon_B) \qquad (1.77)$$

$$= \sum_{\alpha, k} \delta(-\varepsilon_{\alpha, k} - \varepsilon_B). \qquad (1.78)$$

Here, l distinguishes the orbital symmetry of the states. Since the transition moment appearing in equation (1.76) is a slowly varying function of ε_B, we replace it with the average that is dependent on the symmetry parameter, l, as

$$\sigma(\varepsilon_B, \nu) = A \sum_{l} M_l(\nu) \rho^{(l)}(\varepsilon_B). \qquad (1.79)$$

As the conclusion, EDC in the energy band approximation is given as

$$n\left(\varepsilon_B, \nu\right) = A\, l \sum_{\alpha, \mathbf{k}, \mathbf{K}} \left| \left\langle h\nu - \varepsilon_B, \mathbf{k} + \mathbf{K} \middle| p_e \middle| \alpha, \mathbf{k} \right\rangle \right|^2 \delta\left(-\varepsilon_{\alpha, \mathbf{k}} - \varepsilon_B\right). \qquad (1.80)$$

1.6.4 Electron Escape Depth

In the expression of EDC, a quasi-constant factor, l, is included. We have defined this parameter as the mean free path. In case of EDC, this parameter is referred to as the escape depth. The definition of the escape is given in section 1.6.2. The number, N, of primary of electrons survive after travelling the distance, x, is given by

$$N = N_o\, e^{-x/l}. \qquad (1.81)$$

Here, l is the mean free path and thus the escape depth.

The escape depth of the electron, l, is determined by electron-electron interaction at the energy of interest. In the present case, the photoelectron kinetic energy, ε_u is in the range: ε_u = 10-1000 eV. The Born approximation shows that the cross-section for electron-electron scattering σ_{sc} is given by

$$\frac{d\sigma_{sc}}{d\Omega\, d\varepsilon_u} \quad \propto \quad \frac{1}{k^2} \operatorname{Im}\left[\frac{1}{\varepsilon\left(k, \varepsilon_u\right)}\right]. \qquad (1.82)$$

Thus $1/l$ is essentially determined by the dielectric function, $\varepsilon\left(k, \varepsilon_u\right)$, which is dependent on materials. Here, ε_u is the electron energy and $\hbar k$ is its momentum. This material effect on the escape depth will be observed when the kinetic energy is comparable to the binding energy of a valence electron of ~10 eV. Whereas, for the ε_u > 10 eV, the electron in solids can be described by a free-electron gas because the

binding properties are no longer important.   In this case, the inverse escape depth is

described by the mean electron-electron distance r_s which is roughly equal for all

materials. Then one obtain (Höfner , 1996),

$$l^{-1} \cong \sqrt{3} \frac{a_o R}{E_k} r_s^{-3/2} \log\left[\left(\frac{4}{9\pi}\right)^{2/3} \frac{\varepsilon_u}{R} r_s^2\right] \tag{1.83}$$

where, a_o = 0.529 $\overset{o}{A}$, R = 13.6 eV, and r_s is measured in units of Bohr radius a_o.

This gives us the escape depth as function of kinetic energy, which is called

"universal curve".   Suppose the kinetic energy of a photoelectron is not much

different from the photon energy, $h\nu$.   Then around the photon energies of $h\nu$ = 50-

100 eV, the universal curve takes its minimum of ~5 $\overset{o}{A}$.   Hence the photoemission

spectra taken at $h\nu$ = 50-100 eV are most surface-sensitive.   In this thesis, most of the

experiments were carried out in the kinetic energy region between 15 and 30 eV.   At

these energies, the spectra are more surfaces sensitive.

Here, we should consider the effect of the escape depth based on equation

(1.81). Since the escape depth is 5 $\overset{o}{A}$ in the energy range we are concerned with, it is

much shorter than the penetration depth of light, which is in the range of 1,000 $\overset{o}{A}$.

Therefore, we can naturally regard photoelectron as being generated uniformly in the

layer near the surface. Since the lattice constant of Pt is 3.92 $\overset{o}{A}$, survival rate of

photoelectrons produced in the 10-th layer (19.6 $\overset{o}{A}$) from the surface is 2%.

Therefore, it is sufficient for us to consider the first 10 layers from the surface.

Among photoelectrons produced in these layers, only 25% electrons can come out of

the sample as primary electrons. Remaining 75% photoelectrons generated are scattered out inelastically. Among 25% primary photoelectrons, 8.3% electrons are from the first (surface) layer and 16.7% electrons are from the bulk, i.e., the layers below the second layer. Thus the ratio of the numbers of surface photoelectrons versus that of bulk photoelectrons is 4.6 : 3.8 = 6 : 5.

1.6.5 Measurement of EDC's

So far, we have been considering photoelectrons in the sample. Their kinetic energies are representatively expressed as, ε_u. Now we have to relate ε_u to the kinetic energies observed outside the sample. This is not obvious as we mentioned earlier. For instance, the concept shown in Figs. 1.20 and 1.21 must be treated rigorously theoretically.

After simplifying assumption as the three step model to regard the photoelectron to be retarded by the field of the electron affinity when leaves the surface and jump deep into the vacuum. When the electron enters the spectrometer system, the electron sees another retardation or acceleration field. From the consideration of the contact potential, it is verified that the electron enters the spectrometer system with a kinetic energy of ε_k' given as

$$\varepsilon_k' = \varepsilon_u - \chi_s ,\qquad\qquad (1.84)$$

where, χ_s is the work function of the spectrometer entrance point. However, the kinetic energy, ε_k, of a photoelectron is assumed just to be

$$\varepsilon_k = \varepsilon_u - \chi ,\qquad\qquad (1.85)$$

where, χ is the work function of the sample.

Electron emitted from a sample as it is irradiated with monochromatic light are collected with an electron lens, transferred to an energy analyzer and detected with an electron multiplier. As an electron jumps into an electron multiplier, the number of electrons emerging in the output of the electron multiplier is multiplied by a factor of 10^6 and pulse with measurable currents appears. A preamplifier reduces the impedance; a linear amplifier amplifies the pulse heights in an appropriate range; a counter counts the number of pulse per second. If the rate meter is inserted in a manner shown in Fig. 1.32, the number of pulse per unit time can be monitored. The number of pulses per unit time is stored in a microcomputer. Energy analyzers are usually of the electrostatic type, where electrons are either deflected or repelled by the electric field. Commonly used one is made of an electrostatic condenser, in which electrons passing though the space between electrodes are deflected by the electrostatic field of condenser. There, only electrons with specific kinetic energy can pass though slits after moving along the trajectory determined by the field strength. By changing the field strength, electrons are selected according to their kinetic energy. This process is called as the energy analysis. The energy analysis is made by sweeping the voltage applied to the electron lens or to the condenser. The computer controls the action of the whole system including the wavelength scanning of a monochromer.

Since we are dealing with Pt sample, the energy states of which are described well with the energy band picture, we obtain the relation

$$\left. \begin{aligned} h\nu &= \varepsilon_u + \varepsilon_B \\ &= \varepsilon_u - \varepsilon_g. \end{aligned} \right\} \tag{1.86}$$

The relation equation (1.86) are easily derived from relations' equation (1.46) to (1.50). Equation (1.86) indicates the energy conservation of single one-electron as shown in Fig. 1.33.

What we measure, however, is not ε_k' but the kinetic energy, $\hat{\varepsilon}_k'$, which the photoelectron has in the field of the condenser. Usually, the photoelectron is retarded by the electron lens before it enters the entrance slit of the analyzer. The relation between ε_k' and $\hat{\varepsilon}_k'$ under the presence of a retardation voltage, V_R, is shown in Fig. 1.32. In Fig. 1.32, the electron lens are replaced by a retardation electrodes for simplicity. In the spherical electrostatic energy analyzer, the kinetic energy of photoelectron passing though the analyzer is proportional to the voltage, V_P, applied to the condenser. If the proportionality constant is referred to as α, the argument described above gives the binding energy as

$$\varepsilon_B = h\nu - \chi_s - eV_R - \alpha V_p , \qquad (1.87)$$

where χ_s is the work function of the entrance aperture of spectrometer. By the simple condition of the electron motion and the application of the Gauss theorem to the analyzer, it is proved the α is given as

$$\alpha = e\frac{r_1 r_2}{r_2^2 - r_1^2} , \qquad (1.88)$$

where, r_1 and r_2 are radii of inner and outer spheres, respectively.
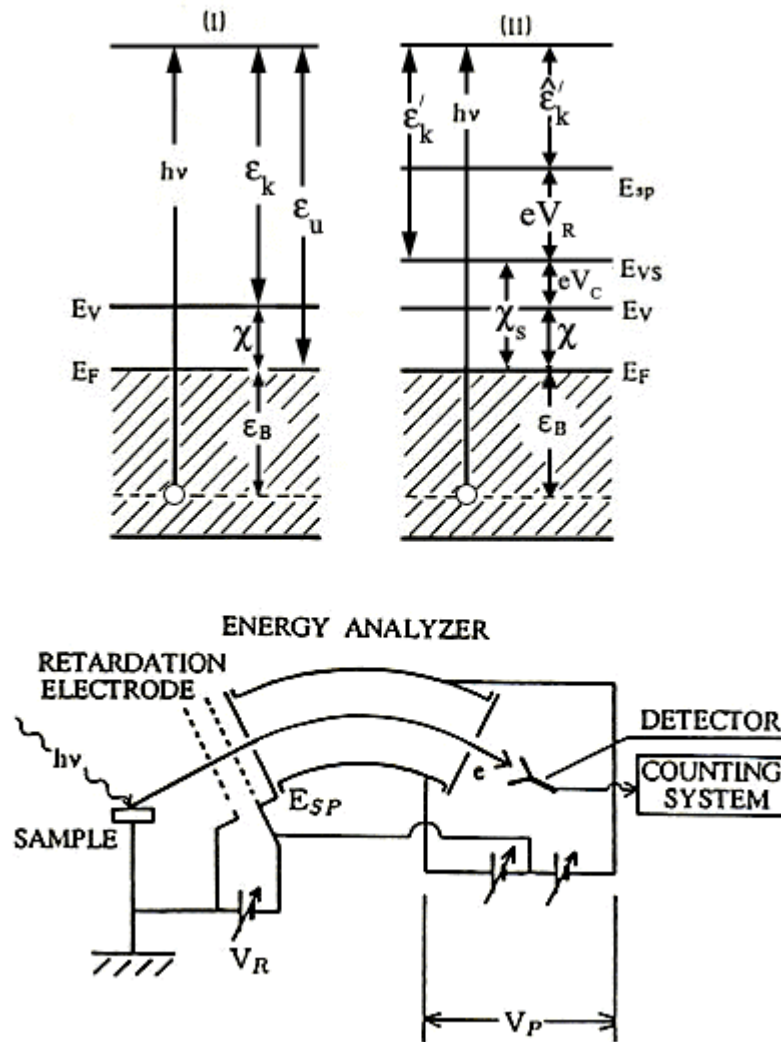
Fig. 1.32 Relation between the kinetic energy of a photoelectron in vacuum and that in the field of an electrostatic energy analyzer. (I): Energy in a sample. (II): Energy in an experimental arrangement. The part of an electron lens is illustrated as retardation electrodes (Ishii, 1989).
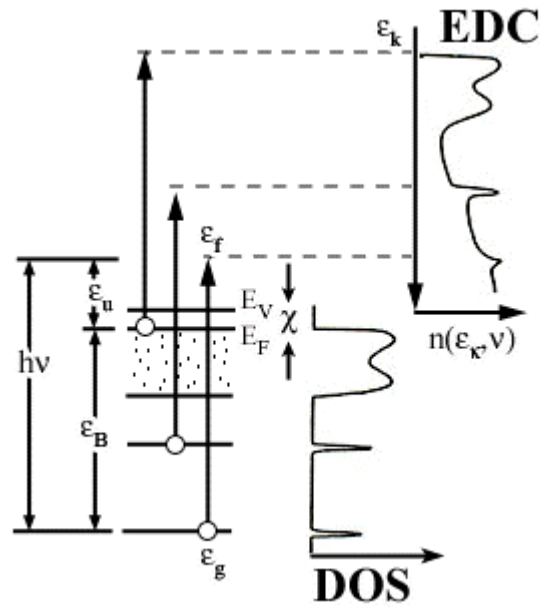
Fig. 1.33 Schematic illustration of photoelectron EDC, corresponding energy levels and the DOS curve. $\varepsilon_f, \varepsilon_g$, E_V and E_F are the energies for the final state, the initial state, vacuum level and Fermi level, respectively (Ishii, 1989).

If an EDC is measured on a metallic sample and a well defined Fermi edge is obtained at parameters (v_F, V_{RF}, V_{PF}), χ_s is given as

$$\chi_s = hv_F - eV_{RF} - \alpha V_{PF} .$$ (1.89)

Since α is obtained by the calibration with monochromatic electron beams using the relation

$$\alpha\,(eV_P - eV_{P0}) = \hat{\varepsilon}'_k - \hat{\varepsilon}'_{ko}$$ (1.90)

we have all measurable quantities on the right hand side of equation (1.89)

One important fact about the electrostatic energy analyzer is that the resolving power is independent of the kinetic energy. By the use of equation (1.88), it is easily shown that

$$\left| \frac{\hat{\varepsilon}'_k}{\Delta \varepsilon} \right| = \frac{R}{w}$$ (1.91)

where, R is the diameter of the electron trajectory in the analyzer. R is given as

$$R = r_1 + r_2 .$$ (1.92)

Thus we have

$$\frac{\hat{\varepsilon}'_k}{\Delta \varepsilon} = \beta$$ (1.93)

where β is a constant determined by the shape and the size of the energy analyzer. In many cases, β is fixed to a value around 100. Equation (1.93) indicates that $\Delta\varepsilon$ is made small if we reduce $\hat{\varepsilon}'_k$ by large retardation.

1.6.6 Angle-Resolved Photoemission Spectroscopy (ARPES)

In angle-resolved photoemission, the number of emitted photoelectrons emitted in the direction (θ,ϕ), the polar and azimuthal angles, with respect to the normal to the sample surface and kinetic energy, ε_k, are analyzed. The photoelectrons are generated by monochromatic light of energy $h\nu$. The energy distribution curve in Fig. 1.33 shows that the primary photoelectrons are observed on the high–energy side of the energy distribution. Somehow they reflect their initial quantum state inside the solid at the detector in vacuum. The most prominent features are the peak of secondary electrons at low kinetic energy, which is due to cascade process created by the primary electrons. In the intermediate energy range, structures due to Auger electrons are observed.

The quantities we measure reflect the state of the electrons in the solid. If we measure the kinetic energy of a photoelectron and its emission direction, we can assign the momentum it has in the vacuum. Let the momentum be **p**. The problem is to obtain the photoelectron momentum inside the sample.   From the equation (1.85), we have

$$\varepsilon_u = \varepsilon_k + \chi .$$

(1.94)

Then the question is whether the electron is deflected when it passes through the surface. The practical assumption we may set up is that only the component of the momentum parallel , $\mathbf{p}_{\shortparallel}$, to the surface is conserved:

$$\mathbf{p}_{\shortparallel} = \hbar\mathbf{k}_{\shortparallel} . \qquad (1.95)$$

Thus, by measuring $\mathbf{p}$, we obtain $\mathbf{p}_{\shortparallel}$ and $\mathbf{k}_{\shortparallel}$ from equation (1.95). Since $\mathbf{k}_{\shortparallel}$ is the wave vector of the photoelectron, then it is the momentum, $\mathbf{k}'_{\shortparallel}$, of the electron in the final state of the transition.

If we use equation (1.86) for the energy band case and the momentum conservation, we have

$$\varepsilon_{c\mathbf{k}'} = \varepsilon_{v\mathbf{k}} + h\nu \qquad (1.96)$$

$$\mathbf{k}' = \mathbf{k} + \mathbf{K}. \qquad (1.97)$$

Here $\mathbf{K}$ is a reciprocal lattice vector. It should be point out that the EDC expressed as by equation (1.76) is further resolved as

$$n(\varepsilon_B, \mathbf{k}, \nu) = A \sum_v \left| \langle c, \mathbf{k}' | p_e | v, \mathbf{k} \rangle \right|^2 \delta\left(\varepsilon_{c\mathbf{k}'} - \varepsilon_{v\mathbf{k}} - h\nu\right)$$
$$\delta\left(\mathbf{k}' - \mathbf{k} - \mathbf{K}\right)\delta\left(-\varepsilon_{v\mathbf{k}} - \varepsilon_B\right) \qquad (1.98)$$

The constraints given in equations (1.96) and (1.97) are the bases for obtaining the energy band dispersion from ARPES.

Before we consider the practical procedure for drawing E-**k** curves, we have to a few important criterions.

1) **k** is originally defined in the reciprocal lattice space, but in practical, it is obtained in the coordinate system in real space. The factor exp(i**kr**) in the Bloch function connects **k** and **r**.

2) The probability for the umklapp process must be small. Otherwise, electrons which are emitted in a specific direction has not unique **k**. Suppose, for instance, photoelectrons with high energies just as the XPS case. Then, in the first Brillouin zone, there are many equi-energy surfaces $\varepsilon_{c,\mathbf{k'}}$ which have the same energy as ($\varepsilon_{v,\mathbf{k}} + h\nu$). Thus there are many cross lines between the equi-energy surfaces $\varepsilon_{c,\mathbf{k'}}$ and the equi-energy surfaces $\varepsilon_{v,\mathbf{k}}$. If we draw vectors from the original to these cross lines, we obtain wave vector **k'** satisfying the energy conservation given by equation (1.96). If we add various **K** to the vectors obtained above, we have the wave vectors **k'** satisfying both the energy and the momentum conservation. Since we have many equi-energy surfaces and **K**, we may have different final state **k'** vectors occurring near the same direction. With a finite angular and energy resolution, different **k'** vectors being oriented comparatively closely cannot be resolved. Since there are many **K** involved in excitations by x-ray, XPS is practically angle-integrated photoemission. For small excitation energies, the transition matrix element occurring in equation (1.80) is small for the transitions in which **K** is not vanishing. If **K** = 0, the number of **k** satisfying both equations (1.96) and (1.97) is limited, and ARPES makes sense. If we ignore the umklapp process, we have

$$\mathbf{k} = \frac{1}{\hbar}\sqrt{2m\,\varepsilon_k}\,\sin\theta$$

$$= 0.51\left(\overset{\circ}{\mathrm{A}}{}^{-1}\right)\sqrt{\varepsilon_k(eV)}\,\sin\theta \qquad (1.99)$$

where θ is the polar angle determining the direction of the photoelectron. Since ε_B is equal to $-\varepsilon_{v,\mathbf{k}}$, we have from equations (1.85) and (1.96)

$$\varepsilon_{v,\mathbf{k}} = \varepsilon_u + \chi - h\nu. \qquad (1.100)$$

If we plot $\varepsilon_{v,\mathbf{k}}$ obtained from equation (1.100) versus $\mathbf{k}_\shortparallel$ obtained from equation (1.99), we obtain the dispersion of the energy band , as

$$\varepsilon_{v,\mathbf{k}} = \varepsilon_v\left(\mathbf{k}_\shortparallel\right). \qquad (1.101)$$

In the case of materials with the two dimensional symmetry, $\mathbf{k}_\perp$ is not a good quantum number and the results obtained as equation (1.101) are the goal of the experiments.

ARPES is quite useful for the two dimensional energy band. On the other hand, the dispersion of the three dimensional band cannot be obtained without making further assumptions, since the component of $\mathbf{k}$ normal to the crystal surface is not known from experimentally observed momentum, $\mathbf{p}$, of the photoelectron in the free space. A model that proved to work well empirically is to adopt the energy free electron approximation for the excited photoelectron. Then, the kinetic energy is given as

$$\varepsilon_u = \frac{(\hbar k)^2}{2m} - E_o, \qquad\qquad (1.102)$$

where $-E_o$ is the potential energy of the interior of the crystal referenced to the Fermi level. If we rewrite equation (1.102) using the measurable energy, we have

$$\frac{(\hbar k)^2}{2m} = \varepsilon_k - (E_o + \chi). \qquad\qquad (1.103)$$

$$= \varepsilon_u + V_o \qquad\qquad (1.104)$$

where V_o is the crystal potential referenced to the vacuum level. Figure 1.34 schematically illustrates the dispersion of the energy band in the approximation described above. The band above the vacuum level is approximated by the nearly free electron band. If we find a photoelectron with a kinetic energy $p^2/2m$, this is equal to ε_k; the electron is in the nearly free electron level given by equations (1.102) and (1.104). In this model, combining equations (1.99) and (1.103), we have

$$k_\perp = \frac{1}{\hbar} \sqrt{2m\left(\varepsilon_k \cos^2\theta + V_o\right)} \qquad\qquad (1.105)$$

$$= \left(0.51 \ \overset{o}{A}^{-1}\right)\sqrt{(\varepsilon_k \cos^2\theta + V_o)(eV)}. \qquad\qquad (1.106)$$

Using equations (1.99), (1.100) and (1.106), we now have $k_{\shortparallel}, k_\perp$, and $\varepsilon_{v,\mathbf{k}}$ expressed in terms of measurable quantities. Thus, if we find V_o appropriately, we can depict the dispersion curve
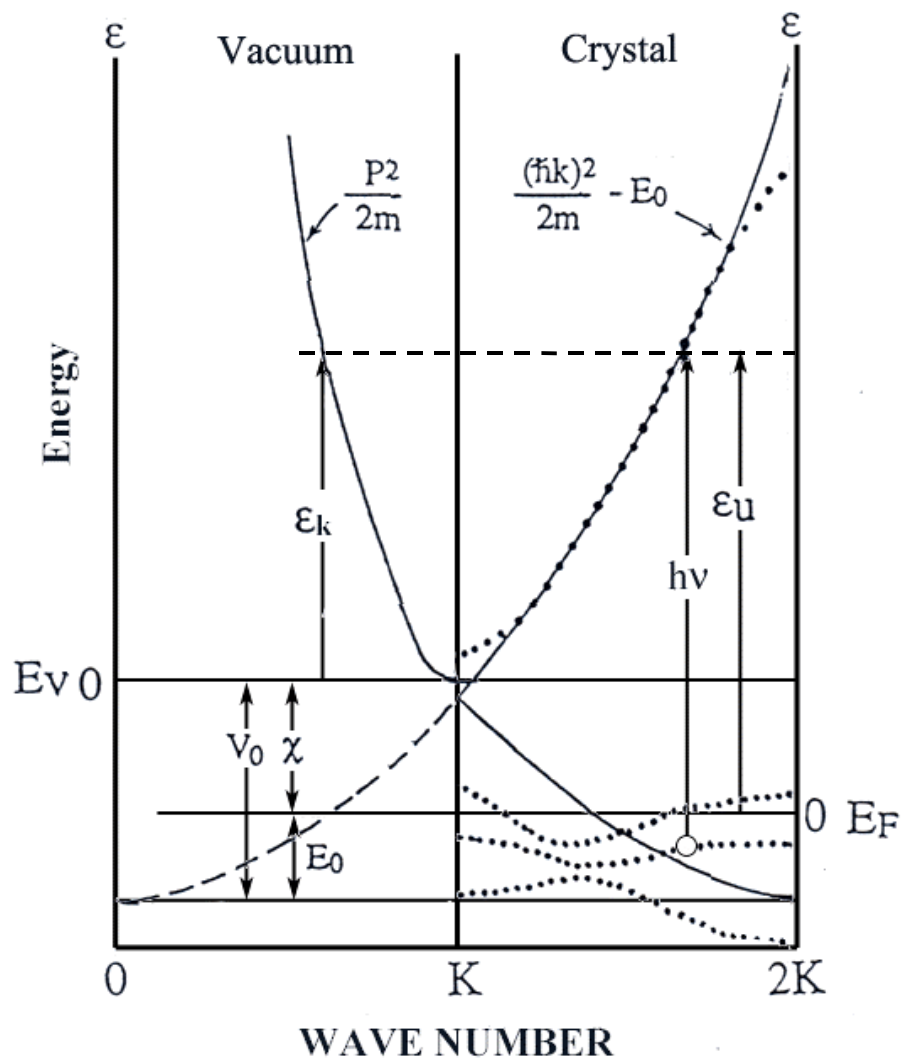
Fig. 1.34 Energy dispersion in the nearly free electron model for photoelectron in ARPES. The right half represents the energy levels in a crystal. Curves illustrated by dots are energy bands. Full lines are energy bands for the nearly free electron model. The reciprocal lattice vector. hv : Photon energy. χ : Work function. ε_u : Kinetic energy in the crystal. ε_k : Kinetic energy in a free space. E_F: The Fermi energy. E_v: Vacuum level (Ishii, 1989).

$$\varepsilon_B = \varepsilon_v\left(\mathbf{k}\right). \qquad\qquad (1.107)$$

In the energy band calculation, the dispersion relation is usually calculated along an axis with specific symmetry. It is rather complicated to select θ and $h\nu$ to obtain $\mathbf{k}$ with specific symmetry. A few methods have been developed so far, but we do not discuss them any further here.

If synchrotron radiation is used as excitation light, the excitation energy is tunable and this is conveniently utilized to obtain the dispersion curve. In this method, only photoelectrons emitted normal to the crystal surface are collected. Then, $k_{\shortparallel} = 0$ and $\theta = 0$, and we have, from equations (1.105) and (1.106)

$$k_\perp = \frac{1}{\hbar}\sqrt{2m\left(\varepsilon_k + V_o\right)} \qquad\qquad (1.108)$$

$$= \left(0.51 \overset{\circ}{A}^{-1}\right)\sqrt{\left(\varepsilon_k + V_o\right)(eV)}. \qquad\qquad (1.109)$$

If a sample is cut so that an important symmetry axis of the crystal lies along the direction normal to the crystal surface, $k_\perp$ give $\mathbf{k}$ along this symmetry axis. If the energy of excitation light is changed, ε_k changes. Thus using equation (1.100), $\varepsilon_{v,\mathbf{k}}$ is obtained. On the other hand, k is obtained from equation (1.108). Thus we obtain the dispersion relation given as equation (1.107).

1.6.7 Parity Determination

ARPES measurements can determine not only the dispersions but also the symmetry of surface states with respect to the mirror axes of a surface Brillouin zone

(SBZ), which is another important physical property of a surface state. It is due to the well known symmetry selection rule of a dipole transition, where the transition probability is proportional to $\langle f | \mathbf{A}\mathbf{p} | g \rangle$, where $|g\rangle$ and $\langle f|$ are the initial and final states wave function, respectively. $\mathbf{A}$ is the vector potential of incident photon and $\mathbf{p}$ is the momentum operator.

Here we have to point that the transition moment is also expressed as $|\langle f | \mathbf{E}\mathbf{r} | g \rangle|^2$ in which $\mathbf{E}$ is the electric vector of excitation light. Furthermore $\mathbf{A}$ is parallel to $\mathbf{E}$. The parity of $\mathbf{r}$ can be assigned easily. $|\langle f | \mathbf{A}\mathbf{p} | g \rangle|^2$ is equivalent to $|\langle f | \mathbf{E}\mathbf{r} | g \rangle|^2$ other than an unimportant factor including energies as far as the parity problem is concerned. Also, the small escape depth is important for the concept described above. Furthermore, it is $\mathbf{E}$ that is incident on a material. $\mathbf{A}$ is defined as $\mathbf{H} = rot\,\mathbf{A}$. In spite of the situation described above, we will discuss the parity of the transition moment in term of $\mathbf{A}\mathbf{p}$ in an abstract way in what follows.

The symmetry of an initial state with a definite symmetry can be selected by the symmetry of $\mathbf{A}$ as well as those of $\langle f | \mathbf{p}$; if $\mathbf{A}$ is even for a given mirror plane only even symmetry of $\langle f | \mathbf{p} | g \rangle$ is excited and vice versa. To secure definite symmetry for $\mathbf{A}$, it is needed to use linearly polarized light and particular geometrical conditions for the measurements. The former is made possible by using the synchrotron radiation as the photon source in ARPES. Synchrotron radiation is inherently polarized. The latter, the geometrical set-up is as follows.

In order to determine the symmetries, two difference measurement geometries, denote as $\mathbf{A}_+$ and $\mathbf{A}_\pm$, are used (Fig. 1.35). In the former geometry $\mathbf{A}_+$, the detector is

arranged so that photoelectron emission always occurs in the plane defined by the surface normal $\hat{\mathbf{n}}$ of the sample and the incident light whose polar angle θ_i from surface normal is fixed. In the present work, the angle is selected as 35°. Since the linear-polarization vector $\mathbf{E}$ thus the vector potential $\mathbf{A}$ of incident synchrotron radiation is always in the plane of emission in this geometry, only the electronic states with even symmetry are excited for a scan along a mirror axis. If not specified in this thesis, a ARPES scan was done in this geometry.

On the other hand, in the latter geometry, $\mathbf{A_\pm}$, the emission is kept in the plane, which contains $\hat{\mathbf{n}}$ and is perpendicular to the plane defined for $\mathbf{A_+}$ geometry. If θ_i is zero in this symmetry, $\mathbf{E(A)}$ is always orthogonal to the plane of emission, thus only the odd-symmetry states can be excited. However, since the actual measurement situation made this condition impossible, θ_i was fixed at 35° and both even- and odd-symmetry states are excited in the geometry $\mathbf{A_\pm}$. Finally through the comparison of spectra taken along a mirror symmetric axis in these two different geometries, we can determine the symmetries of each surface state.

1.7 Synchrotron Radiation

All of the present work, synchrotron radiation was used to excite photoelectrons. The generation of light in a circular accelerator is made by a relativistic beam of electrons (or positrons). Neither a linac nor a heavy particle accelerator emits detectable synchrotron radiation. Whenever an electron is accelerated, it emits radiation in the form of photons. The intensity of emitted light is strong if the acceleration is made by the circular motion. In the vacuum of the storage ring,
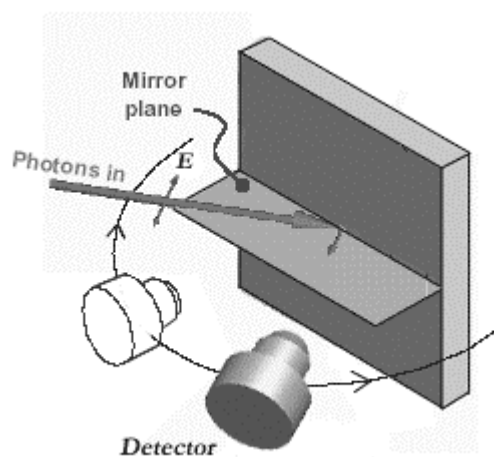
(a) A$_+$ symmetry.
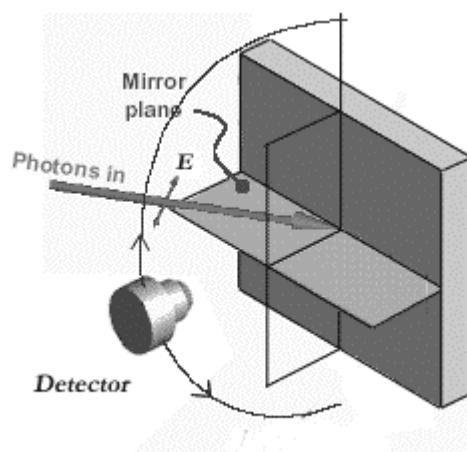
(b) A$_\pm$ symmetry.

Fig. 1.35   Schematic illustration of the ARPES measurement geometries with polarized light.

electrons traveling with a speed near that of light are bent and focused by magnetic fields. Thus, electrons lose their energies in the form of synchrotron radiation. Any energy lost due to emitted radiation is replaced by microwave frequency acceleration. Several excellent properties of synchrotron radiation make it a powerful tool for researches. In the following, distinctive properties of synchrotron radiation are described:

Continuous spectrum: Synchrotron radiation comprises a broad and continuous spectrum of wavelengths with the highest photon flux at ultraviolet or X-ray wavelengths depending on the energy of the accelerator. The higher the energy, the shorter the limit of accessible wavelength.

High flux: The flux from a synchrotron light source is generally much higher than those from conventional sources. This increases magnitudes of signals and reduces measurement time in most experiments. In many cases, the enhanced signal makes it possible to carry out experiments that are prohibitively lengthy if conventional laboratory sources are used.

High brightness: the synchrotron radiation beam is highly collimated owning to the strong forward emission into a narrow cone of a few hundredths of a degree wide. The high collimation combined with the small size of the light source makes the brightness high and allows to perform experiments with high spectral resolution.

Pulsed beam: Since the electron beam in an accelerator consists of a succession of "bunches", synchrotron light is pulsed rather than continuous. Pulsed light makes it possible to follow the progression of a process, such as a chemical reaction. One pulse can be used to initiate a process. Successive pulses can be used to observe events as they take place in real time.

High coherence: Synchrotron radiation has highly coherent nature at long wavelengths. This enables us to carry out phase related experiments.

Linear or circular polarization: Synchrotron radiation can be produced with a high degree of polarization with electric vectors in the plane where the electron beam exists. In a specially designed undulator, circularly polarized light is generated. Synchrotron radiation emitted off the electron orbit plane is elliptically polarized. Polarized light can be used to study the orientation of molecules in matter or on a surface, or to study the orientation of magnetization in magnetic materials. In the present work, this property is used to observe the light polarization dependence of the excitation cross section. The incidence angle dependence of the excitation cross section is definitely determined by the used of this property. The parity dependence of the excitation cross section is also observed using this property.

1.8 Purpose of the Study

The purposes of this thesis work are summarized as follows:

1.) The electronic structures of the clean reconstructed (5x1) and clean unreconstructed (1x1) Pt(100) surfaces will be studied by angle-resolved photoemission spectroscopy.

2.) The experimental determination of the surface energy band structures of Pt (100)-(5x1) and -(1x1) phases along two high symmetry lines ; $\bar{\Gamma} - \bar{\Delta} - \bar{X}$ and $\bar{\Gamma} - \bar{\Sigma} - \bar{M}$, will be carried out.

3.) The experimental observation of the bulk energy band structures of Pt(100)-(5x1) and -(1x1) phases will be carried by normal emission photoemission spectroscopy with s- and p- polarized light.

4.) The experimentally determined energy band structure of Pt(100)-(5x1) and -(1x1) phases will be compared with those obtained by the energy band calculation which have been published elsewhere.

5.) Investigation of odd and even symmetry of Pt(100) surface will be made along the $\overline{\Gamma} - \overline{\Delta} - \overline{X}$ and $\overline{\Gamma} - \overline{\Sigma} - \overline{M}$ lines.

Chapter II

Experimental

In this work, ARPES is employed as the main technique for studying the electronic properties of clean metal surfaces using synchrotron radiation. The processes used to investigate in this technique are highly susceptible to disruption by contamination. Since the mean free paths of photoelectrons in solid are short, the main experimental task in photoemission experiments is the preparation and preservation of clean sample surface (Cardona and Ley, 1978). At an escape depth of 10 $\overset{o}{A}$ and assuming a lattice constant of 4 $\overset{o}{A}$, it is found that the topmost layer of atoms contributes about 30% to total spectrum. It is therefore not surprising that even partial changes in topmost layer that are not intrinsic to the material under study can seriously falsify the results.

In spite of the importance of the sample preparation on which the majority of time for experiments was spent, we will also describe other experimental procedures apparatus in what follows.

2.1 Experimental Apparatus

The experimental apparatus is shown in Fig. 2.1. The experiments were performed in a UHV chamber with a base pressure 2 x 10^{-10} Torr. It was equipped with hemispherical energy analyzer (VSW-50 mm HA 45), a two-axis goniometer for rotating the analyzer, a precision 5-axis sample manipulator to position and rotate the

sample, LEED apparatus and an Auger electron analyzer for characterization of samples, a quadrupole mass spectrometer for residual gas analysis, facilities for argon sputtering and evaporation sources for sample preparation. The details of instruments are described below.

2.1.1 Ultrahigh Vacuum System

Pumping: The UHV system used in the experiments was equipped with a rotary pump and 3 turbomolecular pumps. The pumping system is illustrated in Fig. 2.2. The rotary pump is used for rough evacuation of the system. It reduces the system pressure sufficiently to allow the turbomolecular pump to operate. The turbomolecular pumps in difference pumping speeds, 150 ($1/s$), 500 ($1/s$), and 1500 ($1/s$) are connected to the vacuum chamber through the gate values and manifolds. The pumping is implemented through direct momentum transfer between fast-revolving rotors and the gas molecules. It is not sensitive to the kinds of particular atoms and molecules to be pumped. Very low pressure in the vacuum chamber is realized not only by high pumping speeds of main pumps but the use of turbomolecular pump of 150 ($1/s$) in tandem. The turbomolacular pump must achieve full speed before opening a valve to any low-pressure chamber. So valves must be opened following the proper order. In Fig. 2.2, pneumatic valves are illustrated as V1, V2,....., V8. Evacuation by 3 pumps, we were able to achieve pressure in an order of 2×10^{-10} torr (1 torr = 1.333 mbar).

Pressure measurement: To measure the pressure in the UHV chamber, 3 different pressure gauges, cold cathode gauge (CCG), ion gauge (IG) and Pirani gauge, were employed in this system. The essence of the principle of operation of the cold cathode gauge is that an electron discharge in a modest magnetic field

increases the electron orbit and then the ionization cross section. The current of ionized gases onto the cathode is calibrated to read the pressure; the useful range of the gauge is between 10^{-3} torr to 10^{-7} torr. Below this pressure, the discharge cannot be maintained with the modest high voltage (~1 kV) employed. The main purpose of this gauge was to find the pressure that is low enough to start pumping by a turbomolacular pump.

In order to achieve the UHV state in the range of 10^{-10} torr practically, the vacuum system must not only be pumped properly but it must be free of true and virtual leaks. The latter rise from gases, especially water, adsorbed by the internal chamber walls and instruments. At room temperature these will slowly be desorbed resulting in a large virtual leak which can continue for years. These are eliminated in a few hours by baking the whole system, typically at 150-200 $^{\circ}$C. Several methods of baking exist. The most common is the use of sheath heaters fixed on vacuum chambers and ducts. In the parts having complicated structures or small sizes, heater bands are used around such parts of the system. Whole vacuum system is wrapped with aluminum foil to keep heat so that uniform and efficient baking is realized. In the present experiments, whole vacuum chambers were contained in a box, the walls of which are made of thermal insulators and heating elements were contained in this oven-like shroud. Encased radiation bars were used as heating elements. Whatever approach is taken, it is essential to leave the whole chamber at the required temperature for sufficiently long time even after the temperature is reached over all internal surfaces. By doing this, we can avoid condensation of residual gas molecules in cooler regions. Once the system is to atmosphere, it normally takes several hours

pump down the system to ultra high vacuum. After baking for 12-20 hours, we need similar time for all internal components to cool.

Following baking, degassing of the sample and filament parts is needed.   The heating of the sample is made by electron bombardment of the sample holder for a short time.   This procedure is often referred to as flash baking.   Degassing of filaments is performed just by flowing current on filaments.

After UHV is achieved, the analysis of residual gases shows that they consist of gases that are not main atmospheric constituents. The dominant residuals are usually H_2, H_2O, CO, CO_2 and a variety of hydrocarbons. These promote a reducing environment, which will lead to carbonaceous deposits on all internal surfaces including introduced specimens (O'Connor, Sexton and Smart, 1992).

2.1.2 Sample Holder

The sample holding system was attached to the bottom of manipulator arm. It was made from molybdenum and custom-designed and built for three purposes: (i) to hold Pt sample, (ii) to accurately orient the sample against the detector system, and (iii) to allow efficient sample heating.   In addition, the sample holder has to be designed as compact as possible to allow the sample to be positioned come to the light beam. The manipulator arm is a commercial bellows-type transporter with accurate (x, y, z, θ) degree of freedom.   The bottom of the manipulator arm is a stainless steel cylinder; inside this a stainless steel rod with a vertical travel span of 2 cm is located. This linear motion is actuated by rotating knob and was adapted to give an additional azimuthal degree, ϕ, of freedom.   Molybdenum and tantalum were chosen as the materials of sample holder.   The reason is that their thermal conductivity is low.
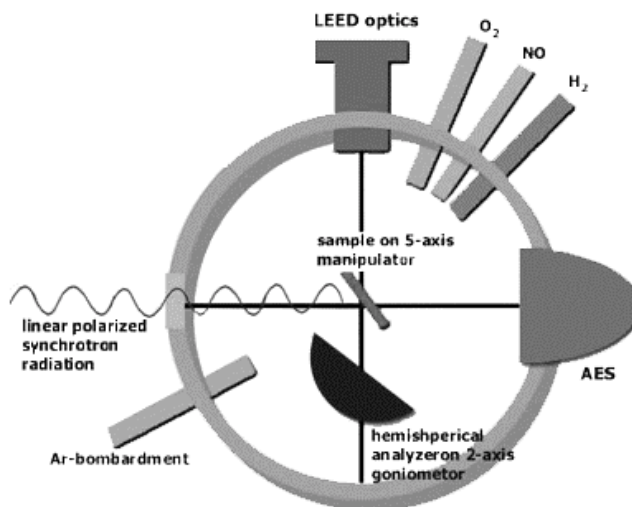
(a) Top View
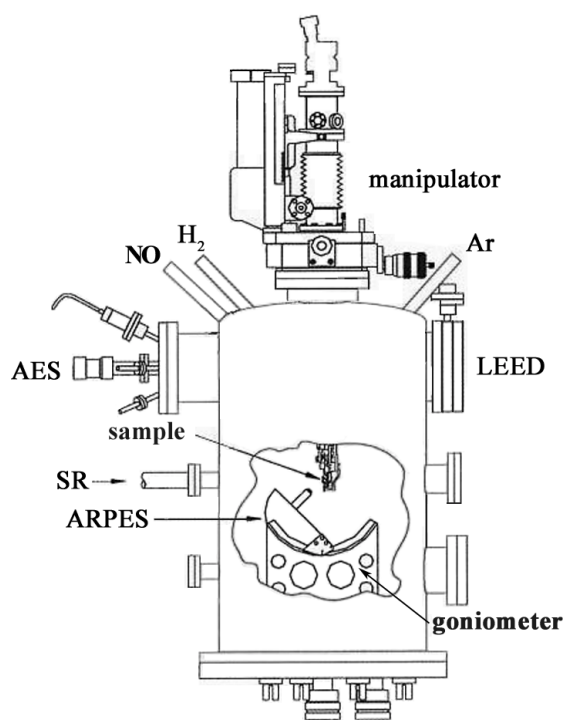
(b) Side View

Fig. 2.1 Schematics of the apparatus used for ARPES experiments.
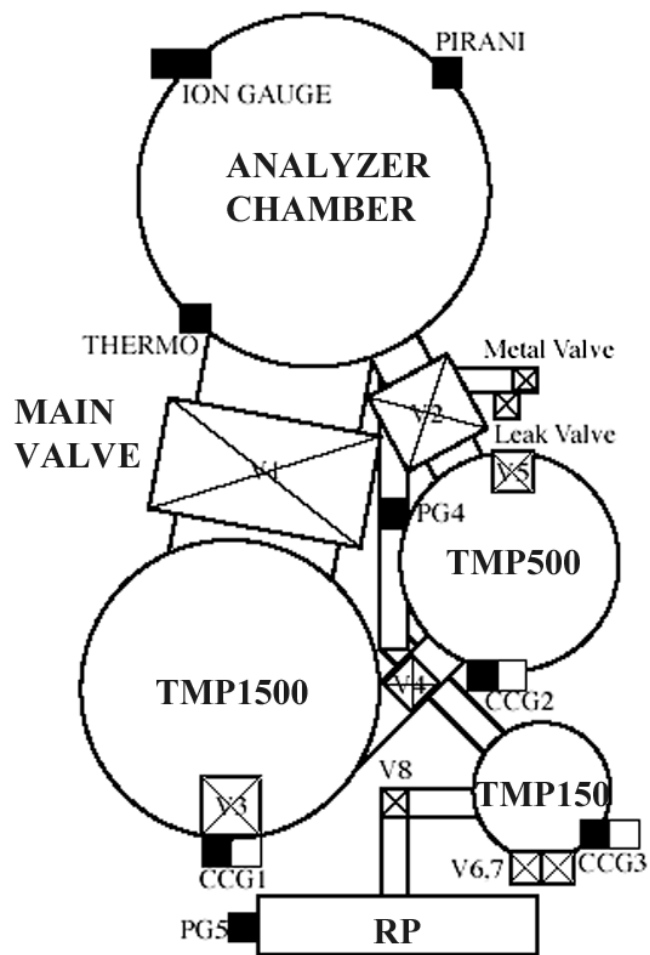
Fig. 2.2 Schematic of pumping system.

This is important to avoid heat conduction away from the sample when the sample is flash heated. The consequences, however, are the necessity of a high current to heat the sample at the time of heating/outgassing of other components.

Heating: A sample is heated by electron bombardment. In this work, tungsten filament is used to connect it with the electric circuit. It is placed behind the sample and separated by insulator ceramics. Electrons from the filament impinge the sample and activate the impurity removing from the surface of the sample.

Temperature measurement: The sample temperature was measure by chromel-alumel thermocouple (K-type) spot welded to the sample.   The manipulator/ sample holder systems are shown in Fig. 2.3.

2.1.3   Low Energy Electron Diffraction (LEED)

One of the most powerful techniques available for surface structure analysis is low energy electron diffraction (LEED).   It is widely used in materials science research to study the surface structure and bonding and the effects of the structure on surfaces. Because it requires single crystals and ultrahigh vacuum conditions, it has a limited value for applied surface science analyses, which are often concerned with polycrystalline or amorphous materials.   LEED has many similarities to X-ray and neutron diffraction but is preferred for surface studies because of the short mean free path of low energy electrons in solids.

LEED is used in this thesis to determine the size and orientation of the unit cells of the clean Pt(100) surfaces with respect to the ideally terminated surface. It is also used to examine the cleanliness of a surface.

The principle of the LEED experiment is reviewed by Jenninges (1992).   The

(a) Manipolator/ sample holder system.

(b) The sample holder with heater and thermocouple lines.

Fig. 2.3 Manipulator and sample holder.

basic LEED apparatus is shown in Fig. 2.4. Electrons are thermally emitted from a hot tungsten filament. The electrons are focussed by a small lens onto the sample surface, which is at the center of several concentric hemispherical grids. Diffracted electrons are scattered inelastically at the sample surface. Elastically scattered electrons, on the other hand, continue past the third grid and are accelerated via a high potential (~2 keV) through the fourth grid onto the final fluorescent screen. The diffraction pattern is viewed through the window as shown in Fig. 2.4.

Figure 2.5 illustrates the simple kinematic scattering model for LEED. Any two-dimensional lattice, such as one occurring at a crystal surface, has a two-dimensional reciprocal lattice in the surface plane. The reciprocal lattice points in the normal direction are distributed along finite rods, called crystal truncation rods. Given this reciprocal-space distribution, the standard Ewald sphere model describes the diffraction scattering. Since the electron energy is lower than 50 eV, the Ewald sphere radius is of the order of the reciprocal lattice dimensions. Intersection between the sphere and the crystal truncation rods give the vector of scattered electrons as shown in Fig 2.5a. Although the LEED patterns observed are determined by this configuration, the intensities are not easily predicted; multiple scattering between the incident electrons and the solid surface preclude a simple structure-factor analysis. Dynamic electron scattering theory must be employed to find the correct intensities. However, such detailed treatment is not necessary for a simple surface structure analysis. More details about LEED experiments are written by Conrad (1996).

For the case of the clean Pt(100) surface in this study, the diffraction pattern of the unreconstructed (1x1) structure appears square as shown in Fig 2.5b. The relative intensities of the spots are energy dependent. In general, at most a 4-fold symmetry is
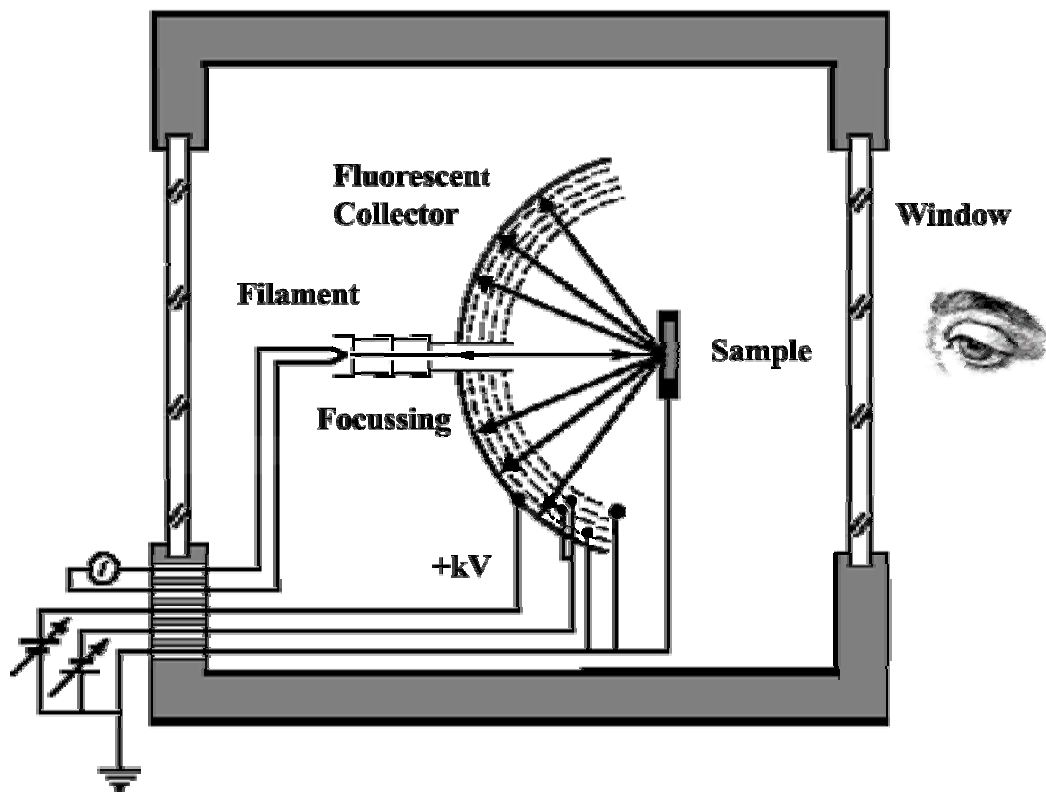
Fig. 2.4 LEED apparatus. Electrons thermally emitted from the filament are focussed onto the sample. Elastically scattered electrons are passed by the grids and accelerated onto the fluorescent collector screen.

observed. Figure 2.5c presents the LEED pattern of reconstructed (5x1) structure from this thesis work, which results from the superposition of two structures rotated 90° to one another (Morgan and Somojai, 1968).

2.1.4 Auger Electron Spectroscopy (AES)

Auger electron spectroscopy (AES) was used in this work to examine some contaminats and impurities on the surface of platinum such as carbon and oxygen. AES is based on the Auger effect that discovered by L. Meitner and P. Auger in 1923. If an atom is ionized by removal of an electron from an atomic core level, a second electron could be ejected with an energy characteristic of the atom. The second electron is the Auger electron, and its energy is independent of the energy of the ionizing electron. This allows the identification of the element from the measurement of the emitted electron energies.

The origin and nature of the Auger process can be understood from the diagram of the electron energy level as shown in Fig. 2.6. Ionizing radiation ejects an electron from an atom in the solid, leaving a hole in one of the atomic core levels. An electron from a higher level shell quickly fills this core level and energy is released. This energy can leave the atom in the form of X-ray fluorescence, or there can be a competing process where another electron gains the energy and is ejected from the atom. This second ejected electron is the Auger electron and its energy depends on the energy of the atomic level involved in its production, not on the energy of the initial ionizing radiation. The energy of the Auger electron can therefore be used for element analysis. Only H and He do not give rise to Auger electrons as two electron shells are needed. Although Li has only one electron per atom in the L shell it can
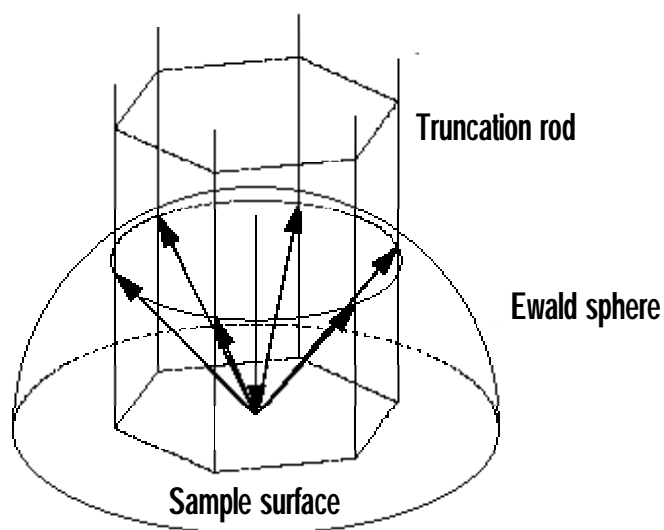
(a) Eward sphere construction for LEED.
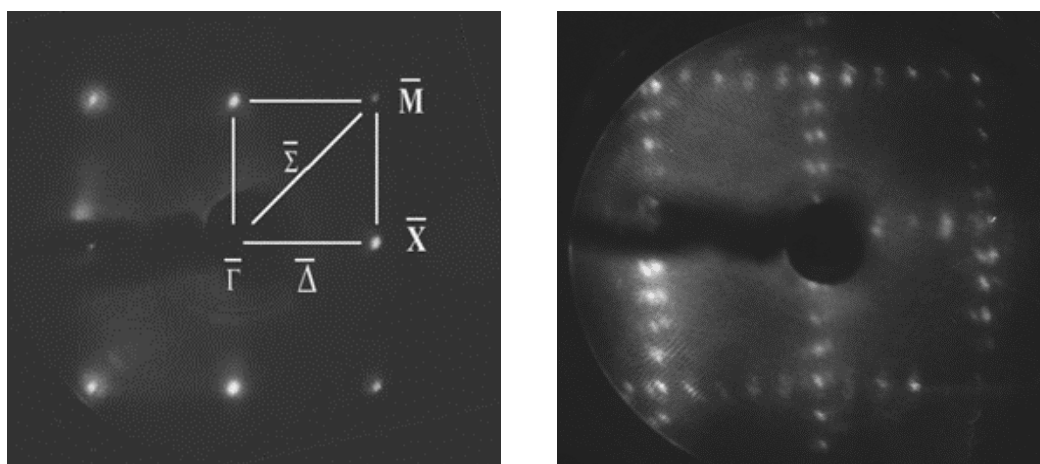
(b) LEED pattern of Pt(1x1) structure   **(c)** LEED pattern of Pt(5x1) structure

Fig. 2.5 LEED pattern. (a) Surface crystal truncation rods intersect the Eward sphere
to determine scattered electron vectors.   (b) LEED pattern obtained from
clean unreconstructed Pt (100) surface, which shows square pattern like from
bulk terminated.   (c) LEED pattern obtained from clean reconstructed Pt
(100) surface, which shows the diffraction beam in (1/5) [th] order position.

share its valence electron in a solid. The energy of Auger electron emitted from a solid surface is largely determined by the binding energies of the atomic energy levels in the participating atom. There are also contributions to the Auger electron binding energy from the screened Coulomb interaction of the final state holes, and relaxation of the surrounding electrons. This relaxation involves both the electrons in the atom itself and in the surrounding material.

The nomenclature used to describe an Auger transition is derived from X-ray terms. The inner electron shell being the K, and higher shells being L, M, N, O and V are used to denote valance states. For example the strong carbon KLL Auger feature around 273 eV is formed by an initial ionization of the inner K shell $1s$ electrons. The valance electrons of the carbon atom are in the two-L shells. One valence electron fills the K shell hole and the other ejected as an Auger electron. The carbon spectrum is very sensitive to the chemical environment and the density of states that the valence electrons occupy. The Auger transition nomenclature can be made more rigorous by including with the X-ray terms, the partial terms for the angular momentum. For s, p and d the terms 1, 2, 3, 4 and 5 are used, e.g. KL_1L_2.

The AES system consists of an ultrahigh vacuum system, an electron gun to bombard the sample surface and an electron energy analyzer to collect and analyze the secondary electron distribution. In this work we use a hemispherical analyzer as the electron energy analyzer. This analyzer consists of an input lens, and two concentric hemispheres forming a condenser-like structure. Electrons from the sample are focused by the input lens onto a slit at the entrance of the field of the hemispheres. A potential difference between the hemispheres is arranged to give a $1/r^2$ field, and electrons with the correct energy are focused into a slit at the exit of the

hemispheres. The resolving power of the analyzer is determined by the slit size, the mid hemisphere radius, and the entrance angle. However, the resolving power of the total system can be changing the input lens retardation. This gives the hemispherical analyzer great flexibility and high-energy resolution.

Auger spectra are normally displayed in one of two ways. The direct spectra is the relation of ε versus $N(\varepsilon)$ where ε is the Auger electron energy. However, the derivative spectra, $d[N(\varepsilon)]/d\varepsilon$, as shown in Fig. 2.7 has been preferred. The direct Auger spectrum consists of weak emission band that overlaps a huge broad background band. Thus, the real emission band cannot be easily resolved. If the derivative curve is plotted, the broad background band that obscures the Auger emission band is eliminated and the Auger band is clearly recognized as the derivative form. In order to obtain the derivative, the voltage supplied to the spectrometer, thus the spectrometer energy, is modulated at several kilohertz. The modulated signal is detected using a lock-in amplifier as the differential form of the $N(\varepsilon)$ signal.

Because of the advance in computer technology, the derivative spectrum is obtainable by computer calculation. What we measure is the raw Auger spectrum, $N(\varepsilon)$. Then computer output gives us the plot of $\Delta N(\varepsilon)$ versus ε, where $\Delta N(\varepsilon)$ is the difference of the intensity between adjacent measured points, i. e.,

$$\Delta N(\varepsilon) = n(\varepsilon_{n+1}) - n(\varepsilon_n)$$

$$= n(\varepsilon_n + \Delta\varepsilon) - n(\varepsilon_n). \qquad (2.1)$$

Since the interval $\Delta\varepsilon$ is a constant, the plot of $\Delta N(\varepsilon)$ gives the derivative spectrum, $dn/d\varepsilon$ versus ε.
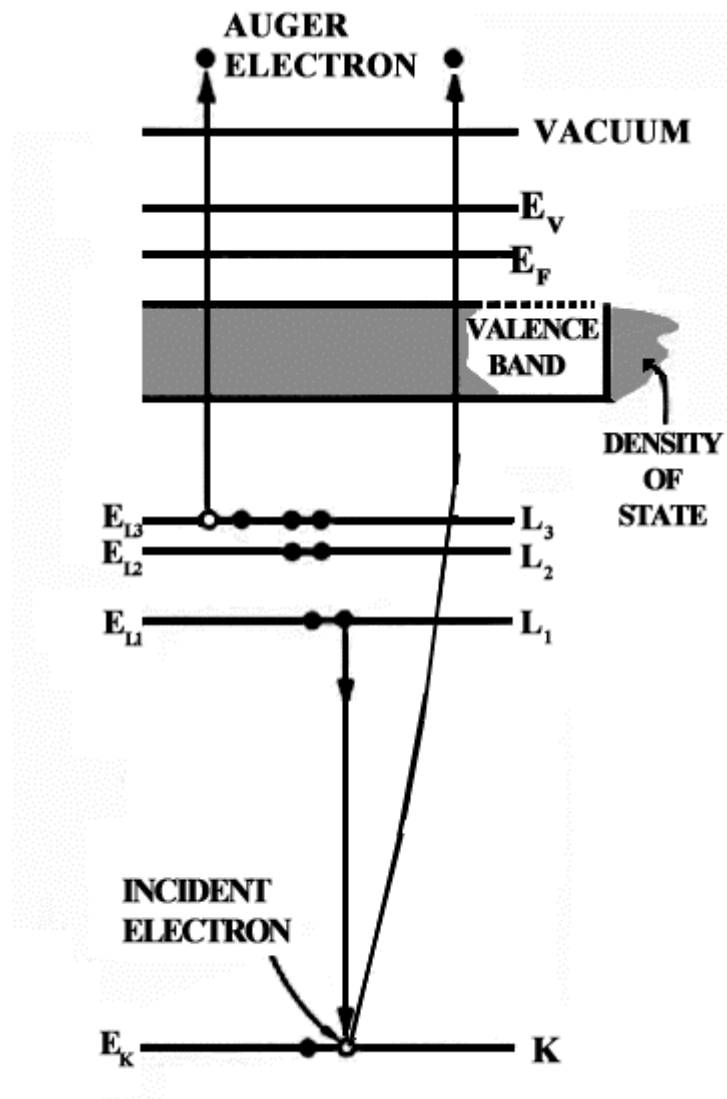
Fig. 2.6 Schematic energy level diagram illustrating the origin of the Auger effect. The Auger process in this figure is the KL_1L_3 process (Wild, 1981).
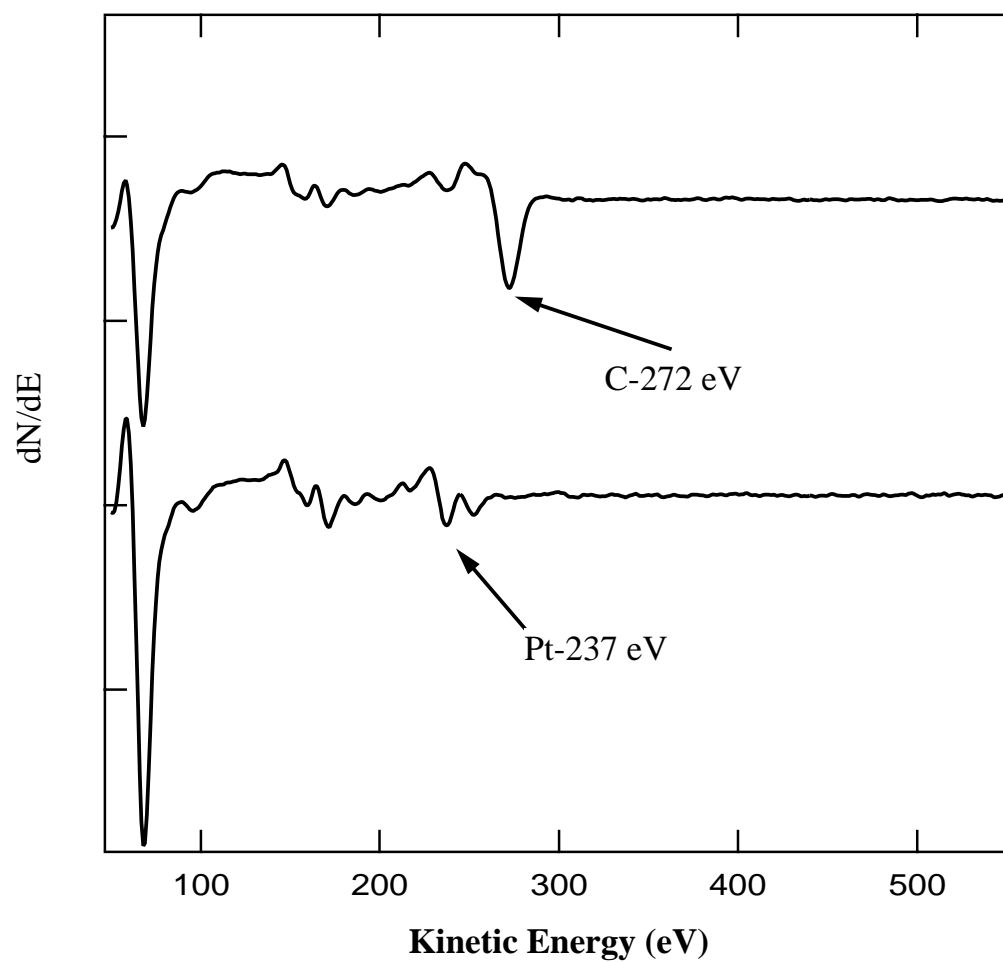
Fig. 2.7 Auger spectrum from $N_{6,7}VV$ Pt in differential spectrum. The upper graph represents the graph with high carbon contamination. The lower graph is the graph from the clean reconstructed Pt(5x1) structure.

2.1.5 Quadrupole Mass Analyzer (Q-mass)

A quadrupole mass analyzer was used for residual gas analysis in the UHV chamber. A quadrupole mass analyzer consists of an ion source, ion optics to accelerate and focus the ions through an aperture into the quadrupole filter. The quadrupole filter has a control voltage supply, an exit aperture, an ion detector and attached electronics and a high-vacuum system. The principle of Q-mass analyzer is that only electric fields are used to separate ions according to their mass to charge ratio (m/z) values. A quadrupole filter consists of four parallel rods or poles through which the ions to be separated are passed. The poles have a fixed DC and alternating RF (AC) voltages applied to them. Depending on the produced electric field, only ions of a particular certain mass-to-charge ratio will be focused on the detector, all the other ions will be deflected into the rods. By varying the strengths and frequencies of electric fields, different ions will be detected. Thus the mass spectrum is obtained. The trajectory of an ion through the quadrupole electrodes is very complex.

The four rods are shown as being circular in the diagram but in practice they have a hyperbolic cross section. Two opposite rods have a potential of + *(U + Vcos(ω t))* and the other two - *(U + Vcos(ω t))* where *U* is a fixed potential and *Vcos(ωt)* represents a radio frequency (RF) field of amplitude *V*. When *cos(ω t)* cycles with time, the applied voltages on opposite pairs of rods vary in a sinusoidal manner but in opposite polarity. Along the central axis of the quadrupole assembly and also the axis between each adjoining rod the resultant electric field is zero. In the transverse direction of the quadrupoles, an ion oscillates between poles in a complex fashion, depending on *m/z, U, V* and, *ω*. By suitable choices of *U, V* and *ω*, only ions

with one *m/z* oscillate stably through the quadrupole mass analyzer and reach the detector.   All other ions have greater amplitudes of oscillation and strike one of the rods.   In practice, the frequency ω is fixed with typical values between 1-2 MHz. The length and diameter of the rods determine the mass range and ultimate resolution that can be achieved by the quadrupole assembly.
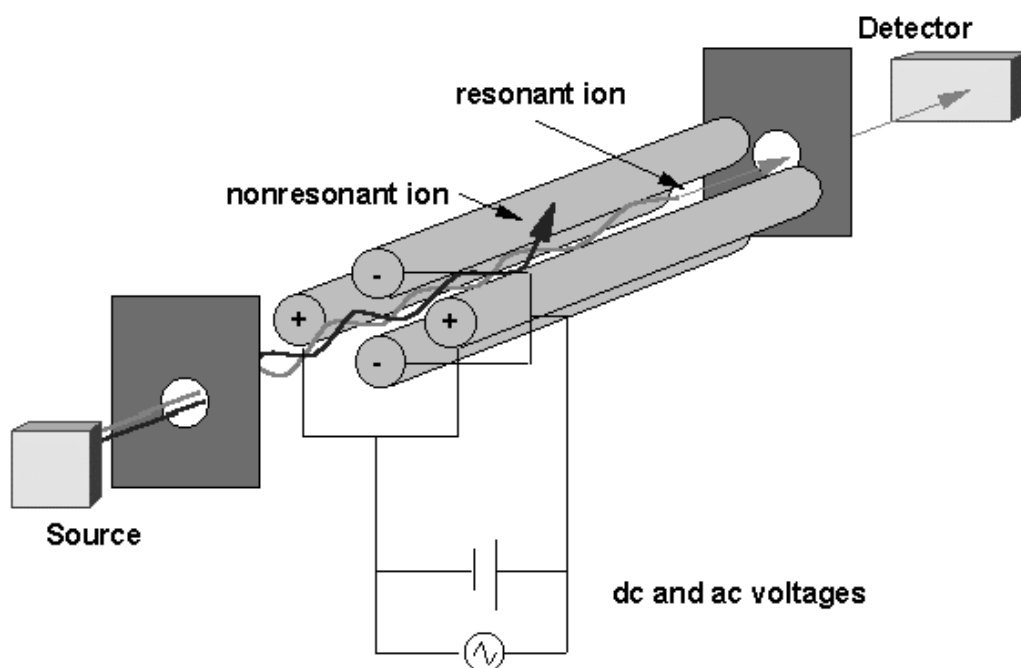
Fig. 2.8 Schematic diagram of a quadrupole mass analyzer:

2.1.6 Photoelectron Energy Analyzer

To analyze photoelectrons in the present work, an electrostatic 180° hemispherical energy analyzer, VSW HA 54 model, was employed. The size of the analyzer is shown in Fig. 2.9. The priciple of energy analysis is partly described in section 1.6.5. The basic concept is that only electrons with an energy of αV_p can pass the energy analyzer. This energy is often referred to as the pass energy. Namely

$$\varepsilon_p = \alpha V_p. \tag{2.2}$$

If the well known theorem that the centripedal force for the central electron trajectory is equal to the force caused by the electric field of the analyzer, the relation equation (2.2) is easily proved. There α is given by equation (1.88).

Another important property of the energy analyzer is that it does not have a focussing power in the radial direction. Thus the beam divergence affects the resolution. Suppose electrons in the energy analyzer move along an orbit with a direction making an angle of φ to the central trajectory. The first integral of the equation of motion gives us

$$\varepsilon_\theta (1+\varphi^2) - \frac{\alpha V_p}{r} = C. \tag{2.3}$$

Here, ε_θ represents the kinetic energy for the polar coordinate motion. Note that

$$\varphi = \frac{v_r}{v_\theta} \tag{2.4}$$

for small φ. For the central field, $\varepsilon_\theta = \varepsilon_p$ and $r = r_\theta$. Since the kinetic energy for the motion toward the radial direction is small, we may take $\varepsilon_\theta = \varepsilon_p$. Thus, we have

$$\Delta\varepsilon = \varepsilon - \varepsilon_p = \varepsilon_p\left(1+\varphi^2\right) - \varepsilon_p = \varepsilon_p\varphi^2 . \tag{2.5}$$

Therefore we have

$$\frac{\varepsilon_p}{\Delta\varepsilon} = \frac{1}{\varphi^2} . \tag{2.6}$$

Obviously this must be added to the resolving power given by equation (1.91). Thus in the inverse resolving power description, the total inverse resolving power is given as

$$\left|\frac{\Delta\varepsilon}{\varepsilon'_k}\right| = \frac{\omega}{R} + \varphi^2 . \tag{2.7}$$

When φ^2 is small, it may be neglected and the resolving power is given as equation (1.91) or (1.93) which expresses how the resolution changes as central orbit changes.

As implicitly mentioned in section 1.6.5, we can reduce the pass energy, which is equal to ε'_k by retarding the speed of photoelectrons coming into the energy analyzer. This is done by the electron lens.

The energy analyzer consists of three stages. The first stage is an electrostatic lens, where photoelectrons emitted from the sample are collected and focused on the entrance slit of the energy analyzer. In this part, it is possible to retard the kinetic energies of photoelectrons variably for scanning the photoelectron energies. The second stage, B, is a hemispherical electrostatic condenser type energy analyzer. In this energy analyzer, the electron beams with different kinetic energies are focused at the different points on the focal plane. Just on the focal plane a multiple channeling electron detector (a microchannel plate electron multiplier and a resistive anode

position encoder) is installed. This detector makes it possible to detect the intensities of photoelectrons with different energies separately at one time. This enhances the efficiency of the measurements.
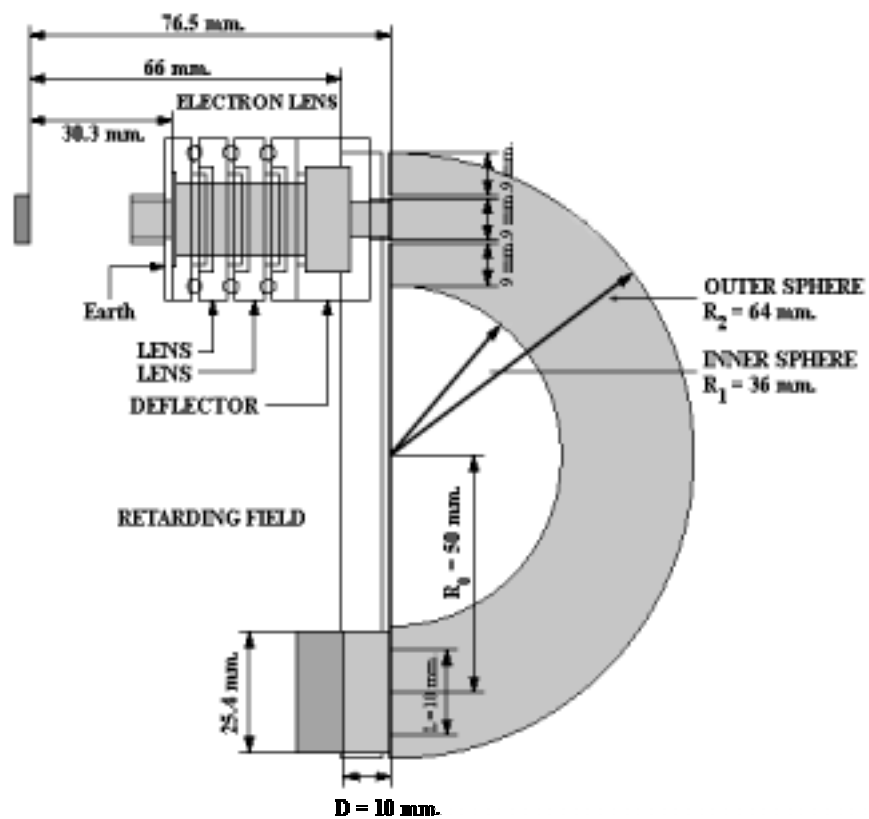
Fig. 2.9 Schematic view of a VSW HA54 model of hemispherical analyzer.

2.1.7 Electron and Ion Guns

In this work, electron guns are used as an electron source for the LEED,the AES and an ion gun for sputtering the surface impurities. The electron guns function in the following manner. A positive electrical potential is applied to the anode. A filament (cathode) is heated until a stream of electrons is produced. The electrons are then accelerated by the positive potential down the column. A negative electrical potential ($!$ 500 V) is applied to the Wehnelt electrode (cap). As the electrons move toward the anode any ones emitted from the filament's side are repelled by the Wehnelt cap toward the optic axis (horizontal center). A collection of electrons occurs in the space between the filament tip and Wehnelt cap. This collection is called a space charge. Those electrons at the bottom of the space charge (nearest to the anode) can exit the gun area through the small (<1 mm) hole in the Wehnelt cap. These electrons then move down the column to be later used in imaging. This process insures several things. That the electrons later used for imaging will be emitted from a nearly perfect point source (the space charge). All electrons later used for imaging have similar energies (monochromatic). Only electrons nearly parallel to the optic axis will be allowed out of the gun area. An electron gun is used to produce a stream of electrons with a well defined kinetic energy. The acceleration stages consisting of a few cylinders are used for this purpose.

The ion gun is used for sputtering the surface impurities. It consists of a chamber, in which Ar^+ ions are produced, the acceleration stage, steering electrons and the focusing elements. The Ar gas is introduced in the gas chamber to a pressure around 10^{-6} torr. Ar^+ ions are formed by ionization through collision with electron from a filament. The ionization current is about 2.0 μA. Generated Ar^+ ions are

extracted by the electric field formed by the extraction electrodes.   The applied voltage is adjusted so that an appropriate value of the ion current is obtained. The ion beam position and the beam direction is also adjusted by the focusing elements and the steering fields.

2.1.8 Light Source : Synchrotron Radiation Source

The experiments were carried out using a synchrotron radiation from BL-11C of Photon Factory (PF) at High Energy Accelerator Research Organization (KEK for the Japanese acronym), Japan.   PF is an accelerator complex dedicated to produce synchrotron radiation for material sciences.   The facility of PF consists of a 2.5 GeV electron/positron linac and a 2.5 GeV storage ring.   Electrons or positrons are accelerated by the linac to 2.5 GeV and transported to the 2.5 GeV storage ring. There are dipole magnets (bending magnets) and insertion devices: wigglers and undulators, located at different sections around the storage ring for generation of synchrotron radiation.   The electrons emit electromagnetic waves in the bending magnet portions. These electromagnetic waves called synchrotron radiation have a remarkably wide spectrum of light.   The generation of synchrotron radiation in the insertion device is more or less similar to the case of the bending magnet portion. Beamlines (BL) installed around the storage ring finally transport the synchrotron radiation to the experimental station for scientific experiments.   Experimental stations are installed in the experimental hall outside the radiation shield wall that separates the storage ring room from the experimental hall.   Figure 2.10 shows the 2.5 GeV storage ring and the beamlines at PF. In Fig. 2.10, the 2.5 GeV storage ring has an oval shape with 28 bending magnets. The beam is injected from the injector linac (upper-right). There are 28 major beamlines installed in the storage ring. Near the

end part of each beamlines, there are a few branch beamlines where some experimental setups and monochromators are installed. On the upper-right corner in Fig. 2.10, the beamlines in the experimental hall at 6.5 GeV in AR (Accumulation Ring) are also depicted. AR was first bulid for accumulating positrons to be injected to the high energy collider ring, TRISTAN, built for seeking top quarks. Now it is used as a fully dedicated X-ray source.

A beamline comprises a radiation absorber, vacuum valves, a radiation beam shutter, a very-fast-closing-valve, vacuum pumps, vacuum monitors (vacuum gages), safety interlocks and a computer system for controlling the operation of the beamline, as shown in Fig. 2.11. The beamlines are so designed as to protect the UHV of the storage ring from an instantaneous hazardous vacuum failure at experimental stations. The beamlines can easily satisfy the requests for transportation synchrotron radiation to the experimental hall. However, it is difficult to satisfy all the requests for protecting the UHV of the storage ring from an unexpected instantaneous vacuum failure in an experimental station and in-rushing air of high pressure when a rupture of experimental setup occurs. Resulting shock waves can results in fatal damage to vacuum components, high power RF klystrons and other components of the storage ring and beamlines. Since normal valves and shutters have a closing time of more than a few seconds or longer reach the storage ring chamber with the sound velocity and cause abrupt pressure rise. This to protect the storage ring and beamlines from such accident. A long acoustic-delay-line is installed in the middle of a beamline to reduce the shock-wave velocity and a special fast-closing valve that can close in 0.001 seconds.
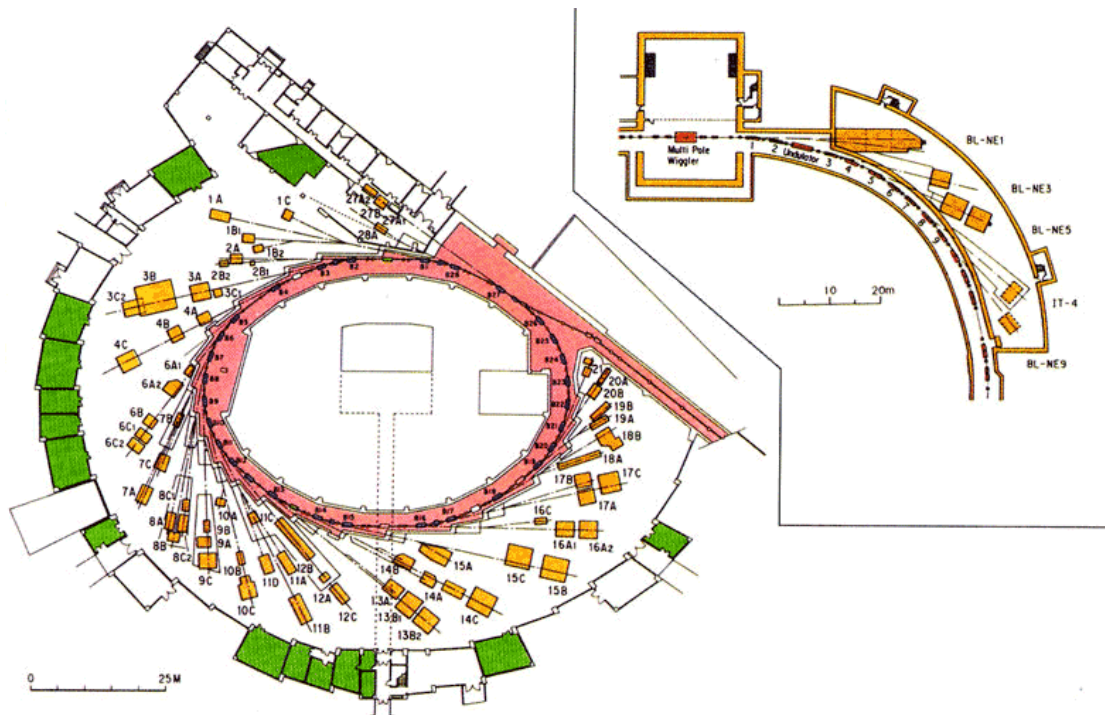
Fig. 2.10   The Photon Factory 2.5 GeV electron/positron storage ring complex (Hori et al., 1999).
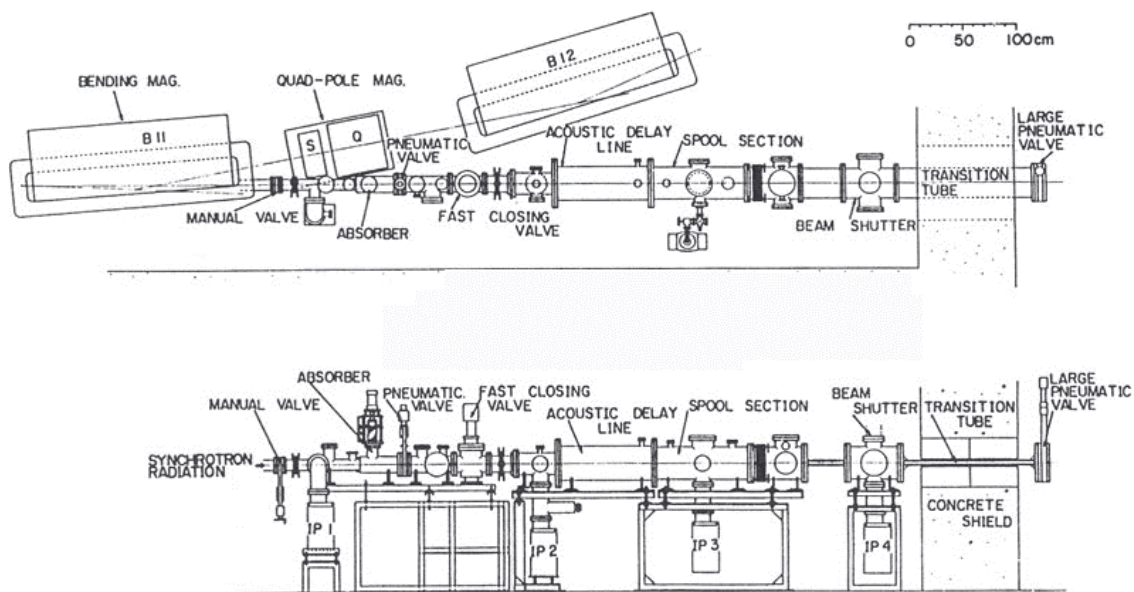
Fig. 2.11 Synchrotron radiation beamline.

Measurements in the present work was carried out at BL-11C in PF. At BL-11, synchrotron radiation from a bending magnet part is used. This beam line consists of four branch beam lines, namely, BL-11A, BL-11B, BL-11C and BL-11D. The BL-11C is installed at the second floor where a Seya-Namioka monochromator is installed to monochromatize synchrotron radiation. The Seya-Namioka mounting of a grating is shown in Fig. 2.12. A concave spherical grating and two slits, incident and exit, are mounted on the Roland circle. The distance between the incident slit, S_1, and the grating, G, is kept equal to that between the exit slit, S_2, and grating, G. The angle, S_1GS_2, is taken to be 70.8^o. In this configuration, the defocusing of the image of S_1 on the S_2 point caused by the rotation of G (spherical and coma aberration) is minimized and a sharp image of S_1 is kept on the S_2 point over a wide range of the rotation angle of G. By the rotation G, light with different wavelengths is selected. A grating having a groove density of 1200 ℓ /mm is used. The available spectral range is form 15 eV to 30 eV. The resolving power, $\varepsilon /\Delta\varepsilon$, is 22000 for a slit width, ω, of 50 μm.

2.1.9 Control and Data Acquisition System

Almost all analysis instruments used in this work are under computer control and data are acquired and stored in digital.

A schematic diagram of an electron spectroscopy data acquisition and processing system is shown in Fig. 2.13. The computer has the direct control, through appropriate interfaces, of the primary excitation source and of the analysis and detection of photoelectrons. The means are provided for data processing operations and output either as a hard copy or in the digital form. The computer used for the control of the measurement is personal computer. The same computer was used for

the data taking in ARPES measurements. The data stored in the computer were transferred to the computer in a private notebook type computer, which was brought back to Thailand. Data processing was carried out with this notebook computer.

2.2 Sample preparation

As described above, in the photoemission measurements on solid materials, the preparation of a clean and well-defined surface is the main experimental task. The contamination of the surface of a solid material is brought about by impurity atoms or ions.from the residual gas in the sample chamber or the impurity ions contained in the bulk material. The important impurity species are oxygen and carbon. The carbon originates in organic molecules in the residual gas. Some time it contained in the bulk migrate to the surface. If the carbon atoms are in the bulk material, it take a long time to remove them. The oxygen atoms may be also contained in the bulk. When oxygen atoms reach the surface, they react with hydrogen in the residual gas to produce H_2O. This water molecules stick to the surface. However, they are easily removed, because they stick to the surface as physisorption.

To removed of foreign atoms contaminating the surfaces is accomplished by heating or by the bombardment with high-energy (1-5 keV) rare gas atoms, usually argon. Heating the specimen makes absorbed atoms come off by the thermal excitation. For the argon ion bombardment, argon gas is ionized by electron bombardment and the ions are accelerated through a lens system towards the sample
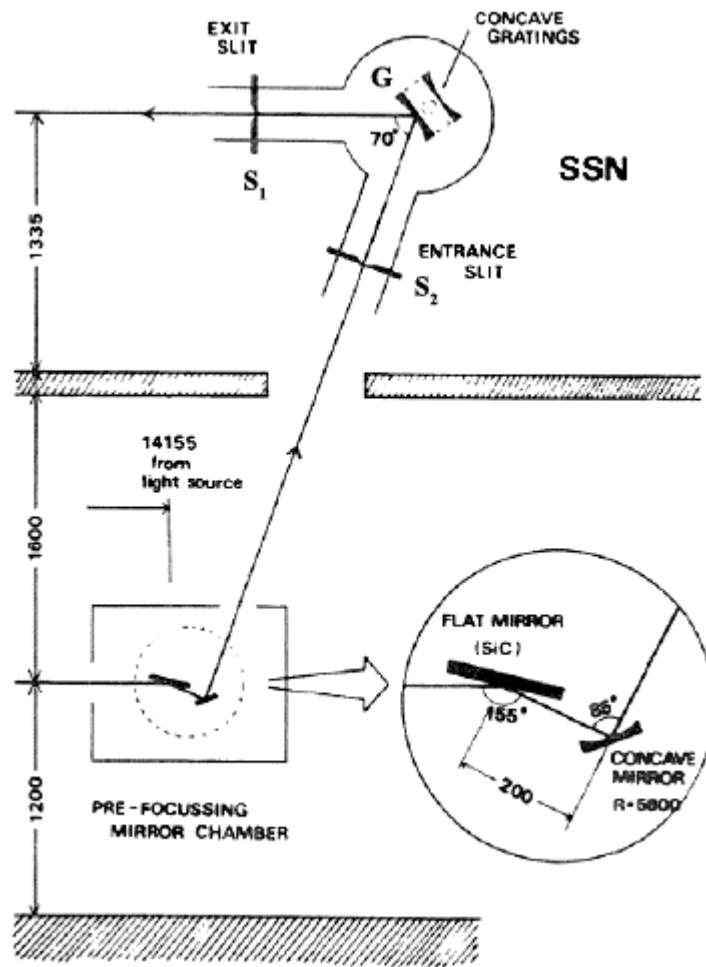
Fig. 2.12 Seya-Namioka monochrometor at BL-11C (Ono, 2003).
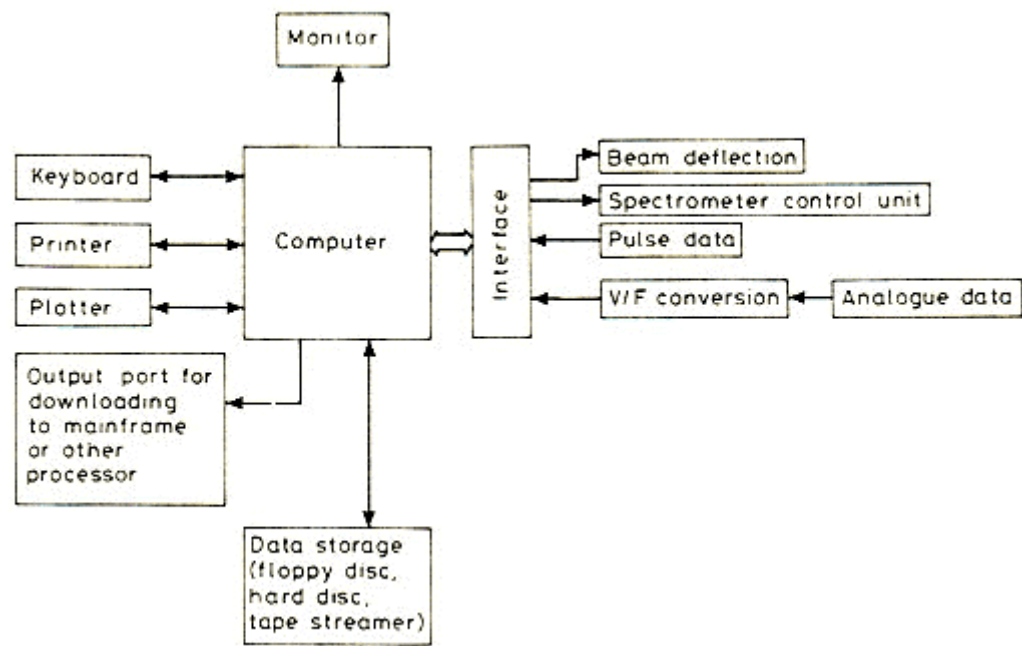
Fig. 2.13 Schematic arrangement of a spectrometer control system with data

acquisition and processing.

as mentioned already. Argon gas pressure in the ion gun chamber is of the order of 10^{-4}-10^{-6} Torr. Depending on the ion current and the sample material, the monoatomic layer of adsorbed atoms or molecules can be removed in a period of seconds or minutes. Argon ion bombardment used in the surface remain on after the bombardment. Annealing of the sample at elevated temperatures after the Ar ion sputtering is therefore mandatory. Even very clean surfaces can accumulate small amounts of molecules from residual gases in vacuum in a long period. However, they can be recleaned by the same method. Procedures that involve heating of the sample after sputtering have to be repeated because oxygen, carbon, or sulfur are often presents as impurities in the bulk and diffuse to the surface upon annealing. The methods to inspect surface cleanliness are carried out by LEED and AES.

In this work, we are dealing with ARPES to investigate the band structure of clean Pt(100) surface in both reconstructed (5x1) and unreconstructed (1x1) surfaces. The preparation of samples were carried out as follows:

1) A single crystal of Pt(100) was cut from a mother block.

2) The surface with a crystallographically well defined surface was polished out.

3) The surface was chemically cleaned.

4) The sutface was cleaned in vacuum.

A period of more than 5 months was necessary to obtained a clean well defined surface. The details of the procedure to obtain clean reconstructed (5x1) and unreconstructed (1x1) surfaces are described below.

2.2.1 The Preparation of Clean Reconstructed Pt (100)-(5x1) Surface

The sample used in the present experiments is 99.99 pure Pt single crystal (from Metal Crystal & Oxide LTD.). It was spark-cut from a single crystal bar and

oriented within $\pm 1°$ of the (100) plane. The crystallographic determination of the (100) plane was implemented by means of the X-ray Raue pattern analysis. The result was found to be consistent with those of LEED patterns measure for analyzing the surface structure. The sample is of nominal 10 mm diameter x 1 mm thick.

Before attaching a sample to the sample holder, the sample must be mechanically polished with alumina (Al_2O_3) dust in various grades of abrasive starting from 0.1 mm down to 0.3 μm. In practice, a cloth similar to emery paper was used. Such polishing was performed to adjust orientation the surface accurately. The Pt(100) surface obtained in this way was flat enough to appear to be a mirror plane.

After mechanical polishing, the sample was chemically etched with dilute (50% H_2O by volume) aqua regia for 15 seconds (Lyon and Somojai, 1967). After the chemical etching, the sample was cleaned by ultrasonic agitation with acetone and distilled water for many times. These treatment produced smooth surfaces relatively free from etch pits. Therefore, the sample with a very small number of crystalline defects as dislocation. Obviously this is brought about by annealing. Chemical etching removes most of the surface damage introduced by the mechanical treatments.

Prior to measurements, the sample was clean in vacuum. As mentioned before, the cleanliness was monitored by AES. Therefore, the Auger electron gun must be cleaned after the polished sample was brought into vacuum. In practice, the filament of the electron gun was heated and degassed. Then, the surface condition was monitored by AES measurents. After this, the sample was heated by electron bombardment. The temperature was monitored by a chromel-alumel thermocouple spot-welded to the sample. The surface was cleaned *in situ* by repeated cycles of argon-ion bombardment, heating in O_2 environment at about 1100K, annealing in

ultrahigh vacuum and flash heating to 1200K. Heating in oxygen removes carbon. By heating, carbon changes to the form of CO_2 or CO.   The subsequent Ar ion sputtering removes CO_2 and CO molecules from the surface.   After all surface treatment, the surface perfectness was examined by LEED observation.   The procedure described above generated a clean reconstructed (5x1) surface characterized by a sharp LEED (5x1) pattern and no impurities from AE spectra.

2.2.2 The Preparation of Clean Unreconstructed Pt (100)-(1x1) Surface

The clean Pt(100)-(1x1) surface was prepared using the method introduced by Bonzel and coworkers (Bonzel and Pirug, 1977; Broden, Pirug and Bozel, 1978). First, the clean (5x1) surface was exposed to NO at 300K until the adsorption reached a saturation level.   The sample was then heated to 470K for 60 seconds.   This decomposed NO into adsorbed oxygen and N_2 gas.   Remaining adsorbed oxygen was removed by exposing the sample to H_2 gas.   Hydrogen sticking to the surface was removed by heating the sample slowly to 390K. This process resulted in a clean (1x1) surface characterized by a sharp LEED pattern.   The clean unresconstructed (1x1) surface was metastable and changed to the (5x1) surface if the sample was heated as high as 400K.

2.3 Experimental Procedure

The experiments have been carried out in the following procedure:

2.3.1 Sample Treatment

The clean Pt(100) surface was prepared as described in sections 2.2.1 and 2.2.2. This step was performed in the Kakizai Laboratory in PF of KEK.

2.3.2 Photoemission Measurements

The photoemission measurement was performed by using synchrotron radiation at BL-11C at PF-KEK. The procedure of photoemission measurement is as follows:

1) A Pt(100) sample was mounted on the sample holder then introduced to the photoemission UHV chamber which equipped with a photoelectron energy analyzer, a LEED equipment, an Auger electron (AE) energy analyzer and a quadrupole mass analyzer.

2) The whole chamber was baked at 150° C-200° C for 24 hr. After baking the chamber, some accessory components, the quadrupole mass analyzer, electron guns, Ar-ion gun, pressure gauges, LEED system were degassed.

3) The sample surface was clean as steps described above and the clean Pt (100) surface obtained.

4) After cleaning the surface, the angle-resolved photoemission spectra were measured on both (1x1) and (5x1) surfaces. The pressure during photoemission measurements was 2.0 x 10^{-10} torr. The total energy resolution was 150 meV. In normal emission measurement, the excitation light of an energy range 15-30 eV was used to perform the bulk band structure determination along $\Gamma - \Delta - X$ direction in the bulk Brillouin zone. In off-normal emission measurement, the surface band structure was mapped along $\overline{\Gamma} - \overline{\Delta} - \overline{X}$ and $\overline{\Gamma} - \overline{\Sigma} - \overline{M}$ directions of the surface Brillouin zone with photon energy 21 and 25 eV. The relation of the bulk and surface Brillouin zone is shown in Fig. 2.14.
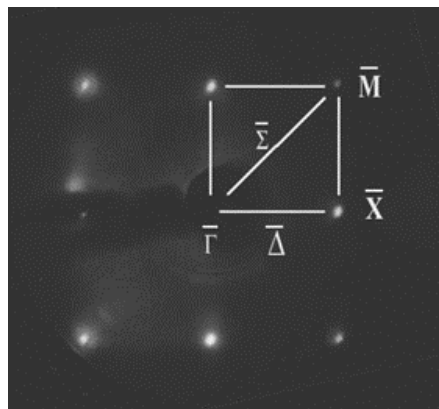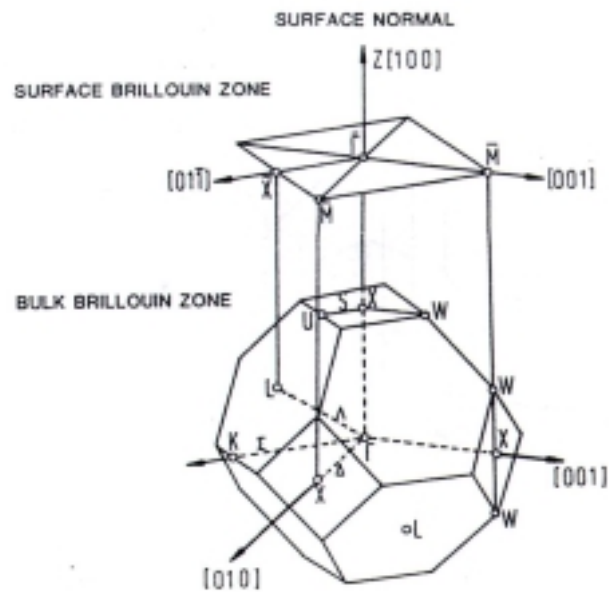
Fig. 2.14 Bulk Brillouin zone of the fcc structure and associated surface Brillouin zone. LEED pattern of the clean unreconstructed Pt(100)-(1x1) surface is presented for comparison.

Chapter III

Experimental Results

3.1 Normal Emission Data

3.1.1 Overall Aspects

Figure 3.1 shows the representative normal emission EDC of the clean reconstructed Pt(100)-(5x1) surface.   This surface was excited by p-polarized light with an energy of 17 eV. The features in the spectrum are indicated by alphabetic notations A though D.   A sharp peak, A, exists just below the Fermi edge.   The location is 0.21 eV of binding energy.   The second peak, B, is located at 0.87 eV below peak A.   The third peak, C, is found around 1.80 eV.   This peak has the shape wider than the widths of peak A and B.   Although it is not easy to identify the fourth peak, D, it does exist around 4.08 eV. The feature is better recognized in a spectrum of the better S/N ratio.   Such a feature is found by scanning over a narrow spectral range.

If the excitation energy is changed, the features found in the spectrum will shift their locations.   However, if we increase the excitation energy to some large extent, the spectral aspect changes qualitatively.   As an example, Fig. 3.2 shows the normal emission EDC measured on the clean reconstructed Pt(100)-(5x1) sample

surface with light at an energy of 27 eV and with the same polarization vector as that of light used in the measurement of spectrum shown in Fig. 3.1. A hump feature is found just below the Fermi edge. It is an artifact caused by the part of the feature A cut by the Fermi edge. Thus, the first peak A is located at 0.69 eV. If we compare the peak A in Fig. 3 .2 with peak A in Fig. 3.1, we find the peak A in Fig. 3.2 is much wider than peak A in Fig. 3.1. The second peak in Fig. 3.2 occurs at 2.36 eV and designates as B. The third peak C is found at 4.08 eV. A very weak feature, D, is found around 6.81 eV.

If we compare the spectrum shown in Figs. 3.1 and 3.2, we find the distinct difference. The spectrum shown in Fig. 3.1 has a sharp clearly separated two peaks near the Fermi edge. On the other hand, we cannot find such clearly resolved peak just below the Fermi edge in Fig. 3.2. If we change the excitation energy, we see the photoemission spectrum changes its shape. In order to show such changes more clearly, the spectra obtained by excitations at various different energies are shown in Fig. 3.3.

Figure 3.3 presents the normal emission spectra measured on the clean reconstructed Pt(5x1) surface. Each spectrum is normalized so that the background intensity is the same. The measurements were carried out with p-polarized excitation light. The photon energies, hv, range from 15 to 30 eV. The excitation photon energies were varied in a 1 eV step. All curves are plotted with respect to the binding energy, ε_B, and the excitation energies are indicated on the right hand side of each curve. The Fermi energy, ε_F, corresponds to $\varepsilon_B = 0$ eV. The features of the curves when excited with different photon energies are marked as $D1$, $D11$, $D2$, $D22$, $D3$,

D4, D5, D6, SE1 and *SE2* band. Apparently, all these bands are located below ε_F.

The *D1* band origins at ε_B = 0.09 eV as $h\nu$ = 15 eV. It shows the clear dispersion of

the features downward to a higher binding energy until ε_B = 0.78 eV at $h\nu$ = 25 eV.

When $h\nu \geq 26$ eV, this band disperses upward to the lower binding energy below ε_F

and stops at ε_B = 0.12 eV at $h\nu$ = 30 eV. At $h\nu$ = 27 eV, *D1* band splits into two

bands. The branch band occuring nearer to the Fermi edge is called *D1* and the other

one is called, *D11*. Both bands show the dispersion. The dispersion of the *D11* band

menifests itself as the occurrence of three features at ε_B = 1.16, 1.17 and 1.14 eV as

$h\nu$ = 28, 29 and 30 eV, respectively. The *D2* band appears at ε_B = 0.93 eV for

excitations at $h\nu$ = 15 eV. This band has the well-defined peak in EDC's obtained

with excitation energies from $h\nu$ = 15 to 19 eV. Above 20 eV, it is the peak, which is

clear and merges into *D1* band at $h\nu$ = 23 eV. At $h\nu$ = 19 and 20 eV, the *D22* band

occurs.   It splits off from the *D2* band.   The *D3* band is composed of the hump

features. They are found in EDC's for excitations at $h\nu$ = 20 to 30 eV. The location

is at ε_B = 2.25-2.4 eV. The band showing prominent dispersion in Fig. 3.3 is the *D4*

band. It exists at ε_B = 1.2 eV in EDC measured at $h\nu$ = 15 eV. The location shifts

to high binding energy with increasing photon energy. However, for excitations at $h\nu$

= 25 to 30 eV, the band does not shift much, though slight dispersion toward low

binding energy in the range of 3.93-4.05 eV is recognized.   The *D5* band does not

show dispersion. It is located at a binding energy around 4.26 eV, while excitations

are made at photon energies in the range 16-21 eV. The *D6* band is located at higher

binding energy.   It is found in EDCs obtained by excitations at $h\nu$ = 26 to 30 eV. It

exhibits a smooth shift toward low binding energy in five EDCs while the excitation photon energy is increased. Another apparent bands in Fig. 3.3 are *SE1* and *SE2*. These two bands show constant kinetic energy aspect. They are also apparent in the results for Pt(111) and Au(111) obtained by Mills, Davis, Kevan, Thornton and Shirley (1980). The features may be due to secondary electrons. The *SE1* band occurs at ε_B = 6.36, 7.05 and 8.4 eV in EDCs for excitations at $h\nu$ = 18, 19 and 20 eV, respectively. The *SE2* band is localed at nearly the same binding energy but only in EDCs obtained in the excitation range of $h\nu$ = 22-24 eV. In EDC measured at an excitation energy of 20 eV, seven features are found while a less number of features are found in EDCs obtained by excitations at other energies. In Figs. 3.3 and 3.4, some features are less prominent and not clearly recognized. However, the features are distinct in EDCs shown in an expanded ordinate scale.

Features in EDCs of Pt(1x1) show the dispersion aspect similar to that of EDCs of Pt(5x1), as is seen in Fig. 3.4. Features having correspondence in EDCs of Pt(1x1) and Pt(5x1) are indicated with the same band names.

For the clean unreconstructed Pt(100)-(1x1) surface, the normal emission EDCs are shown in Fig. 3.4. Each spectrum is also normalized so as to give the same background intensity. The conditions of measurements were the same as those for the reconstructed Pt(5x1) surface. The fact that the dispersion aspect is not much different is ascribed to the situation that the EDCs for the normal emission reflect the bulk-band structure. The fact that the spectra of Pt(1x1) and Pt(5x1) are not completely the same appears to suggest that the surface reconstruction affect the bulk bands slightly. The *D1* band of unreconstructed surface is found at ε_B = 2.26 eV only in two EDCs measured at photon energies of 20 and 21eV. The secondary

electron emission bands, *SE1* and *SE2,* are also found in EDCs for Pt(1x1) surface. The *D6* band found in reconstructed Pt(5x1) surface is not seen in EDCs of the unreconstructed Pt(1x1) surface.

3.1.2 Band Structure from Normal Emission

To determine the dispersion relation of the energy versus momentum **k** of the initial state from the measurements of the peak positions in the raw data, we employed the direct transition model for excitation of electrons in photoemission. Thus, we ignore the umkapp process. In case of normal emission on Pt(100) surface, a detector from, practically the exis of the electron lens attached to the energy analyzer, is placed as to accept only electrons emitted normal to the (100) surface of Pt. From Fig. 2.14, it is recognized that we are dealing with **k** in the $\Gamma - \Delta - X$ symmetry line. The perpendicular component of momentum, $k_\perp$, can be determined if the dispersion of the final state band is known. As we have mentioned regarding Fig. 1.34 in section 1.6.6, we assume the parabolic final state band. Then the perpendicular momentun, $k_\perp$, is given as (1.108) or (1.109). In the direct transition model, the final state momentum perpendicular to the surface is given by

$$k_\perp = \frac{1}{\hbar} \left[2m \left(\varepsilon_k + V_o \right) \right]^{1/2}. \tag{1.108}$$

or

$$k_\perp = 0.51 \ \overset{\circ}{A}^{-1} \sqrt{\left(\varepsilon_k + V_o \right) (eV)}. \tag{1.109}$$

where V_0 is an appropriate parameter referred to as the crystal potential and ε_k is the kinetic energy of photoelectron in vacuum. This is explained concerning equations
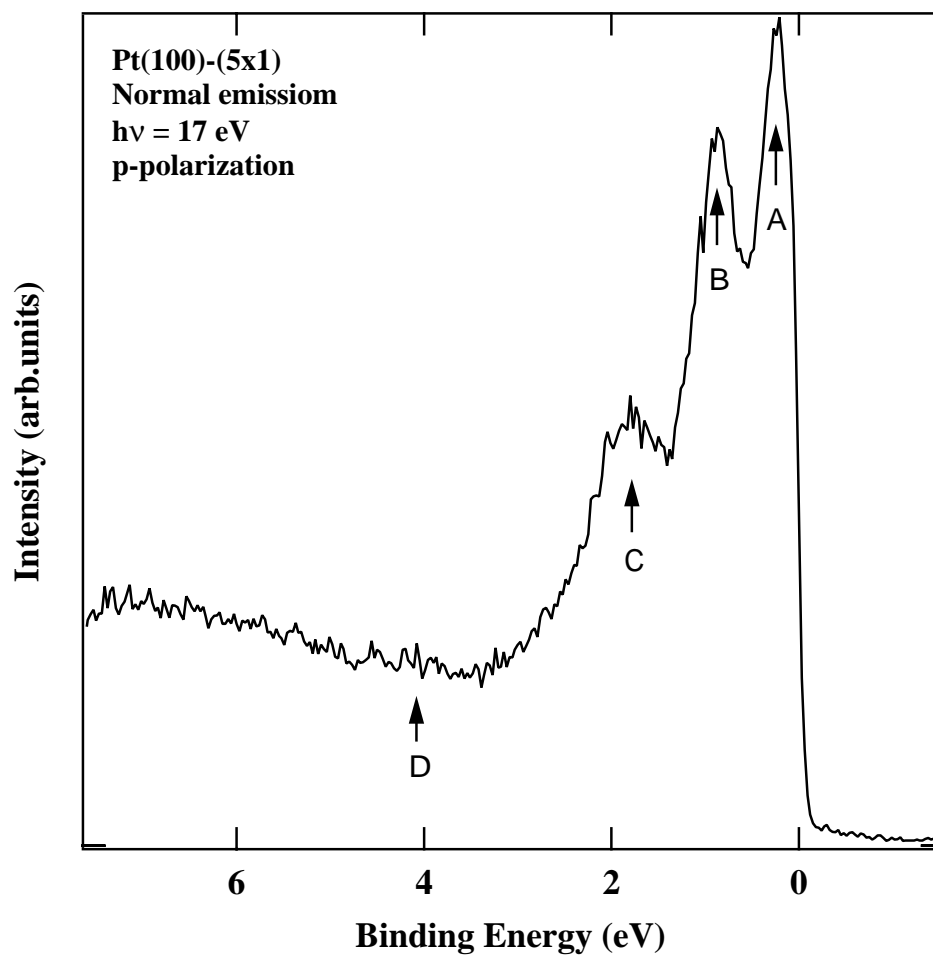
Fig. 3.1 Representative normal emission EDC measured on the clean reconstructed Pt (100)-(5x1) surface with light at a photon energy of 17 eV and *p*-polarized.
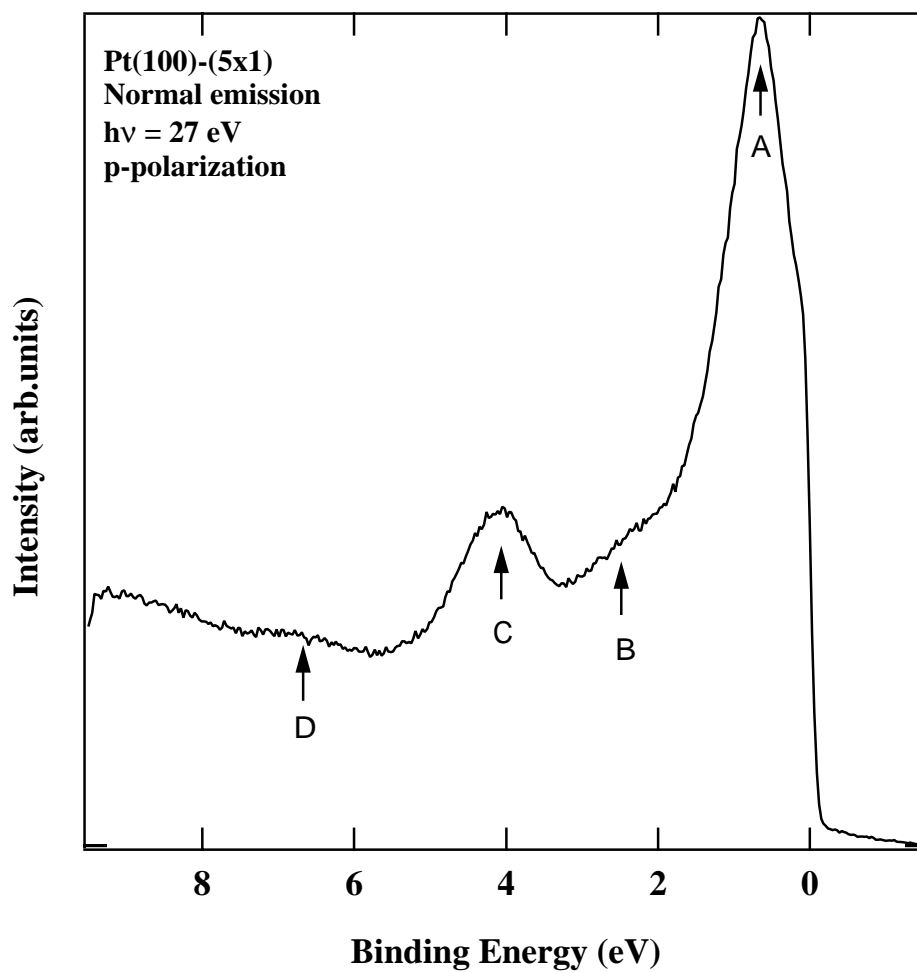
Fig. 3.2 Representative normal emission EDC measured on the clean reconstructed Pt

(100)-(5x1) surface with *p*-polarized light at a photon energy of 27 eV.
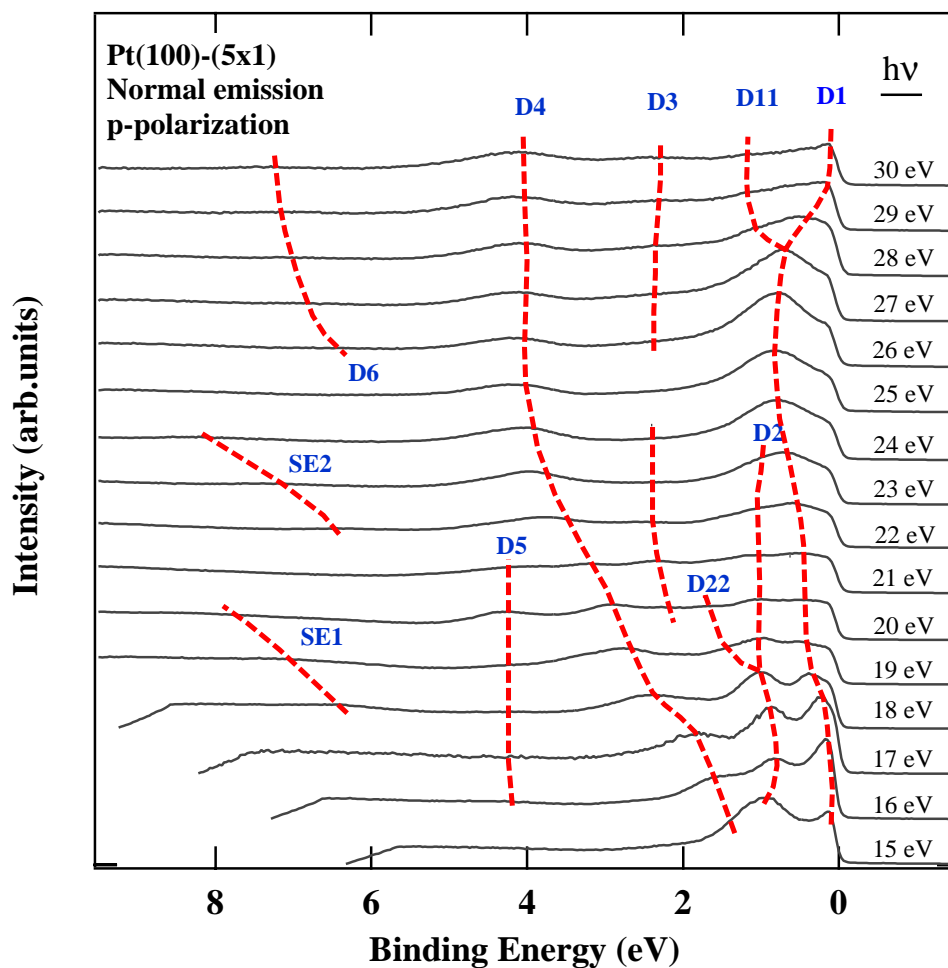
Fig. 3.3   Normal emission EDC's measured on the Pt(5x1) surface with *p*-polarized

light in a photon energy range, $15 \leq h\nu \leq 30$ eV.   The curves have been

normalized so as to give the same background intensity.
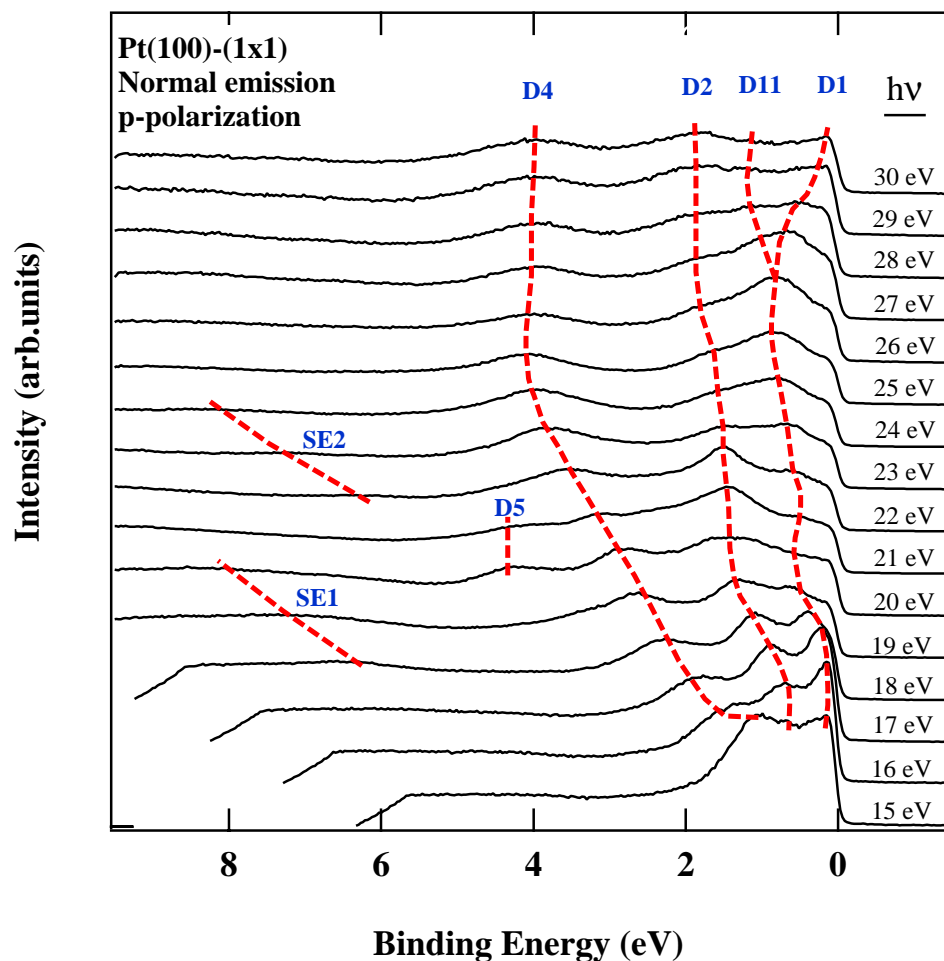
Fig. 3.4 Normal emission EDC's measured on the Pt(1x1) surface with *p*-polarized

light in a range of photon energy, 15≤ *hν* ≤ 30 eV. The curves have been

normalized so as to give the same background intensity.

(1.105) and (1.106). For this specific case of Pt, the Vo = 10 eV gives an appropriate value for finding good fitting of the free-electron parabola with the final experimental bands.

The energy band structure from normal emission of the clean reconstructed Pt (5x1) surface is presented in Fig. 3.5. This dispersion relation results from the excitation with p-polarized light. Corresponding EDCs are presented in Fig. 3.3. Because the Γ-X direction in the bulk of Pt is 1.6 $\overset{o}{A}^{-1}$ so the relation ε_B versus $k_\perp$ in Fig. 3.5 shows the emission arising from final state in the second Brillouin zone. If we remind of the model transition shown in Fig. 1.34, the transition mentioned above is the direct transition in the second Brillouin zone in this approximation. We change such band structure to be lied in the first Brillouin zone by folding–back the Fig.3.5 in the reduced-zone schemed. The result is shown in Fig. 3.6.

Unfortunately, because of the limited photon energy range available in this experiment, the structures can be identified only 60% portions of Γ-X direction. In Fig. 3.7, the $D1$ band occupies nearest Fermi edge in the range of $k_\perp$ around 0.015-0.9 $\overset{o}{A}^{-1}$. The $D3$ band does not show dispersion in the binding energy range measured here. The $D4$ band has the distinct dispersion from 4.2 to 2.6 eV of binding energy corresponding to $k_\perp$ = 0.15-0.92 $\overset{o}{A}^{-1}$. The feature $D5$ occupies the range 0.80-1.08 $\overset{o}{A}^{-1}$ of $k_\perp$ with binding energy 4.26 eV. It does not show dispersion. The $SE1$ and $SE2$ structures show the constant $k_\perp$ at 0.85 and 1.08 $\overset{o}{A}^{-1}$ with changing binding energy. As it found in Fig. 3.3, the peak shift occurs in the manner as $\Delta h\nu = \Delta\varepsilon_B$. In practice, the kinetic energies observed are constant as mentioned already. We ascribe the

peaks are caused by the secondary electron emission. If excited photoelectrons keep losing their energies by elastic scattering until they are thermalized at the minima in the conduction bands, the resultant emission occurs from the minima and the kinetic energies of emitted electrons are constant.

The band structure depicted from normal emission data for the clean unreconstructed Pt(1x1) surface using from equation (1.109) is shown in Fig. 3.7. This ε_B versus $k_\perp$ mapping is illustrated in the reduced–zone scheme. The procedure foe this is the same as that for Fig. 3.6. The original EDCs are those shown in Fig. 3.4. Excitation light is p-polarized and photon energy is in a range of 15-30 eV as shown already.

If we compare the band structure between (5x1) and (1x1) surface, we see that they are not different quantitatively. However the *D1* band of (1x1) surface shows eruptly change in the binding energy at 0.65 $\overset{o}{A}^{-1}$, while as the (5x1) does not. Also the *D2* band of (1x1) surface exhibits the smooth dispersion.

3.1.3 Polarization Dependence

For this experiment, we use synchrotron radiation, which is linearly polarized light. We can identify the initial state symmetry by employing polarized radiation and the dipole selection rule. In the dipole selection rule, the normal emission in the (100) direction, the final state with *even* (Δ_1) symmetry will be excited. The possible initial state with even and *odd* (Δ_5) symmetry can be excited by a component of vector potential, **A**, of polarized light. If **A** is parallel to the crystal surface, the initial state with only *odd* symmetry will be excited. This can be achieved by an incident angle of
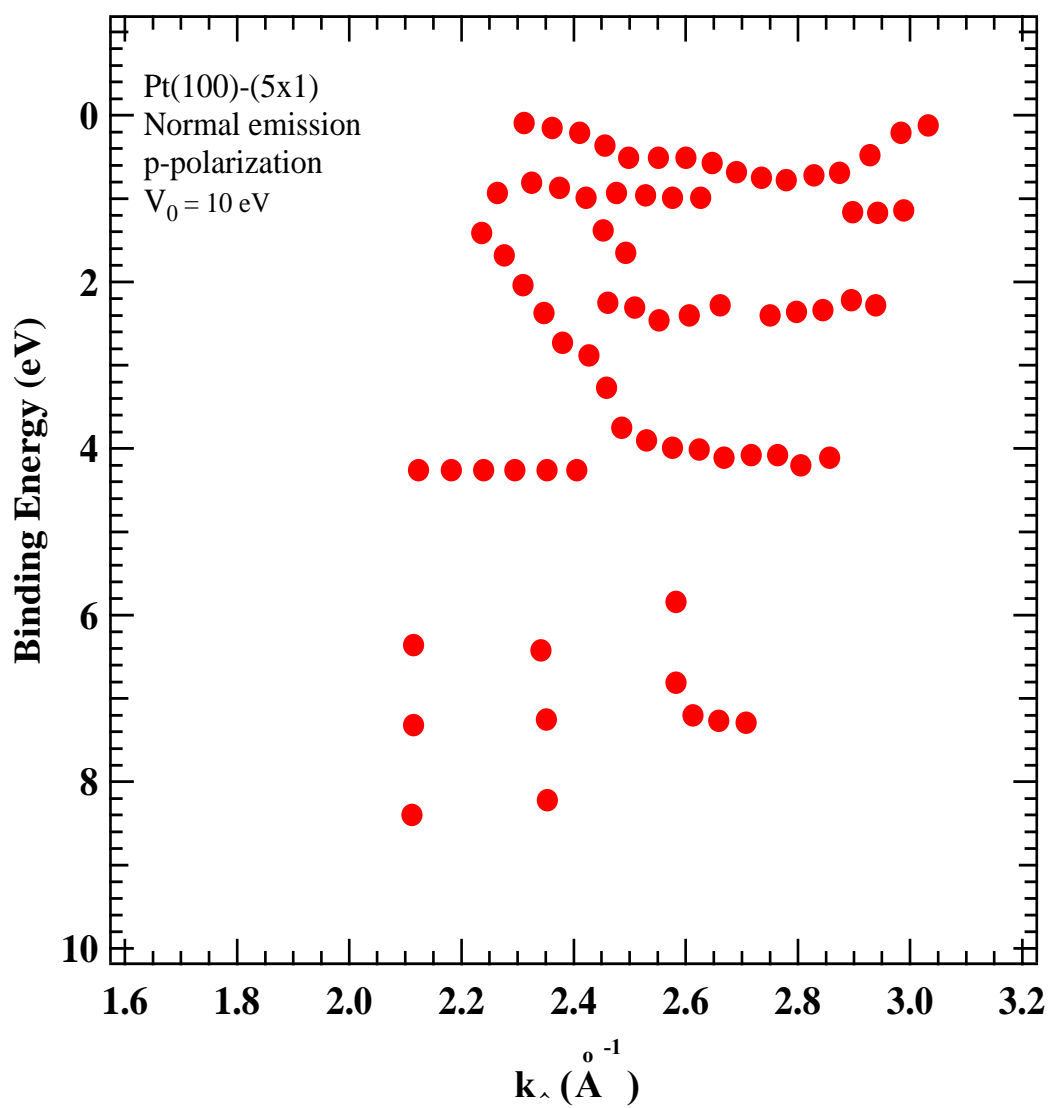
Fig. 3.5 Experimental energy band dispersion determined by normal emission on the clean reconstructed Pt(5x1) surface with *p*-polarized light in the photon energy range $15 \leq h\nu \leq 30$ eV.
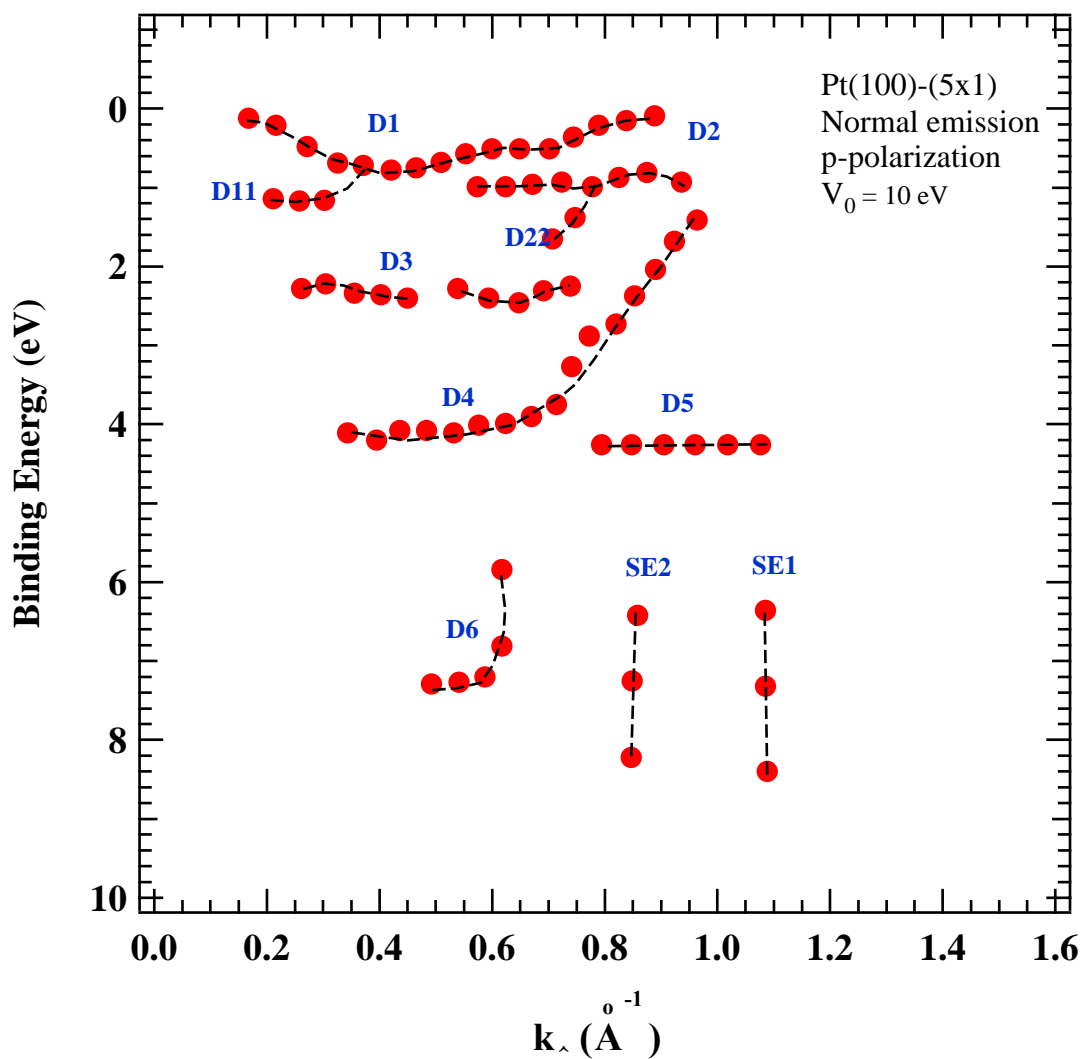
Fig. 3.6 Experimental energy band dispersion of clean reconstructed Pt(5x1) surface

presented in the reduced zone scheme by normal emission with *p*-polarized

light in the photon energy range $15 \leq h\nu \leq 30$ eV.
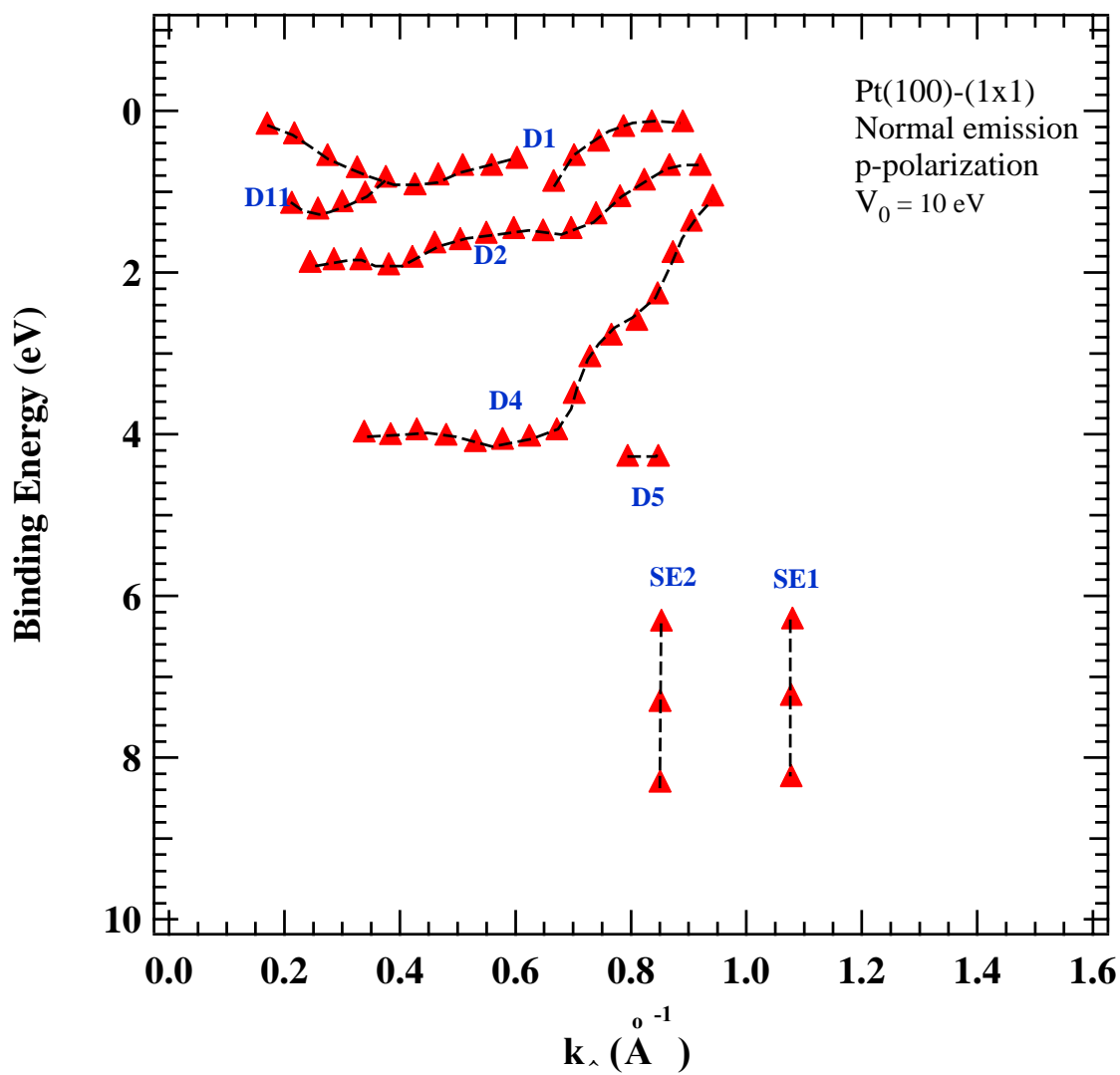
Fig. 3.7 Experimental energy band dispersion of clean unreconstructed Pt(1x1) surface presented in the reduced zone scheme by normal emission with *p*-polarized light in the photon energy range $15 \leq h\nu \leq 30$ eV.

light of 35° respect to the surface normal. The polarized light in this case is called *s*-polarized light. Otherwise, if **A** is perpendicular to the surface by an incident angle of 60^0, the initial state with *even* or *odd* symmetry will be excited. This means that the initial state is excited with *p*-polarized light.

Figure 3.8 shows the typical example the effect of polarized light on the Pt (5x1) surface. All spectra are normalized to the same background intensity.   This experiment were performed with photon energies of 15, 16, 17 and 18 eV in the normal emission mode.   Because we use the imperfect *s*- and *p*-polarization of synchrotron radiation, the states excited by the polarization seemingly are mixed symmetry. As shown in Fig. 3.8, the features arising from the initial state along of Δ direction should be the mixed *even* and *odd* symmetry. The features labeled by *A* (thin line) and *B* (dashed line) show the strong transitions of the initial state with *p*- and *s*-polarized light. However, the transition of initial state *B* by *s*-polarized light occurs at the same binding energy as *B* that by *p*-polarized light but its spectrum has a lower intensity. So the structure *B* which is the primary initial states excited in this experiment could be the Δ_5 symmetry.   In the same way, the feature *A* could be ascribed to the Δ_1 symmetry.

The total results of the measurement on the clean reconstructed Pt(5x1) and clean unreconstructed Pt(1x1) surface with *s*-polarized light are shown in Figs. 3.9 and 3.10, respectively. The band structures estimated by the normal emission from the Pt(5x1) surface by excitations with *s*-polarized light is presented in Fig. 3.11. Corresponding EDC's are those shown in Fig. 3.9. For Pt(1x1) surface, the band mapping made by using EDCs of the normal emission by excitations with *s*-polarized
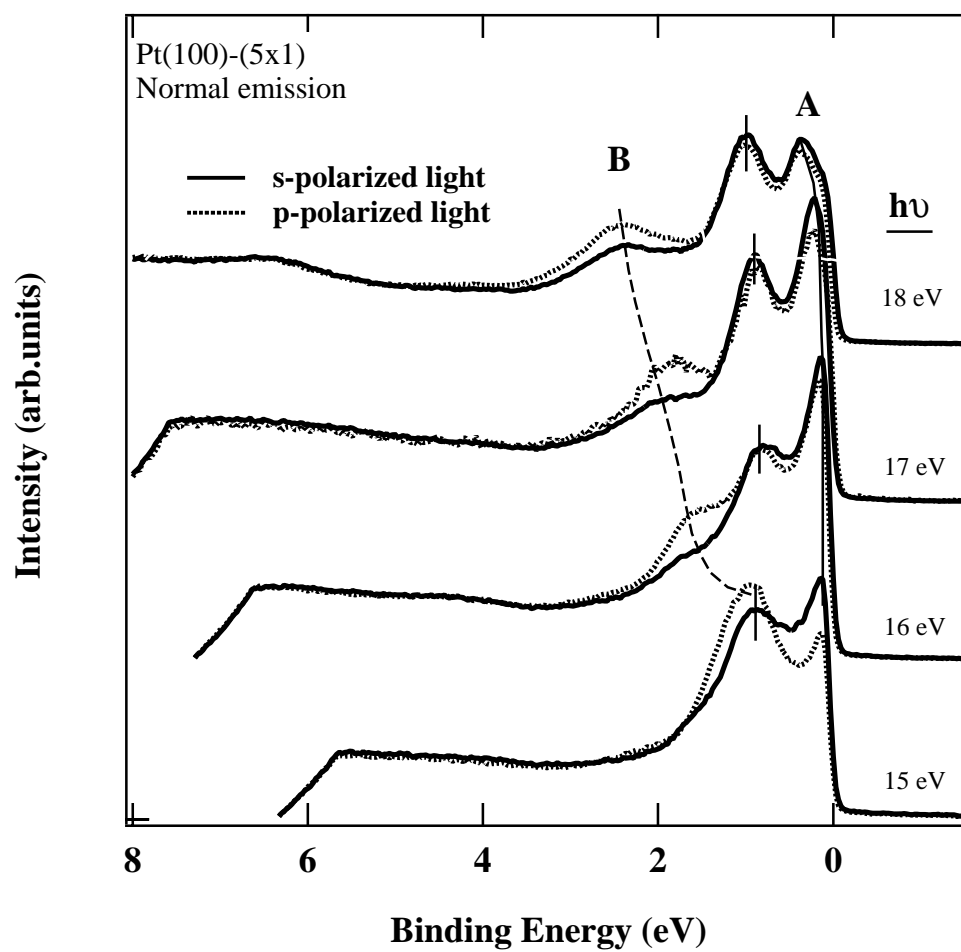
Fig. 3.8 Representative normal emission EDC's of the clean Pt(5x1) surface excited

with *s* and *p*-polarized light.   The curves have been normalized to the same

background intensity.

is shown in Fig. 3.12. In the estimation of $\mathbf{k}_\perp$ in Figs. 3.11 and 3.12, $V_o = 10$ eV is used as the crystal potential.

If we compare all experimental results obtained by the normal emission made by excitations with s-and p-polarized light, we see that the resulting band structure is not depend on the polarization of excitation light. However, the polarization of excitation light affects the intensities of the spectral features.

The discussion of the results obtained by the normal emission mode will be done in Chapter IV.

3.2 Surface Energy Band

If we observe angle-resolved photoemission from the surface layer, we obtain typical two dimensional energy band emission. Thus, the angle-resolved data can be obtained just by changing the polar angle, θ, of electron emission as described already. The $\mathbf{k}$ vector can be estimated from equation (1.99). As in the case of the bulk photoemission, we have prepared two kinds of the surfaces, unreconstructed (1x1) and reconstructed (5x1) ones. We have measured EDC's along the $\bar{\Gamma} - \bar{\Sigma} - \bar{M}$ and the $\bar{\Gamma} - \bar{\Delta} - \bar{X}$ lines in the surface Brillouin zone. The shape of the surface Brillouin zone is shown in Fig. 2.14. The energies of excitation light of 21 eV and 25 eV were employed. Typical EDC's are shown in Figs. 3.13-3.17.

In Figs. 3.13 and 3.14, the spectra measured on the (1x1) and (5x1) surfaces are shown, respectively. In each figure, the spectra were measured along the $\bar{\Gamma} - \bar{\Sigma} - \bar{M}$ direction in an emission angle of −10 degrees. Excitation light is incident at an angle of 45 degrees. The comparison of spectra measured by excitations with light at the
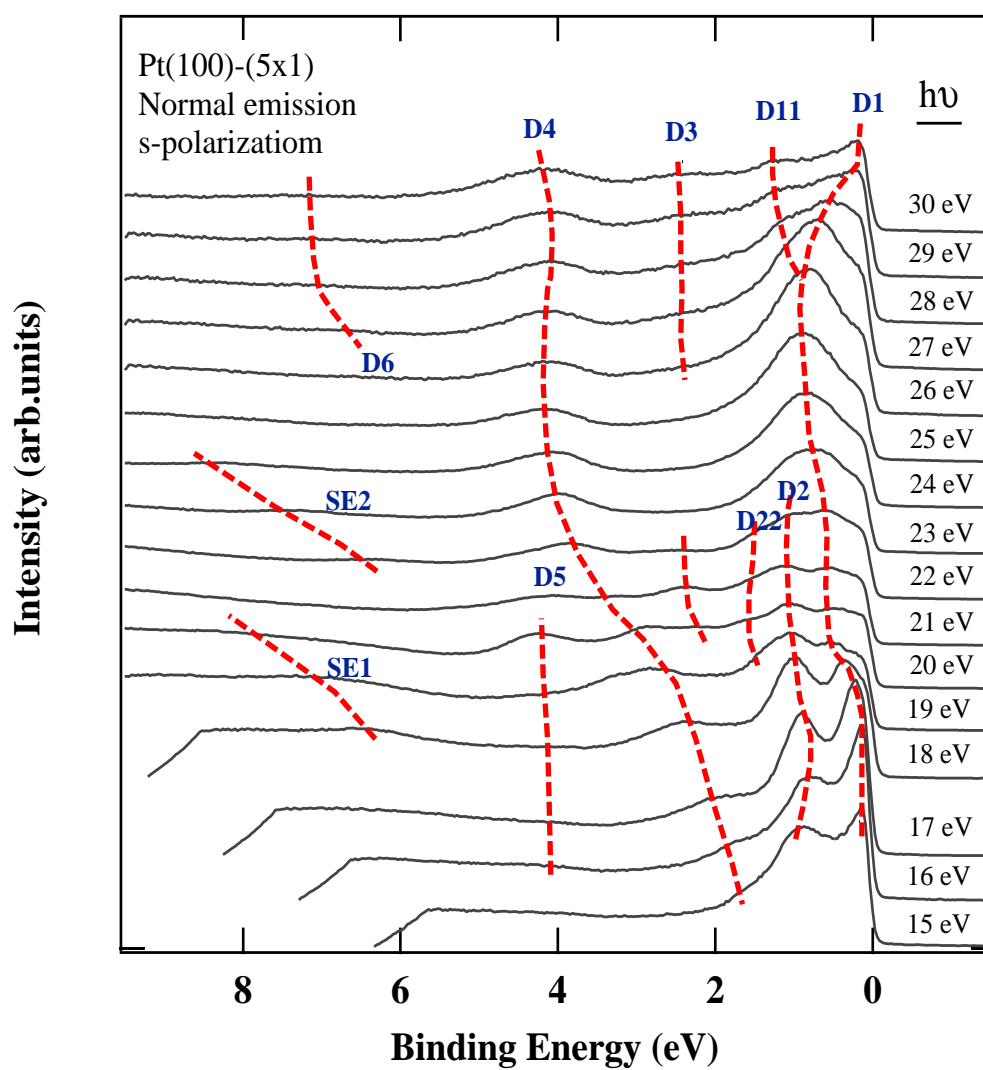
Fig. 3.9 Normal emission EDC's from the Pt(5x1) surface excited by *s*-polarized light in the photon energy range 15≤ *hv* ≤ 30 eV. Each curve has been normalized to the same background intensity.

.
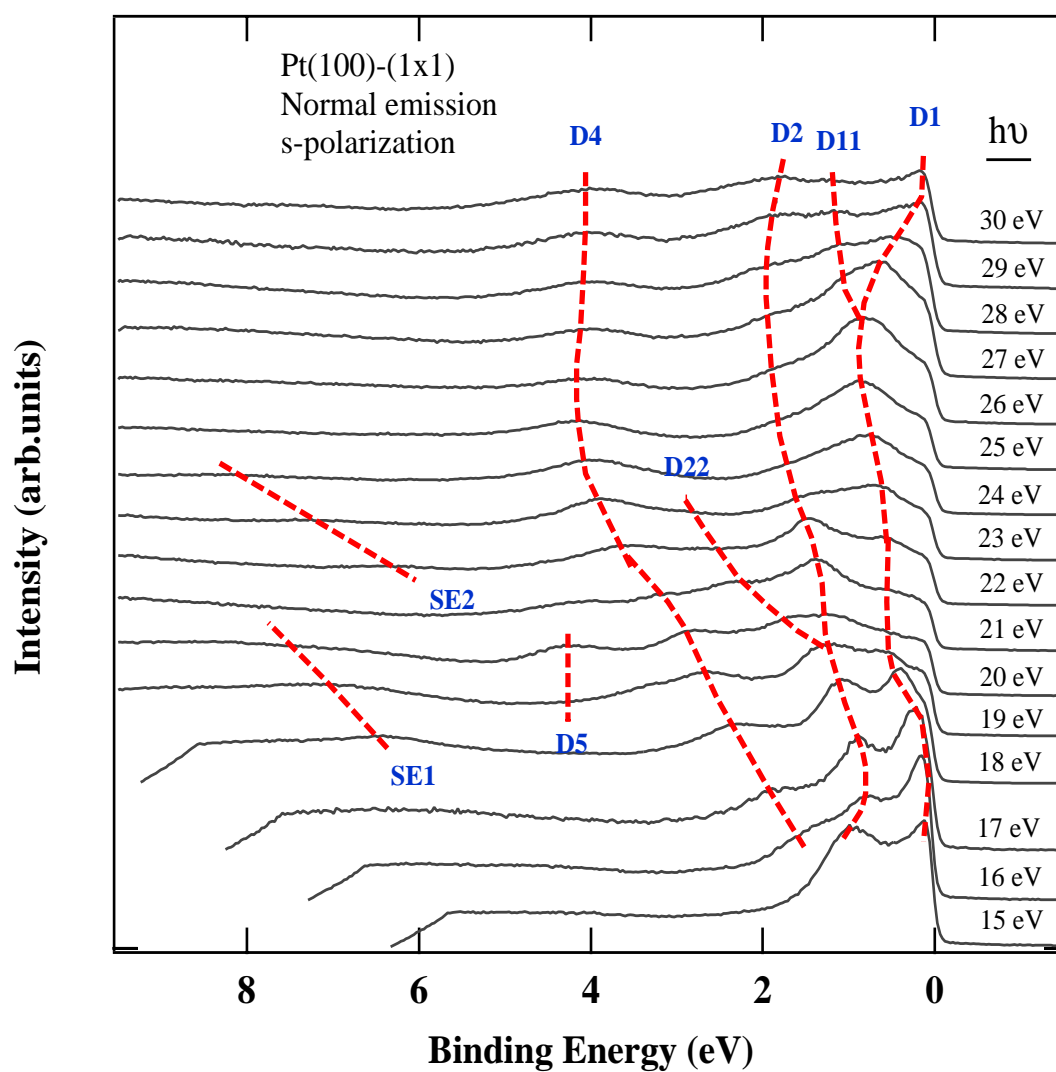
Fig. 3.10 Normal emission EDC's from the Pt(1x1) surface excited by *s*-polarized light in the photon energy range 15≤ *hv* ≤ 30 eV. Each curve has been normalized to the same background intensity.
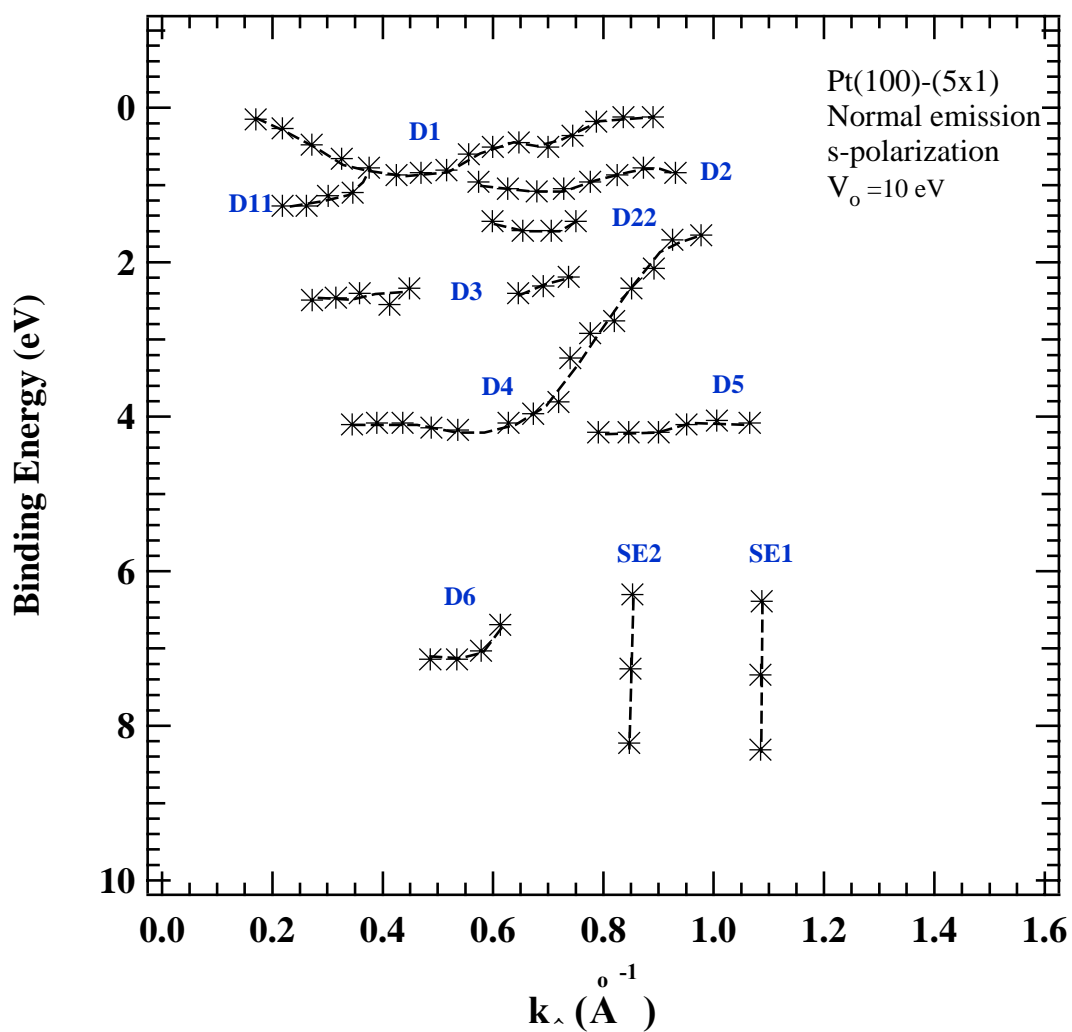
Fig. 3.11   Experimental energy band dispersion presented in the reduced zone scheme as measured by the normal emission from the Pt(5x1) surface by excitations with *s*-polarized light.
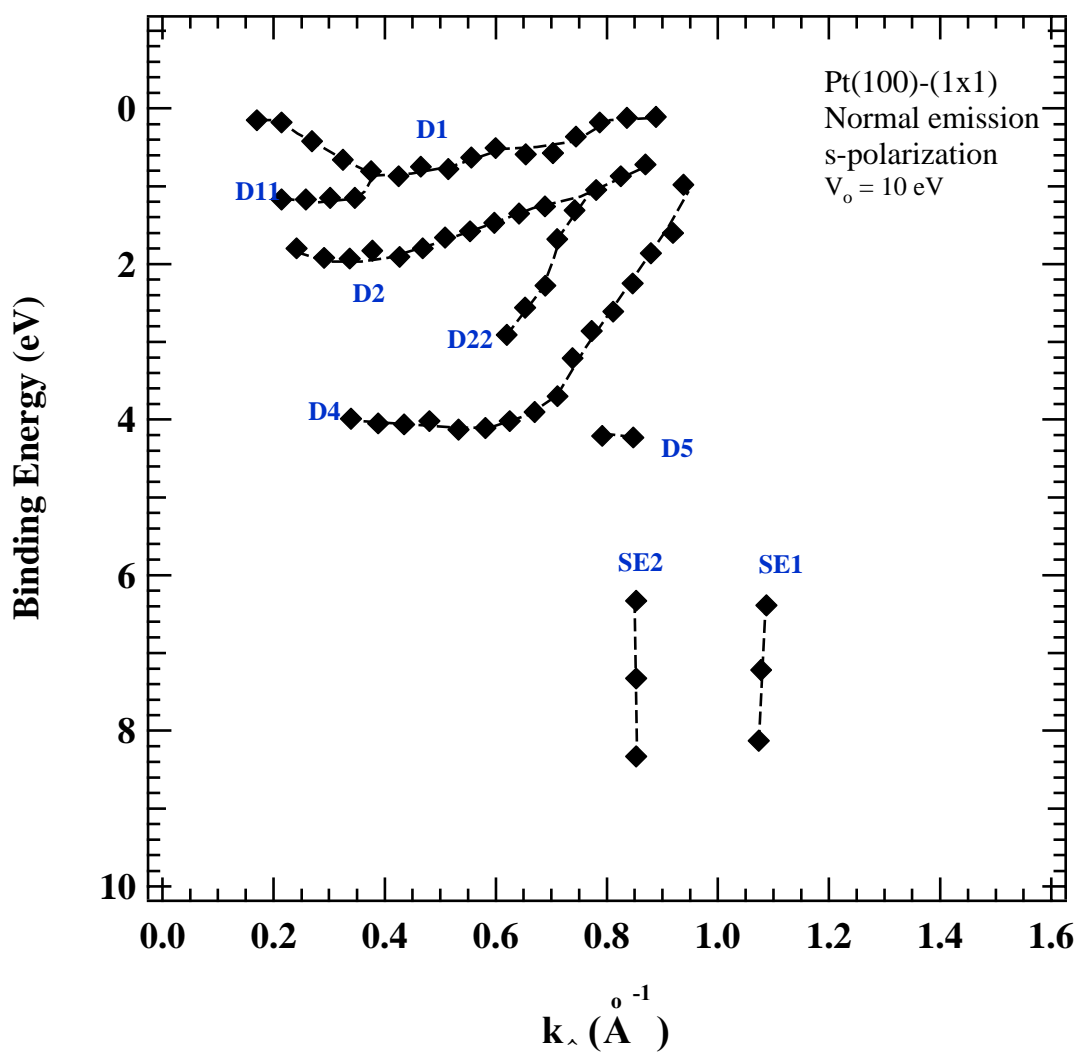
Fig. 3.12 Experimental energy band dispersion presented in the reduced zone scheme as measured by the normal emission from Pt(1x1) surface by excitations with *s*-polarized light.

different energies is made. As is found in Fig. 3.13, the spectrum measured by the excitation at 21 eV is roughly similar to that measured by the excitation at 25 eV. However a closer inspection indicates some differences. The peak occurring around 1.23 eV below the Fermi edge in the spectrum of the 25 eV excitation has a composite structure but the corresponding peak in the spectrum of the 21 eV excitation is clearly single–peaked.

Figure 3.14 shows two spectra obtained by the excitations at 21 eV and 25 eV on the (5x1) surface. In the spectrum obtained by the excitation at 25 eV, a feature showing a composite structure is found about 0.73 eV below the Fermi edge. On the other hand, two well-separated peaks are found in the corresponding spectral region in EDC of the 21 eV excitation.

In this way, the spectra shown in Figs. 3.13 and 3.14 indicate that the change in the excitation energy gives rise to the quantitative change in the spectral profile.

In Figs. 3.15 and 3.16, the spectra measured on the (1x1) and (5x1) surfaces with excitation light with the same energy are compared. As in the case of Figs. 3.13 and 3.14, the spectra were obtained along the $\overline{\Gamma} - \overline{\Sigma} - \overline{M}$ direction with an emission angle -10° and a light incidence angle of 45°. Figure 3.15 shows the spectra obtained by the excitation at 25 eV. The spectrum of the (1x1) surface and that of (5x1) appear to be similar at first glance. However, a closer inspection of both spectra suggests a quantitative difference in the profile. In the spectrum of the (5x1) surface, a tailing is found in the binding energy region around 2 eV. This suggests the existence of an unresolved feature in this region.

Figure 3.16 shows the comparison of the spectra measured with excitation light at 21 eV. Difference in the spectral profile is conspicuous. In the spectrum of the (5x1)

surface, two peaks are clearly resolved in the region below 2 eV whereas only one peak is found in the spectrum of the (1x1) surface. In this way, we recognize that the spectral profile is different, if the surface observed is different.

In Fig. 3.17, EDC of the (5x1) surface measured along the $\overline{\Gamma} - \overline{\Delta} - \overline{X}$ direction is shown. The excitation energy is 21 eV and the observation angle is -10°. If we compare this spectrum with that of the $\overline{\Gamma} - \overline{\Sigma} - \overline{M}$ direction, we find quantitative difference in the EDC measured along the $\overline{\Gamma} - \overline{\Delta} - \overline{X}$ direction from that measured along the $\overline{\Gamma} - \overline{\Sigma} - \overline{M}$ direction. Similar difference is found in the spectra illustrated in Figs. 3.13 to 3.16.

Summarizing the observation shown in Figs. 3.13 to 3.17, we can clearly conclude that the spectral profile is different depending on the excitation energy, the surface structure and the direction of the observation.

We ascribe this to the energy band structure. In order to see this point more clearly, spectra observed with different emission angles are collected in Figs.3.18, 3.19, 3.22, 3.23 for the $\overline{\Gamma} - \overline{\Sigma} - \overline{M}$ direction and Figs. 3.26, 3.27, 3.30, 3.31 for $\overline{\Gamma} - \overline{\Delta} - \overline{X}$ direction in sections 3.2.1 and 3.2.2, respectively.
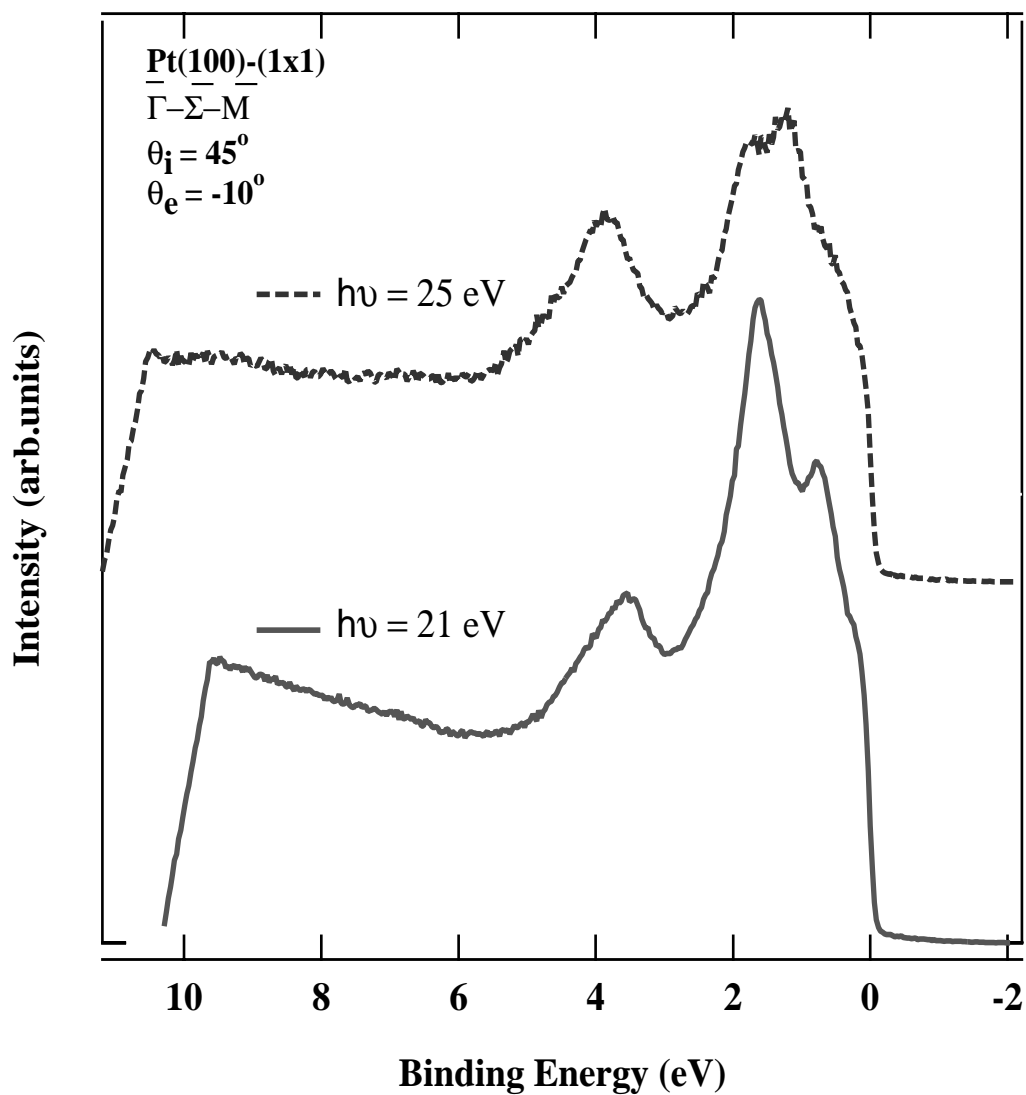
Fig. 3.13 EDC's of the Pt(1x1) surface along the $\overline{\Gamma}-\overline{\Sigma}-\overline{M}$ direction as measured with excitation energies of 21 and 25 eV. The emission angle was -10°. Excitation light was incident at an angle of 45°.

Fig. 3.14 EDC's of the Pt(5x1) surface along the $\overline{\Gamma} - \overline{\Sigma} - \overline{M}$ direction as measured with excitation energies of 21 and 25 eV. The emission angle was -10°. Excitation light was incident at an angle of 45°.

Fig. 3.15 EDC's of the Pt(1x1) and the Pt(5x1) surfaces along the $\overline{\Gamma}-\overline{\Sigma}-\overline{M}$ direction as measured with an excitation energy of 25 eV. The emission angle was -10°. Excitation light was incident at an angle of 45°.
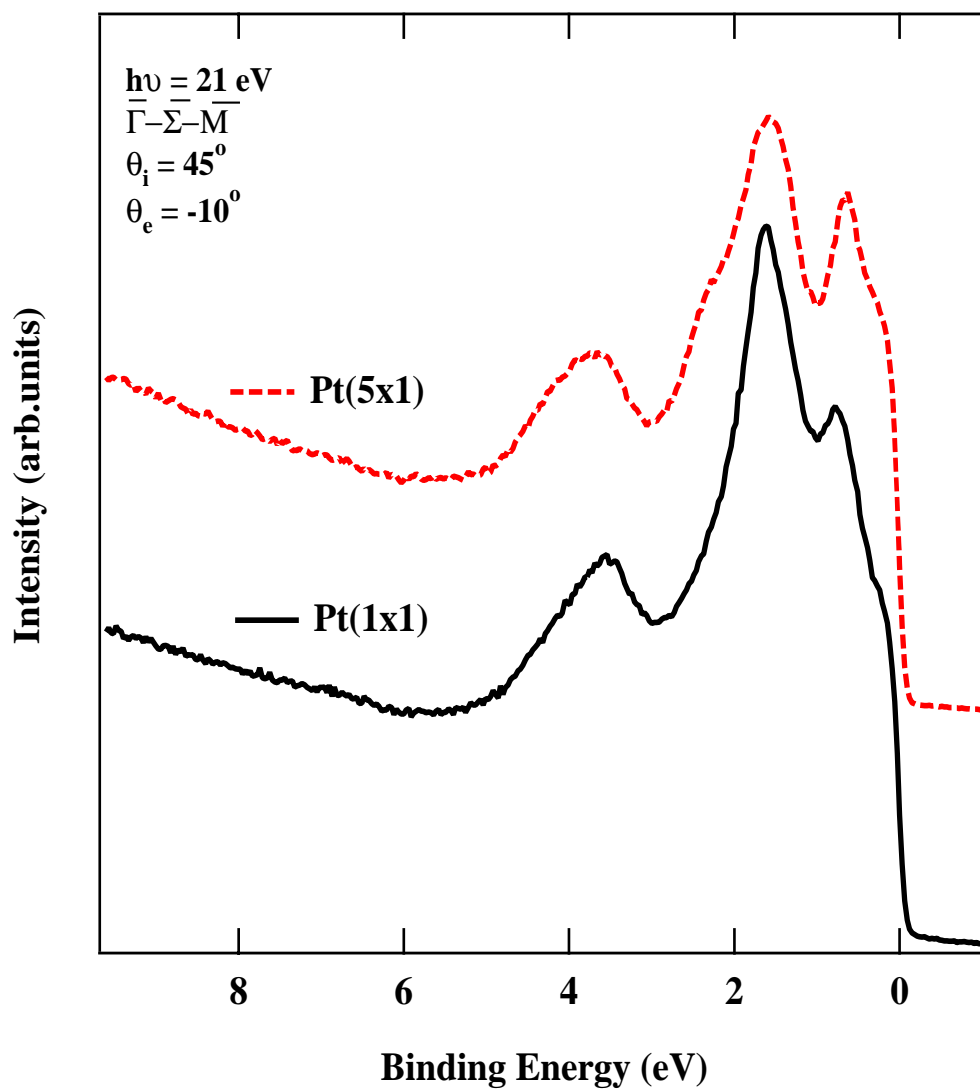
Fig. 3.16 EDC's of the Pt(1x1) and the Pt(5x1) surfaces along the $\overline{\Gamma}-\overline{\Sigma}-\overline{M}$ direction as measured with an excitation energy of 21 eV. The emission angle was -10°. Excitation light was incident at an angle of 45°.
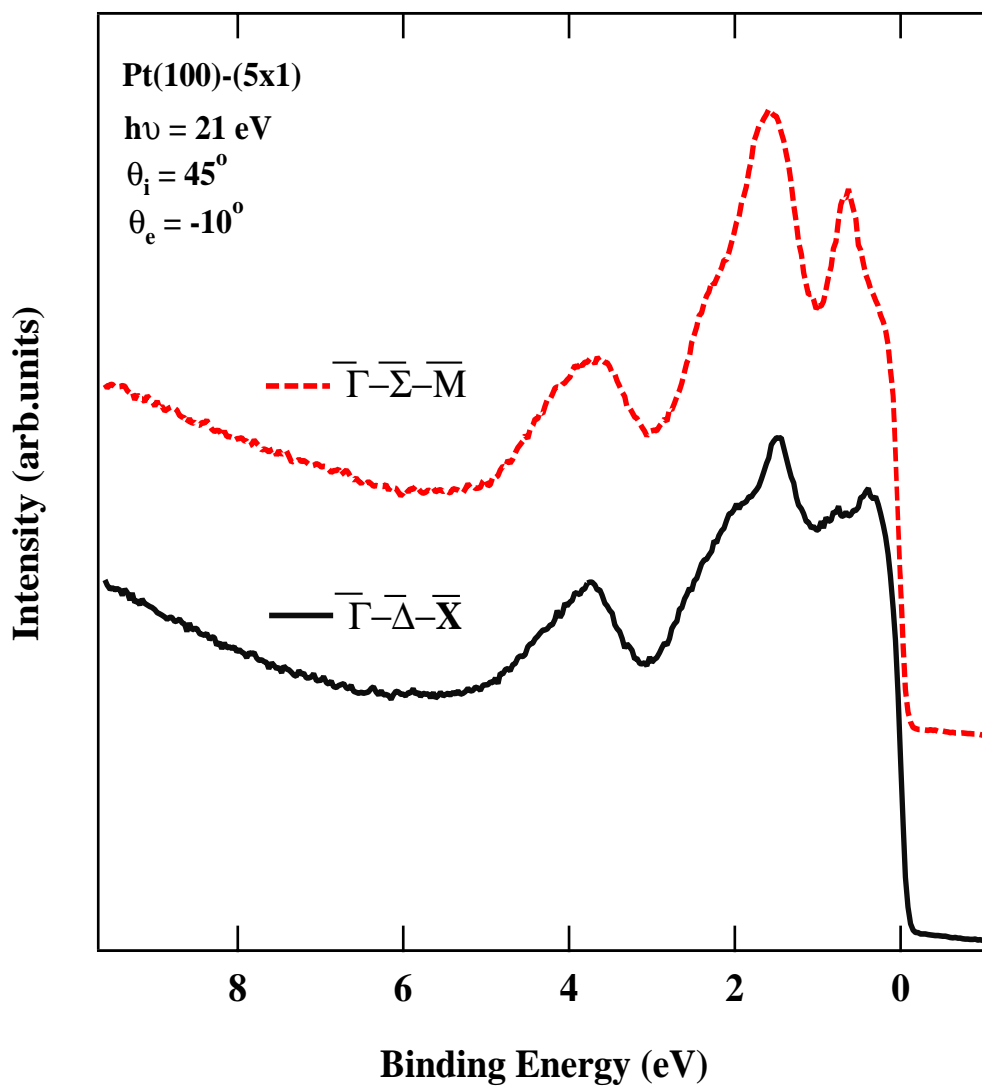
Fig. 3.17 EDC's of the Pt(5x1) surfaces along the $\overline{\Gamma}-\overline{\Sigma}-\overline{M}$ and $\overline{\Gamma}-\overline{\Delta}-\overline{X}$ directions as measured with an excitation energy of 21 eV. The emission angle was -10°. Excitation light was incident at an angle of 45°.

3.2.1 Surface Energy Band Dispersion along $\overline{\Gamma} - \overline{\Sigma} - \overline{M}$ Direction

Figure 3.18 shows the EDC's of the clean unresconstruced Pt(100)-(1x1) surface obtained at different emission angles from -10° to 32°. The experimental arrangement was made so as to record the $\mathbf{k}$ vector along the $\overline{\Gamma} - \overline{\Sigma} - \overline{M}$ direction of the surface Brilluion zone. The excitation photon energy was 21 eV and the incident angle of excitation light was 45°. The broken lines named as *S0, S1, S2, S3, S4, S5, S6* and *S7* represent the variation of the energies of the dominant structures with the emission angle.

The *S0* band occurs only in a narrow angle range. The feature appears around 0.45 and 0.53 eV for the emission angle -4° and -2°, respectively. The *S1* band is found in EDCs for the emission angle from -10° to 26°. The dispersion has such an aspect that the binding energy increases as the emission angle increases from -10° to 0° then the binding energy decreases above 0° and nearly reach the Fermi edge. The *S2* band splits off from the *S1* band around an emission angle of 6°. The intensity of the *S2* peak gradually increases while that of *S1* decreases. Then, at an emission angle of 26°, the *S2* band is predominant while *S1* is nearly invisible. The *S1* band seems to disappear into the region above the Fermi edge above 26°. The *S3* band shows the large dispersion throughout all emission angles. The *S4* band has a weak intensity. It shows dispersion in the binding energy range from 2.37 to 2.58 eV as the emission angle increases from -10° to 6°.

Both *S5* and *S6* bands are found at an emission angle of -10° at binding energies of 3.4 and 4.02 eV, respectively. They disperse in the upward in such opposite manner. At an emission angle of 8°, both bands merge and the resultant band does not show dispersion. The band is localted around 3.84 eV of binding

energy. At emission angles below 8°, the *S5* band exhibits dispersion in the opposite direction to that of the dispersion of the *S6* band. The dispersion of the *S6* band is not large. It is difficult to identify the features at higher binding energies. At emission angles between 18° to 32°, however, the *S7* band can be observed. It shows clear dispersion. The dispersion has the convex shape toward the low binding energy. The peak is located at 5.82 eV at an emission angle of 32°.

If we change the excitation photon energy, the EDC's of the Pt(1x1) surface are changed as shown in Fig. 3.19. In this figure, the measurements were carried out by using an excitation energy of 25 eV along the $\overline{\Gamma} - \overline{\Sigma} - \overline{M}$ direction. The broken lines marked as *S0, S1, S2, S3, S33, S6, S66* and *S* show the dispersion of the features observed by varying the emission angle from -10° to 34°.

The *S0* band in Fig. 3.19 is different from *S0* band in Fig. 3.18. It occurs in a wider emission angle range from 10° to 22°. The band is located almost at the Fermi edge and stays at the binding energy region, 0.15-0.3 eV. The *S1* band excited by 25 eV photon energy is located at higher binding energies than that of the similar band observed with light at 21 eV photon energy. The *S3* band shows clear dispersion. It splits into two bands at an emission angle 6°. One of the split-off band is referred to as *S33*. The bands corresponding to *S4* and *S5* in the EDCs shown in Fig. 3.19 are not found in the spectra obtained by the excitations at 25 eV. Instead, the *S6* band shows clear dispersion below an emission angle of 2° and split into two band at an emission angle of 4°. Above this angle the dispersion is not clear. The split-off band shows definite dispersion. This band is referred to as *S66*. The *S66* band is not clearly found above an emission angle of 22°. A weak band named *S7* is found at high binding energies.

Fig. 3.18 Representative ARPES spectra of the clean unreconstructed Pt(1x1) surface for various emission angles. The measurements were performed along the $\overline{\Gamma}-\overline{\Sigma}-\overline{M}$ direction with an incident angle of 45° of excitation light and a photon energy of 21 eV.

To obtain the energy dispersion of the surface bands shown in Figs. 3.18 and 3.19, we employ the equations (1.99) and (1.101) presented in section 1.6.6. The results are shown in Figs. 3.20 and 3.21. In the figures, broken lines connecting the measured points show the energy band dispersion.

The vertical dotted lines in both figures indicate the positions of the symmetry points, $\bar{\Gamma}$ and $\bar{M}$. Obviously, the $\bar{\Gamma}$ point is located at $k_{||} = 0$. The $\bar{M}$ point is located at $k_{||} = 1.6 \ \overset{\scriptscriptstyle{o}}{A}^{-1}$. As is remarked already, the *S0* band lies near the Fermi edge. In Fig. 3.21, this is more clearly seen. In Fig. 3.20, the bands occuring nearest to the Fermi level is the *S1* abd *S2* band. In other words the locations of S0 and S1 bands are reversed in the two figures. This indicates that the energy band assigment is crucially dependent on the excitation energy. If we compare the energy bands shown in Fig. 3.20 with those of Fig. 3.21, we find qualitative disagreement.   If the approximation made in section 1.6.6 regarding Fig. 1.34 is correct, the disagreement found here cannot be explained.   This point will be discussed in the next chapter.

Figure 3.20 also indicates that the *S0, S2, S3, S4, S5* and *S6* bands have the extrima at the $\bar{\Gamma}$ point. At higher $k_{||}$ which not shown in Fig. 3.18, there are two bands occurring around the $\bar{M}$ point. One band stays between *S2* and *S3* bands, the other band splits off from *S3* band.   If we extend the excitation energy higher values, the energy dispersion is found as shown in Fig. 3.21. In the energy bands observed by excitations at 25 eV, the *S0* band occurs nearer to the Fermi edge in the **k** space of 0.5-1.0 $\overset{\scriptscriptstyle{o}}{A}^{-1}$ of $k_{||}$ as mentioned quanlitatively already. The bands *S4* and *S5* cannot be found by excitations at 25 eV.

Pt(100)-(1x1)
$\overline{\Gamma}-\overline{\Sigma}-\overline{M}$
$\theta_i = 45^o$
$h\upsilon = 25\ eV$
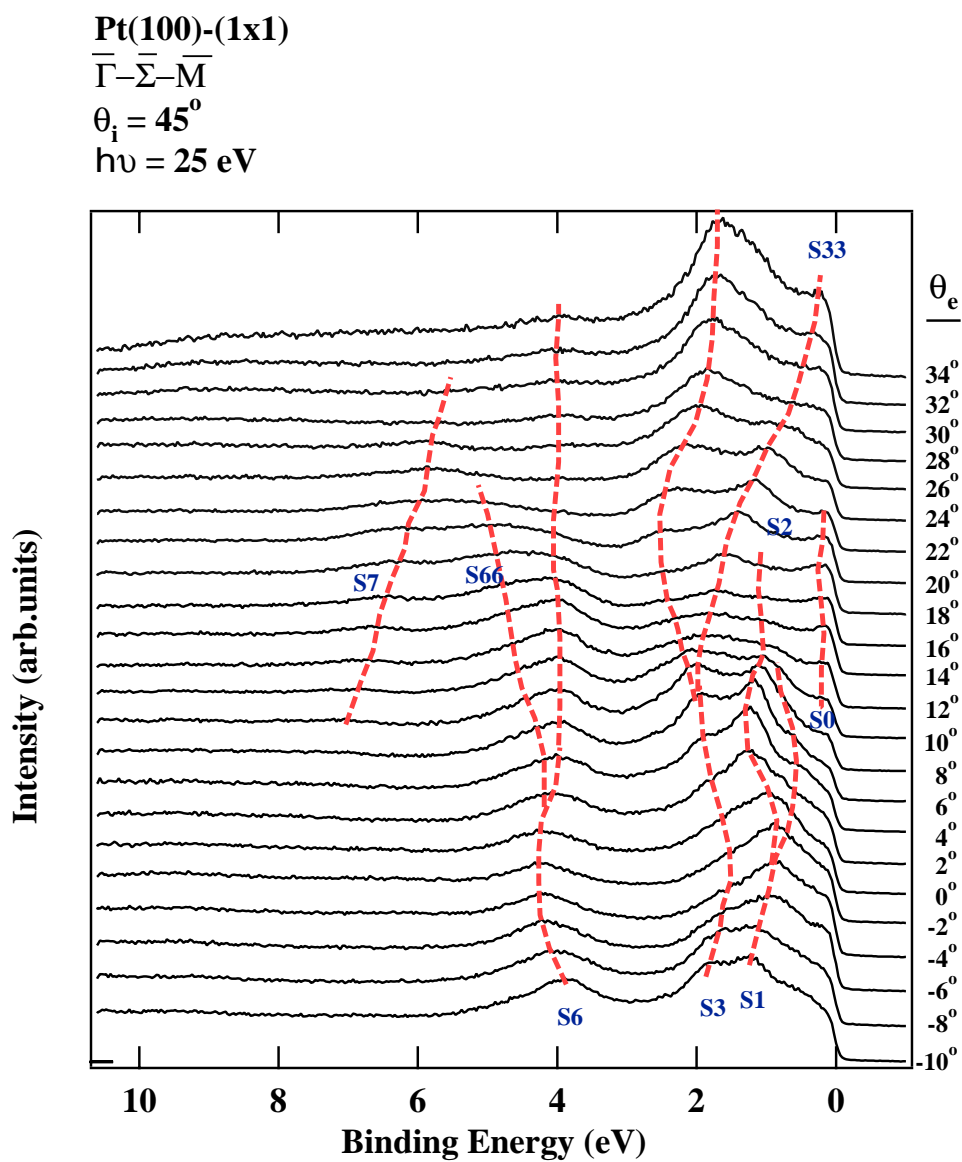
Fig. 3.19 Representative ARPES spectra of the clean unreconstructed Pt(1x1) surface

for various emission angles. The measurements were performed along the

$\overline{\Gamma}-\overline{\Sigma}-\overline{M}$ direction with a light incidence of angle 45° and a photon energy

of 25 eV.
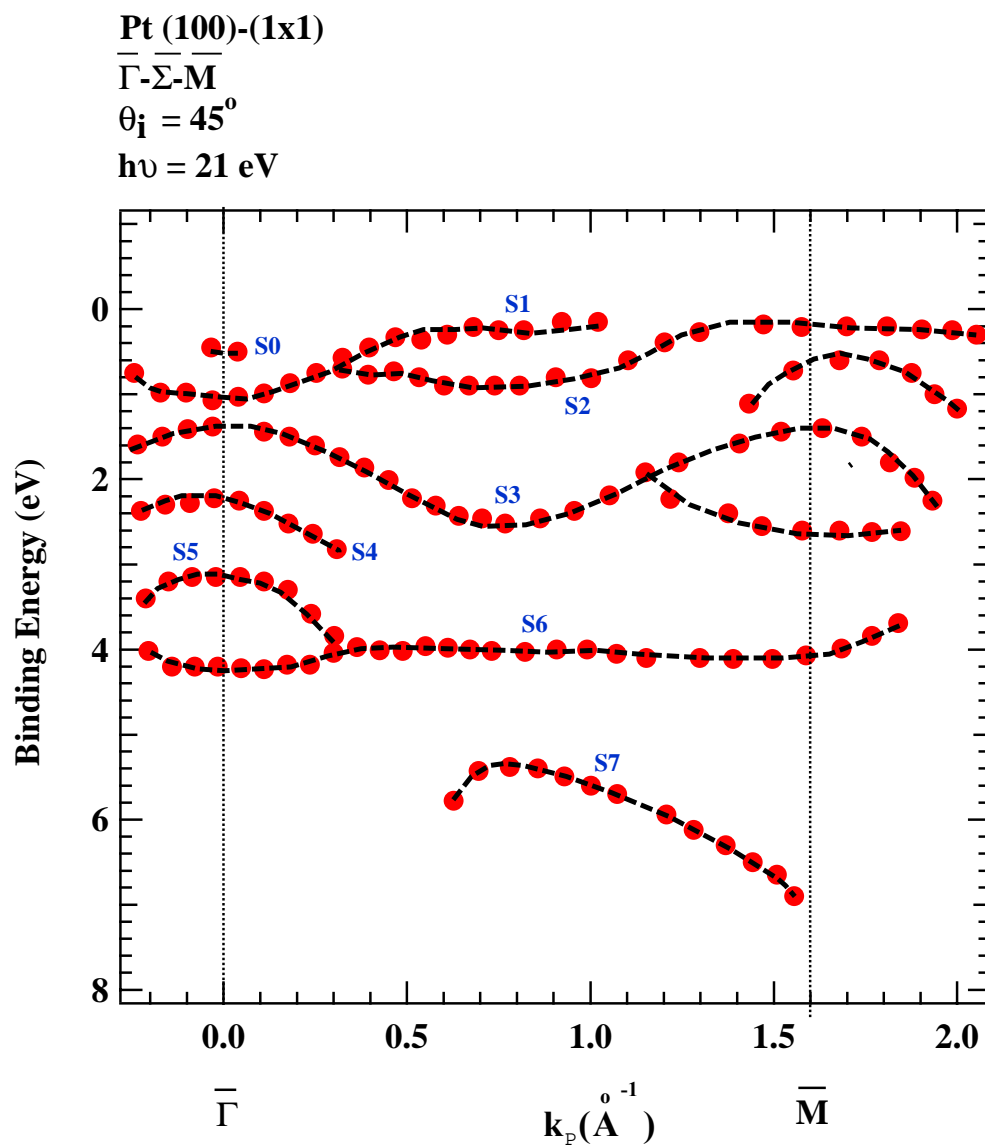
Fig. 3.20 Experimentally determined energy band dispersion of the unreconstructed Pt(1x1) surface along $\overline{\Gamma}-\overline{\Sigma}-\overline{M}$ direction obtained at an excitation energy of 21 eV.

Pt(100)-(1x1)
$\overline{\Gamma}-\overline{\Sigma}-\overline{M}$
$\theta_i = 45^o$
$h\upsilon = 25\ eV$
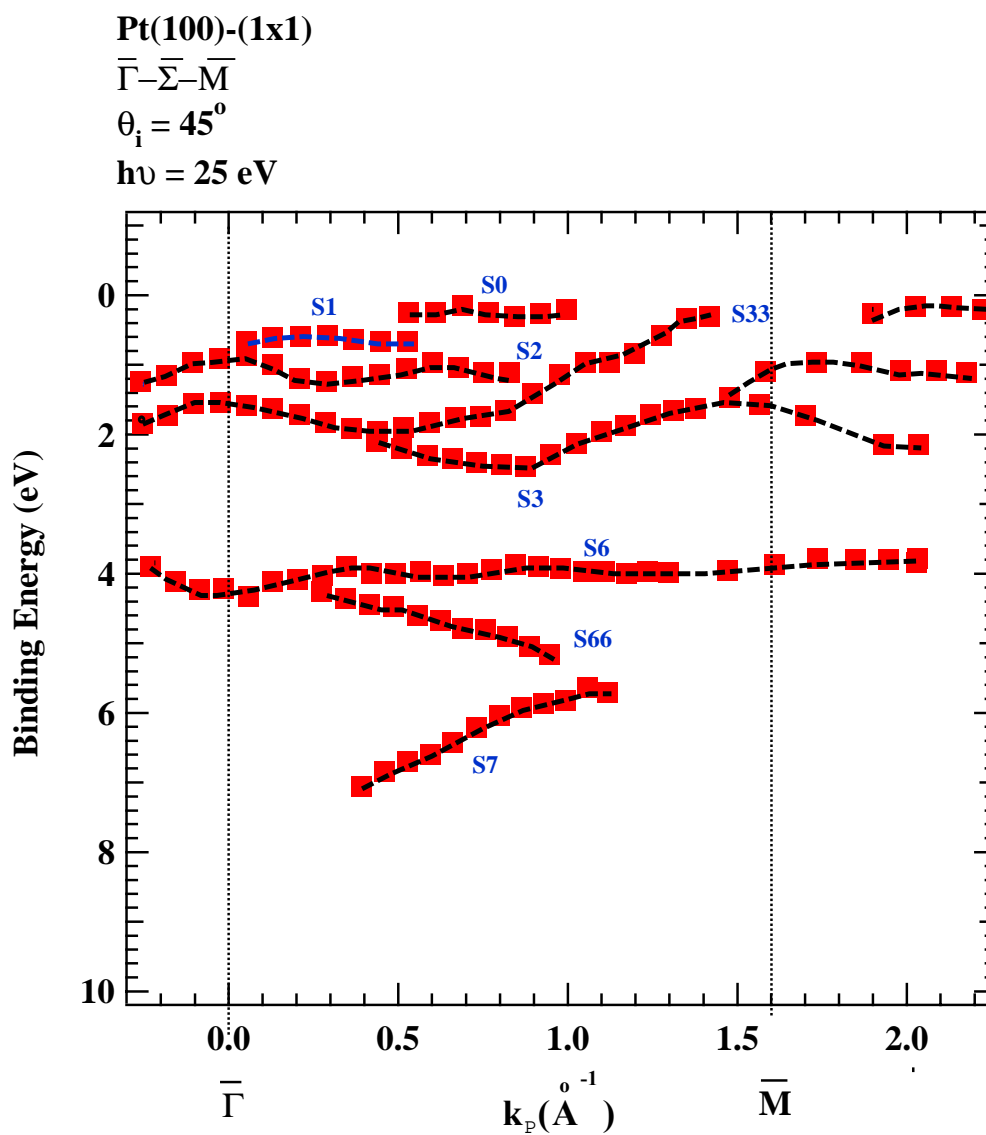
Fig. 3.21 Experimentally determined energy band dispersion of the unreconstructed

Pt(1x1) surface along $\overline{\Gamma}-\overline{\Sigma}-\overline{M}$ direction obtained at an excitation energy

of 25 eV.

For the clean reconstructed Pt(5x1) surface, the ARPES spectra measured along the $\overline{\Gamma}-\overline{\Sigma}-\overline{M}$ direction of the surface Brilluion zone are shown in Figs. 3.22 and 3.23. EDCs presented in Fig. 3.22 were obtained by excitations at 21 eV. EDCs presented in Fig. 3.23 were obtained by excitations at 25 eV. In both cases, excitation light was incident on the sample surfaces at an incidence angle of 45°. This is the same as in other cases for measurements on the Pt(1x1) surfaces. Broken lines indicate the peak shift cause by changing the emission angle. Features are named a *SM*, where *M* is *0, 1, 2, 3, 33, 4, 5, 6* and *7* as in the cases of Pt(1x1).

Some of the bands show clear dispersion. However, the magnitude of the dispersion observed in other bands. Thus, experimentally observed aspect of a small amount of divergence in the $\overline{\Gamma}-\overline{\Sigma}-\overline{M}$ bands, thus mostly the $\overline{\Sigma}$ bands, may be remarkable. This point will be discussed in Chapter IV.

The energy band dispersion which are obtained from the data shown in Figs. 3.22 and 3.23 are presented in Figs. 3.24 and 3.25, respectively. The locations of the $\overline{\Gamma}$ and $\overline{M}$ points are indicated with vertical dotted lines. Characteristic aspects of both Figs. 3.24 and 3.25 are more or less similar to those mentioned so far.

In Fig. 3.24, the energy bands appear to distribute uniformly in the binding energy region below 4 eV. However, it also appears that two groups of the bands exist concerning the distribution of the bands in the binding energy region. One group consists of the bands, *S1-S3*. The other consists of the *S5* and *S6* bands. This tendency is more clearly visible in Fig. 3.25. This shows that the excitation energy, which depends on the observed band shape, is conspicuous.

Fig. 3.22 Representative ARPES spectra of the clean reconstructed Pt(5x1) surface for various emission angles. The measurements were performed along the $\overline{\Gamma}-\overline{\Sigma}-\overline{M}$ direction at a light incidence angle of 45° and excitation an energy of 21 eV.
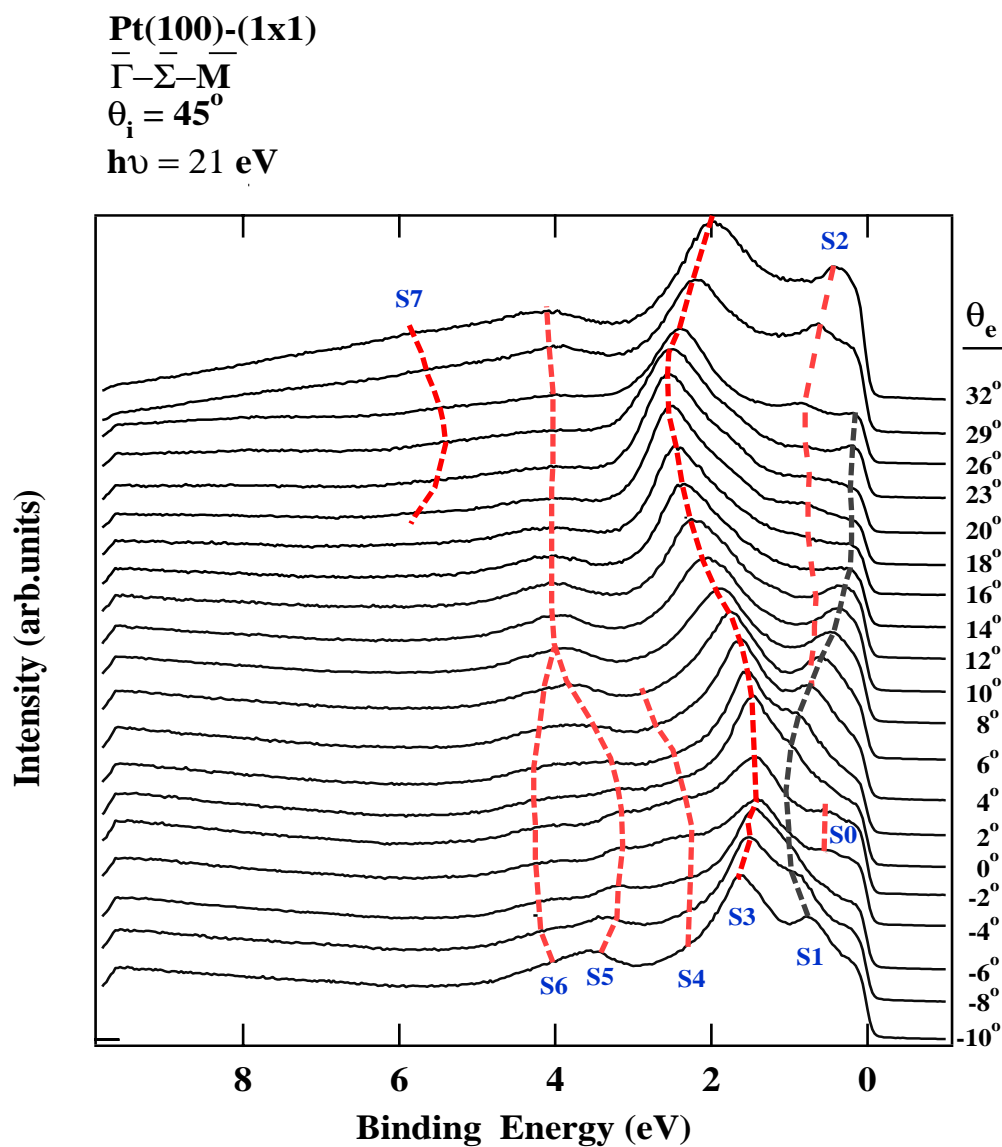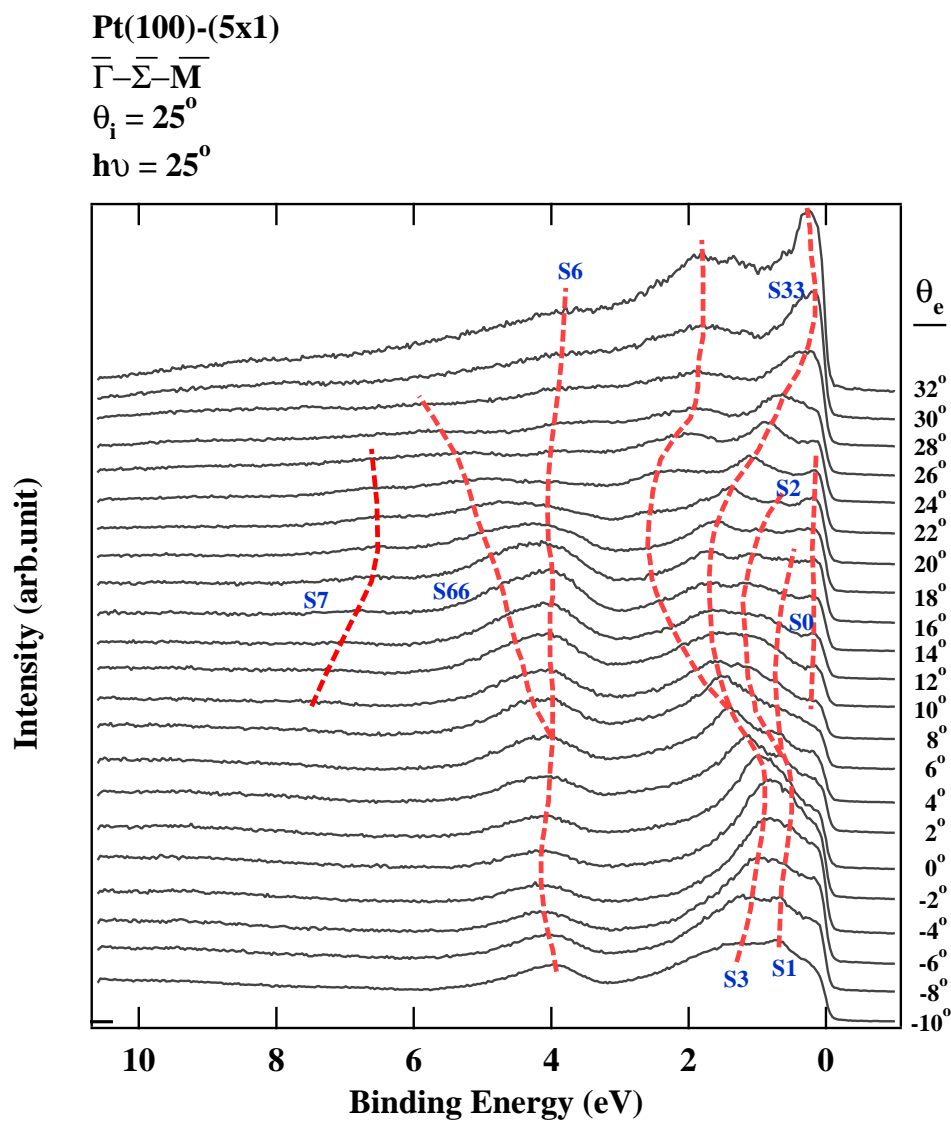
Fig. 3.23 Representative ARPES spectra of the clean reconstructed Pt(5x1) surface

for various emission angles. The measurements were performed along the

$\overline{\Gamma} - \overline{\Sigma} - \overline{M}$ direction at a light incidence angle of 45° and an excitation

energy of 25 eV.
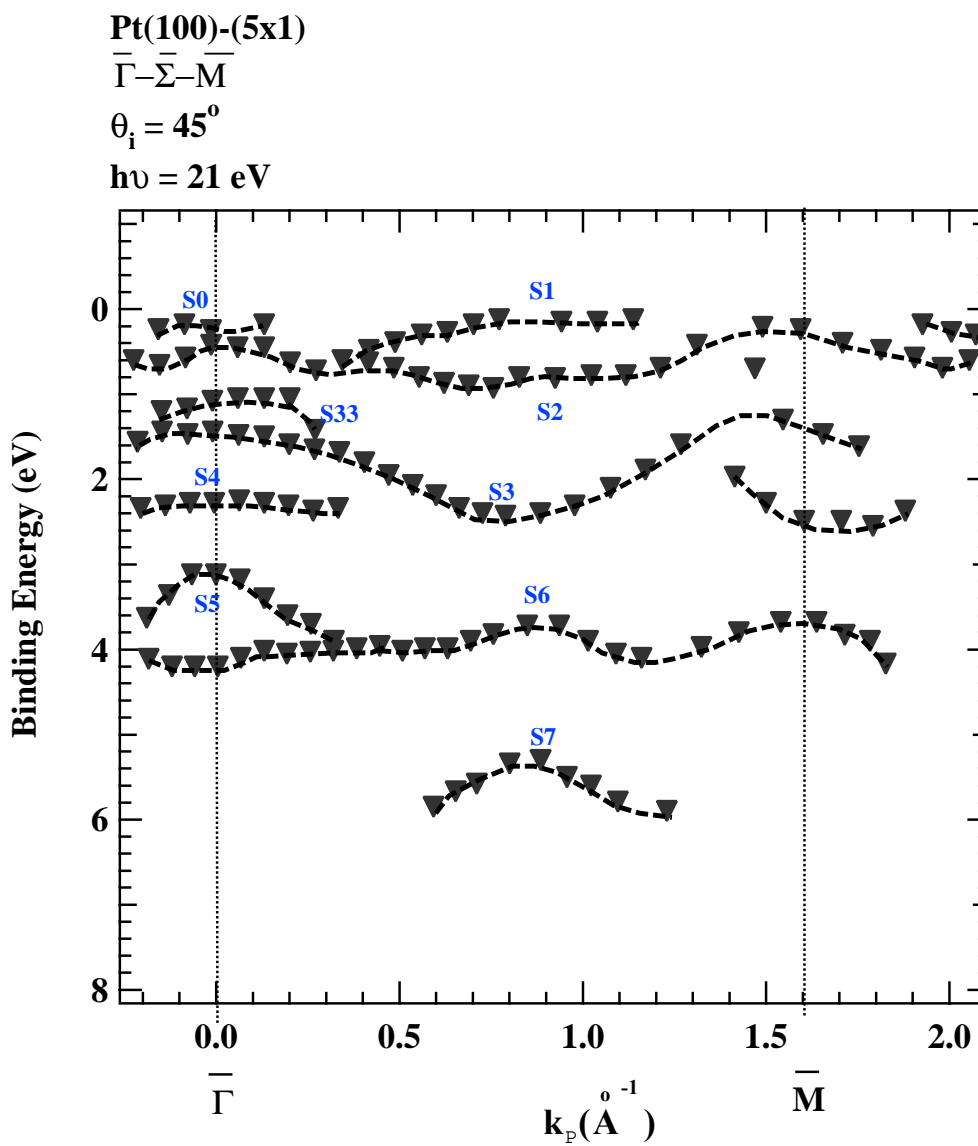
Fig. 3.24 Experimentally determined energy band dispersion of the reconstructed Pt (5x1) surface along the $\overline{\Gamma}-\overline{\Sigma}-\overline{M}$ direction. Excitation light had an energy of 21 eV.

Pt(100)-(5x1)
$\overline{\Gamma}-\overline{\Sigma}-\overline{M}$
$\theta_i = 45^o$
$h\upsilon = 25$ eV
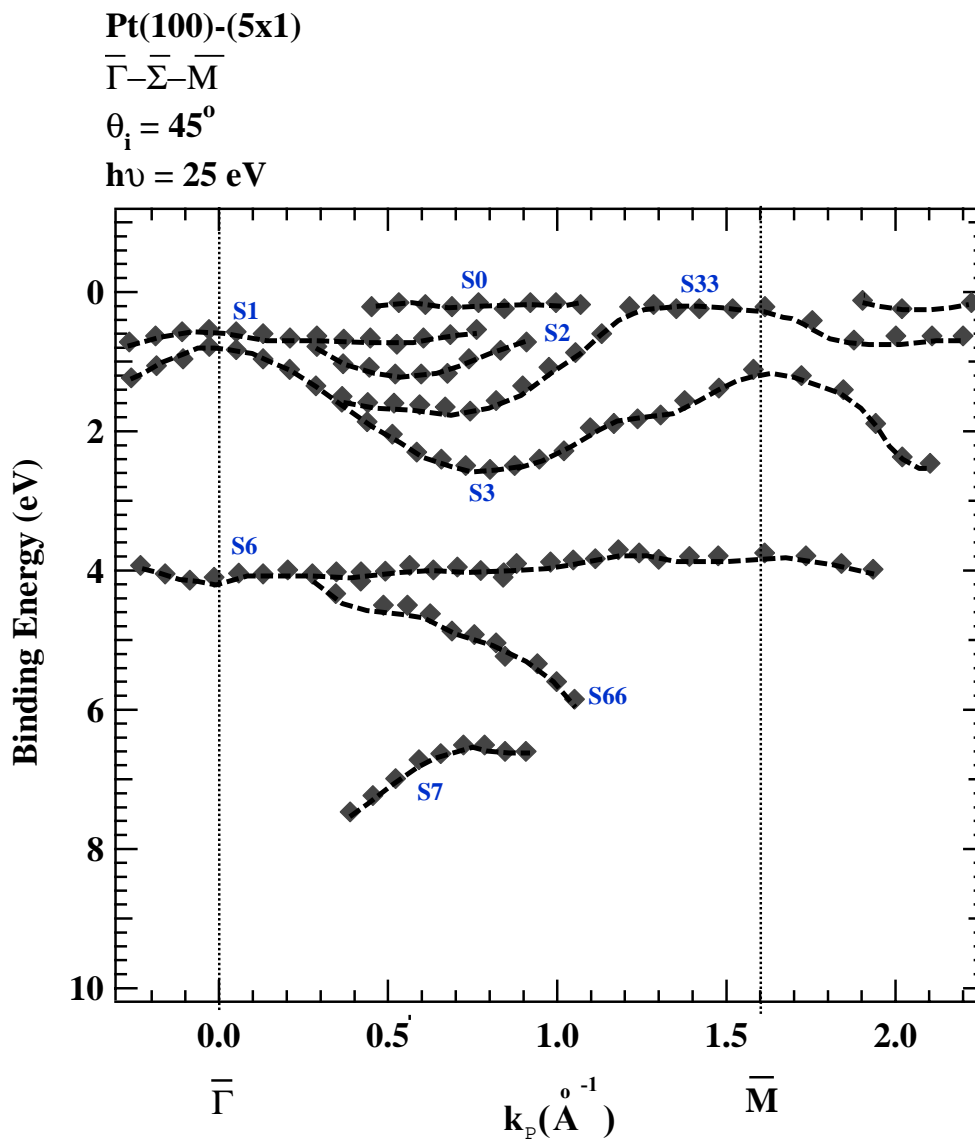
Fig. 3.25 Experimentally determined energy band dispersion of the reconstructed Pt(5x1) surface along the $\overline{\Gamma}-\overline{\Sigma}-\overline{M}$ direction. Excitation light had an energy of 25 eV.

3.2.2 Surface Energy Band Dispersion along $\overline{\Gamma} - \overline{\Delta} - \overline{X}$ Direction

Figure 3.26 show the EDC's of clean unreconstructed Pt(100)-(1x1) surface made so as to record the **k** vector along the $\overline{\Gamma} - \overline{\Delta} - \overline{X}$ direction of the surface Brillouin zone. The experimental was obtained at different emission angles from -10° to 51°. The excitation photon energy was 21 eV. And the incident angle of excitation light was 45°. The broken lines named as *S1, S11, S2, S3, S4, S5* and *S55* represent the radiation of the energies of the dominant structures with the emission angle.

The *S1* band occurs near the Fermi edge. It shows a weak dispersion to the lower binding energy as the emission angle increase from -10° to 22°. At an emission angle 6°, the *S11* band splits off from *S1* band and keeps a small dispersion to higher binding energy from *S1* band until 18°.

The *S3* and *S4* band has a weak intensity. The *S3* band shows dispersion at emission angle of -10° to 36°. At the emission angles 24° to 36°, it exhibits the strong dispersion with the weak intensities. The *S4* does not show dispersion as the emission angle 28° to 51° with the binding energy 2.48 eV.

Both *S2* and *S5* bands show the dispersion continuously all emission angles. The *S2* band is found at an emission angle -10° at binding energy of 1.48 eV. It has a prominent structure with strong intensities at lower emission angles.

S5 band occurs at higher binding energy. It has a prominent structure all emission angles. At an emission angle of 10°, the *S55* band occurs and merges to the *S5* band at an emission angle 8°.

Both *S2* and *S5* bands show the dispersion continuously all emission angles. The *S2* band is found at an emission angle -10° at binding energy of 1.48 eV. It has a prominent structure with strong intensities at lower emission angles.

If we measured the Pt(1x1) surface along the $\overline{\Gamma} - \overline{\Delta} - \overline{X}$ direction by changing the excitation photon energy, the EDC's of Pt (1x1) surface are changed as shown in Fig. 3.27. In Fig. 3.27, the experiments were obtained by using excitation energy of 25 eV. The broken lines marked as *S1, S2, S3, S4, S5, S6* and *S7* represent the dispersion of the features observed by varying the emission angle -10° to 51°.

If we roughly compare the spectrum in Figs. 3.26 and 3.27, we see that the *S1, S2, S3, S4* and *S5* band in both figures look as the same. However, if we see more detail, they are qualitatively different. The weak bands named *S6* and *S7* in the EDC's shown in Fig. 3.27 are found at high binding energies. They are not found in the spectra obtained by the excitations at 21 eV.

To obtained the energy dispersion of the surface bands along $\overline{\Gamma} - \overline{\Delta} - \overline{X}$ shown in Figs. 3.26 and 3.27, we employ the equations (1.99) and (1.101) which is described in section 1.6.6. The results of the surfaces band structure are shown in Figs. 3.28 and 3.29.

In Figs. 3.28 and 3.29, the broken lines connecting the measured points show the energy band dispersion. The vertical dotted lines indicate the positions of the symmetry points, $\overline{\Gamma}$ and $\overline{X}$. The $\overline{\Gamma}$ point is located at $k_P = 0$. The $\overline{X}$ point is located at $k_P = 1.3 \ \overset{o}{A}^{-1}$. If we compare the energy bands shown in Figs. 3.28 and 3.29, we find the qualitatively disagreement. The detail comparison will be made in chapter IV.
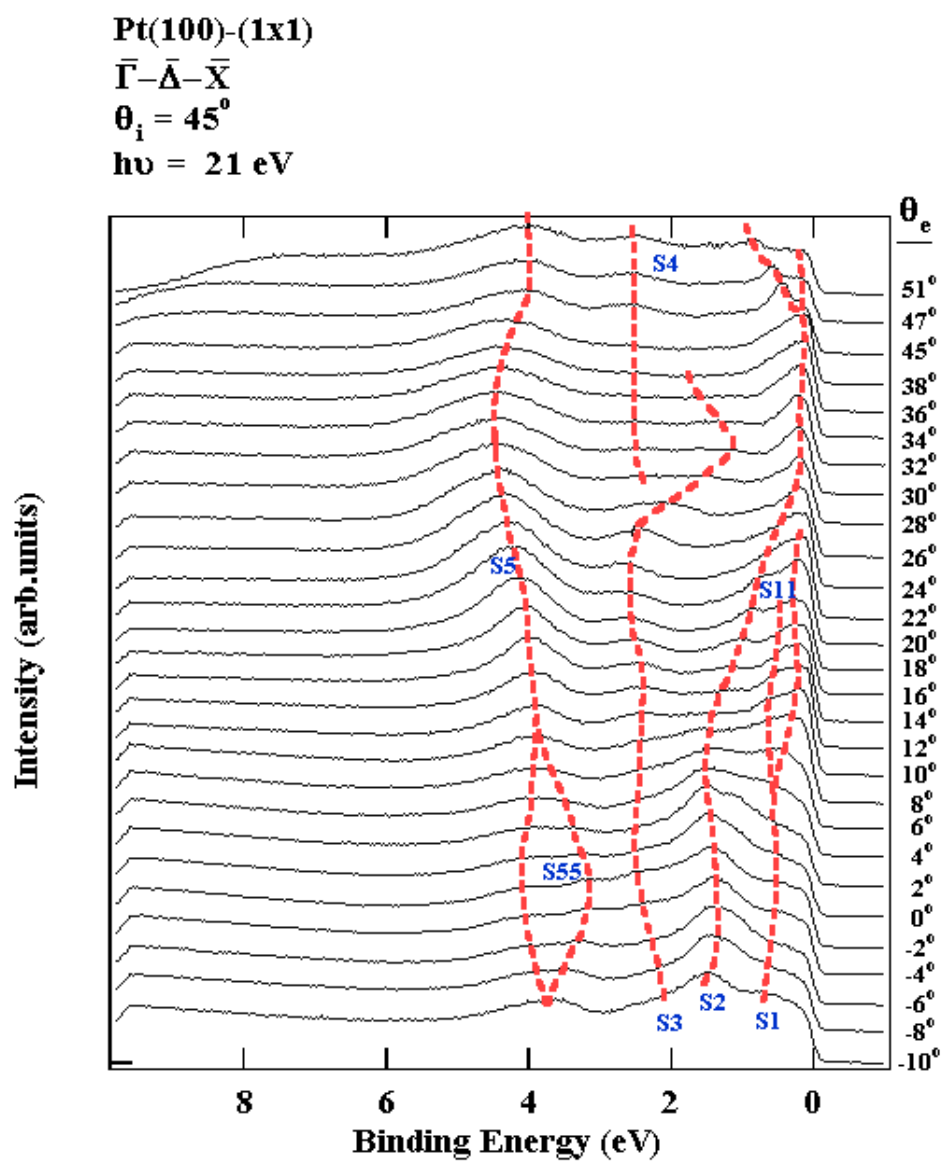
Fig. 3.26 ARPES spectra of the clean unreconstructed Pt(1x1) surface for various emission angles. The measurements were performed along the $\overline{\Gamma}-\overline{\Delta}-\overline{X}$ direction. Excitation light was incident on the sample surface at an angle of 45°. The photon energy was 21 eV.
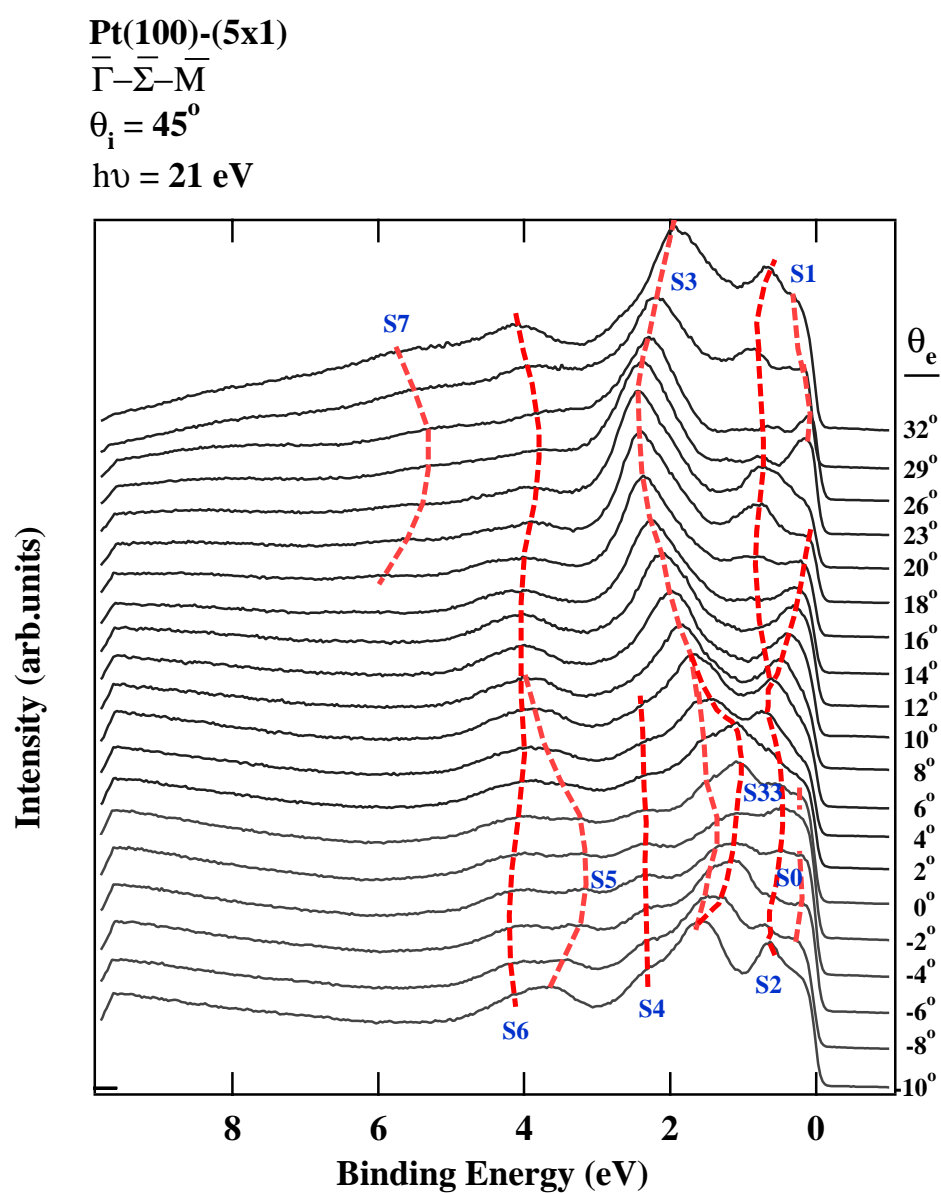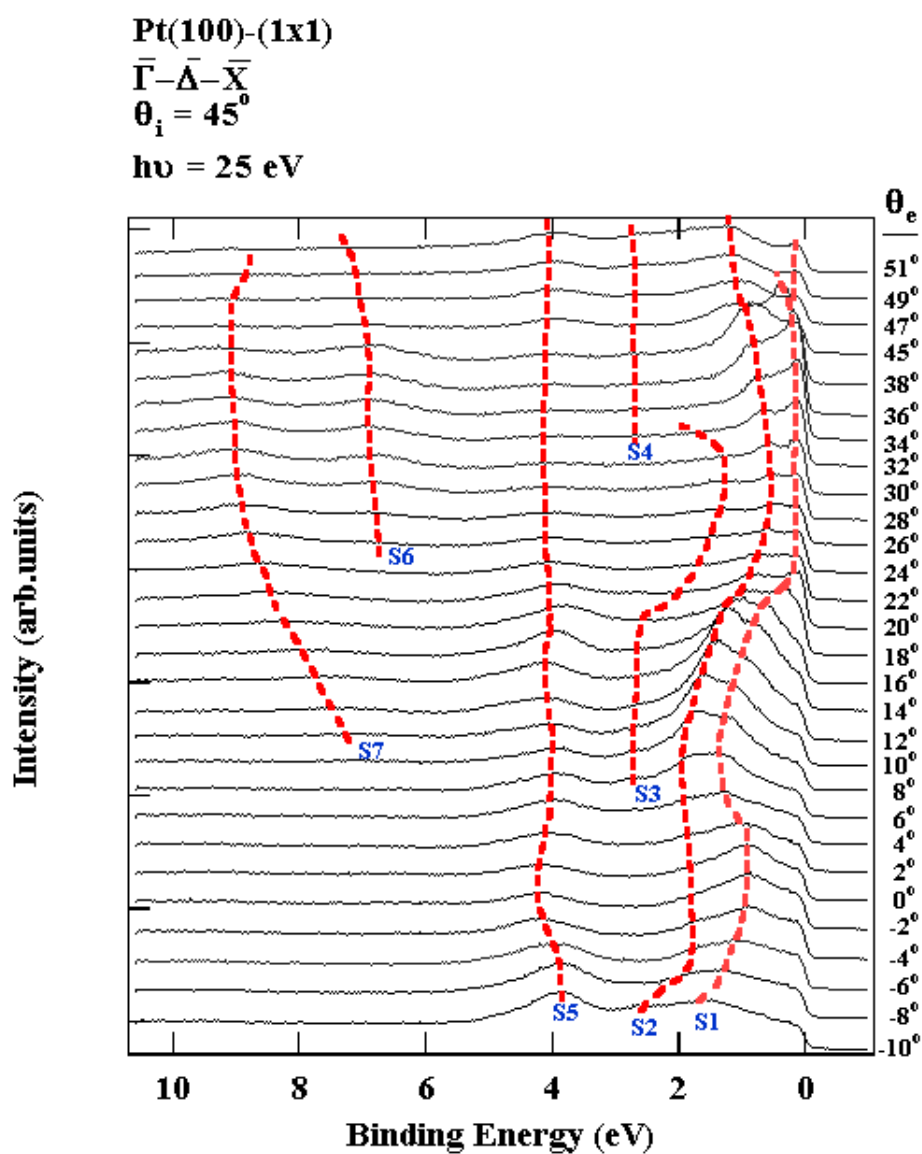
Fig. 3.27 ARPES spectra of the clean unreconstructed Pt(1x1) surface for various emission angles. The measurements were performed along the $\bar{\Gamma} - \bar{\Delta} - \bar{X}$ direction. Excitation light was incident on the sample surface at an angle of 45°. The photon energy was 25 eV.

Pt(100)-(1x1)
$\overline{\Gamma}-\overline{\Delta}-\overline{X}$
$\theta_i = 45$ eV
$h\upsilon = 21$ eV
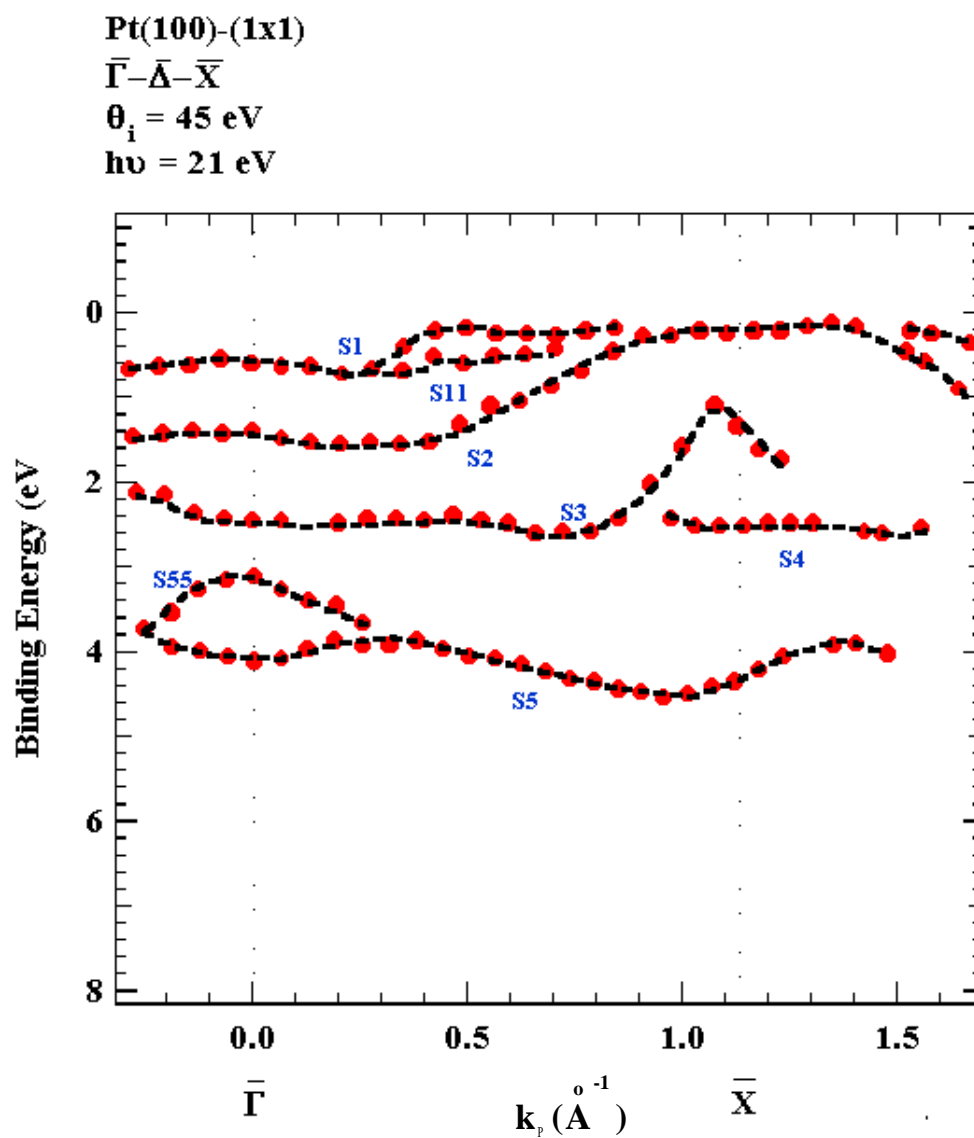
Fig. 3.28 Experimentally determined energy band dispersion of the unreconstructed

Pt(1x1) surface along $\overline{\Gamma}-\overline{\Delta}-\overline{X}$ direction. Excitation energy was 21 eV.
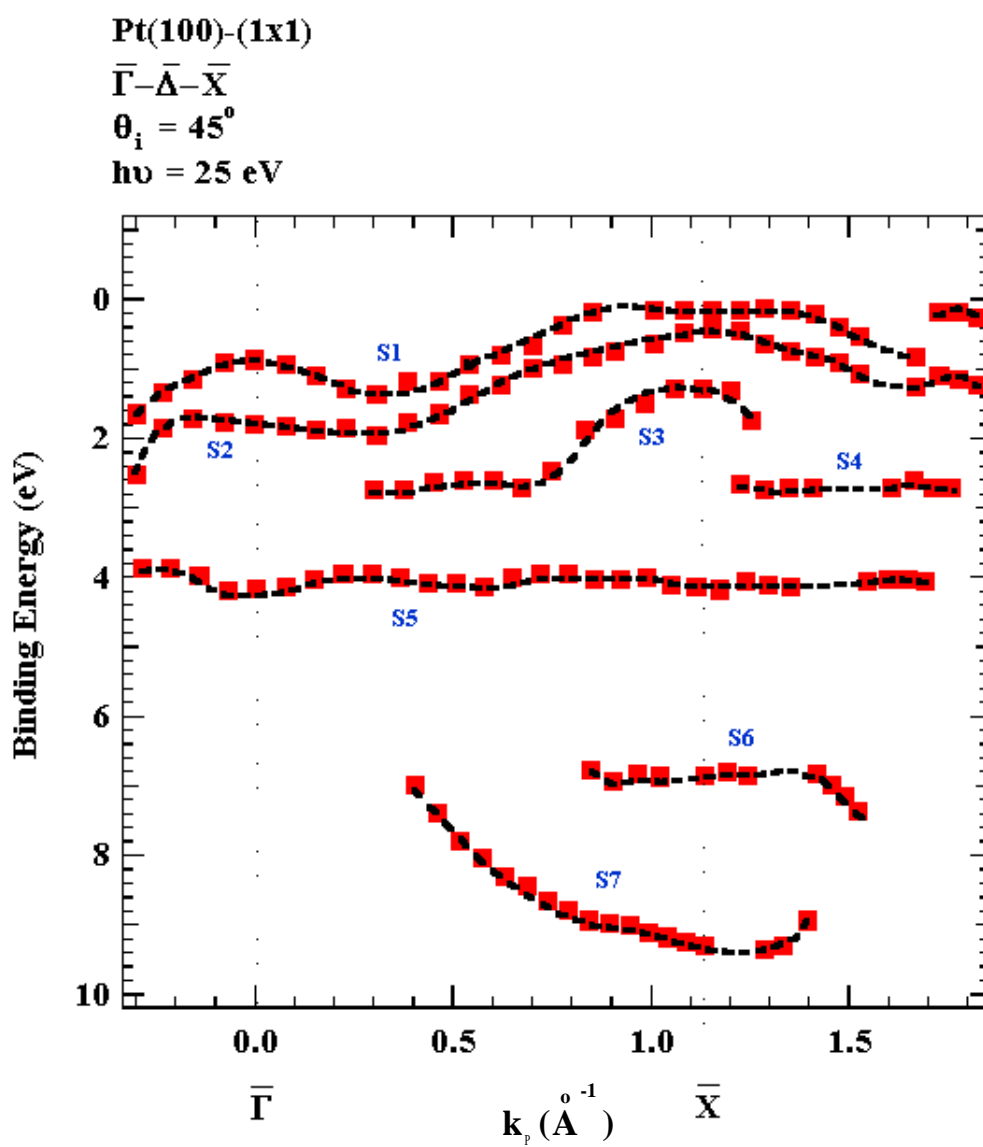
Fig. 3.29 Experimentally determined energy band dispersion of the unreconstructed

Pt(1x1) surface along $\overline{\Gamma}-\overline{\Delta}-\overline{X}$ direction. Excitation energy was 25 eV.

For the clean reconstructed Pt(5x1) surface, the ARPES spectra measured along the $\overline{\Gamma}-\overline{\Delta}-\overline{X}$ direction of the surface Brilluion zone are shown in Figs. 3.30 and 3.31. The data shown in Fig. 3.30 was obtained by excitations at 21 eV. The data shown in Fig. 3.31 was obtained by excitations at 25 eV. Broken lines indicate the shift of peaks as the emission is changed. The values of emission angle are shown on the right hand side of each EDC. Peaks are named as *S1*, *S11*, *S2*, *S22*, *S3*, *S4*, *S5*, *S55*, *S6* and *S7*.

The *S5* band as well as the *S55* band is clearly seen in spectra obtained by excitations at 21 eV. The intensity of the *S5* bands in EDCs measured by excitations at 25 eV are low. For this excitation energy, the *S55* band is not found. The *S55* band shows somewhat peculiar dispersion. Although it is possible that one more different band exists in the spectral region where the *S5* and *S55* bands occur, we tentatively ignore this possibility and assign the features as shown in the figures.

In Fig. 3.31 where EDCs obtained by excitations at 25 eV are exhibited, two features we named as *S6* and *S7* are recognized. However, the bands corresponding to these are not found in EDCs obtained by excitations at lower photon energy, 21 eV. This point will be argued in the next chapter.

The $\varepsilon(\mathbf{k})$ curves energy band dispersion obtained from the analyses of data shown in Figs 3.32 and 3.33, respectively. In Figs. 3.31 and 3.33, vertical dotted lines represent the locations of $\overline{\Gamma}$ and $\overline{X}$ points.

The energy bands consist of three groups of bands. One group consists of the *S1* to *S4* bands. The second group bands are the *S5* and *S55*. The third group consists of the *S6* and *S7* bands. As is recognized in Fig. 3.21 they are very weak. As is found in Fig. 3.20, they cannot be detected by excitations at 21 eV.

Pt(100)-(5x1)
$\overline{\Gamma}-\overline{\Delta}-\overline{X}$
$\theta_i = 45^o$
hυ = 21 eV
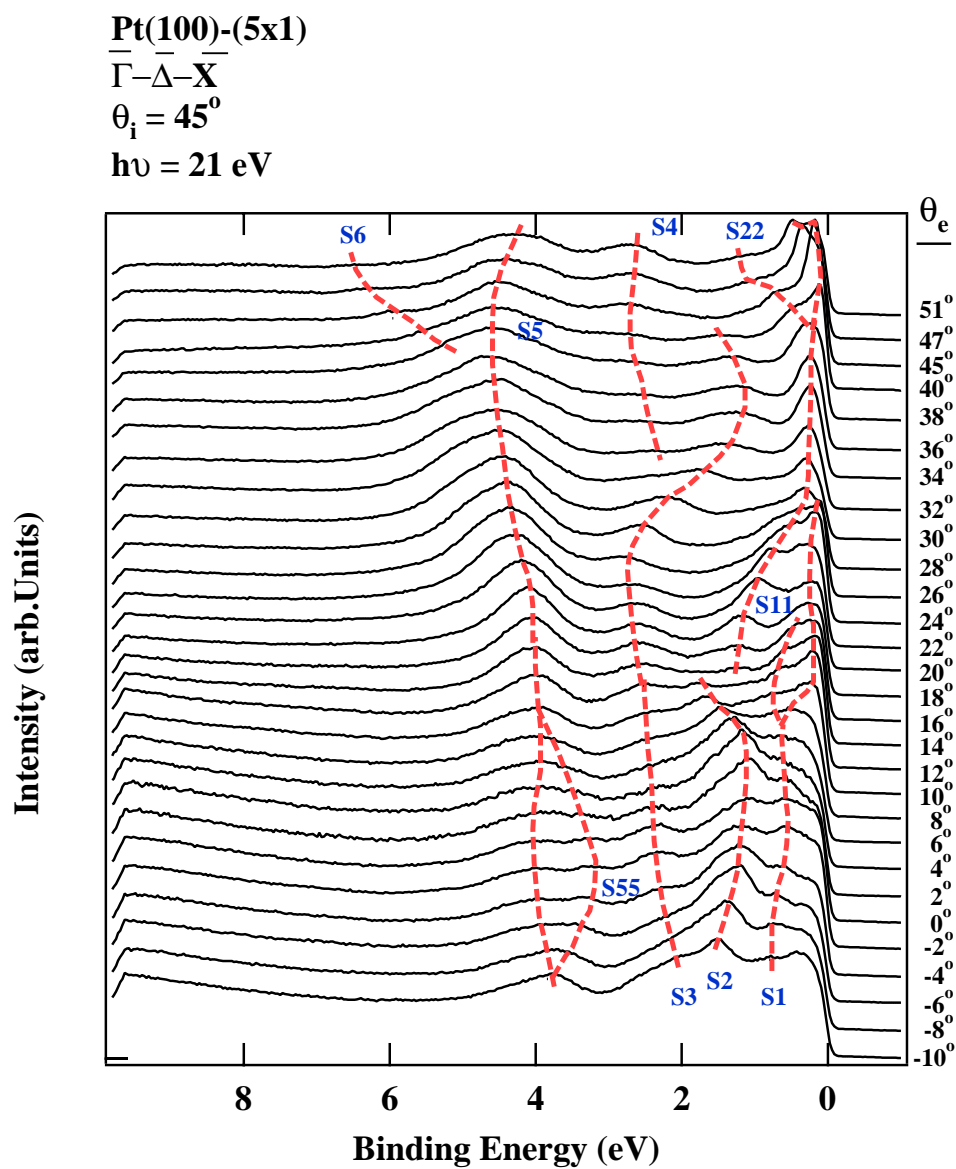
Fig. 3.30 ARPES spectra of the clean reconstructed Pt(5x1) surface for various emission angles. The measurements were performed along the $\overline{\Gamma}-\overline{\Delta}-\overline{X}$ direction. Excitation light was incident on the sample surface at an angle of 45°.The photon energy was 21 eV.

Pt(100)-(5x1)

$\overline{\Gamma}-\overline{\Delta}-\overline{X}$

$\theta_i = 45^o$

$h\upsilon = 25\ eV$
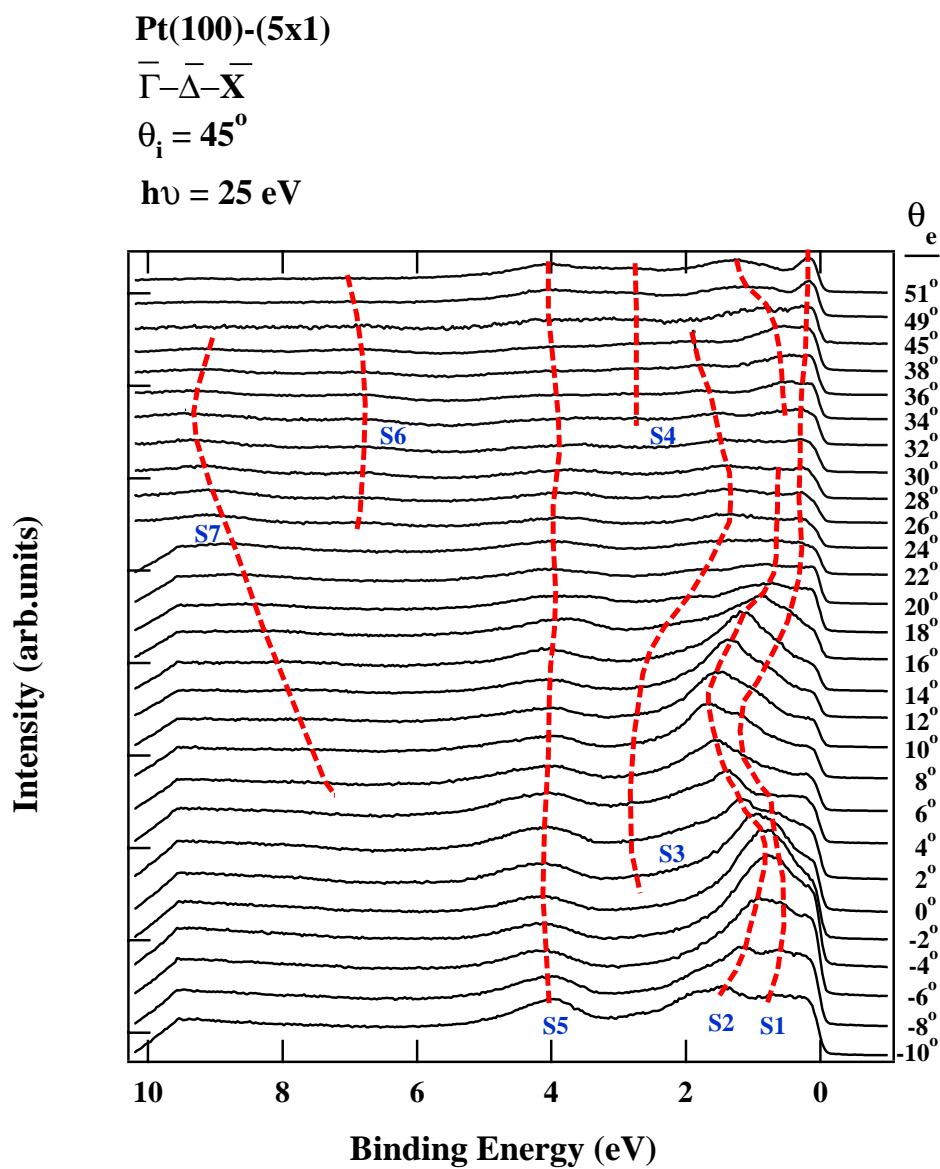
Fig. 3.31 ARPES spectra of the clean reconstructed Pt(5x1) surface for various emission angles. The measurements were performed along the $\overline{\Gamma}-\overline{\Delta}-\overline{X}$ direction. Excitation light was incident on the sample surface at an angle of 45°. The photon energy was 25 eV.
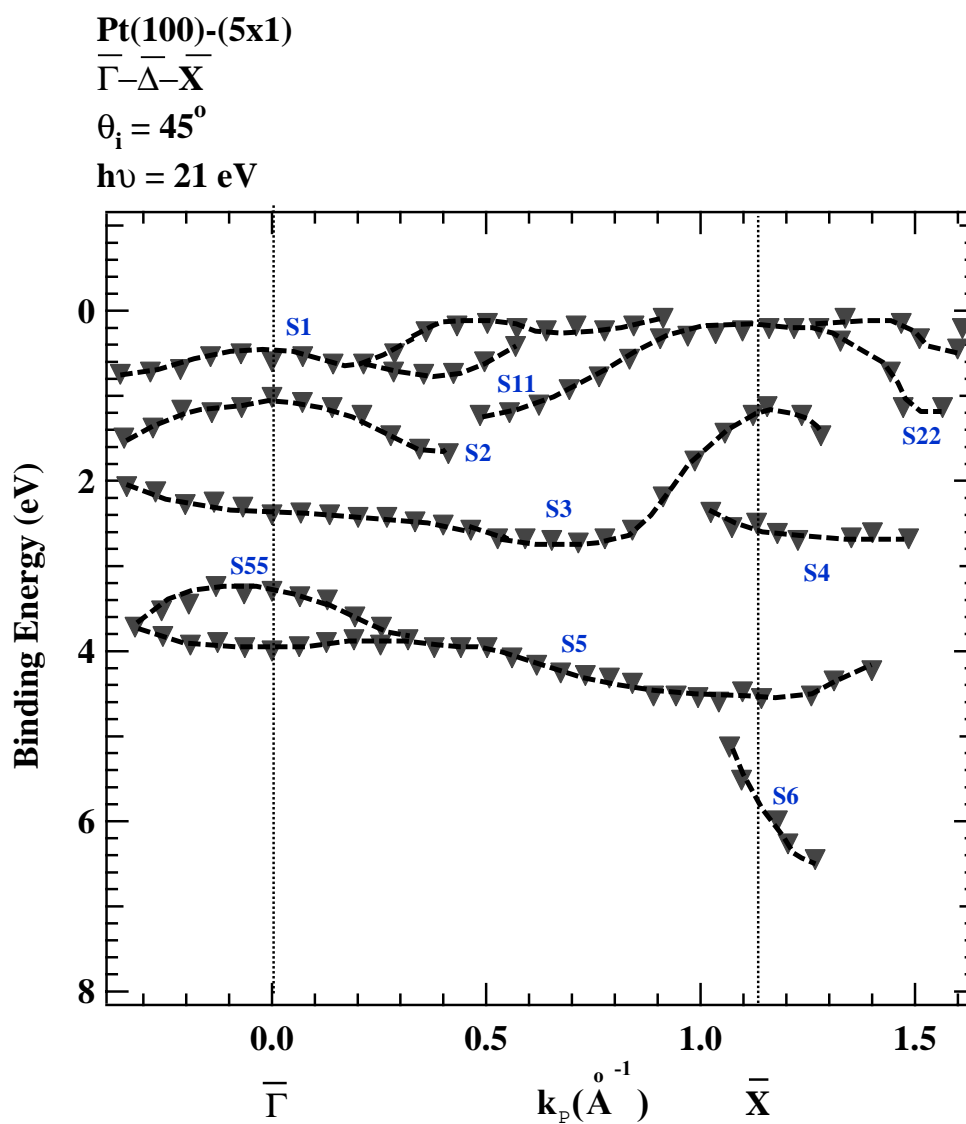
Fig. 3.32 Experimentally determined energy band dispersion of the reconstructed Pt

(5x1) surface along the $\overline{\Gamma}-\overline{\Delta}-\overline{X}$ direction. Excitation energy was 21 eV.
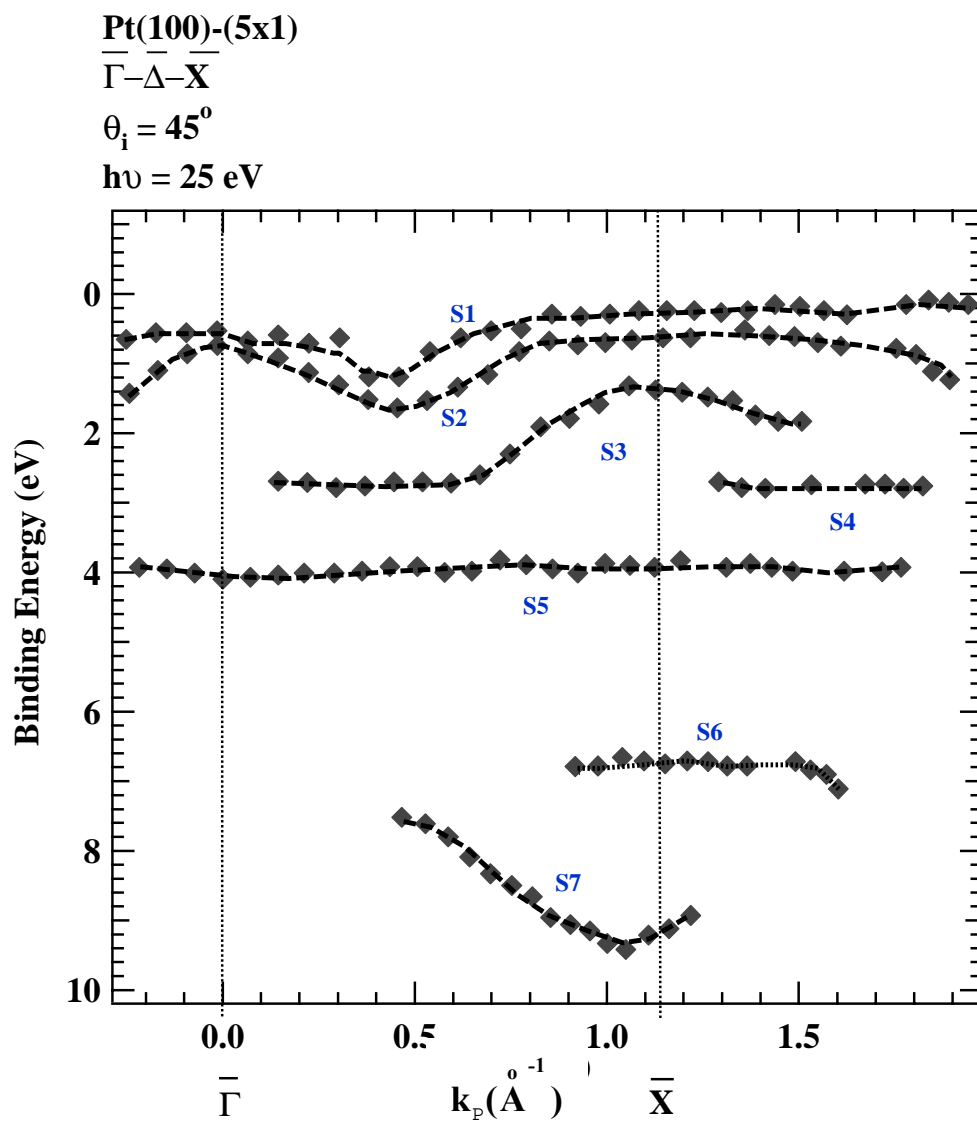
Fig. 3.33 Experimentally determined energy band dispersion of the reconstructed

Pt(5x1) surface along the $\bar{\Gamma}$–$\bar{\Delta}$–$\bar{X}$ direction. Excitation energy was 25 eV.

The first group bands appear to be simpler in the data obtained by excitations at 25 eV. Slightly complicated aspect in the data obtained by excitations at 21 eV is caused by the splitting of the *S1* band in the region around $k_\parallel = 0.5 \, \overset{o}{\mathrm{A}}{}^{-1}$. Apart from this, the *S1* and *S2* bands appear similar qualitatively in both figures. Qualitative agreement is also found in case of the *S3* and *S4* bands.

The aspect of the *S5* band is different. In the energy band obtained by excitations at 25 eV does not show dispersion. However, the *S5* band found in the data obtained by excitations at 21 eV is qualitatively different. At present, the cause for this difference cannot be found.

3.2.3 Polarization Dependence and Symmetry of the Surface State

As mention in Chapter I, the photoemission intensity is dependent on the polarization of excitation light. The state whose eigenfunction of which has the mirror symmetry and the node is in the mirror plane is not excited by the light polarized in this plane. The state, whose eigenfunction has the *odd* symmetry with respect to the mirror plane, is not excited with the light polarized perpendicularly to the mirror plane. Also the intensities of the emitted electrons are dependent on the direction of observation with respect to the direction of light polarization. To study the effect of the polarization dependence on photoemission processes, we have investigated the polarization dependence in the off-normal emission mode in the two emission planes containing the $\overline{\Delta}$ and $\overline{\Sigma}$ directions using the two different measurement geometry, $\mathbf{A}_+$ (*Even*) and $\mathbf{A}_\pm$ (*Odd*), as explained in section 1.6.7. The results of the measurement are presented in Figs. 3.34 and 3.35.

Figures 3.34 and 3.35 show EDC's of Pt(1x1) and Pt(5x1) surfaces taken for *Even* (lines) and *Odd* (dots) geometry along the $\overline{\Delta}$ and $\overline{\Sigma}$ directions, respectively. The experiments were carried out by excitations at energy 21 eV for various emission angles. The incidence angle of light was 35°.

In Fig. 3.34, *S*, *B1*, and *B2* are the three main features arising in ARPES spectra for the two kinds of geometry of the (5x1) and (1x1) surface measurements. It can be seen that the results for the two surfaces are the same qualitatively. The intensities of the *S* peaks are dramatically increased with the emission angle in the *Even* and *Odd* spectra. The feature, *B1*, in the *Odd* spectra shows dispersion while the *B1* feature in the *Even* spectra does not. The both *B2* spectra show dispersion neither in *Even* nor *Odd* spectra as increasing the emission angle. They are localized around 4 eV of binding energy. The result different for (5x1) and (1x1) surfaces is that the feature *S* of the *Odd* spectra of the (5x1) surface is higher intensity than that of (1x1) surface.

The result along $\overline{\Sigma}$ direction presented in Fig. 3.31 is different from that for the $\overline{\Delta}$ direction. The features, *B1*, of the *Even* spectra of two surfaces reveal dispersion along the $\overline{\Sigma}$ direction while the *B1* feature in the *Odd* spectra shows dispersion slightly. However, the *B2* feature in spectra for both surfaces symmetry, which is the same as in the $\overline{\Delta}$ direction case. The *B2* feature is localized around 4 eV of binding energy. The *S* feature in the *Odd* spectra occurs also for the (5x1) surface.

From the polarization dependence experiments, it is concluded that the states with their **k**-vectors in a mirror plane of the crystal, the state with either *even* or *odd* with respect to the mirror plane can be excited. With the *Even* geometry only electrons from *even* states would be emitted, whereas with the *Odd* geometry

emission from states with *odd* symmetry would dominate. From the results in Figs. 3.34 and 3.35, it can be seen that, in the (5x1) surface, the *S* feature appears with much larger intensity in *Odd* geometry than in the *Even* geometry. Therefore, we expect that the *S* feature have *odd* symmetry with respect to both emission planes if these planes are not mirror planes in the (5x1) surface structure. Also, it is interesting to note that the symmetry of the *B1* feature in the *Odd* spectra is primarily *odd* along the $\bar{\Delta}$ direction and the *B1* feature is *even* along the $\bar{\Sigma}$ direction for both (1x1) and (5x1) surfaces.

Pt(100) : Even and Odd Symmetry
$\theta_i = 35^o$

$h\upsilon = 21$ eV

—— **Even**
········· **Odd** with Respect to $\overline{\Delta}$ **Mirror Plane**
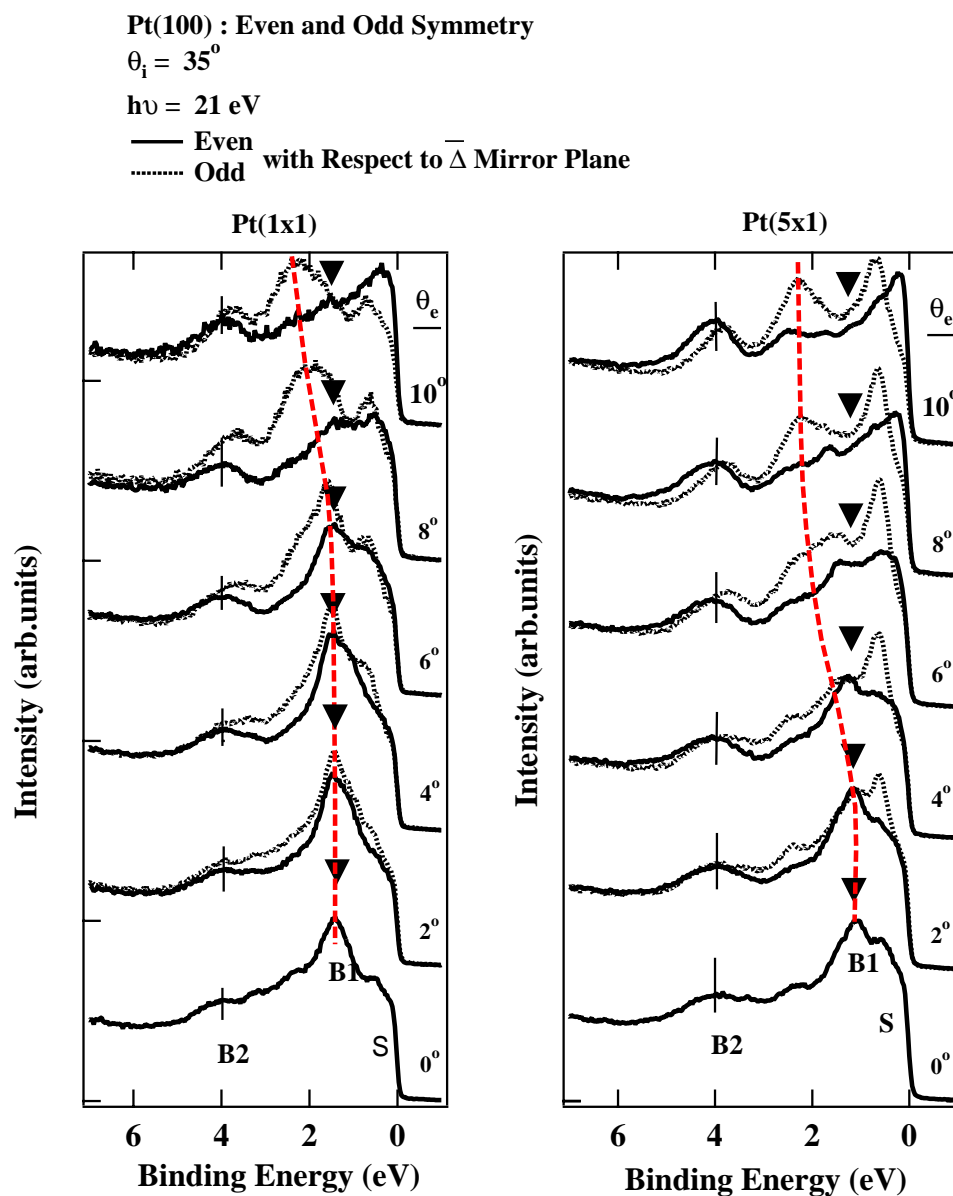
Fig. 3.34 EDC's for *even*-and *odd*-symmetry of Pt(1x1) and Pt(5x1) surfaces along

the $\overline{\Gamma} - \overline{\Delta} - \overline{X}$ direction. The excitation energy was 21 eV and the light

incidence angle was 35°
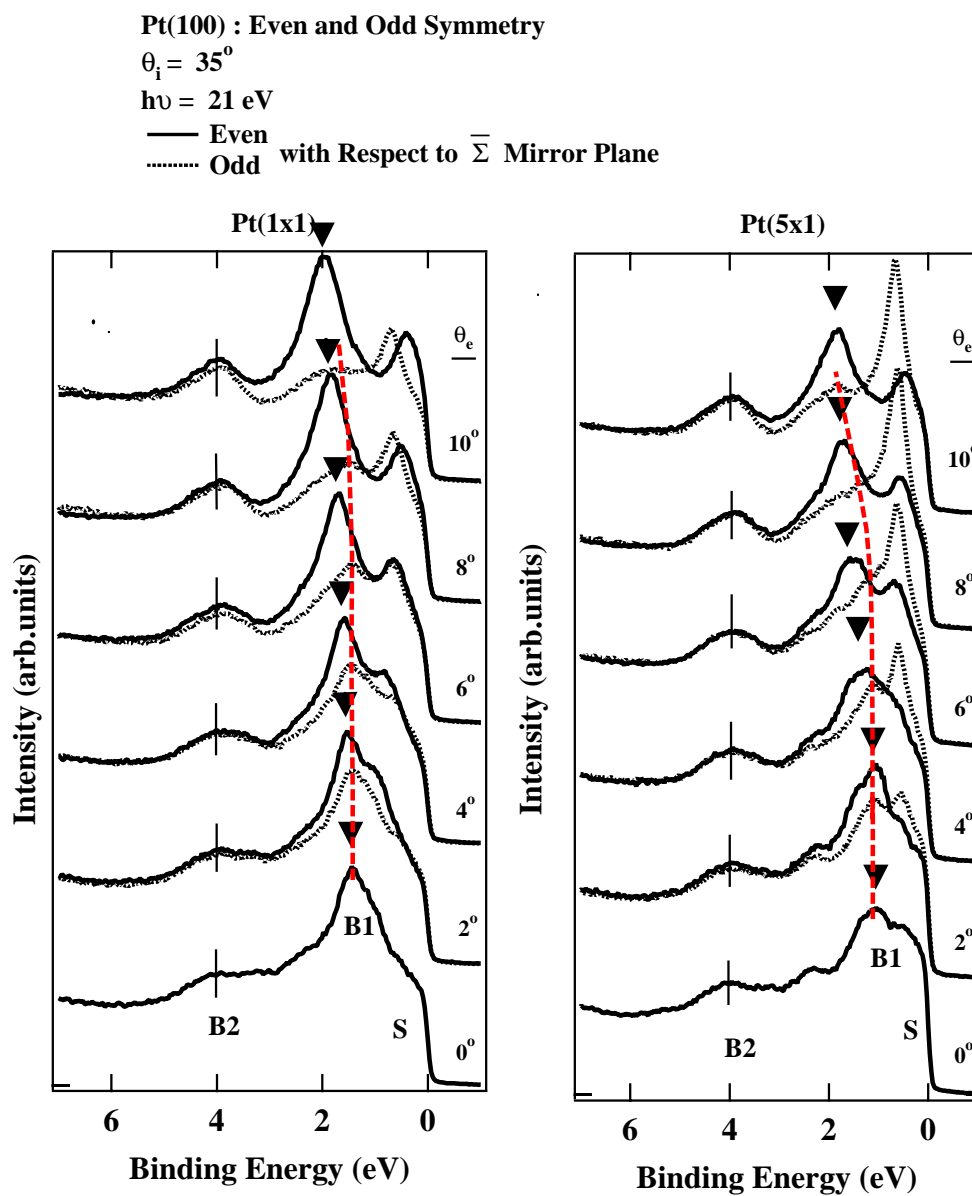
Fig. 3.35 EDC's for even-and odd-symmetry of Pt(1x1) and Pt(5x1) surfaces along the $\overline{\Gamma} - \overline{\Delta} - \overline{M}$ direction. The excitation energy was 21 eV and the light incidence angle was 35°.

Chapter IV

Discussion and Conclusion

The main purpose of this work is to obtain the energy band structure of the Pt (100)-(1x1) and -(5x1) surfaces. The obtained information is fundamental for understanding the electronic properties relevant surfaces. Some theoretical and experimental data have been reported on the energy band structure of both surfaces. Thus, it is important to compare the data obtained in this work with those reported so far. In what follows, such comparisons are made.

4.1 Obtained Data

By ARPES analyses, the following data have been obtained:

(1) Energy band map

- By normal emission mode measurements (bulk).

  Varied photon energy excitation.

  - Pt(100)-(1x1), along $\Gamma - \Delta - X$ axis

  - Pt(100)-(5x1), along $\Gamma - \Delta - X$ axis

- By varied emission angle mode measurements (surface).

  Fixed excitation energy.

- Pt(100)-(1x1), 21 eV excitations, along the $\overline{\Gamma}-\overline{\Sigma}-\overline{M}$ axis

- Pt(100)-(1x1), 21 eV excitations, along the $\overline{\Gamma}-\overline{\Delta}-\overline{X}$ axis

- Pt(100)-(1x1), 25 eV excitations, along the $\overline{\Gamma}-\overline{\Sigma}-\overline{M}$ axis

- Pt(100)-(1x1), 25 eV excitations, along the $\overline{\Gamma}-\overline{\Delta}-\overline{X}$ axis

- Pt(100)-(5x1), 21 eV excitations, along the $\overline{\Gamma}-\overline{\Sigma}-\overline{M}$ axis

- Pt(100)-(5x1), 21 eV excitations, along the $\overline{\Gamma}-\overline{\Delta}-\overline{X}$ axis

- Pt(100)-(5x1), 25 eV excitations, along the $\overline{\Gamma}-\overline{\Sigma}-\overline{M}$ axis

- Pt(100)-(5x1), 25 eV excitations, along the $\overline{\Gamma}-\overline{\Delta}-\overline{X}$ axis

- Parity consideration

Dependence of emission intensities on the polarization direction of excitation light.

Excitation energy is fixed at 21 eV. Varied emission angle.

- Pt(100)-(1x1), even coordination against the $\overline{\Delta}$ mirror plane, along the $\overline{\Gamma}-\overline{\Delta}-\overline{X}$ axis

- Pt(100)-(1x1), odd coordination against the $\overline{\Delta}$ mirror plane, along the $\overline{\Gamma}-\overline{\Delta}-\overline{X}$ axis

- Pt(100)-(5x1), even coordination against the $\overline{\Delta}$ mirror plane, along the $\overline{\Gamma}-\overline{\Delta}-\overline{X}$ axis

- Pt(100)-(5x1), odd coordination against the $\overline{\Delta}$ mirror plane, along the $\overline{\Gamma}-\overline{\Delta}-\overline{X}$ axis

- Pt(100)-(1x1), even coordination against the $\overline{\Sigma}$ mirror plane, along the $\overline{\Gamma}-\overline{\Sigma}-\overline{M}$ axis

- Pt(100)-(1x1), odd coordination against the $\bar{\Sigma}$ mirror plane, along the $\bar{\Gamma}-\bar{\Sigma}-\bar{M}$ axis

- Pt(100)-(5x1), even coordination against the $\bar{\Sigma}$ mirror plane, along the $\bar{\Gamma}-\bar{\Sigma}-\bar{M}$ axis

- Pt(100)-(5x1), odd coordination against the $\bar{\Sigma}$ mirror plane, along the $\bar{\Gamma}-\bar{\Sigma}-\bar{M}$ axis

4.2 Problems

We have found some aspects of the data that cannot be explained simply. For facilitating the discussion that is made in this chapter, such issues are summarized in the following:

(1) The bulk energy bands obtained by the measurements in the normal emission mode cover the $\mathbf{k}$ region along the Δ axis less than 50%, the surface reconstruction is found to affect the bulk band in the observed region in the Brillouin zone.

(2) Features appear at constant $\mathbf{k}$ values. The locations are not affected by the excitation energy.

(3) Even in case of the bulk energy bands, the surface reconstruction changes the band structure quantitatively. In the present work, the energy bands are measured on the (1x1) and (5x1) structures. As far as the bulk bands along the Δ axis is concerned the surface structure change by 20% cannot much affect the band structure.

(4) In all surface energy band obtained here, i.e., the bands along the $\bar{\Sigma}$ and $\bar{\Delta}$ axes for the (5x1) and (1x1) surface structures, clear difference of the band structure is found between the data obtained with excitations at 21 eV and those at 25 eV.

(5) The obtained energy band structures does not coincide well with the calculated ones reported so far. This issue shall be discussed later.

4.3 Discussion

4.3.1 Normal Emission Band Structure

First, we consider the observation that the bulk band structure along the Δ axis is affected by the surface reconstruction. In the three step model, the photoelectron number arriving at the surface is given as (1.56). If we write $l\cos\boldsymbol{q}$ as l using the average over $\boldsymbol{q}$ for simplicity and integrate over $d\Omega$, the number of photoelectrons coming out from the layer dz at z is given as.

$$N = I_o \boldsymbol{h} \exp\left\{-\left(\boldsymbol{h}\hat{l}+1\right)\frac{d}{\hat{l}}\right\},$$ (4.1)

where, $\hat{l}$ is the effective escape depth and $\boldsymbol{h}$ is the absorption coefficient.

The fraction, F, of the number of primary photoelectrons coming out of the layer at the surface with thickness d is given as

$$F = \frac{\int_0^d N dz}{\int_0^\infty N dz} = \frac{\left[\boldsymbol{h}\hat{l}/\left(\boldsymbol{h}\hat{l}+1\right)\right]\left(1-e^{-\left(h\hat{l}+1\right)d/\hat{l}}\right)}{\left[\boldsymbol{h}\hat{l}/\left(\boldsymbol{h}\hat{l}+1\right)\right]}$$

$$= 1 - e^{-\left(h\hat{l}+1\right)d/\hat{l}}.$$ (4.2)

Since $\boldsymbol{h}=1$, F is written as

$$F = 1 - e^{-d/\hat{l}}.$$ (4.3)

We assume that the effective escape depth is 8 $\overset{\text{o}}{\text{A}}$ as discussed in section 1.6.2. Since the lattice constant of Pt is about 4 $\overset{\text{o}}{\text{A}}$, the first surface layer takes ½ as the value of $d / \hat{l}$. We summarize the value of F given in (4.3) as well as that of (1-F) to represent the bulk contribution in table 4.1.

Table 4.1 Fraction of the number of photoelectrons from the layer at the surface and of the bulk contribution.

Number of atomic layers	1	2	3	4	5	6	7
Value of $d / \hat{l}$	0.5	1.0	1.5	2.0	2.5	3.0	3.5
F (surface)	0.39	0.63	0.78	0.86	0.92	0.95	0.97
F (bulk) = 1-F (surface)	0.61	0.37	0.22	0.14	0.08	0.05	0.03

Table 4.1 shows that 39% of primary photoelectrons are coming out of the first atomic layer at the surface. Another 39% of primary photoelectrons are from the second and third layers and 78% of primary photoelectrons are from the first three atomic layers from the surface. If we consider that the bulk energy bands are found by electrons in the region down from the second atomic layer, the majority of the bulk energy band photoemission occurs in the second and third layers.

If the surface is reconstructed, it is natural to assume that the electronic potential as well as the atomic structure in the second layer is affected by the

reconstruction. The third layer may not be much affected but slight effect may remain there. This situation is the cause of the observed effect of the surface reconstruction on the bulk energy band structure.

In EDCs obtained by measurements in the normal emission mode, weak bands occur at constant kinetic energies. In the previous chapter, we attribute the emission bands to scattered and thermalized. As in Fig. 1.34, the assumption of a parabolic band for excited electrons well explains the normal emission spectra. However, the assumption of the parabolic band is based on the following situation.

Consider the energy bands in the extended zone scheme. Suppose an electron in the first Brillouin zone is excited to the bands in the second or third Brillouin zone. If this situation is treated in the reduced zone scheme, there are many bands that can accept the excited electron in the first Brillouin zone. They are found by folding the excited state bands in the second and the third zone to the first Brillouin zone. If we take the experimental resolution in both energy and momentum, the equi-energy surface that can accept excited electrons cover the whole first Brillouin zone. Therefore, the assumption of the single parabolic band makes sense since the band has complete spherical symmetry.

If we consider the scheme described above, the energy bands that have the shape different from one shown schematically in Fig. 1.34 must exist. Suppose the bands are those shown in Fig. 4.1 representative manner. The e_1 and e_2 bands in Fig. 4.1 is assumed to be such bands. Excited electrons are scattered either by electrons or phonons. The scattering reduces electron energies until the electrons come to the band minima, where the electrons cannot loose energies by that scattering that let electrons stay in the same bands. We call the electrons falling in the band minima the
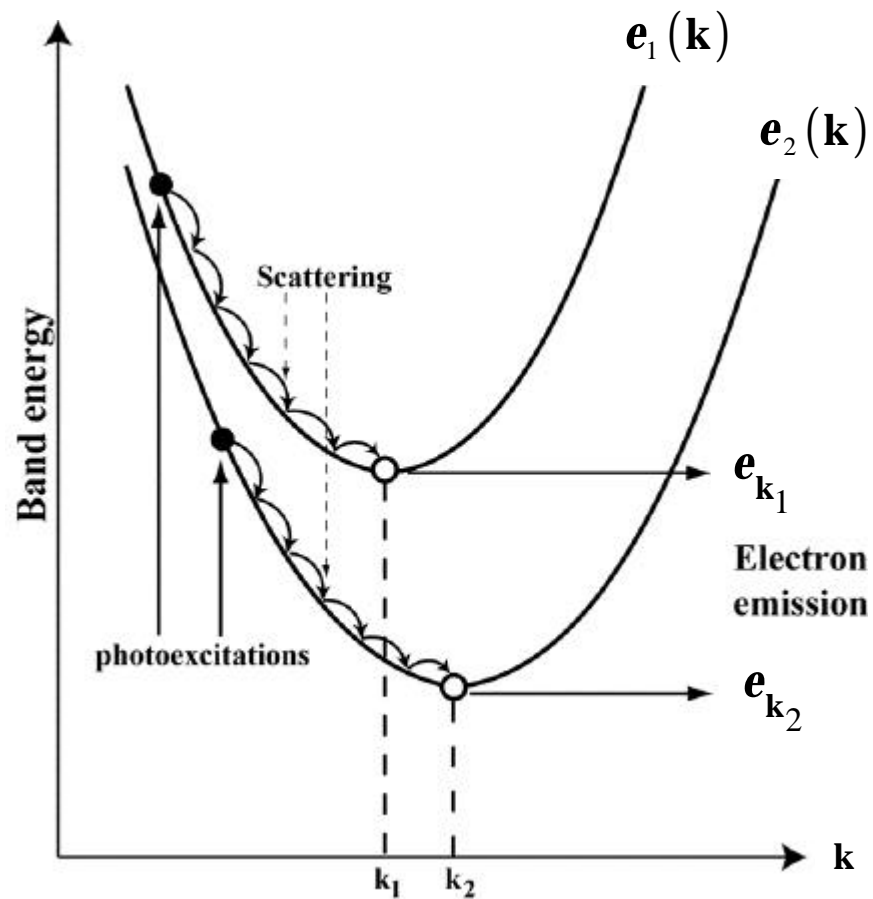
Fig. 4.1 Explanation of thermalization of excited electrons. Excited electrons are scattered fast until they are thermalized at band minima $\left(e(\mathbf{k}_1),\mathbf{k}_1; e(\mathbf{k}_2),\mathbf{k}_2\right)$. Thermalized electrons are ejected out of the sample.

thermalized electrons. This scattering occurs fast. Obviously, the thermalized electrons have longer lifetime than electrons not thermalized. Thus the thermalized electrons have the higher probability to escape the sample.

Since the band minima occur at fixed energies and fixed momenta. Thus, we observe thermalized electrons at constant kinetic energies and momenta. The process described above is similar to the idea of the adiabatic potential explanation of the Stokes shift of the fluorescence line.

For ARPES recorded by means of the normal electron emission, the interpretation of experimental data is made based on determination of the possible direct transitions between the bulk energy bands along the high symmetry direction specified by the surface normal. Peaks that disperse with photon energy in normal emission spectra are generally interpreted as representing the energy band dispersion. In the present work, we measured EDCs on a fcc Pt single crystal with the (100) surface. Therefore, the rod into the bulk Brillouin zone extends along the Γ to X direction. Accordingly, electrons with $\mathbf{k}$ vector in the [100] direction in the $\mathbf{k}$ are excited. This is the Δ axis in the Brillouin zone. Obviously, the symmetry of the state we observe is the Δ symmetry. The energy bands along Δ axis are classified into 4 bands. They are called $\Delta_1, \Delta_2, \Delta_{2'}$ and Δ_5. In Pt $5d$ electrons give rise to eigenfunctions, Bloch functions, either of the "*odd*" which is made of the linear combination of the d_{xy}, d_{xz}, and d_{yz} functions or of the "*even*" type arising from d_{x^2}, d_{y^2}, and d_{z^2} functions. The Δ_1 state is formed by the "*even*" type functions (*s*-symmetry). The Δ_5 state is formed by the "*odd*" type functions (*p*-symmetry). If the final state is the Δ_1 state, the dipole excitation restricts the possible initial state bands to Δ_1 and Δ_5

symmetries. For the clean fcc (100) surface, with perfectly *s*-polarized light ($\mathbf{A} \perp$ [100]), the allowed initial states are Δ_5 symmetry, with perfectly *p*-polarized light ($\mathbf{A} \parallel$ [100]), the allowed initial states are of the Δ_1 symmetry instead. Dipole selection rules for the normal emission of fcc crystal are summarized in table 4.2.

Table 4.2 Dipole allowed initial state symmetries for normal emission of fcc crystals (Hermanson, 1977). For each face the irreducible representations of the initial states and the final states are listed in single group notation. $\mathbf{A}$ is the vector potential of the incident light.

Crystal face	Axis			Allowed final state	Initial state		
	x	**y**	**z**		$\mathbf{A} \parallel \mathbf{x}$	$\mathbf{A} \parallel \mathbf{y}$	$\mathbf{A} \parallel \mathbf{z}$
(001)	$[100]$	$[010]$	$[001]$	Δ_1	Δ_5	Δ_5	Δ_1
(110)	$[001]$	$[1\bar{1}0]$	$[110]$	Σ_1	Σ_3	Σ_4	Σ_1
(111)	$[01\bar{1}]$	$[2\bar{1}\bar{1}]$	$[111]$	Λ_1	Λ_3	Λ_3	Λ_1

Our results of the comparison of the experimental band structure measured with *s*-and *p*-polarized light with the calculated band structure are shown in Figs. 4.2 and 4.3, respectively. In Fig. 4.2, the bulk band structure of Pt(100) obtained by the measurements in the normal emission mode. An incident angle of light, $\mathbf{q} = 35^{\circ}$, (*s*-polarized geometry) was employed. The photon energy, $h\mathbf{n}$, ranges from 15 eV to 30 eV. The abscissa represents the wave vector perpendicular to the surface ($k_{\perp}$) in inverse $\overset{\circ}{\mathrm{A}}$ngstrong($\overset{\circ}{\mathrm{A}}{}^{-1}$). The ordinate represents the binding energy of electron in

electron volt (eV). The asterisks represent the energy bands measured on the sample with the clean reconstructed (5x1) surface and the solid squares represent the energy bands of the sample with the unreconstructed (1x1) surface. The solid lines are theoretical bands calculated by Noffke and Eckardt, using the fully relativistic self-consistent method. This calculation is based on the Kohn-Sham one particle scheme using the exchange-correlation potential of Gunnarsson (Gunnasson, Lundqvist and Wilkins, 1974). The bands have been calculated by the linear rigorous cellular (LRC) method of Fritsche (Fritsche, Rafat, Glocker and Noffke, 1979) for energy $\boldsymbol{e} < \boldsymbol{e}_F$ and by the linearized augmented plane wave (LAPW) method for $\boldsymbol{e} > \boldsymbol{e}_F$.

If the calculated energy bands are available, we can analyze the experimentally observed $\boldsymbol{e}(\mathbf{k})$ dispersion curve though the comparison with the theoretically calculated $\boldsymbol{e}(\mathbf{k})$ curve in the analysis of the $\boldsymbol{e}(\mathbf{k})$ dispersion curve. In Figs. 4.2 and 4.3, such comparison is made. In the figures, the energy bands calculated by Noffke and Eckart are shown by solid lines. The bands are calculated along the Δ axis and independent of the surface structure in principle. Thus, the same calculated bands are shown in Figs. 4.2 and 4.3. In Fig. 4.2, data points shown with squares represent the bands along the Δ axis measured on the (100)-(1x1) surface and those shown with asterisks represent the bands along the Δ axis measured on the (100)-(5x1) surface.

In both figures, the bands with considerable dispersion are observed around the region $k_\perp = 0.35\text{-}1.0 \ \overset{\mathrm{o}}{\mathrm{A}}{}^{-1}$ and $\boldsymbol{e}_B = 1 - 4$ eV. These bands correspond to *D4* band

($k_\perp = 0.35$-1.0 $\overset{o}{A}{}^{-1}$) named in Figs. 3.3 and 3.4. They show the weakest density of state features.

In the comparison of the experimentally observed bands with those of theoretically calculated bands, we have to select the appropriate energy bands calculated theoretically. A few pieces of energy band calculation have been reported on Pt so far. Since the platinum mass is large, the spin-orbit interaction is not negligible and the energy band calculation is made on this metal using a relativistic approximation.   The results of calculations by different authors are similar qualitatively. Even in the quantitative manner, there is no crucial difference except in the region near the Fermi level. Since we are not concerned with the Fermi surface as in the case of the analysis of measurements of the deHaas-van alphen effect. Therefore we use the theoretical energy bands calculated by Noffke and Eckart in Figs. 4.2 and 4.3.

Before we discuss the comparison of the observed bands with the calculated bands, we remark the effect of the surface reconstruction. In Figs. 4.2 and 4.3, it is recognized that the surface reconstruction does not much affect the energy bands along the Δ axis. However, quantitative difference is found in some bands. The difference is more pronounced in the data measured with p-polarized light.   As already pointed out in the previous chapter, we find from the data shown in Figs. 4.2 and 4.4 that the bulk potential change caused by the surface reconstruction in a few atomic layers near the surface is appreciable.   However, the majority of the bands are not affected, as the bulk bands should be.

If we compared our observed bands with the calculated bands, we find that qualitative disagreement exist between both kinds of the bands. The bulk energy band

structure has been measured by a few investigators. However, most of the measurements were carried out along the Λ axis, i.e., along the $\langle 111 \rangle$ direction (Leschik et al., 1984; Wern, Courths, Leschik and Hüfner, 1985; Garbe and Kirschner, 1989). The reported energy band structure in this case agrees well with the calculated energy band structure. The data along the Δ axis are found in the report by Thornton et al. (1980) and Leschik et al. (1984). Their data appear to agree with the calculated bands.

If we compare our observed data with the theoretical data, the source of the disagreement appears to be inherent in the range of crystal momentum $k_\perp$ in the observed band, the observed $\boldsymbol{e}(\mathbf{k})$ dispersion curves change more toward the tendency of $\boldsymbol{e}(\mathbf{k})$ calculated theoretically. In obtaining experimental $\boldsymbol{e}(\mathbf{k})$ curve, we used the relation (1.109). We used V_o only as an adjustable parameter. However, the selection of the value of V_o cannot alter the range of the $\mathbf{k}$ value. This is obvious from the relation (1.108). Suppose the value of $k_\perp$ corresponding to the observed values of $\boldsymbol{e}_k$ given as $\boldsymbol{e}_1$ and $\boldsymbol{e}_2$ to be k_1 and k_2 respectively. Then we have from (1.108)

$$k_1^2 - k_2^2 = \frac{\sqrt{2m}}{\hbar}\left(\boldsymbol{e}_1 - \boldsymbol{e}_2\right). \tag{4.4}$$

Relation (4.4) indicates that the range of $k_\perp^2$ is not affected by V_o. The value of V_o affects the location of $k_\perp$.

Relation (4.4) shows that the span of the $\boldsymbol{e}(\mathbf{k})$ curve obtained from the observed values of $\boldsymbol{e}_k$ is altered by the value of the electron mass, m. In obtaining the

$e(\mathbf{k})$ curves shown in Figs. 4.2 and 4.3 we used the relation, (1.109), as mentioned already. There, the value of the free electron mass is used. Relation (4.4) indicates that the value of m affects the span of the $e(\mathbf{k})$ curve as

$$\Delta k \equiv k_{\mathrm{max}} - k_{\mathrm{min}} = \frac{1}{\hbar k_o} \cdot \sqrt{\frac{m}{2}} \Delta e, \qquad (4.5)$$

where $k_o \equiv (k_{\mathrm{max}} + k_{\mathrm{min}})/2$ is the value of $k_\perp$ at the center of the band and Δe is the range of e_k. If we select V_o so that the value of k_o is unchanged, the relation (4.5) gives

$$\frac{\Delta k}{\Delta k_{ob}} = \sqrt{\frac{m}{m_o}}, \qquad (4.6)$$

where Δk_{ob} is the observed energy band distribution (the distribution of the value of $\mathbf{k}$). From the results shown in Figs 4.2 and 4.3, we will obtained better coincidence of the energy band distribution with the theoretically calculated energy band distribution if the value $\Delta k / \Delta k_{ob}$ is 1.3. This requires the ratio of the mass to be 1.7. Thus, we need to use the mass value about 70% larger than the free electron mass. We do not know if this suggests the collapse of the free electron energy approximation for the final state photoelectrons.

As mentioned already, parameter V_o originating in the crystal potential, E_o, as given in (1.103), does not much affect the spans of the observed energy bands. From (1.108), we have

$$k_{\perp max} = \frac{1}{\hbar}\sqrt{2m(\boldsymbol{e}_{kmax} + V_o)}$$

$$k_{\perp min} = \frac{1}{\hbar}\sqrt{2m(\boldsymbol{e}_{kmin} + V_o)}.$$

Then, we have

$$\left(\frac{k_{\perp max}}{k_{\perp min}}\right)^2 = \frac{(\boldsymbol{e}_{kmax} + V_o)}{(\boldsymbol{e}_{kmin} + V_o)}. \qquad (4.7)$$

If we insert $\boldsymbol{e}_{kmax}$ and $\boldsymbol{e}_{kmin}$ obtained from the measured value as shown in Figs. 3.3 and 3.4 and select the ratio, $(k_{\perp max} / k_{\perp min})^2$, so as to make the values of $k_{\perp max}$ and $k_{\perp min}$ meet the calculated energy band spans, we obtain the negative value of V_o, which is not reasonable.

The origin of the qualitative disagreement we found here between the measured and calculated energy bands are not known. One possibility is that the cause is inherent in the characteristics of the electron energy analyzer we used for the measurements. The electron lens attached to it reject the electrons of low kinetic energies. Therefore we cannot observe electrons with light binding energies. Another possible cause is the collapse of the free electron approximation of the photoelectron final states. Tamura et al. (1989) and Drube et al. (1988) have suggested that the photoemission spectra of Pt should be analyzed by assuming the realistic final state energy band. However, the discrepancy of the energy band cannot be explained by this. Thornton et al. (1980) used the value, 1.15 m_o, as the electron mass in the nearly free electron approximation in the final state of photoemission and found better agreement of the experimentally observed bands and theoretically calculated bands.

The experimental band structures of clean Pt(100) in normal emission mode has been reported only by Thornton et al (1980). They have determined the valence-band structure between Ã to X by analysis of direct transition features in the ARPES spectra were taken in the range 6 eV ≤ $h\boldsymbol{n}$ ≤ 32 eV with p-polarized light ($\boldsymbol{q}$ = 63°). Comparison the present results with those reported by Thornton et al. is depicted in Fig. 4.4. The circles represent the experimental band structure of Thornton et al. The downward triangles are present experimental band structure obtained by excitations with p-polarized light on Pt(100)-(5x1) surface. As mentioned before, the spans of the energy bands are too narrow in the present work. If this point is corrected, the present work is in agreement with the work of Thornton et al., as seen in Fig. 4.4. Since their work is good agreement with the calculated bands, our data will also agrees with the theoretical band if the band span is corrected.

One remarkable aspect of the observed energy band is that the energy bands are dependent on the polarization of excitation light. As mentioned already, the light polarization dependence is introduced through the excitation cross section and the energy levels are not affected by the polarization direction of excitation light. This issue is also puzzling.

Since the qualitative disagreement is found between the observed energy bands and the calculated ones, quantitative comparison of the observed energy bands with the calculated ones does not makes sense. However, one aspect is worth mentioning. In the present data, no features to be compared with the calculated bands are found below 5 eV. In the calculation bands, the $\ddot{A}_6^+$ band occurs in the region between 7 eV and 10 eV in the binding energy. Also a band extending from 4 eV to
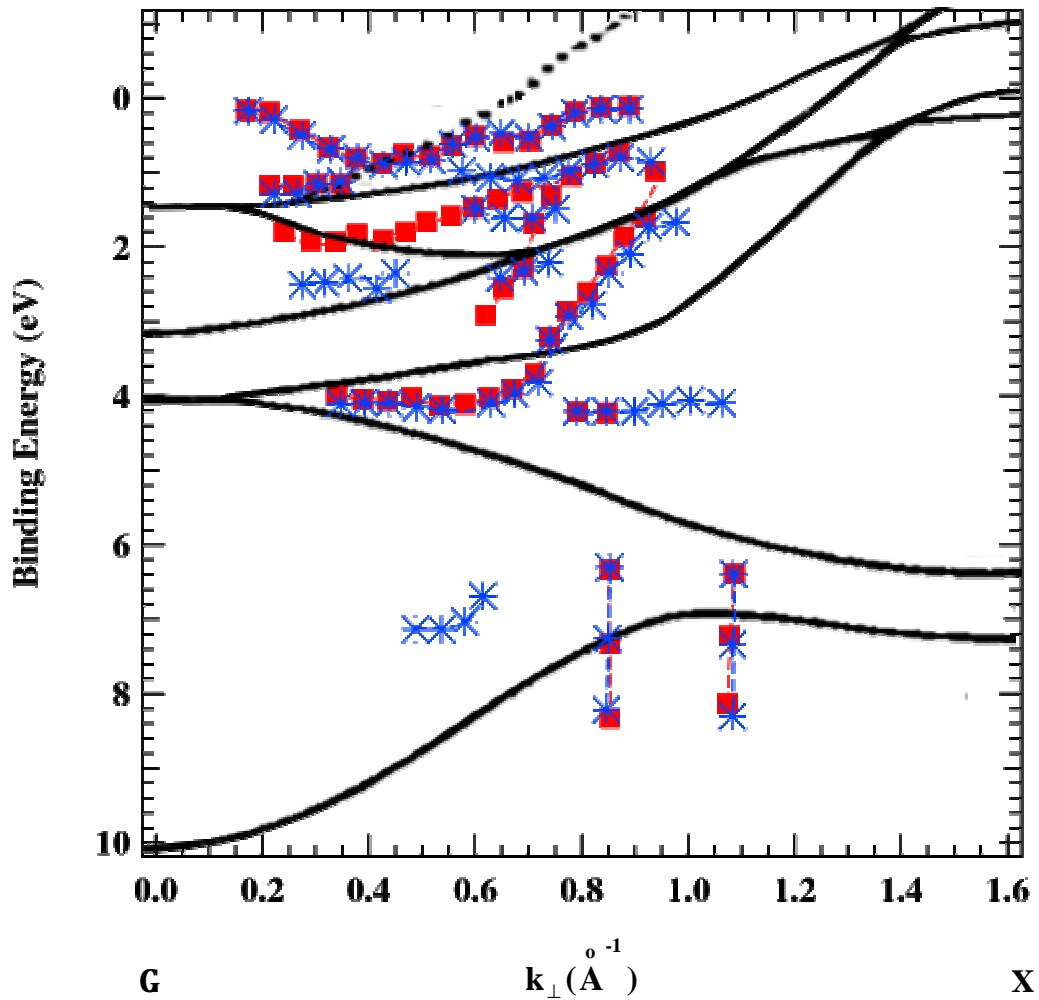
Fig. 4.2 The experimental bulk band structure of Pt measured on the (100) surface along Δ axis (Γ-X direction) with *s*-polarized light. The data points shown by squares represent the bands measured on the (1x1) surface and the asterisks represent the bands measured on the (5x1) surface. The solid lines are theoretical bulk bands calculated by Noffke and Eckardt.
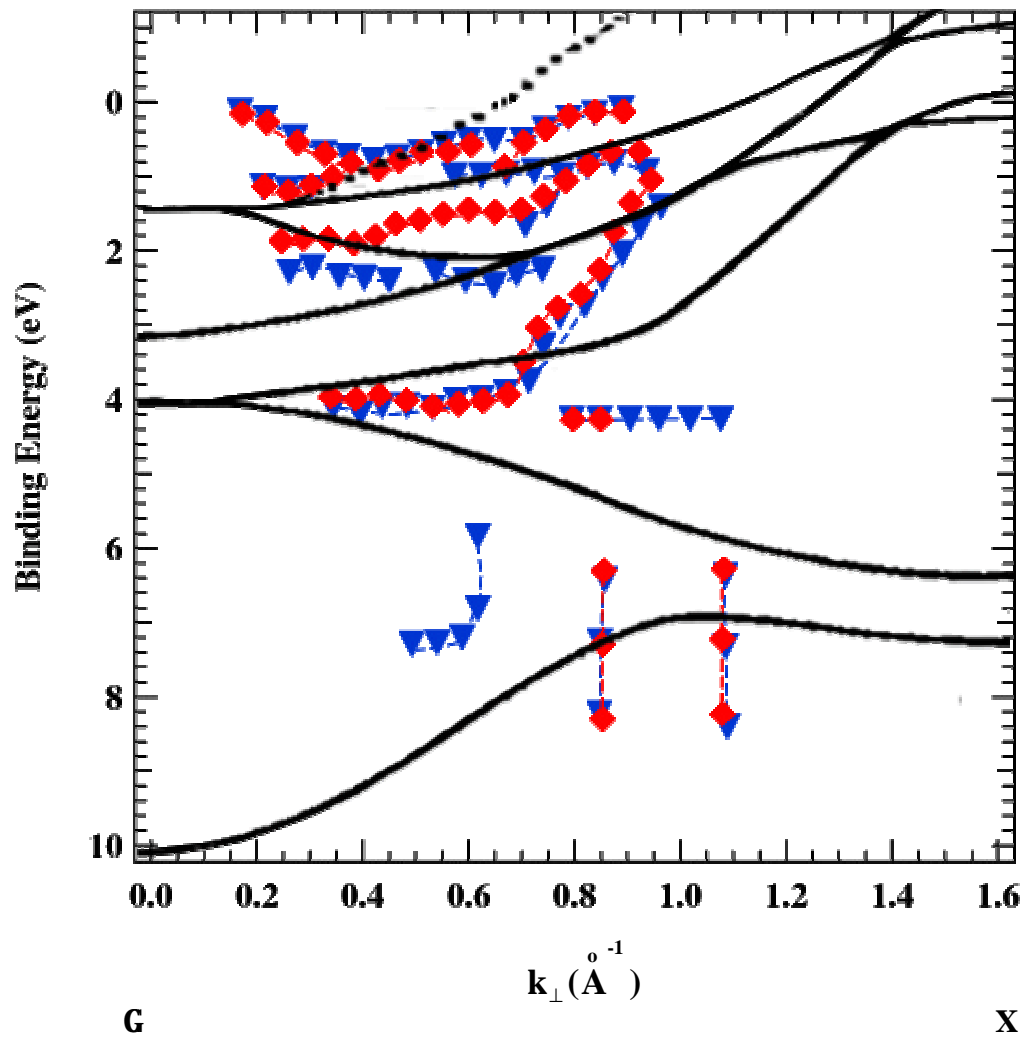
Fig. 4.3 The experimental bulk band structure of Pt measured on the (100) surface along Δ axis (Γ-X direction) with *p*-polarized light. The data points shown by squares represent the bands measured on the (1x1) surface. The downward triangles are the bands obtained on the (5x1) surface. The solid lines are theoretical bulk bands calculated by Noffke and Eckardt.
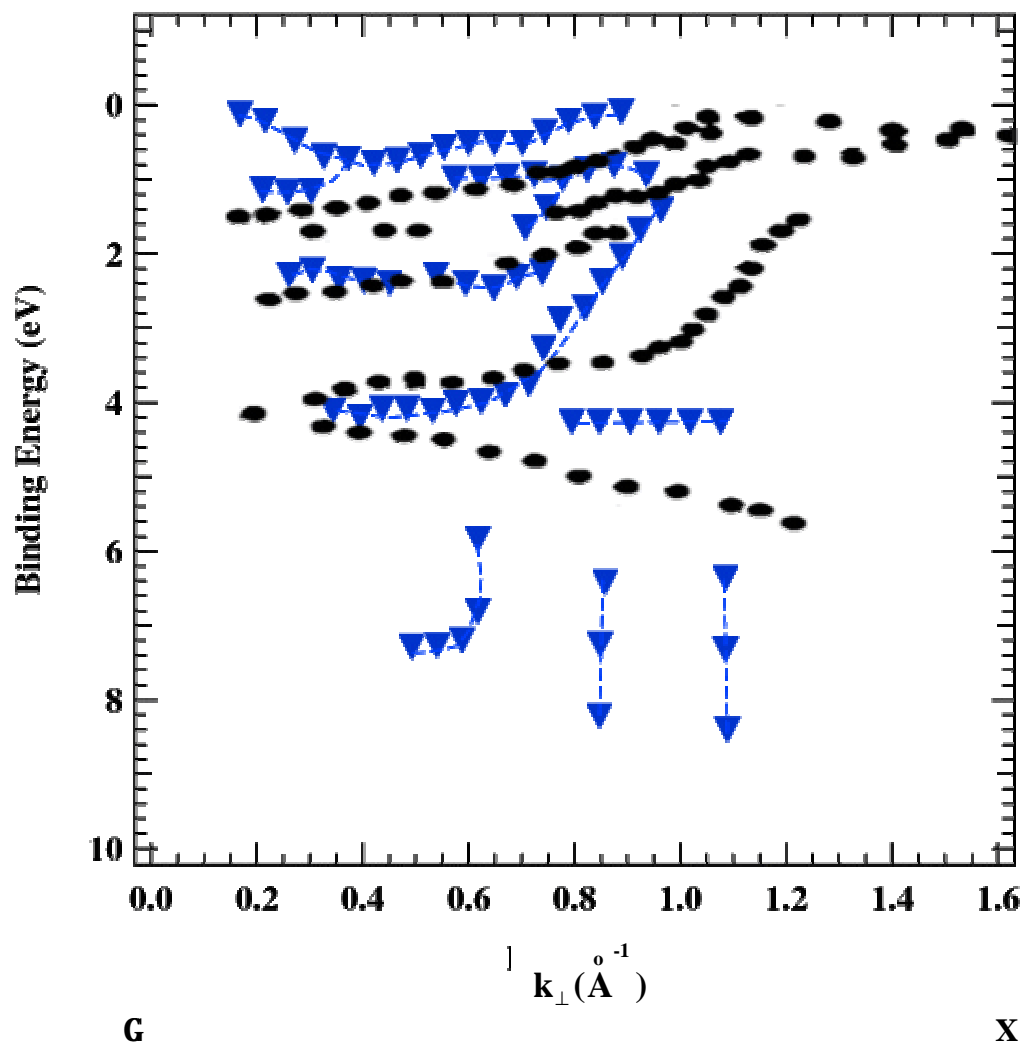
Fig. 4.4 The experimental bulk band structure of Pt(5x1) surface along Δ axis (Γ-X direction). The downward triangles represent our work with *p*-polarized light *(q = 60°)* in energy range 15 eV $\leq h\boldsymbol{n} \leq$ 30 eV. The circles represent the Thornton's work with *p*-polarized light *(q = 65°)* in photon energy range 6 eV $\leq h\boldsymbol{n} \leq$ 32 eV.

6 eV (Δ_7^+ band) exists. The Δ_6^+ band corresponds to the Δ_1 band in the single group

representation (omitting the spin-orbit interaction) and arises from the s states. Such a

deep band cannot be detected in the present measurements because of the low

excitation cross section and the strong retardation of photoelectrons with the

corresponding kinetic energies by the electron lens attached to the energy analyzer.

4.3.2 Surface Band Structure

In the investigation of the surface band structure in present work, EDC's were

recorded at selected excitation energies of 21 and 25 eV. Emission angles were

varied so that $k_{\square}$ is scanned along the high symmetry lines, $\overline{\Gamma} - \overline{\Delta} - \overline{X}$ and $\overline{\Gamma} - \overline{\Sigma} - \overline{M}$

directions on the surface Brillouin zone of Pt(100) surfaces. A necessary condition for

assigning observed structure to be of surface origin is the determination of its two

dimensionality in the wave vector dependence on the initial state energy and the

inspection of the sensitivity to impurities. A surface related structure must not show

change in its $\varepsilon_B(k_{\square})$ dispersion when the photon energy and thus the $k_\perp$ value are

changed. In this section, we will look into the data obtained by fixing photon energy

and varying the emission angle. The band structures obtained by clearing these

conditions are the band structures with the two-dimensional or surface band nature.

Because the main purpose of this work is to find the difference in electronic

structure between the reconstructed (5x1) and unreconstructed (1x1) phases of clean

Pt(100) surfaces, the comparison of experimental band structures between two

surfaces are performed as shown in Figs. 4.5, 4.6, 4.7 and 4.8. In these Figs., the

theoretical bulk band structures calculated by Noffke and Eckared are also presented

so as to compare the experimental surface band structures. The comparison with the
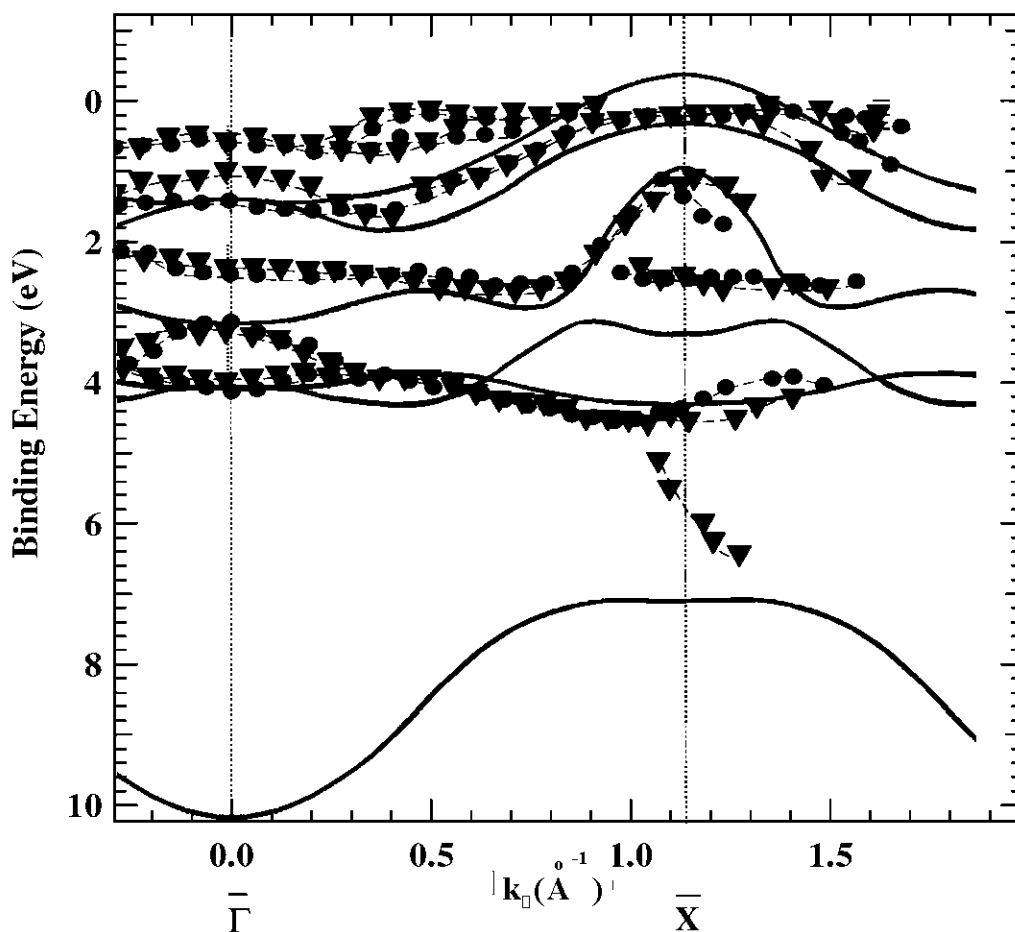
Fig. 4.5 The experimental surface band structure of Pt(100) surface along the $\overline{\Delta}$ axis $\left(\overline{\Gamma}-\overline{X} \text{ direction}\right)$ obtained by excitation at $h\nu = 21$ eV. The circles represent the band from (1x1) structure. The downward triangles represent the band of the surface with the (5x1) structure. The solid lines are the theoretical bulk bands calculated by Noffke and Eckardt (Leschik et al., 1984).

215

Fig. 4.6 The experimental surface band structure of Pt(100) surface along the $\overline{\Delta}$ axis

($\overline{\Gamma} - \overline{X}$ direction) obtained by excitation at $h\nu = 25$ eV. The crosses

represent the bands of the surface with the (1x1) structure. The

parallelograms represent the bands of the surface with the (5x1) structure.

The solid lines are the theoretical bulk bands calculated by Noffke and

Eckardt (Leschik et al., 1984).

Fig. 4.7 The experimental surface band structure of Pt(100) surface along the $\overline{\Sigma}$ axis

($\overline{\Gamma} - \overline{M}$ direction) obtained by excitation at $h\nu$ = 21 eV. The circles

represent the band of the surface with the (1x1) structure. The downward

triangles represent the band of the surface with the (5x1) structure. The solid

lines are the theoretical bulk bands calculated by Noffke and Eckardt

(Leschik et al., 1984).

Fig. 4.8 The experimental surface band structure of Pt(100) surface along $\overline{\Sigma}$ axis $\left(\overline{\Gamma} - \overline{M}\ \text{direction}\right)$ obtained by excitation at $hv = 25$ eV. The crosses represent the bands of the surface with the (1x1) structure. The parallelograms represent the bands of the surface with the (5x1) structure. The solid lines are the theoretical bulk bands calculated by Noffke and Eckardt (Leschik et al., 1984).

bulk band makes sense, since the majority of photoelectrons is excited from the bulk band.

Figure 4.5 are the surface band structure of Pt(100)-(1x1) and -(5x1) surfaces measured along the $\overline{\Gamma} - \overline{\Delta} - \overline{X}$ direction with excitation energy 21 eV. From Fig. 4.5, it is clear that the surface band structures measured on both surfaces almost correspond each other. However, disagreement is found for the high binding energy band, around the $\overline{X}$ point. This band appears only in the (5x1) phase. Also, a small of disagreement is found for the second band from the Fermi edge around the $\overline{\Gamma}$ point.

In the spectra obtained by excitation at 25 eV, disagreement between the measured bands of the surfaces of the (5x1) and (1x1) phases are found around the $\overline{\Gamma}$ point for bands near the Fermi edge, (as show in Fig. 4.5). Through extensive comparison of the present data with theoretical bulk band structure calculated by Noffke and Eckard, it is found tha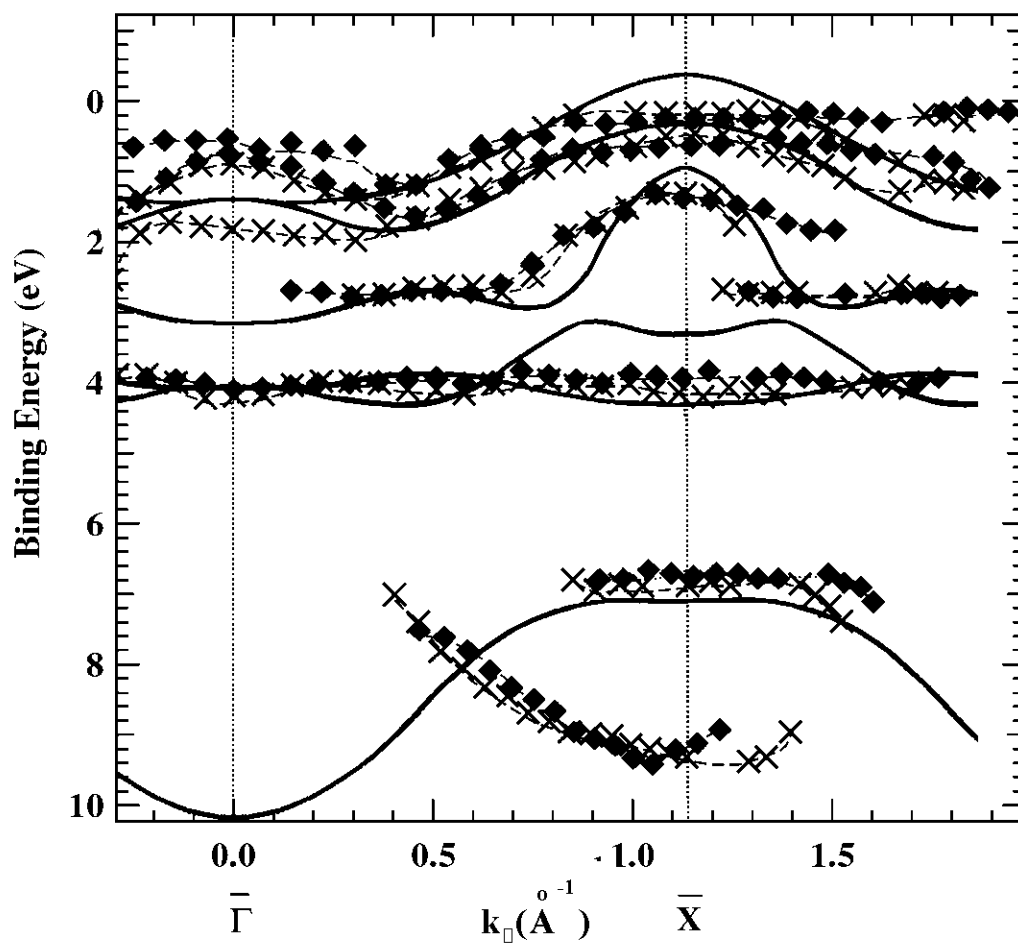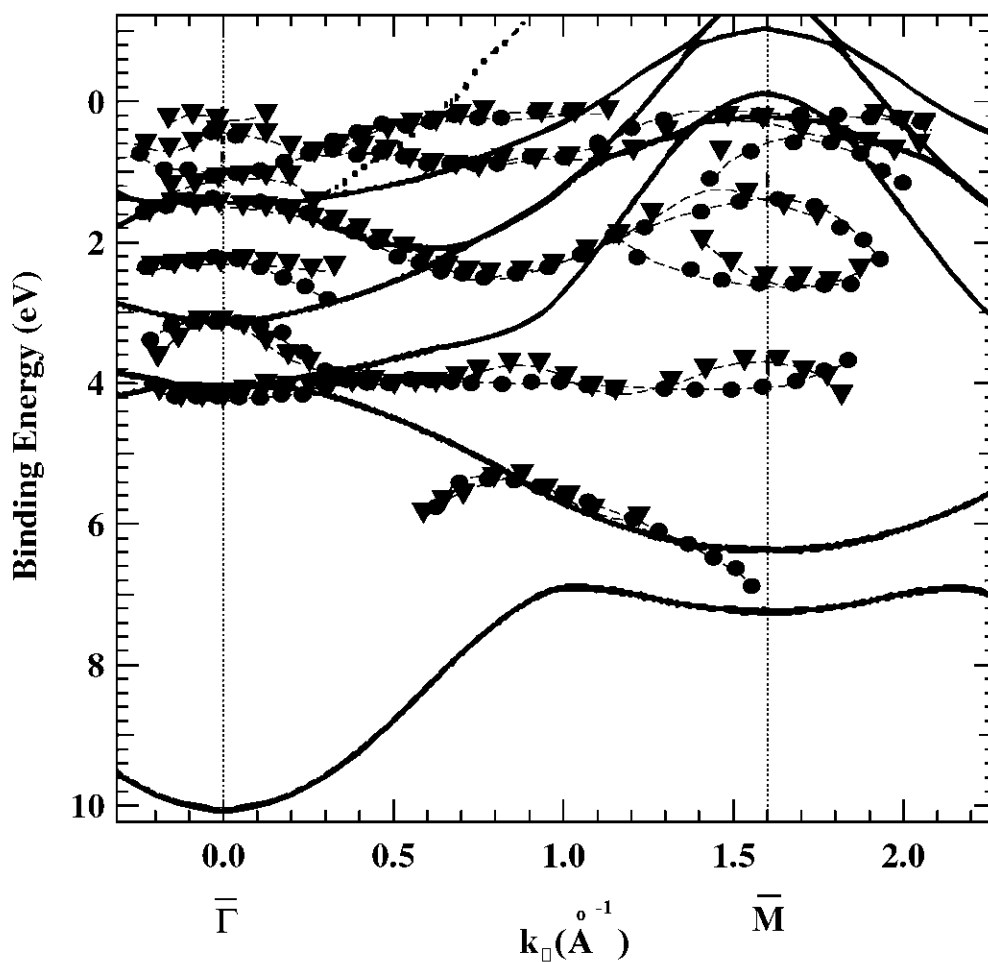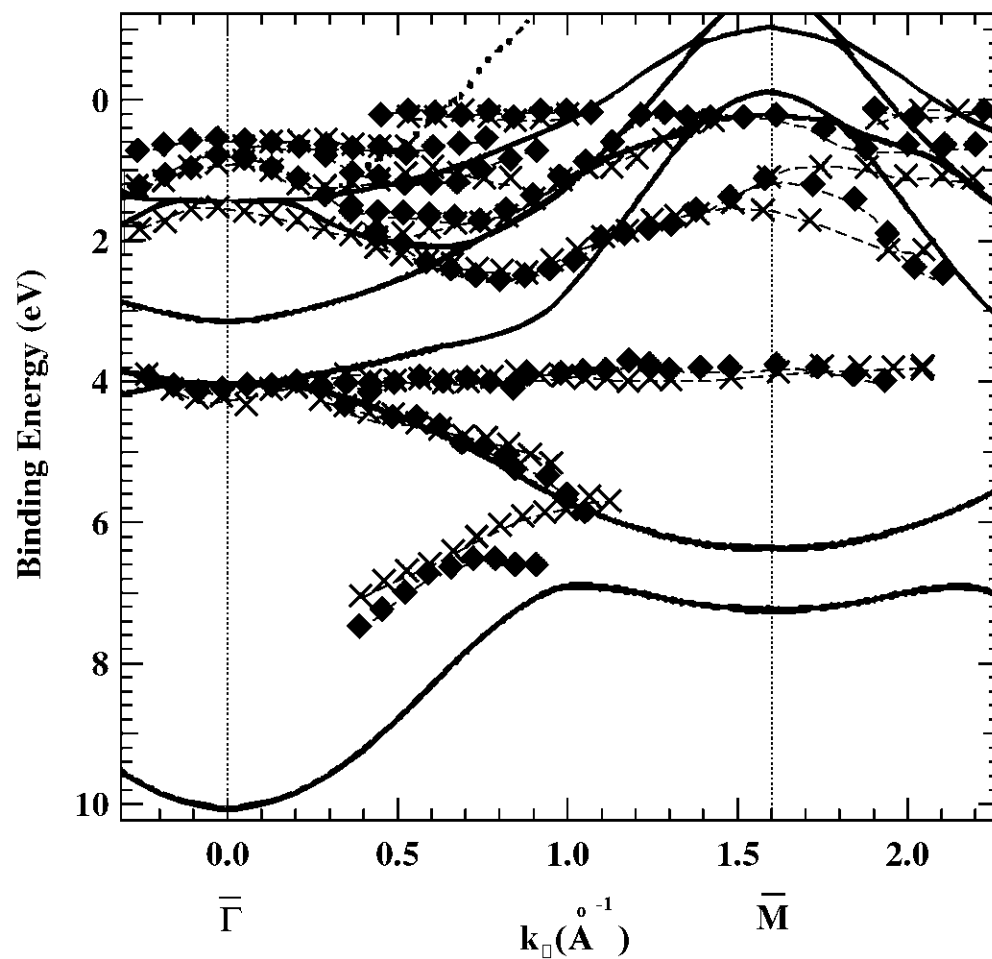t the experimental surface bands for both surfaces along the $\overline{\Gamma} - \overline{\Delta} - \overline{X}$ direction are good agreement with calculated band structure, except the bands around the $\overline{\Gamma}$ point near the Fermi edge and those around the $\overline{X}$ point at high binding energy. It is suggested that the structures from two phases present the bulk character.

The comparison of experimental surface band structures between the (5x1) and (1x1) phases along $\overline{\Gamma} - \overline{\Sigma} - \overline{M}$ direction is shown in Figs. 4.7 and 4.8. They are the experimental band structures obtained by excitation at energies 21 eV and 25 eV. From Figs. 4.7 and 4.8, we find that the overall feature of the surface band structure shows a good agreement between the (1x1) and (5x1) phases, except to the bands around the $\overline{\Gamma}$ point near the Fermi edge. Two bands are found only in the (5x1)

structure in the spectra observed excitation at energy 21 eV. When we compare experimental surface band structures observed here with the theoretical bulk band structure, we note discrepancy around the $\overline{\Gamma}$ point near the Fermi edge and the $\overline{M}$ point as shown in Figs. 4.7 and 4.8. Moreover, distinct discrepancy is found around ε_B = 4 eV over the whole range of the $\overline{\Gamma}-\overline{\Sigma}-\overline{M}$ direction.

For a more complete discussion of the experimental surface band, comparison with reported calculated surface band structures is necessary. The calculated surface band structure of Pt(100) has been reported only on the Pt(100)-(1x1) surface. We have found 2 papers regarding this. One is the surface state and surface resonance bands calculated by Benesh, Liyanage and Pingel (1990). The other is the surface energy bands calculated By Fiorentini, which has been referred by Stampfl et al. (1995) as a form of private communication. Benesh et al. have calculated surface state and surface resonance bands using the surface embedded Green function method for a semi-infinite geometry of the unreconstructed Pt(1x1) surface along $\overline{\Gamma}-\overline{\Sigma}-\overline{M}$ and $\overline{\Gamma}-\overline{\Delta}-\overline{X}$ directions. The results of their calculation are presented in Figs. 4.9 and 4.10. In Fig. 4.9, the experimental ARPES surface band structure of Pt(100)-(1x1) surface along the $\overline{\Gamma}-\overline{\Delta}-\overline{X}$ direction is compared with the surface state and surface resonance bands. We find that the calculated bands occurring in the region of 6-5.2 eV and about 3 eV do not appear in our measurement. For the bands in the $\overline{\Gamma}-\overline{\Sigma}-\overline{M}$ direction, the comparison is shown in Fig. 4.10. Agreement is found in the band, which has distinct dispersion starting around 1.6 eV. However, the disagreement is found at the high binding energy near the $\overline{\Gamma}$ point.

In the paper by Stampfl et al., the surface band structure of the clean Pt(100)-(1x1) surface calculated by Fiorentini is shown. The method of calculation is not mentioned in the paper. However, Fiorentini's band structure is more detailed. Fiorentini and Stampfl et al. suggest that the strong relativistic effects found in Pt are responsible for the hex-phase reconstruction. The comparison of calculated surface bands by Fioentini and present work is shown in Figs. 4.11 and 4.12. In these figures., the theoretical bulk band structures by Noffke and Eckard are also depicted. The general appearance of the surface band structures obtained in our experiments is different from those obtained by Fiorentini. However, the corresponding band structures along $\overline{\Gamma} - \overline{\Delta} - \overline{X}$ direction are found at $k_{\Box} \approx$ 0.3-0.7 $\overset{\circ}{A}^{-1}$ with binding energies 1.2-0.8 eV.

The last comparison is the present and reported experimental band structures from ARPES experiments. The experimental surface band structures obtained by ARPES have been reported by Stampfl et al. They have determined surface band structure for the unreconstructed Pt(100)-(1x1) phase along $\overline{\Gamma} - \overline{\Delta} - \overline{X}$ and $\overline{\Gamma} - \overline{\Sigma} - \overline{M}$ direction at various photon energies, 24 eV, 30 eV and 40 eV. The comparison experimental bands of Pt(100)-(1x1) surface from our work and those from Stampfl et al.'s work is presented in Figs. 4.13 and 4.14 for data along the $\overline{\Gamma} - \overline{\Delta} - \overline{X}$ and $\overline{\Gamma} - \overline{\Sigma} - \overline{M}$ directions, respectively. The good agreement is found in the low binding energy region for both symmetry directions. The distinct discrepancy is appeared around the $\overline{\Gamma}$ point and binding energies 6 eV. The features corresponding to these can not be found in our work.
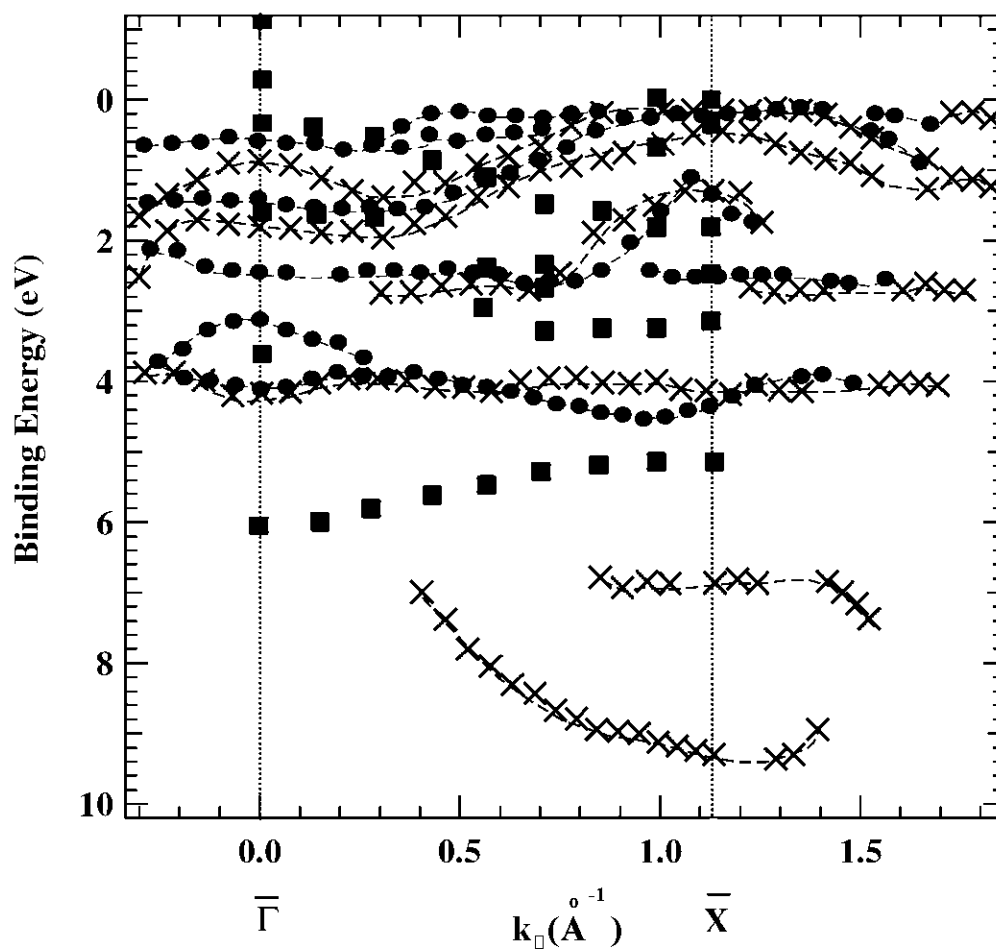
Fig. 4.9 The experimental surface band structure of Pt(100)-(1x1) surface along the

$\overline{\Delta}$ axis ($\overline{\Gamma} - \overline{X}$ direction). The solid circles and the crosses illustrate the

bands of the present work obtained by excitations at hv = 21 eV and 25

eV, respectively. The solid squares represent the surface state and surface

resonance bands calculated by Benesh, Liyange and Pingel (1990).

Fig. 4.10 The experimental surface band structure of Pt(100)-(1x1) surface along the

$\overline{\Sigma}$ axis ($\overline{\Gamma} - \overline{M}$ direction). The solid circles and the crosses illustrate the

bands of the present work obtained by excitations at $h\nu$ = 21 eV and 25

eV, respectively. The solid squares represent the surface state and surface

resonance bands calculated by Benesh, Liyange and Pingel (1990).
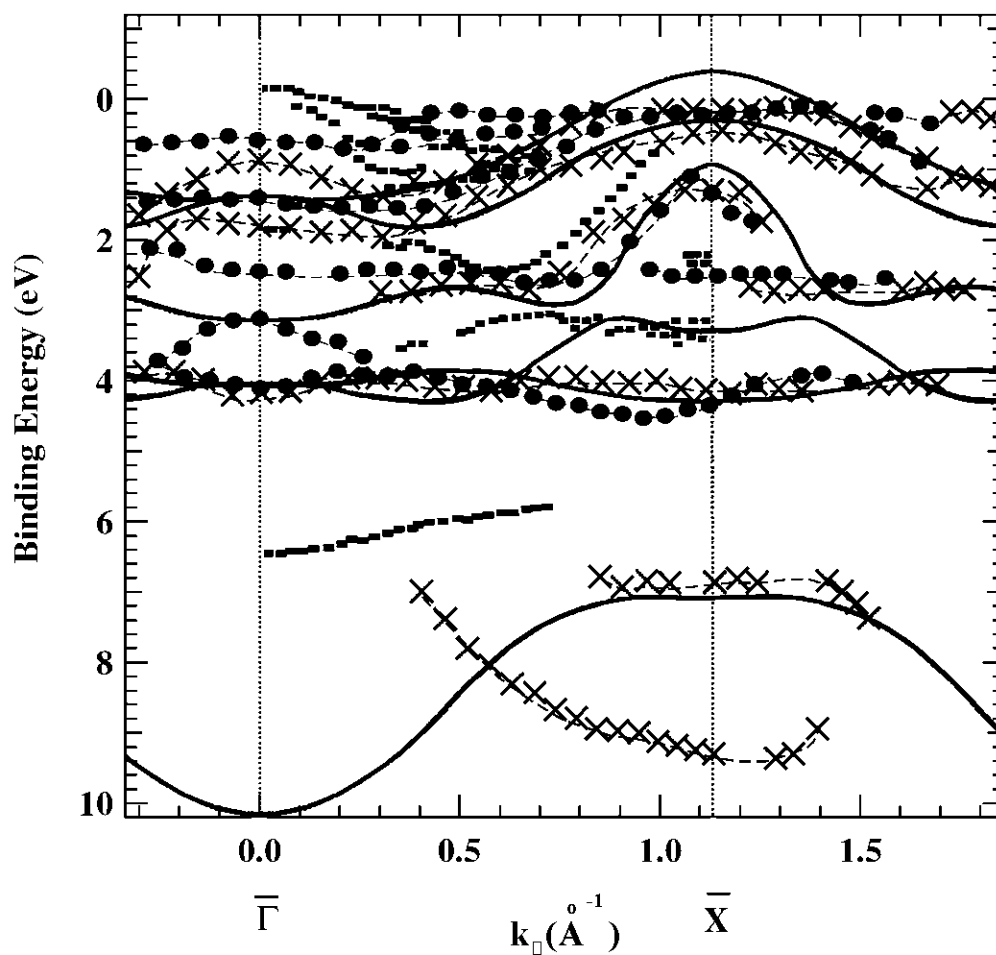
Fig. 4.11 The experimental surface band structure of Pt(100)-(1x1) surface along the

$\overline{\Delta}$ axis $\left(\overline{\Gamma} - \overline{X} \text{ direction}\right)$. The solid circles and the crosses represent the

bands of the present work measured at $h\nu = 21$ eV and 25 eV, respectively.

The solid squares are the surface bands calculated by Fiorentini (Stampfl et

al., 1995). The solid lines are the theoretical bulk bands calculated by

Noffke and Eckardt (Leschik et al., 1984).
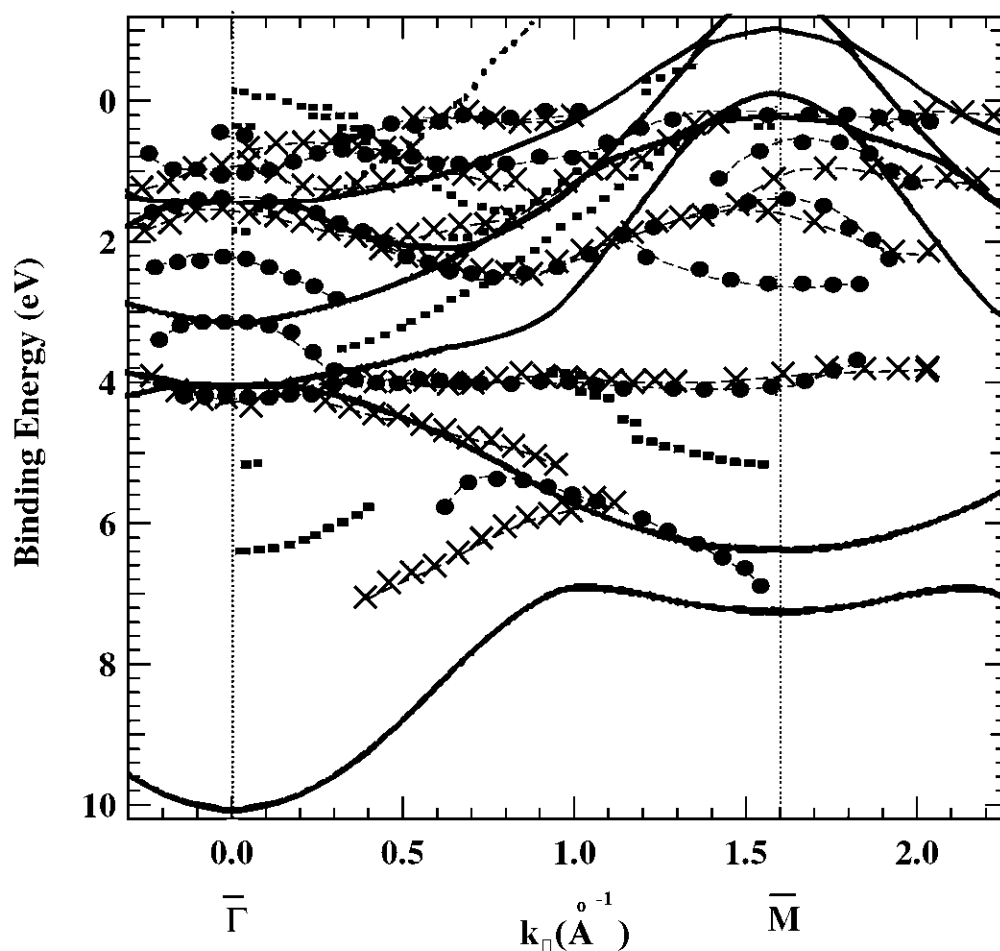
Fig. 4.12 The experimental surface band structure of Pt(100)-(1x1) surface along the

$\overline{\Sigma}$ axis $\left(\overline{\Gamma} - \overline{M} \text{ direction}\right)$. The solid circles and the crosses represent the

bands of the present work measured at $h\nu = 21$ eV and 25 eV, respectively.

The solid squares are the surface bands calculated by Fiorentini (Stampfl et

al., 1995). The solid lines are the theoretical bulk bands calculated by

Noffke and Eckardt (Leschik et al., 1984).
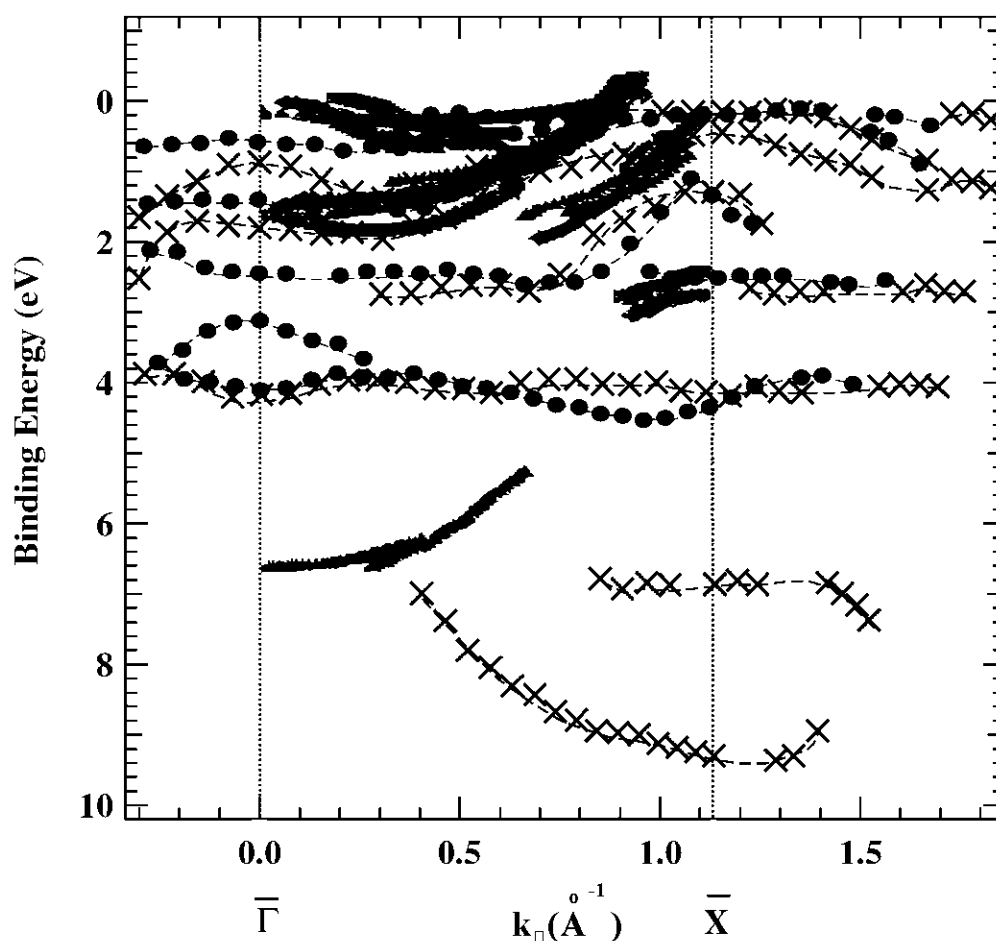
Fig. 4.13 The experimental surface band structure of Pt(100)-(1x1) surface along the

$\overline{\Delta}$ axis $\left(\overline{\Gamma} - \overline{X} \text{ direction} \right)$. The solid circles and the crosses represent the

bands of the present work measured at $h\nu = 21$ eV and 25 eV, respectively.

The black signs are the experimental surface bands of Stampfl et al. (1995)

performed by ARPES at various photon energies, $h\nu = 24$ eV (squares), $h\nu$

$= 30$ eV (daimonds) and $h\nu = 40$ eV (triangles).
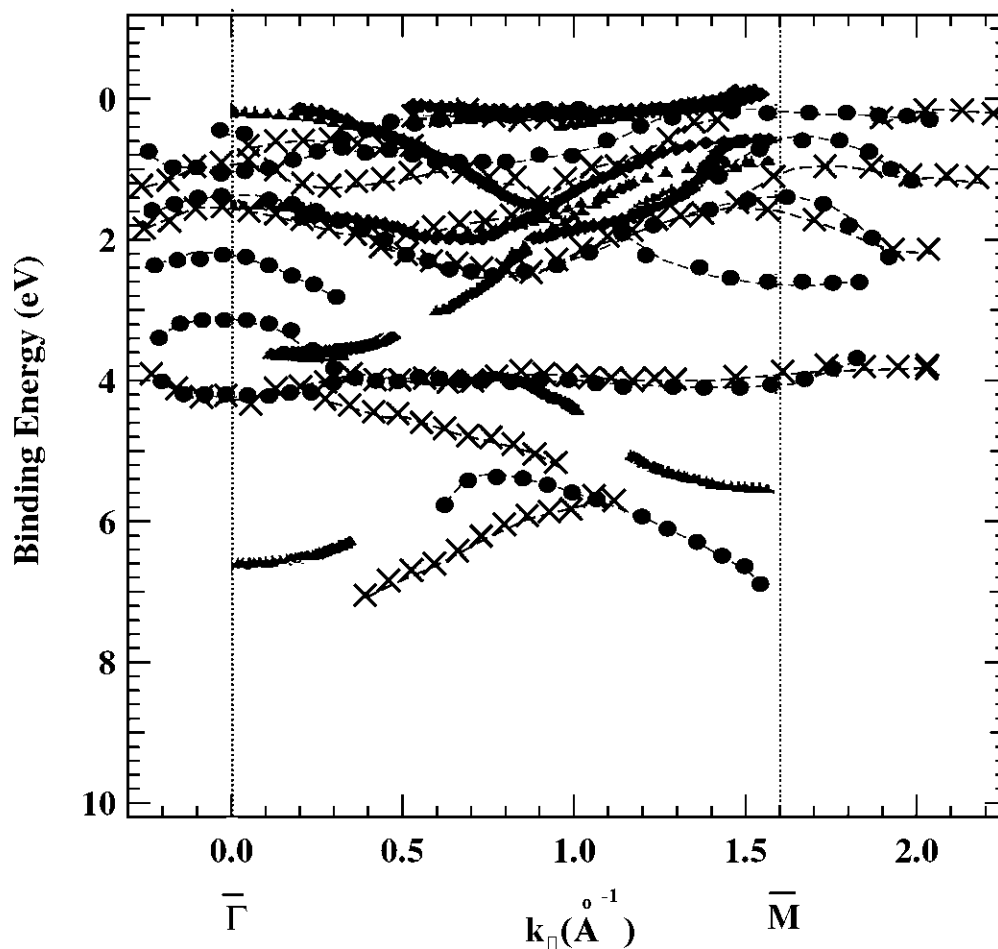
Fig. 4.14 The experimental surface band structure of Pt(100)-(1x1) surface along the

$\overline{\Sigma}$ axis $\left(\overline{\Gamma}-\overline{M}\ \text{direction}\right)$. The solid circles and the crosses represent the

bands of the present work measured at $h\nu = 21$ eV and 25 eV, respectively.

The black signs are the experimental surface bands of Stampfl et al. (1995)

performed by ARPES at various photon energies, $h\nu = 24$ eV (squares), $h\nu$

$= 30$ eV (daimonds) and $h\nu = 40$ eV (triangles).

4) In general, calculated surface energy bands cannot be reproduced by the dispersion curves, $\varepsilon_B(\mathbf{k}_!)$, observed here.

5) Stamfl et al.'s data show the independence of the band dispersion on the excitation energy. The present data show the dependence of the band dispersion on the excitation energy.

Before we proceed further discussion on the distinctive aspects of the energy bands we have observed, we should remark the nature of the surface photoemission. We have plotted the bond dispersion, $\varepsilon_B(\mathbf{k}_!)$, using the relation, (1.99) and (1.101), as

$$\varepsilon_v(\mathbf{k}) = \varepsilon_v(\mathbf{k}_!) = \varepsilon_B(\mathbf{k}_!) \qquad (1.101)$$

$$\mathbf{k}_! = \frac{1}{\hbar}\sqrt{2m\varepsilon_k}\,\sin\theta \qquad (1.99)$$

Here we must emphasize that we observe the dispersion just formally. What are observed here are

(i) Some features occurring in the angle-resolved EDCs.

(ii) Even if we observe θ dependence on ε_k featured and depict $\varepsilon_B(\mathbf{k}_!)$ using $\mathbf{k}_!$ obtained from (1.99), it is not confirmed that the resultant curves are the dispersion curves of the surface energy bands. There is the possibility that the bulk band dispersion is obtained there. Namely, the part of $\mathbf{k}_!$ is dependence of the $\mathbf{k}$ dependence. Naturally the bulk band projected on the surface can be observed. There must be the peaks of the DOS curves.

(iii) Therefore we have to confirm that what we observe is the surface-originated bands. They are not only the intrinsic surface states but the surface resonance states. The result of the energy band calculation by Fiorentini shows that the surface band almost overlaps the bulk band projected on the surface. Thus what we can observe are the surface resonance bands. The surface resonance bands may indicate the two-dimensional dependence on the crystal momentum.

(iv) In the consideration of the surface sensitivity of the photoemission processes, it is quit useful to discuss about the fraction of photoemission emitted from the surface layer which is defined as the first atomic layer of Pt (100). Suppose that light is incident on the sample at an incident angle of $\hat{\theta}$ and primary photoelectrons emitted toward the direction making an angle of θ from the surface normal are detected.

In the formula expressing the photoemission intensity, (1.53), we have to replace η with $\eta/\cos\hat{\theta}$ so that we obtain the correct formula to express the photoemission intensity. Then we integrate the corrected formula of the emission intensity to obtain the fraction of the surface emission as

$$F \equiv \frac{N(d)}{N(\infty)} = \frac{\int_0^d (dN/dz)\,dz}{\int_0^\infty (dN/dz)\,dz}$$
$$= 1 - \exp\left\{-\left(\eta l \cdot \frac{\cos\theta}{\cos\hat{\theta}} + 1\right)\frac{1}{\cos\theta}\frac{d}{l}\right\}. \tag{4.8}$$

As mentioned already, we have selected $\hat{\theta}$ as 35°. As we found in the experimental data presented in the proceeding chapter, θ varies between -10° and 32°. Thus, we have

$$1 > \cos\theta > 0.848$$
$$\cos\theta = 0.819$$
$$1.18 > \cos\theta / \cos\hat{\theta} > 1.04$$

Therefore in the expression of F, we may consider the factor $\cos\theta / \cos\hat{\theta}$ is almost unity. η is a value with an order of magnitude of 10^6 cm^{-1}. On the other hand, l takes a value between 5 $\overset{o}{A}$ and 8 $\overset{o}{A}$. Then, ηl take a value of an order magnitude of 10^{-10} to 10^{-2}. Thus, ηl can be omitted from the expression of F. Also, we approximate $1/\cos\theta$ (1.18) as 1. Therefore we have

$$F = \frac{N(d)}{N(\theta)} = 1 - \exp\left(-\frac{d}{l}\right). \tag{4.9}$$

Since d/l takes a value of 0.39 for $l = 5$ $\overset{o}{A}$ and 0.245 for $l = 8$ $\overset{o}{A}$, since the size of the first layer thickness, d, is

$$d = \frac{a}{2} = \frac{3.92}{2} = 1.96 \overset{o}{A},$$

where a is the lattice constants. Using the values given above, we obtain

$$F = 1 - \exp(-0.392) = 1 - 0.676 = 0.324 \quad \text{for} \quad l = 5 \overset{o}{A}.$$

$$F = 1 - \exp(-0.245) = 1 - 0.783 = 0.217 \quad \text{for} \quad l = 8 \overset{o}{A}.$$

This tell us that the fraction of photoelectrons emitted from the surface layer of Pt (100) is only 32% in case of the escape depth being 5 $\overset{o}{A}$ and 22% in case of the

escape depth of 8 $\overset{\circ}{\text{A}}$. Therefor the majority of the photoelectrons we accept in the energy analyzer are from the bulk crystal.

The remark we made above explain the energy band dispersion curves we obtain from the photoemission data agree with the bulk energy bands theoretically calculated. However, $\mathbf{k}_!$ in the $\overline{\Gamma} - \overline{\Sigma} - \overline{M}$ line in the surface Brillouin zone is parallel to the $\mathbf{k}_!$ in the $\Gamma - \Delta - X$ direction in the bulk Brillouin zone. Also $\mathbf{k}_!$ in the $\overline{\Gamma} - \overline{\Sigma} - \overline{M}$ line in the surface Brillouin zone is parallel to $\mathbf{k}_!$ in the $\Gamma - \Delta - K$ line in the bilk Brillouin zone. In this case, however, the sizes of the reciprocal lattice vectors are different. These relations are well depicted in Fig. 2.14.

It is also possible that the two dimensional bands we observe are the surface resonance bands if they show dispersion. However, we have not confirmed whether the two dimensional bands we obtained here are really surface-originated or not. If we observed the pure bulk band in the two dimensional mode measurements, for instance, if we observed the band along $\Gamma - \Lambda - L$, what we obtained in the bulk band projected on the surface. Therefore the contribution from the $\mathbf{k}_\perp$ components give a considerable width to the dispersion curve. If we are observing the bands that have only the $\mathbf{k}_\perp$ components, what we observe are the bands that have not dispersion along the $\mathbf{k}_!$ line.

4.4 Conclusion

The present work is summarized as following conclusion.

1) ARPES have been carried out on the reconstructed (5x1) and unreconstructed (1x1) structures of the clean Pt(100) surface.

2) The background for the research is described.

3) The experimental procedure is described in detail. There, in addition to the experimental apparatus, sample preparation and experimental procedure are explained.

4) The normal emission and surface band mapping are made on both surfaces. The results are compared each other as well as with reported results of the energy band calculation.

5) The parity selection rule combined with the polarization selection rule is used to investigate the symmetry of the initial states to be excited in photoemission processes.

References

References

Abukawa, T., Kashiwakura, T., Okane, T., Sasaki, Y., Takahashi, H., Enta, Y., Suzuki, S., Kono, S., Sato, S., Kinoshita, T., Kakizaki, A., Ishii, T., Park, C. Y. and Yu, S. W. (1992). Angle resolved photoemission study of a single-domain Si(001)2x1-K surface with synchrotron radiation: symmetry and dispersion of surface states. **Surf. Sci.** 261: 217-223.

Andersen, O. K. (1970). Electronic structure of the fcc transition metals Ir, Rh, Pt and Pd. **Phys. Rev. B.** 2 (4): 883- 906.

Andersen, O. K. and Mackintosh, A. R. (1968). Fermi surfaces and effective masses in fcc transition metals. **Solid State Commun.** 6: 285-290.

Benard, J., Berthier, Y., Delamare, F., Hondros, E., Huber, M., Marcus, P., Masson, A. Oudar, J. and Rhead, G. E. (1983). **Adsorption on metal surfaces.** New York: Elsevier Scientific Publishing Company.

Benesh, G.A., Liyanage, L.S.G. and Pingel, J.C. (1990). The surface electronic structure of (1x1) Pt(100). **J. Phys: Condens. Matter.** 2: 9065-9076.

Berglund, C.N. and Spices, W.E. (1964). Photoemission studies of copper and silver: Theory. **Phys. Rev.** 136(4A): A1030-A1044.

Boeglin, C., Carriere, B., Deville, J.P. and Scheurer, F., Guillot, C. And Barrett, N. (1992). Photoemission study of the Co/Pt(100) interface. **Phys. Rev. B.** 3834-3837.

Bonzel, H. P. and Pirug, G. (1977). Photoelectron spectroscopy of NO adsorbed on Pt(100). **Surface Sci.** 62: 45-60.

Bouchaert, L.P., Smoluchowski, R. and Wigner, E. (1936). Theory of Brillouin zones and symmetry properties of wave functions in crystals. **Phys. Rev.** 50: 58-67.

Broden, G., Pirug, G. and Bonzel, H.P. (1978). Chemisorption of CO on the unreconstructed Pt(100) surface. **Surface Sci.** 72: 45-52.

Cardona, M. and Ley, L. (eds). (1978). **Photoemission in solid I.** Berlin: Springer-Verlag.

Chang, C. S., Su, W. B., Wei, C. M. and Tsong, T. T. (1999). Large Fermi density waves on the reconstructed Pt(100) surface. **Phys. Rev. Lett.** 83 (13): 2604-2607.

Conrad, E. H. (1996). Diffraction methods. In W. N. Unertl (ed.). **Handbook of surface science; V.1.** (pp 271-360). Netherlands: Elsevier Science B.V.

Drube, R., Dose, V. and Goldmann, A. (1988). Empty electronic states at the (1x1) and (5x20) surfaces of Pt(100): An inverse photoemission study. **Surface Sci.** 197: 317-326.

Eckardt, H., Frische, L. and Noffke, J. (1984). Self-consistent relativistic band structure of the noble metals. **J. Phys. F.: Metal Phys.** 14: 97.

Feuerbacher, B. and Willis, R.F. (1976). Photoemission and electron states at clean surfaces. **J. Phys. C: Solid State Phys.** 9: 169-216.

Fiorentini, V., Methfessel, M. and Scheffler, M. (1993). Reconstruction mechanism of fcc transition metal (001) surface. **Phys. Rev. Lett.** 71 (7): 1051-1054.

Fritsche, L., Rafat mehr, M., Glocker, R. and Noffke, J. (1979) Electronic structure calculations by the linear rigorous cellular method. **Z. Phys. B.** 33, 1.

Garbe, J. and Kirschner, J. (1989). Spin-resolved photoemission from the (111) face of platinum. **Phys. Rev. B.** 39 (3): 1530-1534.

Grant, J. T. and Haas, T. W. (1969). The structure of the Pt(100) surface. **Surface Sci.** 18: 457-461.

Gunnarsson, O., Lundqvist, B. I. and Wilkins, J. W. (1974). Contribution to the cohesive energy of simple metals: Spin-dependent effect. **Phys. Rev. B.** 10:1319-1327.

Hagstrom, S., Lyon, H. B. and Somorjai, G. A. (1965). Surface structures on the clean platinum (100) surface. **Phys. Rev. Latt.** 15 (11): 491-493.

Heilmann, P., Heinz, K. and Müller, K. (1979). The superstructures of the clean Pt (100) and Ir(100) surfaces. **Surface Sci.** 83: 487-497.

Heine, V. (1960). **Group theory in quantum mechanics.** London: Pergamon Press.

Hermanson, J. (1977). Final-state symmetry and polarization effects in angle-resolved photoemission spectroscopy. **Solid State Comm.** 22: 9-11.

Hori, Y., Igarashi, N., Ito, K., Kakizaki, A., Kobayashi, Y., Murakami, Y., Tomita, N., Watanabe, N. and Yagishita, A. (eds). (1999). **Photon factory activity report 1998.** Ibaraki: High Energy Accelerator Research Organization (KEK).

Hüfner, S. (1996). **Photoelectron spectroscopy** (2nd ed). Berlin: Springer-Verlag.

Inoue, S.T., Asano, S. and Yamashita, J, (1971). Crystal potentials and the Fermi surface of the alkali metals (I). **J. Phys. Soc. Jpn.** 30:1546-1554.

Irmer, N., David, R., Schmiedeskamp, B. and Heinzmann, U. (1992). Experimental verification of a spin effect in photoemission: Polarized electrons due to phase-shift differences in the normal emission from Pt(100) by unpolarized radiation. **Phys. Rev. B.** 45 (7): 3849-3852.

Ishii, T. (1989) Solid state spectroscopy in the vacuum ultraviolet and soft x-ray region. In H. Winick, D. Xian, Ming-han Ye and T. Huang (eds). **Applications of synchrotron radiation** (pp 371-514). New York: Gordon and Breach Science Publishers.

Jennings, P. J. (1992). Low energy electron diffraction. In D. J. O'Connor, B. A. Sexton and R. St. C. Smart (eds.). **Surface analysis methods in materials science** (pp 275-289). Berlin: Springer-Verlag.

Kevan, S.D. (1992). **Angle-resolved photoemission.** Netherlands: Elesvier Science Publishers B.V.

Kittel, C. (1963). **Quantum theory of solids.** New York: John Wiley & Sons, Inc.

Kittel, C. (1967). **Introduction to solid state physics**. New York: John Wiley & Sons, Inc.

Kittel, C. (1991). **Introduction to solid state physics (6th ed.).** Singapore: John Wiley & Sons, Inc.

Knox, R. S. (1963). **Theory of exitons in solid state physics.** New York: Academic Press.

Leschik, G., Courths, R., Wern, H. and Hüfner, S., Eckardt, H. and Noffke, J. (1984). Band structure of platinum from angle resolved photoemission experiments. **Solid State Commun.** 52 (2): 221-225.

Leroux, C., Cadeville, M.C., Peierron-Bohnes, V., Inden, G. and Hinz, F. (1988). Comparative of $L1_o$ NiPt and CoPt phases; the role for magnetism. **J. Phys. F : Met. Phys.** 18: 2033-2051.

Lin, M. T., Kuo, C.C., Her, H. Y., Wu, Y.E., Tsay, J.S. and Shern, C.S. (1999). Giant enhancement of magneto-optical response and increase in perpendicular

magnetic anisotropy of ultrathin Co/Pt(111) films upon thermal annealing. **J. Vac. Sci. Technol.** A17(5):3045-3050.

Lyon, H. B. and Somorjai, G. A. (1967). Low-energy electron-diffraction study of the clean (100), (111) and (110) faces of platinum. **J. Chem. Phys.** 46 (7): 2539-2550.

Mackintosh, A. R. (1966). **Bull. Am. Phys. Soc**. 11, 215.

Mahan, G.D. (1975). Theory of photoemission in simple metals. **Phys. Rev. B.** 2: 4334-4350.

Mills, K.A., Davis, R.F., Kevan, S.D., Thornton, G. and Shirley, D.A. (1980). Angle-resolved photoemission determination of Λ-line valence bands in Pt and Au using synchrotron radiation. **Phys. Rev. B.** 22 (2): 581-592.

Morgan, A. E. and Somorjai, G. A. (1968). Low energy electron diffraction studies of gas adsorption on the platinum (100) single crystal surface. **Surface Sci.** 12: 405-4025.

Morgan, A. E. and Somorjai, G. A. (1969). Low energy electron diffraction studies of the adsorption of unsaturated hydrocarbons and carbon monoxide on the platinum (111) and (100) single crystal surface. **J. Chem. Phys**. 51 (8): 3309-3321.

Morikawa,Y., Kobayashi, K., Terakura, K. and Blügel, S. (1991). Theoretical support to the double-layer model for potassium adsorption on the Si(001) surface. **Phys. Rev. B.** 44: 3459-3462.

Moruzzi, V. L., Janak, J. F. and Williams, A. R. (1978) **Calculated electronic properties of metals.** New York: Pergamon.

Needs, R. J. and Mansfield, M. (1989). Calculations of the surface stress tensor and surface energy of the (100) surfaces of iridium, platinum and gold. **J. Phys: Condens. Matter.** 1: 7555-7563.

Fritsche, L., Noffke, J., and Eckardt, H. (1987). A relativistic treatment of interacting spin-aligned electron systems: application to ferromagnetic iron, nickel and palladium metal. **J. Phys. F. : Metal Phys.** 17: 943.

O'Connor, D. J., Sexton, B. A. and Smart, R. St. C. (eds.). (1992). **Surface analysis methods in materials science.** Berlin: Springer-Verlag.

Ono, K. (2003). **BL-11C Solid state spectroscopy beam line** [On-line]. Available: http://pfwww.kek.jp/users_info/users_guide_e/station_spec_e/bl11c.pdf

Palmberg, P.W. and Rhodin, T. N. (1967). Surface structure of clean Au (100) and Ag (100) surfaces **Phys. Rev**. 161:586.

Ray, P. N., Chowdhuri, J. and Chatterjee, S. (1983). Electronic energy bands and optical properties of Ir and Pt. **J. Phys. F: Met. Phys.** 13: 2569-2580.

Ritz, G., Schmid, M., Varga, P. Borg, A., Ronning, M. (1997). Pt(100) quasihaxagonal reconstruction: A comparison between scanning tunneling microscopy data and effective medium theory simulation calculations. **Phys. Rev. B.** 56(16): 10518-10525.

Rodriguez, J. A. and Kuhn, M. (1995). Chemical and electronic properties of Pt in bimetallic surfaces: Photoemission and CO-chemisorption studies for Zn/Pt (111). **J. Chem. Phys.** 102 (10): 4279-4289.

Rhead, G. E. (1973). On the anomalous surface structures of gold and platinum. **J. Phys. F: Met. Phys.** 3: L53-L56.

Seitz, F. (1940). **Modern theory of solids.** New York: McGraw-Hill, Inc.

Slater, J.C. (1965). **Quantum theory of molecules and solids (Vol. II).** New York: McGraw-Hill, Inc.

Smith, N.V. (1974). Photoemission spectra and band structure of *d*-band metals. III. Model band calculations on Rh, Pd, Ag, Ir, Pt and Au. **Phys. Rev. B.** 9(4): 1365-1376.

Smith, N.V., Wertheim, G.K., Höfner, S. and Traum, M.M. (1974). Photoemission spectra and band structures of d-band metal. IV. X-ray photoemission spectra and densities of states in Rh, Pd, Ag, Ir, Pt and Au. **Phys. Rev. B.** 10 (8): 3197-3206.

Soda, K., Mori, T., Onuki, Y., Komatsubara, T. and Ishii, T. (1988). Optical density of states of valence electrons in $CeCu_2Si_2$. **J. Phys. Soc. Japan.** 57: 1699-1706.

Somorjai, G.A. (1967). Note to the paper by D.G. Fedak and N.A. Gjostein, on the anomalous surface structure of gold. **Surface Sci.** 8: 98-100.

Spicer, N.E. and Krolikowski, W.F. Photoemission studies of the nobel metal: I. Copper. **Phys. Rev**. 185 (3): 882-900.

Stampfl, A. P. J., Martin, R., Gardner, P. and Bradshaw, A. M. (1995). Electronic band structure of the Pt{100} surface. **Phys. Rev. B.** 51 (15): 10197-10200.

Tamura, E., Piepke, W. and Feder, R. (1989). Spin-resolved photoemission from (111) surfaces of Pd, Ir and Pt by circularly polarized light: theory and comparison with experiment. **J. Phys.: Condens. Matter.** 1: 6469-6482.

Thiry, P., Chandesris, D., Lecante, J., Guillot, C., Pinchaux, R. and Petroff, Y. (1979). E vs **k** and inverse lifetime of Cu(110). **Phys. Rev. Lett.** 43 (1): 82-85.

Thornton, G., Davis, R.F., Mills, K.A. and Shirley, D.A. (1980) An angle-resolved photoemission determination of the band-structure of platinum between Γ and X. **Solid State Commun.** 34: 87.90.

Van Hove, M. A., Koestner, R. J., Stair, P. C., Biberian, J. P., Kesmodel, L. L., Bartos, I. and Somorjai, G. A. (1981). The surface reconstructions of the (100) crystal faces of iridium, platinum and gold. **Surface Sci.** 103: 189-217.

Venus, D., Garbe, J., Suga, S., Schneider, C. and Kirschner, J. (1986). Hybridization of electronic bands along the <110> axis in platinum observed by spin-polarized, momentum-resolved photoemission. **Phys. Rev. B.** 34 (12): 8435-8443.

Weller, D. (1996). **Spin-orbit influenced spectroscopies of magnetic solids.** Heidelberg: Springer-Verlag.

Wern, H., Courths, R. , Leschik, G. and Hüfner, S. (1985). On the band structure of silver and platinum from angle-resolved photoelectron spectroscopy (ARPES) measurements. **Z. Phys. B-Condensed Matter.** 60: 293-310.

Wild, K. (1981). Auger electron spectroscopy (AES) for surface analysis. **Vacuum**. 3: 183-194.

Ziman, J. M. (1963). **Principles of the theory of solids.** London: Cambridge University Press.

Curriculum Vitae

Miss Wichuda Suraban

Date of birth :   August 17, 1967

Nationality :   Thai

Address :   Department of Physics, Faculty of Science Srinakharinwirote

University 114 Sukumvit 23, Watthana Bangkok 10110, Thailand.

Education

Academic year

1986-1989   Bachelor of Education (Science-Physics)

Srinakharinwirote University, Bangkok, Thailand.

1990-1994   Master of Science (Physics)

Srinakharinwirote University, Bangkok, Thailand.

1999-2003   Ph.d. in Physics.

Suranaree University of Technology.

Nakhon Ratchasima, Thailand.

Academic Experience

1994-1997   Lecturer, Faculty of Science

The University of Thai Chamber of Commerce.

Bangkok, Thailand.

1998-at present   Lecturer, Department of Physics, Faculty of Science.

Srinakharinwirote University, Bangkok, Thailand.